Developing novel non-invasive MRI techniques to assess cerebrospinal fluid-interstitial fluid (CSF-ISF) exchange

Payam Nahavandi

Centre for Advanced Biomedical Imaging (CABI)

Division of Medicine

UCL

A thesis submitted for the degree of Doctor of Philosophy

Declaration

I, Payam Nahavandi, confirm that the work presented in this thesis is my own. Where information has been derived from other sources, I confirm that this has been indicated in this thesis.

Payam Nahavandi

30th October 2019

Abstract

The pathological cascade of events in Alzheimer's disease (AD) is initiated decades prior to the onset of symptoms. Despite intensive research, the relative time-course/interaction of these events is yet to be determined. Recent evidence suggests that impairments to brain clearance (facilitated by the compartmental exchange of cerebrospinal-fluid (CSF) with interstitial-fluid (ISF)), contributes to the build-up of amyloid and tau (AD hallmarks). Therefore, abnormalities in CSF-ISF exchange dynamics, may represent an early driver of downstream events.

Clinical evaluation of this hypothesis is hampered due to the lack of non-invasive CSF-ISF exchange assessment techniques. In this thesis, the primary aim was to develop a physiologically relevant, non-invasive CSF-ISF exchange assessment technique that would circumvent the limitations associated with current procedures (primarily their invasiveness). Towards this goal, animal studies were conducted to investigate the feasibility of a contrast enhanced-magnetic resonance imaging (CE-MRI) approach as a potential non-invasive CSF-ISF exchange imaging technique. Another aim of this thesis was to investigate whether the proposed MRI platform could detect abnormalities in CSF-ISF exchange, a condition hypothesised to occur in the early stages of AD. As such, pharmacological intervention studies were conducted to alter CSF-ISF exchange dynamics.

CE-MRI, in conjunction with high-level image post-processing, demonstrated high sensitivity to physiological CSF-ISF exchange. This novel, non-invasive platform, captured dynamic, whole-brain infiltration of contrast agent from the blood to the CSF and into the parenchyma, via a pathway named 'VEntricular-Cerebral TranspORt (VECTOR)'. Additionally, the platform detected significant abnormalities in CSF-ISF exchange following pharmacological intervention, demonstrating the potential of VECTOR in the study of the parenchymal accumulation of aberrant proteins.

Development of this platform is a breakthrough step towards the clinical assessment of CSF-ISF exchange abnormalities to study its role in disease onset/progression, an approach that may inform understanding of the causal sequence of pathological events that occurs in AD development.

Impact statement

Alzheimer's disease (AD) is a fatal neurodegenerative condition that presents with cognitive impairment and memory loss. Since the incidence of AD is climbing to epidemic proportions (driven by the global ageing population growth), it is vital to develop early, sensitive and clinically relevant biomarkers towards development of more effective therapeutic strategies.

Despite having a very high metabolic demand, the brain lacks a traditional lymphatic system (the system that clears toxins, waste and other unwanted materials from the body). Hence, for decades scientists were puzzled regarding how toxins and waste products are cleared from the brain until recent pre-clinical (animal) studies (using invasive surgical procedures) discovered brain specific clearance pathways/mechanisms, which they coined the 'glymphatic' system. Scientists also provided evidence that impairments to the brains' glymphatic clearance system, leads to the build-up of toxic proteins that are implicated in AD and hence may contribute to disease onset/progression.

Hence, due to the links between impaired brain clearance function and disease onset/progression, it is vital to develop a non-invasive, clinically relevant technique for the assessment of brain clearance function.

In this project, a non-invasive platform for imaging brain clearance function was developed (using only MRI and intravenous delivery of clinically available contrast agents) towards an early non-invasive biomarker of AD. This platform provides the potential opportunity to assess the sensitivity of the new brain clearance functional biomarker, compared to current biomarkers of AD. Translation of this platform to the clinical setting, if successful, may revolutionise the way brain clearance function is assessed due to the non-invasiveness and the non-ionizing nature of the assessment, which minimises post assessment side effects and improves care and recovery of patients (e.g. by reducing the risk of post-operative infection). As for the clinicians, this platform eliminates the need for invasive techniques (such as cranial window) where the risks of complications are higher. This novel technique will also reduce the cost to the health care system, firstly due to lower procedure costs (simpler assessment technique requiring only MRI and contrast agents, which are widely available in the clinic) but also due to lower after-care (in-patient) costs (e.g. patients will be more capable/independent in performing routine tasks and will therefore be able to return home sooner).

Acknowledgements

My PhD has taken me on a remarkable journey that cannot be described by words, somehow similar to a roller-coaster ride. Not only it has provided me with immaculate academic skills that I will carry with me in the future, but it has also transformed me from an inexperienced undergraduate student to an independent and capable individual, and for that I am indebted to many people who supported me in this journey.

I would like to say huge thanks to my supervisor Prof. Mark Lythgoe for the opportunity to conduct the research described in this thesis in his laboratory. CABI fosters a pleasant work environment and I could not have asked for a better working environment for my PhD studies. I'm grateful for Mark's incredible flexibility and patience, but most importantly, the trust he put in me in becoming an independent scientist.

The next person who I'd like to acknowledge, is my second supervisor, Dr. Jack Wells. Jack is one of the most patient, kind and thoughtful persons I've come across and I'm grateful for his extensive support, which pulled me through my PhD. I cannot thank Jack enough.

I would like to thank all my colleagues at CABI. An extra special mention to: Matin Mohseni, Ian Harrison, Arun Niranjan, Yolanda Ohene, Phoebe Evans, Ozama Ismail, Yichao Yu, Tom Carson, John Connell, Tammy Kalber, Stephen Patrick, May thin, Daniel Stuckey, Ben Hipwell, Natalie Holroyd, Claire Walsh, Da Ma and Morium Ali.

I would also like to thank all my close friends and family. The strongest thanks goes to my parents for supporting me in this journey and through difficult times. Thanks to my sister, my grandmother and especially my uncle for all their love and positive energy that kept me inspired.

Publications arising from research conducted in the context of this thesis

P Nahavandi, A Niranjan, IF Harrison, Y Ohene, D Ma, O Ismail, TK Murray, Z Ahmed, MJ O'Neill, SG Solomon, MF Lythgoe, JA Wells. fMRI in the rTg4510 Model of Tauopathy: Tau-Driven Pathology Does Not Impair Functional Hyperaemic Response to Visual Stimuli; *Scientific Reports* (under review).

P Nahavandi, IF Harrison, JJ Connell, MZ Thin, TL Kalber, SP Patrick, P Evans, Y Ohene, O Ismail, T Marczylo, A Laycock, JA Wells, MF Lythgoe. Brain-wide Ventricular-Cerebral Transport (VECTOR) Imaged by Non-invasive Dynamic MRI; manuscript in preparation.

Y Ohene, IF Harrison, **P Nahavandi**, O Ismail, EV Bird, OP Ottersen, EA Nagelhus, DL Thomas, MF Lythgoe, JA Wells. Non-invasive MRI of brain clearance pathways using multiple echo time arterial spin labelling: an aquaporin-4 study. *Neuroimage*. 2019 Mar;188:515-523.

IF Harrison, B Siow, AB Akilo, PG Evans, O Ismail, Y Ohene, **P Nahavandi**, DL Thomas, MF Lythgoe, JA Wells. Non-invasive imaging of CSF-mediated brain clearance pathways via assessment of perivascular fluid movement with diffusion tensor MRI; *Elife.* 2018;7:e34028.

PG Evans, M Sokolska, A Alves, IF Harrison, Y Ohene, **P Nahavandi**, O Ismail, E Miranda, MF Lythgoe, DL Thomas, JA Wells. Non-Invasive MRI of Blood-Cerebrospinal Fluid Barrier Function; *Nature Communications* (under review).

IF Harrison, O Ismail, A Machhada, N Colgan, JA Wells, Y Ohene, **P Nahavandi**, Z Ahmed, A Fisher, S Meftah, TK Murray, RA Johnson, EC Collins, MJ O'Neill, MF Lythgoe. Impaired Glymphatic Function and Clearance of Tau in an Alzheimer's Disease Model; *Brain* (under review).

Y Ohene, IF Harrison, O Ismail, **P Nahavandi**, P Evans, DL Thomas, MF Lythgoe, JA Wells. Increased Blood-Brain Barrier Permeability to Water in a Mouse Model of Ageing measured using non-invasive Multiple Echo Time Arterial Spin Labelling; manuscript in preparation.

Table of Contents

Index of Figures

Index of Tables

Chapter 1: Alzheimer's disease and the cerebrospinal fluid-interstitial fluid (CSF-ISF) exchange

It is believed that impairments in brain's ability to remove aberrant brain proteins that define many neurodegenerative conditions, leads to build-up of these harmful proteins and therefore contributes to the onset and/or progression of disease. One such brain-cleaning system relies on the compartmental exchange of CSF with ISF for the transport and drainage of proteins/solutes in the brain (i.e. CSF-mediated solute transport). Currently, the routine clinical assessment of such brain clearance function (i.e. CSF-ISF exchange) has been hampered due to lack of non-invasive techniques. Hence, in this PhD project, the main focus was to develop a non-invasive technique for the assessment of CSF-ISF exchange. In this chapter, I will therefore provide a brief overview of the CSF-ISF exchange literature, but beforehand, I will provide a brief overview of Alzheimer's disease as it's of particular interest in this PhD project.

1.1 Introduction

Alzheimer's disease (AD), named after Alois Alzheimer, the doctor who initially described the disease is an extremely destructive brain dementia characterised by loss of neuronal cells and brain tissue. It's one of the most common forms of dementia which affects a large population of adults worldwide. Its main symptoms interfere with daily activities and include cognitive impairment, loss of memory, problem solving difficulties and confusion. First described over a century ago, there is still no cure for this devastating disease despite all efforts. From the onset of clinical symptoms, it usually takes about 8.5 years on average until ones death (Francis *et al*., 1999). Figure 1.1 broadly illustrates some abnormalities associated with an AD brain.

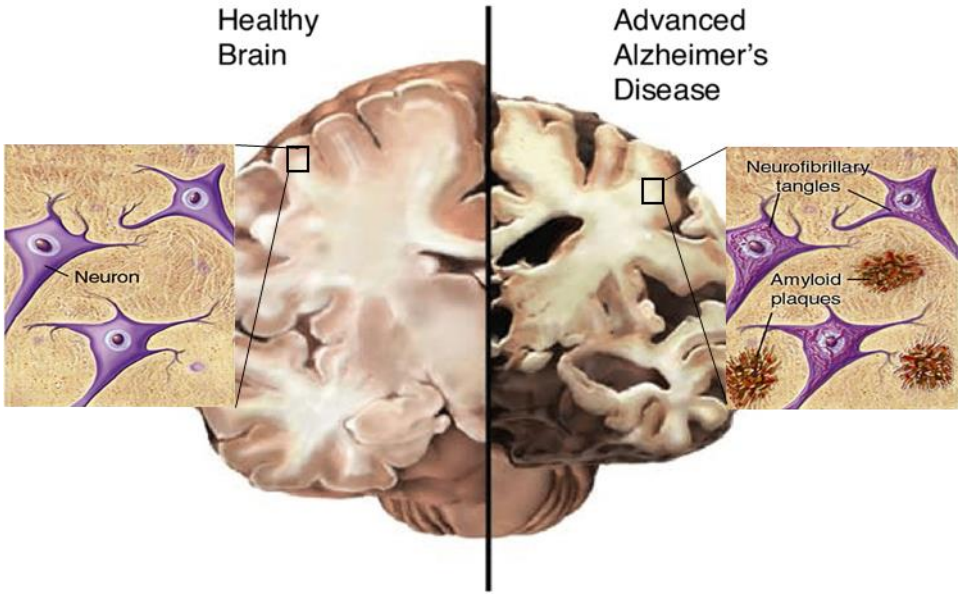

Figure 1.1: Healthy brain (left) against advanced Alzheimer's disease brain (right). AD brain is characterised by brain shrinkage and loss of neuronal cells. Intra-cellular neurofibrillary tangles and extracellular amyloid plaques are histopathological hallmarks of an AD brain. (Images adopted from www.alz.org *&* www.brightfocus.org*)*

Extracellular deposits of amyloid plaques as well as intracellular neurofibrillary tangles of hyperphosphorylated tau (NFTs) are histopathological hallmarks of AD revealed by post-mortem analysis (Graeber *et al*., 1977). These findings were crucial in our understanding of AD and the advancements that have been made regarding early disease detection and management. The rest of this chapter will therefore focus on hypotheses describing some of the mechanisms underlying the disease as well as the diagnostic strategies and the associated biomarkers.

1.2 Alzheimer's disease diagnosis/biomarkers

It is now believed that the cascade of pathological events in AD are initiated several decades before the onset of clinical symptoms (Bateman *et al*., 2012, Masters *et al*., 2015). This window provides a great opportunity for medical intervention and reversing the disease phenotype before considerable irreversible damage occurs. Therefore, an early diagnosis of AD is required for planning possible treatment strategies and supportive counselling. Currently, there is no definitive method of confirming AD in a patient until post-mortem autopsy examination (although a clinical diagnosis of AD while the patient is alive may be possible with an accuracy of up to 90% utilising the currently available CSF biomarkers - section 1.2.1). Hence, careful clinical evaluation of the patient's history and symptoms is key for an accurate clinical diagnosis of the disease. This requires access to patients' medical and familial

records (50% increased risk of developing the disease in familial AD) as well as mental status and neurological tests, such as the mini mental state examination (MME). MME is a common measure of cognitive impairment indicating the progression and severity of the disease. MME is a neurological test for dementia (Tombaugh & McIntyre, 1992) and as a result the clinical evaluation of AD is often inconclusive, leading to classification as mild cognitive impairment (MCI) (MCI is defined as the intermittent phase between normal aging process and the earliest signs of dementia). Those diagnosed with MCI carry 50% increased risk of developing dementia (AD or other forms of dementia) within a few years (Gauthier *et al*., 2006). The clinical evaluation of AD can therefore be ambiguous and as a result considerable efforts have been made towards the development of biomarkers that offer heightened sensitivity to early pathological processes that precede clinical symptoms and cognitive impairment. An early diagnosis has been posited to be hugely beneficial to emerging therapeutic strategies which may be effective during the early stages of the disease. Additionally, early diagnosis allows patients and their families more time to better manage and plan the future.

Identifying a biomarker that exhibits all ideal characteristics such as non-invasiveness, non-ionizing, high sensitivity, high specificity and reproducibility, is challenging. However, there are currently several AD biomarkers which are sensitive to unique early neuropathological changes and may therefore be useful for an early diagnosis of disease (Jack *et al*., 2010).

1.2.1 Cerebrospinal fluid (CSF) biomarkers

Perhaps the most sensitive biomarker of AD at this moment in time is CSF sampling for traces of amyloid-beta (1-42), total tau and phosphorylated tau (Blennow and Zetterberg, 2009). Total tau and phosphorylated tau are markers of neuronal injury/tau phosphorylation whereas amyloid-beta (1-42) is a marker of plaque formation. In fact, several studies have reported abnormal tau and amyloid concentrations in the CSF of AD patients (Blennow and Hampel, 2003, Andreasen and Blennow, 2005). CSF biomarkers have relatively high sensitivity and specificity (80-90% in discriminating between AD patients and healthy controls (Blennow and Hampel, 2003, Andreasen and Blennow, 2005)). A limitation of this biomarker however is the need for a lumbar puncture, in other words its invasiveness. Also, there is a problem in terms of limited affinity to clinical status later in life (e.g. some studies have shown that the levels of CSF tau and Aβ42 do not change substantially over time in symptomatic AD patients and therefore there is no strong correlation between the severity of the disease stage and the levels of the CSF biomarkers

(Buchhave *et al*., 2009)). This limitation complicates disease staging and the early accurate diagnosis of AD (i.e. before clinical symptoms emerge). The limitations associated with CSF biomarkers (principally their invasiveness) reduces their clinical utility and therefore non-invasive imaging techniques with deep body imaging capabilities such as MRI and positron emission tomography (PET) have gained much interest.

1.2.2 MRI biomarkers

MRI techniques that have been widely explored as potential biomarkers of AD include structural, functional, diffusion and perfusion MRI. Structural MRI provides a measure of cerebral atrophy and neurodegeneration, functional MRI provides an indirect measure of neuronal activity (via MR signal changes due to changes in blood flow), diffusion tensor imaging is a measure of microstructural changes (often in white matter) and perfusion MRI is a measure of cerebral perfusion (Frisoni *et al*., 2010, Sperling, 2011, Ewers *et al*., 2011, Bozzao *et al*., 2001). Although these biomarkers have all been widely explored in the clinical setting, there are concerns regarding the reliability and reproducibility of functional, diffusion and perfusion MRI biomarkers (specifically due to inconsistent findings in individuals at-risk for AD (i.e. prior to the emergence of clinical symptoms), including subjects with MCI (Sperling, 2011, Sheikh-Bahaei *et al*., 2017, McConathy and Sheline, 2015, Bayram, Caldwell, and Banks, 2018, Hays, Zlatar and Wierenga, 2016)). At this moment in time, structural MRI is the most established AD MRI biomarker where marked differences are detected between a healthy and an AD brain.

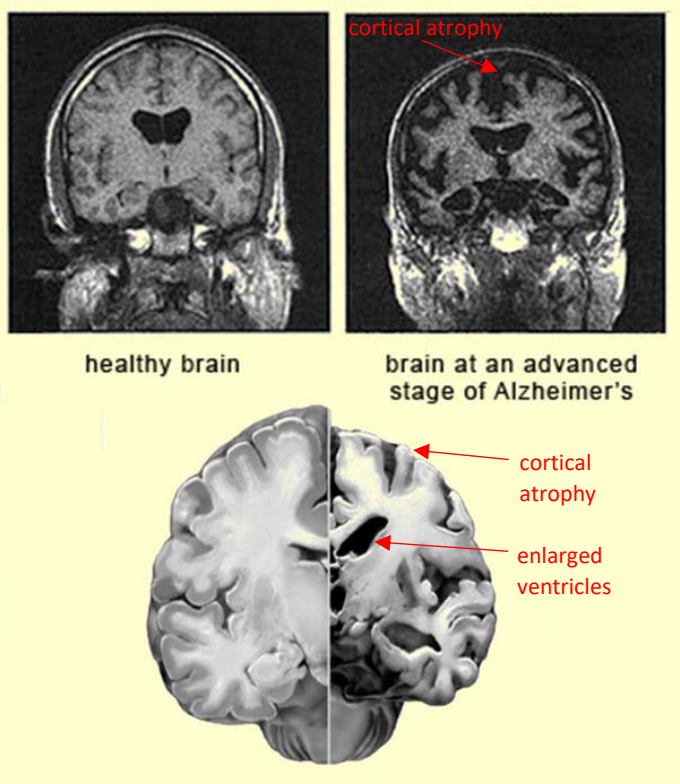

Figure 1.2: Structural MRI of a healthy brain (left) against an AD brain (right) where cortical atrophy is readily visualised. Autopsy of AD brain clearly demonstrates cerebral atrophy together with enlarged ventricles (bottom). (Image adapted from https://thebrain.mcgill.ca/)

Although cerebral atrophy and structural differences are readily visualised on structural MRI between a healthy and an AD brain, these changes are only detected at later stages of the disease where the disease has greatly progressed. Additionally, cerebral atrophy is not unique to AD and occurs in several other neurodegenerative diseases. Hence, structural MRI is regarded as a biomarker of neuronal injury and not an early biomarker of AD (compared to histopathological amyloid and tau deposition for example).

1.2.3 PET biomarkers

A non-invasive imaging technique that can provide indirect measure of amyloid and tau deposition is positron emission tomography (PET). PET is sensitive to radiolabelled tracers that can specifically bind to amyloid plaques or NFTs, namely amyloid and tau PET tracers. In amyloid and tau PET scans, abnormally high signal intensity could be indicative of AD (indirect measure of amyloid/tau deposition – figure 1.3) (Ishii, 2013, Okamura *et al*., 2018).

The first tracer used for imaging amyloid burden was the carbon-based tracer, Pittsburgh compound B (^{11}C-PiB). This tracer was developed by modifying the histological dye, thioflavin-T (a dye which has high affinity to amyloid oligomers) (Márquez and Yassa, 2019). The half-life of this radiotracer is very short (20 minutes), hence alternative fluorine-based tracers (^{18}F) with longer half-lives (110 minutes) have now been developed (e.g. florbetapir, florbetaben and flutmetamol) which facilitated the widespread use of amyloid PET imaging (Márquez and Yassa, 2019).

Human post-mortem studies have revealed that NFT density is a correlate of neurodegeneration and cognitive decline (Bierer *et al*., 1995), hence, the major strength of tau PET imaging is that it provides a measure of NFT deposition (Márquez and Yassa, 2019). Using the fluorine-based tau PET tracer [^{18}F]-1451 (or T-807), a close relationship has been identified between patterns of tau deposition and atrophy measures (Márquez and Yassa, 2019). Although tau PET's reliability is still under investigation (e.g. post-mortem validation of tracer binding characteristics), several studies have demonstrated the ability of tau PET imaging in differentiating AD patients from healthy controls (Okamura *et al*., 2014, Wang *et al*., 2016, Márquez and Yassa, 2019).

Another clinical PET technique is the fluorine-based fluorodeoxyglucose PET (FDG-PET) which is a measure of glucose activity. Cerebral glucose hypometabolism has been attributed to synaptic activity impairment and neurodegeneration, hence, in an FDG-PET scan, decreased FDG tracer uptake and presence of hypometabolic regions could be indicative of AD (Ishii, 2013, Márquez and Yassa, 2019).

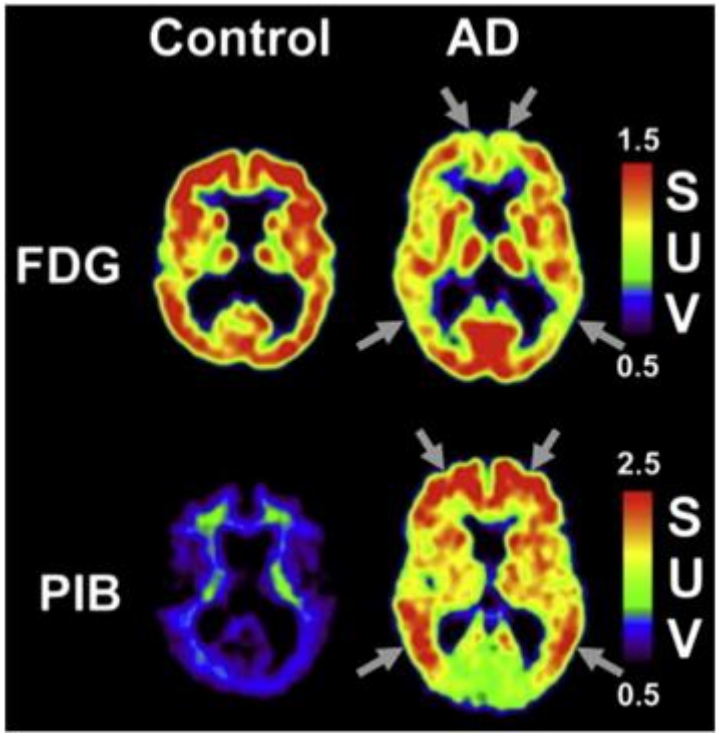

Figure 1.3: Representative FDG-PET (top row) and amyloid-PET (bottom row) images from AD (right) and control (left) subjects. A reduced glucose metabolism is observed in distinct regions of the AD brain compared to the control participants (the characteristic regional pattern of hypometabolism includes the posterior temporoparietal and frontal cortices as indicated by arrows). On the other hand, AD demonstrates greater accumulation of amyloid-PET tracer in these regions. Colour bars represent standardised uptake values (SUV). (Images adopted from Cohen and Klunk, 2014)

As described earlier, there are limitations associated with each AD biomarker. The need for radioactivity (i.e. ionizing) is a limitation of PET biomarkers, which may specifically raise concerns regarding the radiation doses delivered to the patients in longitudinal studies (radiation dose is further compounded if CT scans are simultaneously acquired for anatomical localisation). The usually short half-life of radiopharmaceuticals is also a practical limitation that needs to be considered (e.g. decay of radioactivity during transportation or during labelling of the radioligand and patient preparation). An additional limitation is regarding the specificity of these techniques, for example, a great proportion of cognitively normal subjects (20-40%) also demonstrate high amyloid-tracer binding similar to that seen in AD patients (Roberts, Dunn and Rabinovici, 2013).

1.2.4 The dynamic biomarker model

The dynamic biomarker model explains the sensitivity of the aforementioned biomarkers against disease timeline (Jack *et al*., 2010). In the dynamic biomarker model of the AD pathological cascade, amyloid abnormalities (detected by CSF and PET) precede tau, structural and cognitive abnormalities. Biomarkers are represented by parallel sigmoidal curves suggesting that these pathophysiological correlates of disease progression are rapid initially but slow down later in disease progression.

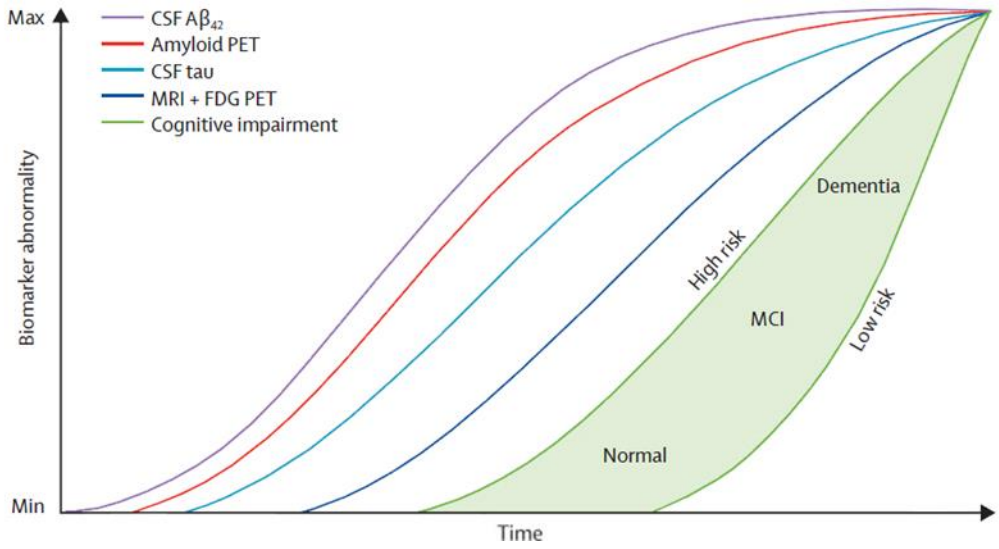

Figure 1.4: The dynamic biomarker model of the AD pathological cascade. The biomarker demonstrating the highest sensitivity is CSF amyloid. This is followed by amyloid PET, CSF tau, structural MRI/FDG-PET and cognitive impairment. (Image adopted from Jack et al., 2010)

However, a few years later, Jack *et al*. (Jack *et al*., 2013) realised that the dynamic biomarker model could not explain the observations made by Braak and Braak (NFT deposition precedes amyloid deposition - section 1.3.2.3). Despite acknowledging that tau pathology is the first pathophysiological process in the AD pathological cascade, in support of their original model, Jack *et al*., argued that the sensitivity of the current tau biomarkers is lower than the detection threshold, hence in practical terms amyloid biomarkers offer higher sensitivity at earlier time-points. However, they updated their model to incorporate these changes (Jack *et al*., 2013) (figure 1.5).

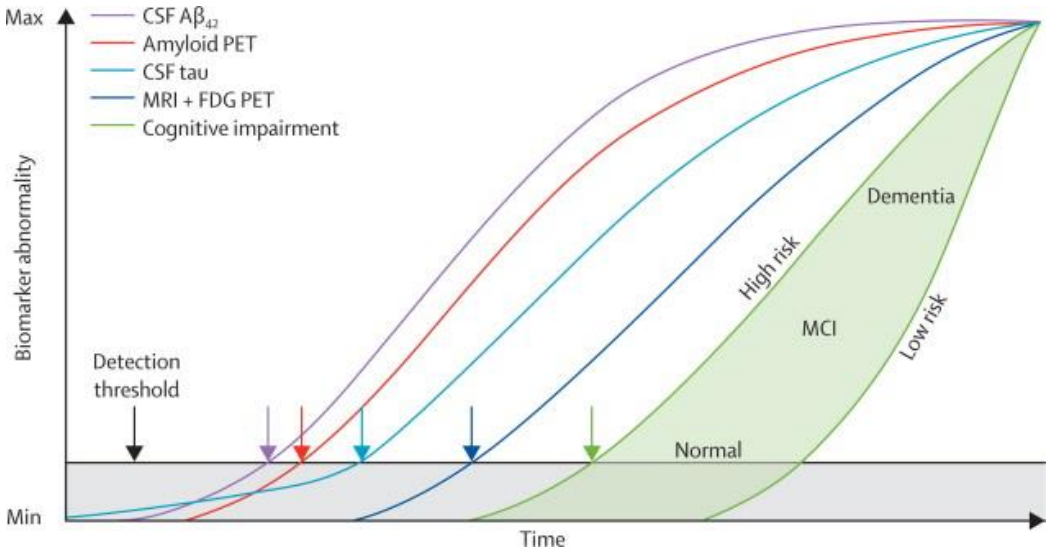

Figure 1.5: Updated dynamic biomarker model. Tau pathology is the first pathophysiological process in the AD pathological cascade, however the sensitivity of the current tau biomarkers is below the detection threshold. (Image adopted from Jack et al., 2013)

1.2.5 CSF-ISF exchange assessment as a potential AD biomarker

As discussed, biomarkers listed above each have their own limitation (e.g. invasiveness, ionizing and sensitivity), hence it would be highly desirable to develop an early AD biomarker without the aforementioned limitations. Recent evidence suggests that impairments in brains ability to remove aberrant brain proteins lead to build-up of these harmful proteins and therefore contribute to the onset and/or progression of disease (Wildsmith *et al*., 2013, Mawuenyega *et al*., 2010). A particular brain-cleaning system that appears important in the clearance of amyloid relies on the compartmental exchange of CSF with ISF for the transport and drainage of proteins/solutes in the brain (i.e. CSF-mediated solute transport). Therefore, detecting early abnormalities in CSF-ISF exchange pattern (i.e. dysfunction to this brain clearance system) non-invasively, may present as a promising non-invasive biomarker of early AD development. CSF-ISF exchange abnormalities can be studied from invasive MRI tracer studies (where MRI tracers are delivered intracerebrally) that monitor ingress/egress of tracers into and from the brain parenchyma (Ringstad *et al*., 2018). The limitation however, is the requirement for invasive tracer delivery procedures (e.g. intra-thecal), hampering the routine assessment of brain clearance function (i.e. CSF-ISF exchange) in the clinic. As described earlier, the main goal of this thesis is to develop a non-invasive technique for the assessment of CSF-ISF exchange (chapters 3 & 4). Additionally, in chapter 6 of this thesis, attempts will be made for imaging CSF-ISF exchange abnormalities.

1.3 Causes of Alzheimer's disease

1.3.1 Familial AD

The underlying cause of AD is not clear at this moment in time, however, in some rare early onset (familial) cases of AD, genetic mutations play a key role. These genetic mutations are attributed to either amyloid precursor protein (APP), presenilin 1 (PS1) or presenilin 2 (PS2) genes (Goate *et al*., 1991, Sherrington *et al*., 1996, Rogaev *et al*., 1995). Increased amyloid-beta production and aggregation, as well as increased extracellular levels of amyloid-β_{1-42} are consequences of mutations in these genes (Dong *et al*., 2012). Mutations also occur in the microtubule associated protein tau (MAPT) gene, such as the autosomal dominant frontotemporal dementia (FTD) chromosome-17 type (Hutton *et al*., 1998). Although mutation in this gene is linked to tauopathies rather than AD (e.g. FTD), the neuropathological alterations caused by this mutation are similar to those seen in AD (such as cortical atrophy, aggregation of NFTs and behavioural changes) (Forman *et al*., 2006).

1.3.2 Sporadic AD

The majority of AD cases are late onset (sporadic) forms of the disease with no single definitive genetic mutation. However, several different susceptibility genes have been identified that are associated with increased risk of sporadic AD (Lambert *et al*., 2009, Hollingworth *et al*., 2011) (with the most common genetic factor being the ε4 allele of the apolipoprotein ε (APOE) gene (Saunders *et al*., 1993). Since no single definitive genetic cause can be attributed to sporadic AD, several different hypotheses are proposed by the scientific community which aim to explain the underlying cause of the disease. Some of the more established hypotheses will be described below.

1.3.2.1 The cholinergic hypothesis

The cholinergic hypothesis was one of the earliest hypotheses attempting to explain the cause of AD. Upon post-mortem biochemical inspection of AD brains, it was revealed that there was a significant deficit of the neurotransmitter acetylcholine (ACh), compared to elderly controls (Davies and Maloney, 1976). Since Ach is a major neuromodulator essential for normal functioning of the brain, the cholinergic hypothesis suggests that large deficits of this neurotransmitter significantly contribute to disease progression and cognitive impairment (Bartus *et al*., 1982). Not surprisingly, the majority of the currently FDA approved AD drugs include acetylcholinesterase inhibitors (AChEIs) to prevent further break-down of Ach by AChE (Birks, 2006). Despite some encouraging results, such as slowing down

disease progression and mild symptomatic relief of AD (Rountree *et al*., 2009), AChEIs do not reverse disease phenotype nor do they restore cognitive abilities. Additionally, Ach deficits don't seem to be observed in patients with early AD (Davis *et al*., 1999), suggesting that this hypothesis cannot explain the early pathological changes that drive disease progression.

1.3.2.2 The Amyloid cascade hypothesis

First introduced by Hardy and Higgins in 1992 (Hardy and Higgins, 1992), the amyloid cascade hypothesis states that the cascade of pathological events in AD is caused by the mis-metabolism of APP. In other words, proteolytic cleavage of APP causes aggregation of amyloid-beta into amyloid plaques which will further lead to the formation of NFTs and degradation of neurons.

Subsequent findings regarding the role of genetic mutations in APP, PS1 and PS2 genes in early onset AD (section 1.3.1), together with post-mortem histopathological evaluation of AD brains (consistently demonstrating high levels of amyloid plaques) were in support of the amyloid cascade hypothesis. However, the fact that amyloid plaque build-up is also seen in 'asymptomatic' healthy individuals (Maccioni *et al*., 2010) suggests that amyloid plaque build-up alone cannot explain the complex AD pathophysiology. Interestingly, several drugs targeting amyloid plaque build-up have also failed to produce positive results (Mullane and Williams, 2013), further suggesting that the amyloid cascade hypothesis cannot solely explain all the mechanisms involved in AD.

1.3.2.3 The tau hypothesis

Under normal physiological conditions, tau's role in the human brain is to stabilise microtubules and facilitate intracellular transport (it's a cytoplasmic protein that binds to tubulin during its polymerisation) (Garcia and Cleveland, 2001). Therefore, tau plays an important role in the integrity of neuronal cytoskeleton, morphology and stability. In some neurological disorders, tau becomes abnormally phosphorylated and aggregates in the form of NFTs, which are toxic to neurons. As a result, the tau hypothesis states that it is tau (and the associated hyperphosphorylation) that is the underlying cause of AD. In support of the tau hypothesis, the post-mortem work by Braak and Braak identified subjects whose brains included NFTs in the absence of extracellular amyloid-β (Braak and Braak, 1997). Also, as mentioned above, the fact that many healthy adults demonstrate high levels of amyloid plaque (i.e. despite lack of neurological deficits), provides further evidence for the role of tau in the initiation of AD symptoms (Maccioni *et al*., 2010). Additionally, NFT burden has been shown to

be correlated with dementia severity (Bierer *et al*., 1995). Furthermore, there are other neurological disorders that are predominantly characterised by the aggregation of tau and NFTs (in the absence of amyloid plaques), these are more generally known as tauopathies (e.g. FTD, Pick's disease and progressive supranuclear palsy). The involvement of tau in these tauopathies (i.e. dementias other than AD) strengthens its position as a key element in the AD pathological cascade. Interestingly, several therapeutic strategies targeting tau (e.g. stabilising microtubules, prevention of phosphorylation and aggregation of tau) have shown promise in pre-clinical trials (Matsuoka *et al*., 2007, Brunden *et al*., 2010).

1.3.2.4 Other AD hypotheses

Other compelling AD hypotheses include the glutamate dysfunction and the vascular hypotheses respectively. Glutamate is the main neurotransmitter in the central nervous system (CNS) and one of its key roles include the activation of N-methyl-D-aspartate (NMDA) receptors (Butterfield and Pocernich, 2003). The hypothesis states that glutamate dysfunction can account for many of the neurochemical and behavioural deficits observed in AD (Maragos *et al*., 1987). Although the exact reason for glutamate dysfunction is not known, several reasons such as impaired metabolism, oxidative stress and mitochondrial dysfunction have been proposed (Mattson *et al*., 1999, Parameshwaran, Dhanasekaran and Suppiramaniam, 2008). Another interesting AD hypothesis, is called the vascular hypothesis of AD. This hypothesis states that vascular risk factors and cerebrovascular abnormalities are a key feature of AD with persuasive arguments to suggest that vascular pathology may be the critical initiator of the cascade of events that precedes dementia (de la Torre, 2002, Zlokovic, 2005, Zlokovic, 2011).

Despite the compelling hypotheses described above, a recent proposition has also gained a lot of interest in the scientific community. It has been suggested that impairments in brains ability to remove aberrant brain proteins leads to build-up of these harmful proteins and therefore, it is brain clearance dysfunction that is the initiating factor in AD pathology, rather than for example, increased amyloid production (Wildsmith *et al*., 2013, Mawuenyega *et al*., 2010). As such, attention was shifted towards the CSF-ISF exchange (CSF/ISF drainage) literature (since brain clearance is partly facilitated by the compartmental exchange of CSF with ISF). Hence, below I will describe the CSF-ISF exchange (CSF/ISF drainage) literature in more detail, with special attention to the recently proposed glymphatic system.

1.4 CSF-mediated brain solute transport/drainage mechanisms

The brain and the spinal cord are characterised by a very high metabolic rate despite their relatively small sizes (Wang *et al*., 2012). The lymphatic system is a network of very small nodes and vessels that run throughout the body and helps facilitate the clearance of waste and toxins from the body. The density of the lymph vessels correlates with the metabolic activity of that tissue (Jessen *et al*., 2015), however, despite having a very high metabolic demand, the brain is void of any lymphatic vessels/nodes. The concept of drainage from the brain dates back to the 18th century, where Quincke suggested the role of arachnoid villi in the removal of CSF from the brain (Pollay, 2010). About the same time, Schwab observed that substances injected into the subarachnoid space will find their way to the cervical lymph nodes (Pollay, 2010). Shortly after, Key and Retzius identified tracer pathways and confirmed the role of arachnoid villi and cervical lymph nodes in removal of subarachnoid CSF from the brain (Key and Retzius, 1875). Almost a century later, tracer studies also confirmed the role of cervical lymph nodes and arachnoid villi in removal of CSF from the brain and identified pathways the tracers used to reach the cervical lymphatic system, such as the olfactory and the optic nerves (Jackson, Tigges and Arnold, 1979, Gomez *et al*., 1988, Kida, Pantazis and Weller, 1993, Koh, Zakharov and Johnston, 2005) (figure 1.6). These findings collectively provided evidence regarding CSF drainage from the brain.

In terms of ISF drainage from the brain, evidence was provided regarding the role of lymphatic system in drainage of ISF (Bradbury, Cserr and Westrop, 1981, Cserr, Harling-Berg and Knopf, 1992, Weller, Kida and Zhang, 1992). Bradbury, Cserr and Westrop (Bradbury, Cserr and Westrop, 1981) demonstrated that drainage of intra-cerebrally delivered tracers is facilitated by the perivascular spaces. Further transport of ISF/tracers from the perivascular spaces towards the nose (and subsequently the lymph nodes) was hypothesised to occur via the subarachnoid space (figure 1.7). Interestingly, in support of these findings (i.e. the role of lymph nodes in ISF drainage), meningeal lymphatic vessels (MLVs) were recently identified in the brain (as it has been shown that MLVs are in communication with the cervical lymph nodes (Louveau *et al*., 2015)).

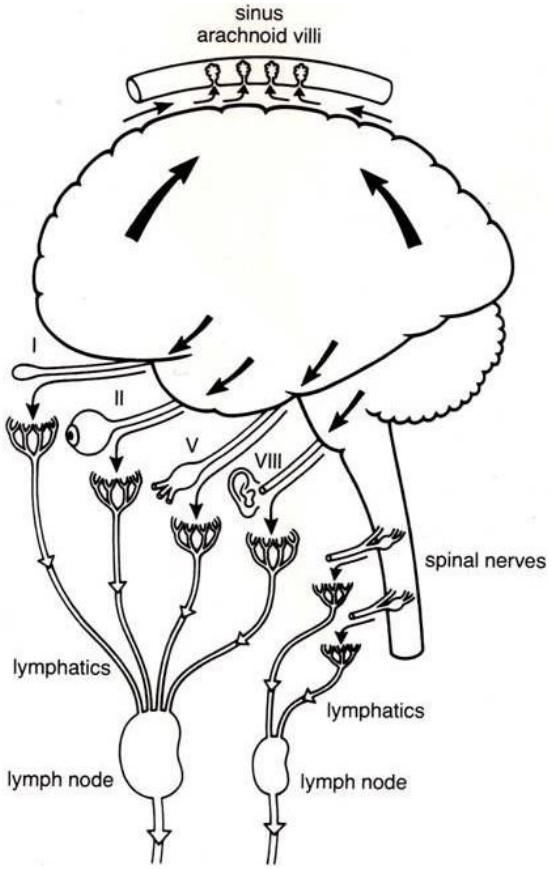

Figure 1.6: Schematic illustrating the drainage pathways of CSF from the subarachnoid space. Subarachnoid CSF is removed to the lymphatic system across the arachnoid villi or along certain nerves. I, olfactory nerve; II, optic; V, trigeminal; VIII, acoustic. (Image adopted from Cserr et al., 1992)

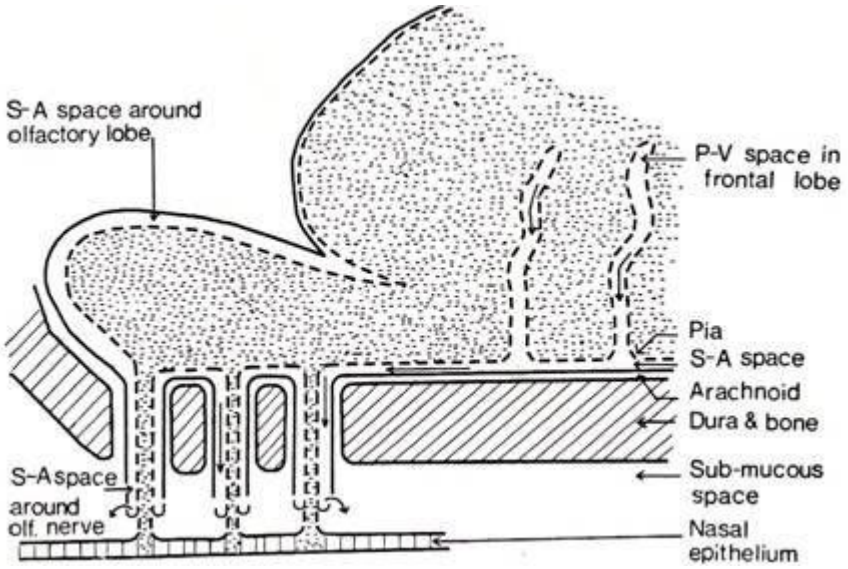

Figure 1.7: Hypothesised transport route of solutes/proteins injected into the caudate nucleus towards the submucous space of the nose. Perivascular spaces facilitate transfer of solutes to the subarachnoid space, from which solutes reach the nose and

subsequently the lymph nodes. (Image adopted from Bradbury, Cserr and Westrop, 1981)

The earlier findings of ISF drainage discussed above, additionally provided indirect evidence regarding the compartmental exchange of ISF with CSF (as essentially tracers injected into the brain interstitium were transferred to the CSF and subsequently in the lymph nodes). In fact, there exists a wide classical literature regarding the compartmental exchange of CSF with ISF (more commonly referred to as brain clearance or solute transport) which dates back to the 1960s (Heisey, Held and Pappenheimer, 1962, Cserr, 1965). For example, work of Brightman (Brightman, 1965) demonstrated that ferritin when injected into the lateral ventricle, crosses the ependyma and penetrates into the interstitial space of the brain with little difficulty (which is evidence of ventricular to ISF solute transport in the brain). Similarly, in the pioneering tracer studies of Cserr and colleagues (Cserr, Cooper and Milhorat,1977), it was demonstrated that horseradish peroxidase (HRP) when injected into the caudate nucleus, moves along preferential pathways of the brain, specifically towards perivascular and periventricular areas in addition to the lateral ventricles.

These findings collectively, support the notion of solute transport into, and through, the brain interstitial space. It is now believed that transport in the interstitial space is essential for healthy brain function (Holter *et al*., 2017, Ray, Iliff and Heys, 2019). For example, transport facilitates the transit and removal of aberrant brain proteins in the interstitial space. Additionally, the dynamics of nutrients and also extra-synaptic signalling of neuromodulators are dependant on interstitial transport. However, the exact mechanism of solute transport in the brain (i.e. that contribute to brain clearance) has been long a matter of debate (for example the contributions of diffusive versus convective transport). Since brain clearance dysfunction (i.e. reduced rates of solute/waste clearance) contributes to disease onset/progression (due to the abnormal build-up of aberrant brain proteins), it is vital to improve our understanding of flow and transport in the interstitial space. Hence, below I will describe in more detail the evidence and also the controversies regarding solute transport in the brain (Holter *et al*., 2017, Syková and Nicholson, 2008, Ray, Iliff and Heys, 2019).

1.5 Solute transport in the brain. Convective or diffusive?

Solute transport in the brain's extracellular space was believed by many to be primarily diffusive and nondirectional (Katzman, Schimmel and Wilson, 1968, Fenstermacher and Patlak, 1976). Rall and colleagues (Rall, Oppelt and Patlak, 1962) reported the movement of intra-ventricularly injected solutes (radioactive inulin

and sucrose) into the brain without significant restriction (from CSF and across the ventricular ependyma). The mode of transport was consistent with diffusion as the concentration of the compound in the tissue decreased as a function of distance from the ventricular surface. In a separate study, transport of solutes (urea and creatinine) in the brain tissue following aqueductal-fourth ventricular perfusion was consistent with Fick's diffusion law (Pollay and Kaplan, 1970a). In another study by Pollay and Kaplan (Pollay and Kaplan, 1970b), movement of intra-ventricularly administered thiocyanate (SCN-) into the brain tissue appeared to be compatible with diffusion. Whilst these authors supported the notion of intracerebral diffusion, others supported a more directional and convective (i.e. driven by bulk flow) mechanism of solute transport in the brain (Cserr, Cooper and Milhorat, 1977, Rennels *et al*., 1985). For example, Rennels *et al*. (Rennels *et al*., 1985) demonstrated that HRP when injected into the cisterna magna, moves rapidly into the brain along para-arterial pathways. Cserr and colleagues also supported the notion of bulk flow but argued that bulk flow is restricted to the perivascular or Virchow-Robin space surrounding the capillaries, rather than being through the entire interstitial space (Ichimura, Fraser and Cserr, 1991).

More recently, Syková and Nicholson (Syková and Nicholson, 2008) suggested that bulk flow is only confined to the paravascular spaces and doesn't take place throughout the extracellular space. Similarly, using simulation techniques (computational and analytical modelling), Asgari and colleagues (Asgari, de Zélicourt and Kurtcuoglu, 2016) also acknowledged the presence of fast para-arterial solute transport but debated the presence of directed bulk fluid motion throughout the interstitial space and suggested that diffusion and local mixing are the dominant drivers of ISF solute transport. Using a similar modelling approach, Holter *et al*. (Holter *et al*., 2017) also showed that permeability and solute movement in the narrow and torturous interstitial space is constrained and that solute movement occurs by diffusion rather than by bulk flow. On the other hand, Bedussi *et al*. (Bedussi *et al*., 2015) argued that a convective mechanism of transport was responsible for the transport of intra-striatally injected tracers from the striatum to the ventricles. Similarly, Iliff and colleagues concluded the presence of pressure-mediated CSF bulk flow in the subarachnoid and paravascular spaces, and also through the interstitial space (Iliff *et al*., 2012). This system that is defined by the bulk influx of subarachnoid and paravascular CSF into the brain interstitium (facilitated by arterial pulsations and aquaporin-4 channels) was named the glymphatic system. Iliff *et al*. demonstrated that impairments to this system cause significant build-up of amyloid-beta and as a

result, many have postulated that impairment to the glymphatic system is the initiator of AD pathology. Accordingly, in this PhD thesis, my initial aim was to develop a non-invasive imaging platform for the imaging of glymphatic system. Hence, below I will describe the glymphatic system in more detail.

1.6 Glymphatic pathway

The glymphatic pathway is a recently proposed waste clearance pathway (Iliff *et al*., 2012) based on the continuous exchange of CSF and ISF. From its primary source of production, the choroid plexus, CSF moves throughout the CSF spaces (aqueduct, lateral, third, and fourth ventricles), and into the subarachnoid spaces (running along the surface of the brain). A combination of CSF pressure gradients, pulsatility and respiration is hypothesised to drive the convective flow of CSF into the Virchow-Robin space, also known as the perivascular spaces (figure 1.8). Subsequent transport into the dense brain parenchyma is mediated by polarised aquaporin-4 (AQP-4) channels that reside on the glial astrocytic end-feet that ensheath the vasculature (Jessen *et al*., 2015). It is hypothesised that as a result of CSF movement into the brain parenchyma, a convective interstitial fluid flux towards the paravenous spaces is created, which then drains out of the brain toward the cervical lymphatic system (Murtha *et al*., 2014) (figure 1.9).

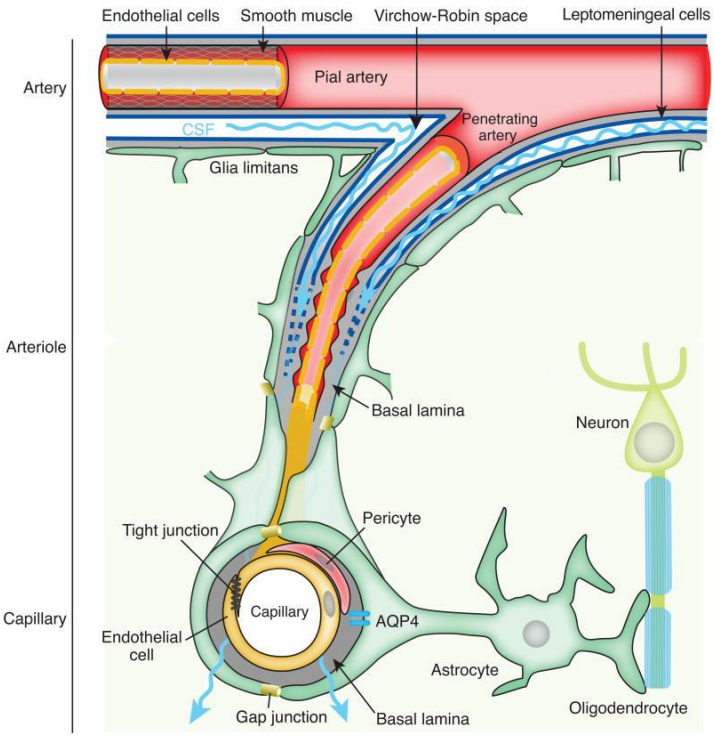

Figure 1.8: The neurovascular unit. Convective flow of CSF in the Virchow-Robin space (space along the penetrating artery) is facilitated by CSF pressure gradients, pulsatility and respiration. Further inflow into the parenchyma is mediated by the

aquapourin-4 channels located on the astrocytic vascular endfeet. (Image adopted from Jessen et al., 2015)

This rapid CSF-ISF exchange, mediated by the convective flow through the highly polarised AQP-4 channels that reside on the end feet of astrocytes (the most common glial cells in the brain), was termed the 'glymphatic' pathway, due to the proposed overlap of functionality with the lymphatic system, derived from the combination of the words, glial and lymphatics.

The schematic below further illustrates the basic components of the glymphatic pathway.

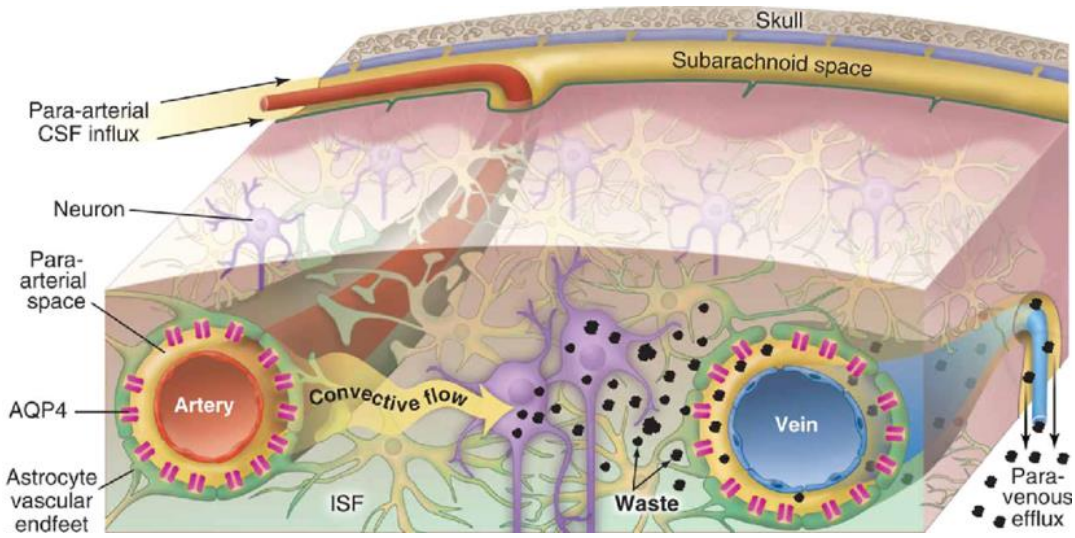

Figure 1.9: An overview of the glymphatic system. Waste clearance is facilitated by the convective flow of interstitial fluid (created as a result of a paravascular CSF inflow through the astrocytic AQP-4 channels into the brain parenchyma) towards the paravenous spaces, which then drains out of the brain toward the cervical lymphatic system. (Image adopted from Nedergaard, 2013)

The dynamics of the glymphatic system were initially characterised in-vivo by Iliff *et al*. (Iliff *et al*., 2012), using invasive two-photon microscopy in mice. Studies in mouse models have demonstrated that impairment of the glymphatic system, will reduce the clearance of amyloid-beta (Aβ) from the brain (Iliff *et al*., 2012, Xu *et al*., 2015). Hence, it has been suggested that impairments to the glymphatic system might contribute to the onset of AD pathology (e.g. by build-up of amyloid-beta) and therefore clinical assessment of this system, may provide an early window for detection and therapeutic intervention. To date, clinical assessment of the glymphatic function has been hindered due to the lack of non-invasive techniques. Assessment of the glymphatic function had been performed in rodents, by injection of contrast media

such as fluorescent tracers or gadolinium contrast agents, intra-thecally, intra-ventricularly or by direct injections into the brain parenchyma (Yang *et al*., 2013, Bedussi *et al*., 2015, Smith *et al*., 2017). Hence, the initial aim of this PhD thesis was to develop a novel non-invasive method (using MRI and gadolinium contrast agent) to characterise glymphatic inflow (or more broadly CSF-ISF exchange). In the next chapter, I will therefore describe the principles of magnetic resonance imaging (MRI) with special attention to sequences and concepts related to contrast enhanced MRI.

Chapter 2: Magnetic Resonance Imaging (MRI)

Throughout the course of this PhD project, several independent imaging modalities were employed, for the purpose of CSF-ISF exchange imaging. However, magnetic resonance imaging (MRI) was the central imaging modality in this PhD project. Hence in this chapter, I will describe the basic MRI principles including fundamental contrast mechanisms and pulse sequences required for the generation of contrast in an MR image. A more detailed description of contrast mechanisms/sequences that will later be utilised in this thesis will also be provided.

2.1 Introduction

Magnetic Resonance Imaging (MRI) or Nuclear Magnetic Resonance (NMR) is a powerful non-invasive clinical imaging technique used to image anatomy and the physiological processes of the body. Since its inception in the 1970s, it has become one of the most valuable imaging modalities in the field of biomedical imaging/research, primarily due to its non-invasiveness, deep tissue imaging capability as well as high soft tissue contrast and relatively high spatial resolution. Most of the human body is composed of water molecules. Each water molecule contains two hydrogen atoms and each hydrogen atom contains a single positively charged proton in the nucleus. Protons can be influenced by a magnetic field due to an intrinsic property known as the spin (i.e. angular momentum of atomic nucleic). When placed in an external magnetic field (B_0), there are two possible spin states specified by the quantum number (*m*), either + ½ (parallel) or – ½ (anti-parallel) as shown on figure 2.1. Under a strong external magnetic field (B_0), a greater proportion of the spins are aligned in the direction of the magnetic field (determined by the Boltzmann distribution – equation 1.1) and a net magnetic moment (*M*) will be induced as shown on figure 2.2, thus, MRI employs powerful magnets that are capable of generating strong magnetic fields (typically 1.5 or 3 Tesla for clinical imaging and 7 or 9.4 Tesla for pre-clinical imaging).

$$\frac{N_{anti-parallel}}{N_{parallel}} = e^{\left(\frac{-\Delta E}{kT}\right)} \tag{1.1}$$

In equation 1.1, *T* is the temperature in Kelvin, *ΔE* is the energy difference between the two states and *k* is the Boltzmann constant.

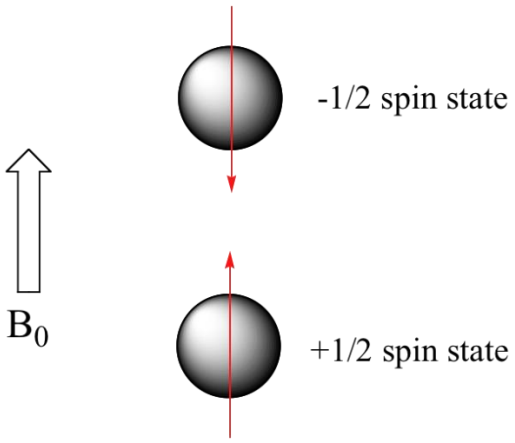

Figure 2.1: Possible alignment of spins when placed in an external magnetic field (B_0). There are two possible spin states specified by the quantum number, either + ½ or – ½. (Imaged adopted from https://chem.libretexts.org)

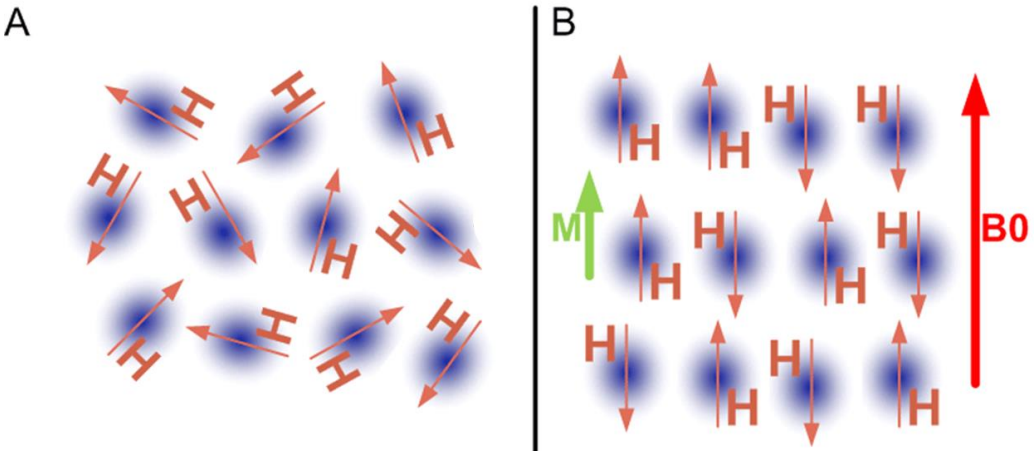

Figure 2.2: A- Orientation of hydrogen protons outside an external magnetic field. B- A greater proportion of the spins are aligned in the direction of the external magnetic field (B_0) and a net magnetisation (M) is induced (conventionally defined to be aligned in the z direction of a Cartesian coordinate system). (Image adapted from Burns, 2014)

The net magnetic moment (*M*) of a volume of tissue is therefore given by the equation:

$$M = P_D . V_{voxel} . C . (\frac{B_0}{T}) \quad (1.2)$$

where P_D is the proton density, V_{voxel} is volume of voxel, *C* is Curies constant, B_0 is the magnetic field (note dependence on magnetic field) and *T* is temperature in Kelvin.

B_0 is conventionally defined to be aligned in the z direction hence the net magnetisation (*M*) is also aligned in the z direction (M_z). In fact, the signal in MRI is derived by the manipulation of this net magnetisation. When placed in an external magnetic field, the net magnetisation (spins) precess at the Larmor or resonant frequency (42.6 MHz/T for the hydrogen proton). Precession frequency is defined by the following formula:

$$\omega_0 = \frac{\gamma B_0}{2\pi} \tag{1.3}$$

where ω_0 is the precession frequency, B_0 is the main magnetic field strength and γ is the gyromagnetic ratio. Upon application of a radio frequency (RF) pulse (B_1) perpendicular to the direction of the magnetic field at the precession frequency, energy will be transferred to the spins and they will move to an excited energy state. Now tilted from the z plane into the x-y plane (exited state), the magnetisation will generate a signal which is detected by an RF receiver coil. Figure 2.3 below, further illustrates the concept of net magnetic moment induction and spin excitation.

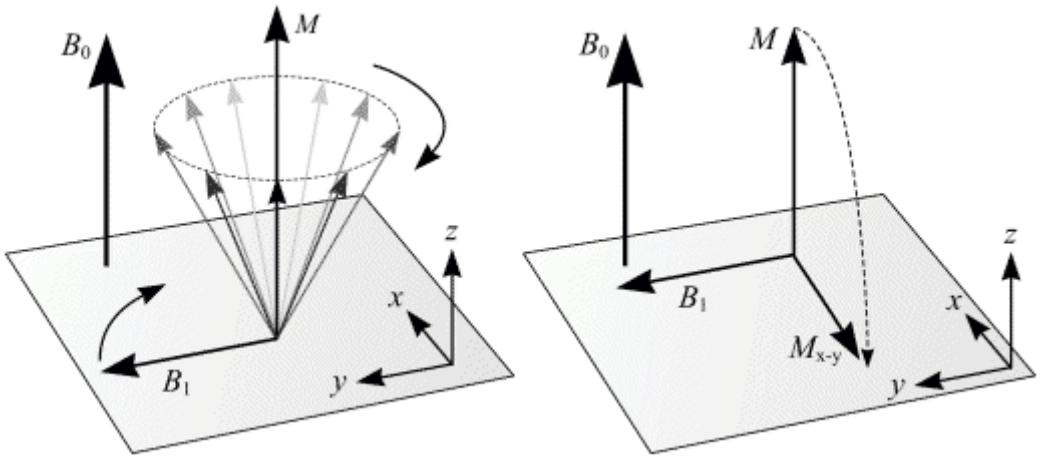

Figure 2.3: Left- The main magnetic field (B_0) induces a net magnetic moment (M) that precesses at the resonant frequency of the nucleus. Right- Application of an RF pulse (B_1) perpendicular to B_0 at the Larmor frequency causes spin excitation and tipping into the x-y plane (viewed from the rotating frame). (Image adopted from http://www.wikidoc.org)

Spins will not indefinitely reside in the exited state and will rapidly return to equilibrium (i.e. relax) once the RF pulse has been switched off. The de-excitation has two components: a) exchange of spin energy with the surroundings, otherwise known as the spin-lattice or longitudinal relaxation (T_1 relaxation), and b) interaction of neighboring spins (via their oscillating magnetic fields), otherwise known as the spin-

spin relaxation (T_2 relaxation). Below both relaxation mechanisms will be explained in more detail.

2.2 MRI relaxation mechanisms

2.2.1 T_1 relaxation

Once the RF excitation pulse is switched off, the exited spins return to equilibrium magnetisation by the interchange of thermal energy with the lattice, hence the name spin-lattice relaxation (figure 2.4 – left). As shown on figure 2.4 (left), different tissues have different T_1 relaxation rates and this is the source of contrast in a T_1-weighted MR image (section 2.4.1). The equation describing T_1 relaxation (M_z) at any time (*t*) is:

$$M_z = M_0 . (1\text{-}e^{-\frac{t}{T_1}}) \quad (1.4)$$

where time constant T_1 is the time it takes for 63% of the M_z magnetisation to recover.

2.2.2 T_2 relaxation

On the other hand, the T_2 relaxation is the rate at which magnetisation in the x-y plane returns to a net zero magnetisation. The de-excitation in this scenario is due to the interaction of neighbouring spins together, hence the name spin-spin relaxation (figure 2.4 – right). Immediately following the B_1 excitation pulse, all the spins are in phase (in the x-y plane). However, this coherency is gradually lost as the magnetic field (and the precession frequency) of each proton is slightly altered by the oscillating magnetic field of the adjacent spins, causing the spins to move out of phase and the x-y magnetisation thus gradually decays. As shown on figure 2.4 (right), different tissues have different T_2 relaxation rates and this is the source of contrast in a T_2-weighted MR image (section 2.4.2). The equation describing the T_2 relaxation at any time (*t*) is given by the equation:

$$M_{xy} = M_0 . e^{-\frac{t}{T_2}} \quad (1.5)$$

where time constant T_2 is the time it takes for 63% of the M_{xy} magnetisation to decay.

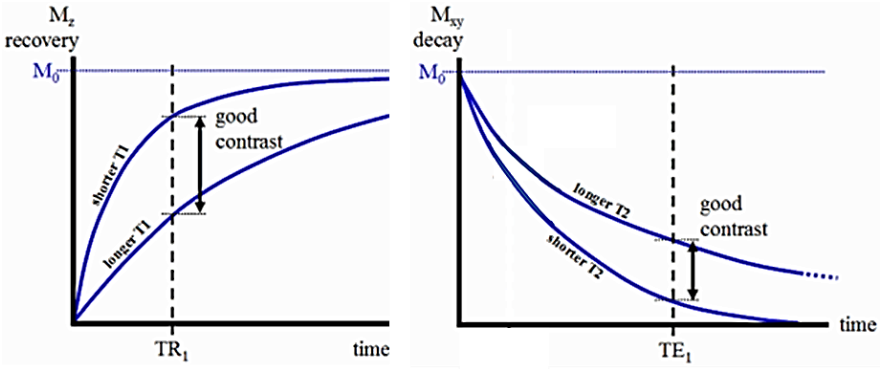

Figure 2.4: Schematic illustrating the spin-lattice (T_1) relaxation (left) and the spin-spin (T_2) relaxation (right). The differences in the tissue relaxation rates (i.e. different tissue T_1 and T_2 time constants) is the principle behind generation of contrast in an MR image. (Image adapted from www.ReviseMRI.com)

Furthermore, on top of the spin-spin interaction, the spins also loose coherence due to magnetic field inhomogeneities. This further de-phasing of the spins is known as the T_2* relaxation (otherwise known as the free induction decay - figure 2.5). However, application of a $180°$ RF refocusing pulse (section 2.3.1) will effectively correct dephasing due to magnetic field inhomogeneities hence T_2 relaxation is specifically associated with spin-spin interaction as shown on figure 2.5.

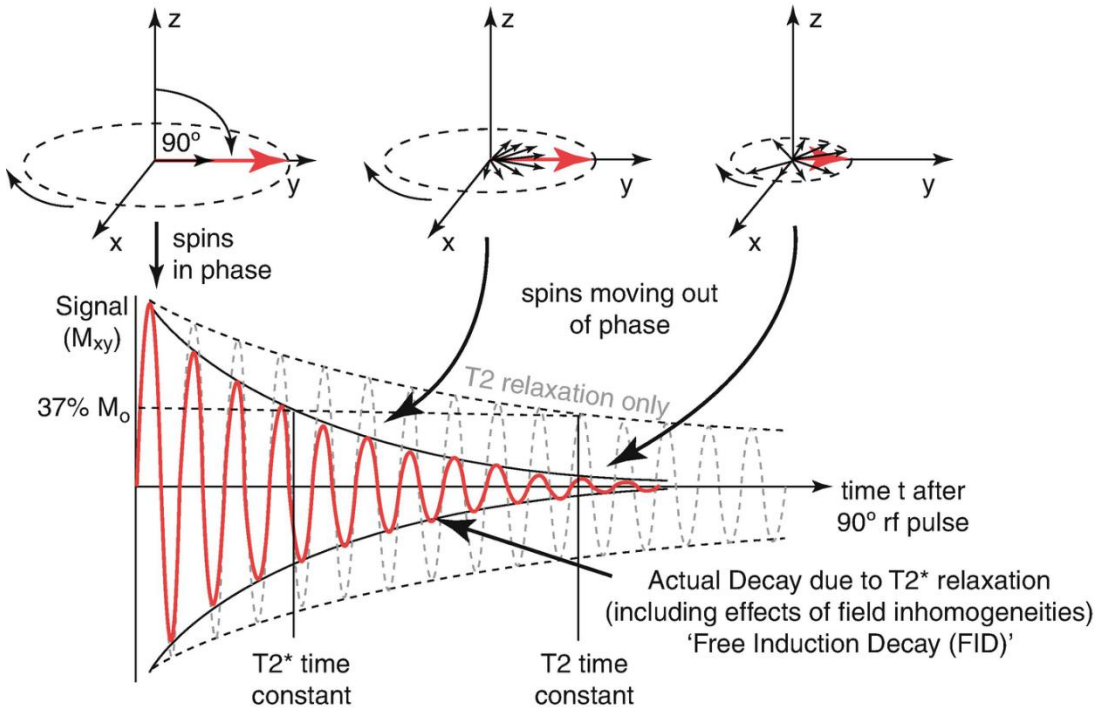

Figure 2.5: Immediately after application of a $90°$*excitation pulse, the spins de-phase due to spin-spin interactions (*T_2*) but additionally due to magnetic field inhomogeneities (*T_2**). *T_2** decay is also known as the free induction decay. (Image adopted from Imazio et al., 2019)*

2.3 Pulse sequences and localisation of MRI signal

For the formation of an MR image, we need to know where the signal is coming from (i.e. the location of the spins). The signal that is received by the receive coil comes from a large imaging region and therefore the signal is not localised. For spatial encoding, additional gradient fields are added to the main field (three extra set of gradient coils). Encoding spatial information in the x, y and z directions are conventionally known as the frequency encoding (G_x), phase encoding (G_y) and slice select (G_z) respectively. For example, application of a gradient along the z-direction, linearly increases or decreases the precession (resonant) frequency of the spins depending on their location (from -z to +z). Location z=0 is defined as the isocentre and spins at this location resonate at the Larmor frequency. Hence, we can selectively excite spins at any location by the application of an RF excitation pulse at that specific resonating frequency. There are two fundamental pulse sequences for the localisation of the signal and generation of an MR image, the spin echo and the gradient echo.

2.3.1 Spin-echo (SE)

Immediately following the $90°$excitation pulse, magnetic field inhomogeneities and spin-spin interactions cause dephasing of spins. After application of the $180°$ refocusing pulse, the spins will rephase after a certain amount of time, known as the echo time (TE). This $180°$ pulse specifically corrects for spin dephasing due to the magnetic field inhomogeneities and hence produces an echo which follows true T_2 relaxation. Additional magnetic gradients fields are simultaneously used to provide spatial encoding required for image reconstruction. The whole process is repeated after a certain amount of time, known as the repetition time (TR). The number of repeats depends on the number of phase encoding steps (usually the same as the image matrix size).

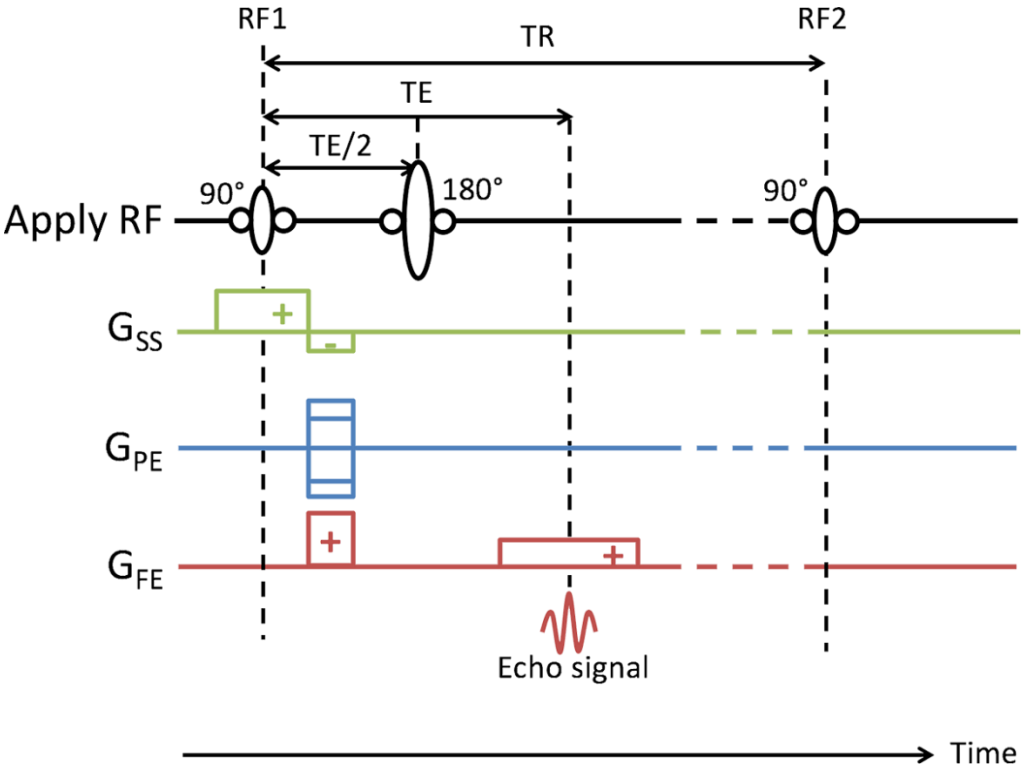

Figure 2.6: The spin-echo pulse sequence. G_{SS} is the slice select gradient, G_{PE} is the phase encode gradient and G_{FE} is the frequency encode gradient. (Image adopted from https://www.radiologycafe.com)

2.3.1.1 Fast spin-echo (FSE)

A conventional spin-echo sequence would take several minutes to acquire an image data set, depending on the number of phase encoding steps, the TR and the number of imaging slices. For example, imaging one brain slice (TR = 2s, matrix size = 256 x 256) would take approximately 512s or about 8.5 minutes. Fast spin-echo imaging techniques have been developed which dramatically speed up spin-echo imaging.

Briefly, multiple 180° refocusing pulses are applied sequentially after each 90°excitation pulse to obtain a series of spin echoes (figure 2.7). The number of successive 180° pulses is called the echo train length (ETL). Compared to a conventional spin-echo sequence, the acquisition time is reduced by a factor proportional to the ETL.

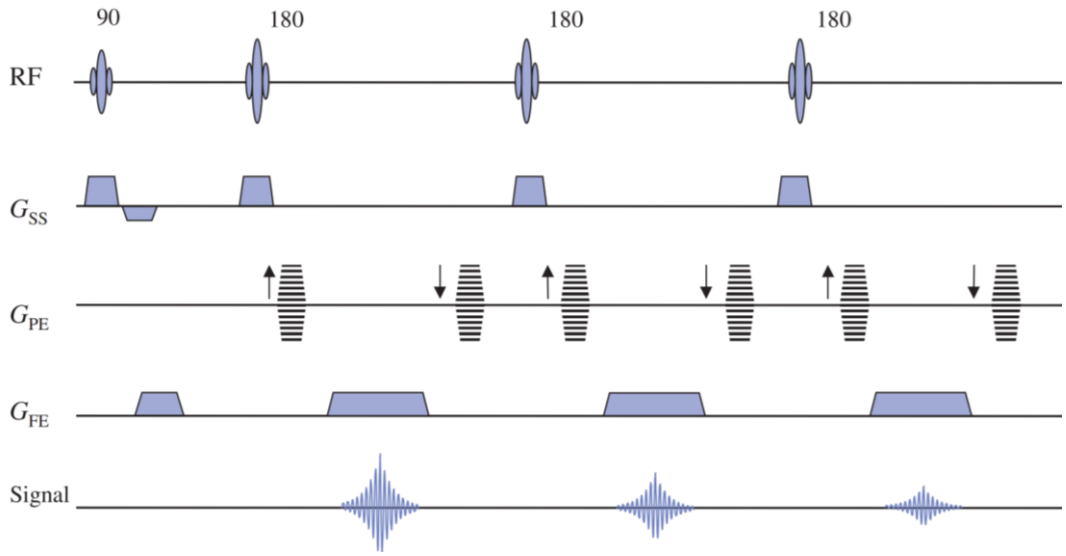

Figure 2.7: The fast spin-echo (FSE) pulse sequence with an ETL of 3. This sequence reduces the acquisition time by one-third compared to a conventional SE sequence. (Image adopted from Mcrobbie et al., 2006)

2.3.1.2 Fast spin-echo multi-slice (FSEMS)

The fast spin-echo sequence is still a relatively long sequence due to the need for long TR values (required for spins to return to equilibrium). In order to reduce the imaging time in FSE even further, additional slices are routinely incorporated into the TR delay (provided that all the RF pulses are made slice selective), a technique known as the fast spin-echo multi-slice (FSEMS) (figure 2.8). In chapter 3, a FSEMS technique will be implemented for the generation of MR images sensitive to brain CSF spaces.

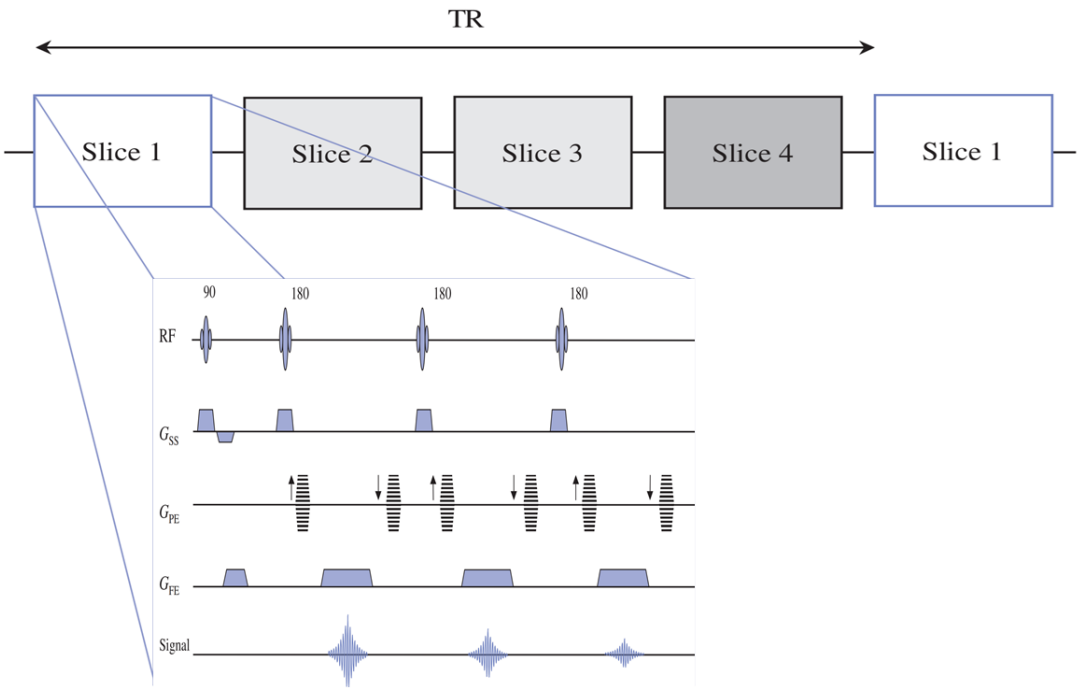

Figure 2.8: The fast spin-echo multi-slice (FSEMS) pulse sequence incorporating 4 consecutive slices in one TR delay and an ETL of 3. The imaging time is reduced by a factor of 12 compared to a conventional spin-echo sequence (4 x 3 = 12).

2.3.2 Gradient-echo (GE)

In a gradient-echo sequence an RF pulse is applied with a flip angle α (usually <$90°$). A positively pulsed frequency-encode gradient is applied immediately after an equal but opposite (i.e. negative) gradient (to ensure spins rephase at echo time). TE is reached when the positive gradient area matches that of the negative gradient area. In gradient-echo images, magnetic field inhomogeneities (causing dephasing of the spins between the excitation pulse and the formation of the echo) are not corrected by the application of the positive gradient (it only compensates for the dephasing caused by the negative gradient), therefore, signal at the echo time will be influenced by T_2* relaxation. A gradient-echo sequence is typically much faster than a spin-echo sequence due to the absence of the $180°$refocusing pulse. Moreover, using a low angle excitation pulse means that the equilibrium M_z magnetisation prior to each RF pulse is greater for a given TR (i.e. amount of available signal is higher) and therefore shorter TR values can be adapted. Hence for the same number of phase-encoding steps, the acquisition is faster compared to a spin-echo sequence and thus more suitable for procedures such as dynamic contrast enhanced imaging.

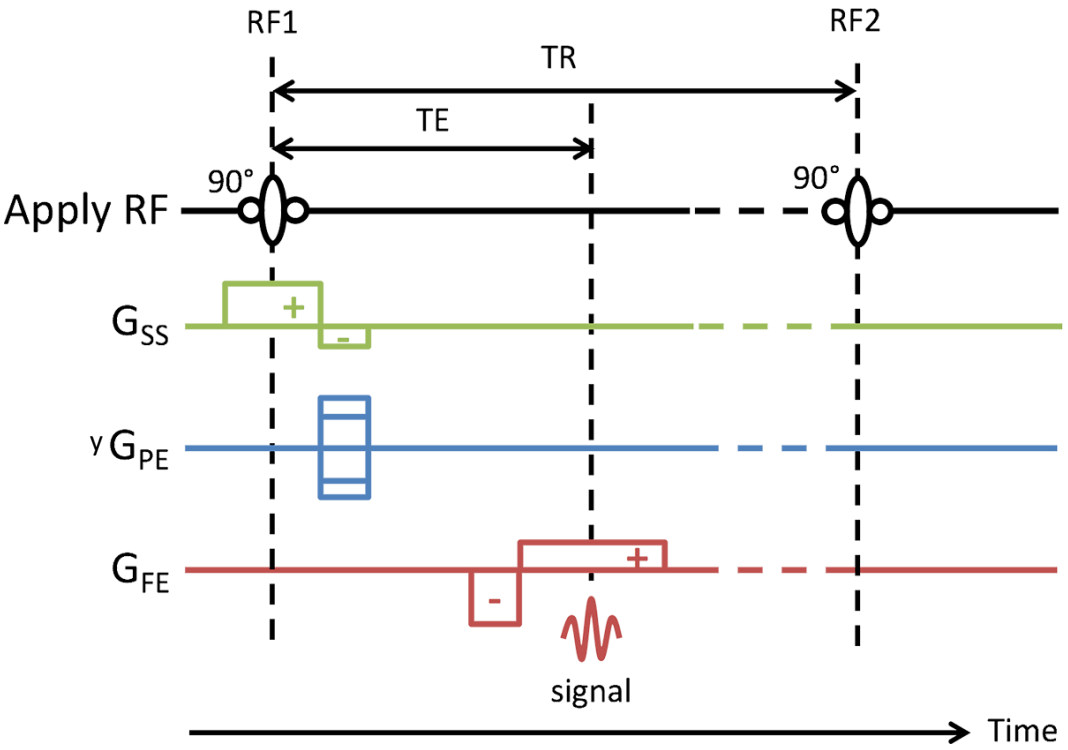

Figure 2.9: The gradient-echo pulse sequence. G_{SS} is the slice select gradient, G_{PE} is the phase encode gradient and G_{FE} is the frequency encode gradient. (Image adopted from https://www.radiologycafe.com)

A popular faster GE sequence is known as the fast low angle shot (FLASH) sequence which combines a low-flip angle RF pulse with a short TR.

2.3.2.1 3D gradient-echo

'3D' MRI sequences utilise a RF pulse that excites all the spins in the imaging volume, hence there are no slice-selective RF pulses. Instead of selecting individual slices, we separately phase encode in the slice-select direction, hence in the 3D MRI pulse sequence there will be two phase encoding gradients in total (figure 2.10). If a FLASH method was to be acquired with a spin-echo sequence with a TR value of 1s, it would take approximately 20 hours to obtain a 256 x 256 x 256 image. Hence, the FLASH method is instead acquired with a gradient-echo sequence with very short TR values (few milliseconds) taking around 10 minutes to acquire the same image dataset. In chapter 3, a high spatial resolution 3D FLASH (GE) sequence will be implemented for the detailed visualisation of possible CSF-mediated contrast agent infiltration into the brain parenchyma.

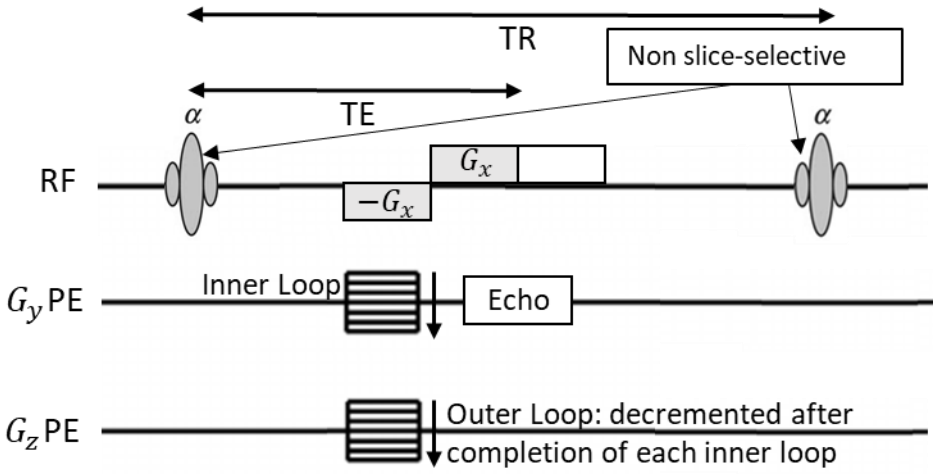

Figure 2.10: The 3D gradient echo (FLASH) pulse sequence. Phase encoding occurs in two directions for 3D spatial discrimination. There are no slice-select RF pulses as all the spins in the field of view need to be excited.

2.4 Contrast in MR images

MRI inherently benefits from fairly reasonable contrast due to the intrinsic properties associated with spins and protons (e.g. diverse set of relaxation mechanisms (T_1, T_2, T_2*)). In practice, with careful selection of pulse sequence parameters (e.g. TR and TE), contrast in an MR image can be emphasised between particular tissues of interest (e.g. contrast can be emphasised between grey and white matter in a T_1-weighted image or between CSF and brain tissue in a T_2-weighted image). For instance, a spin-echo sequence can generate both T_1 and T_2-weighted images depending on TR and TE values chosen:

$$SE_{max} \propto M_0.[1-\exp\left(-\frac{TR}{T_1}\right)].\exp\left(-\frac{TE}{T_2}\right) \quad (1.6)$$

It can be seen how choosing short TR and TE values could generate T_1 weighting and choosing long TR and TE values could generate T_2 weighting. The flexibility in choosing image contrast makes MRI a powerful diagnostic tool in biomedical imaging/research.

Image weighting	TE	TR
T_1	Short	Short
T_2	Long	Long

Figure 2.11: TR/TE values in a spin-echo image and the corresponding contrast.

In this PhD project, mainly T_1, T_2 and diffusion-weighted (section 2.5) images are acquired for the imaging of systemic gadolinium contrast agent transfer into the CNS (i.e. all in a contrast enhanced (CE)-MRI setting). Hence below I will provide more information regarding the generation of these images (principles of CE-MRI will also be covered).

2.4.1 T_1-weighted image

In T_1-weighted MRI, contrast depends on the T_1 relaxation time of different tissues. A T_1-weighted image can be acquired from both a gradient-echo (GE) and a spin-echo (SE) sequence. In this study, I primarily utilised a GE sequence for the generation of T_1-weighted images (for the imaging of possible systemic gadolinium contrast agent transfer into brain tissue – chapter 3). In a GE sequence, the requirement for the achievement of T_1-weighted contrast, in addition to a relatively long flip angle, is to keep TE and TR relatively short. This is to capture the T_1 contrast that is developed between different tissues during early phases of longitudinal relaxation. In addition, keeping TE short further enhances T_1-weighting by limiting the amount of developed T_2* contrast. T_1-weighted images have a good range of contrast, hence attributed the name 'anatomical scans'. For example, CSF appears dark (due to the long T_1 relaxation of water) whereas fat appears bright. White matter and grey matter are also distinguishable in these images as white matter appears brighter due to the relatively short T_1 relaxation time (figure 2.12).

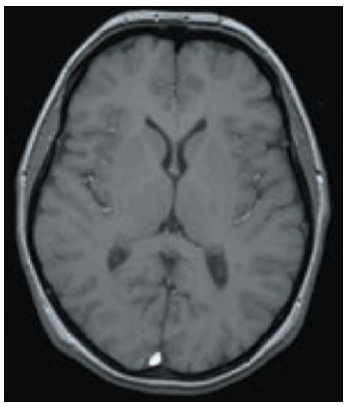

Figure 2.12: A GE T_1-weighted image of the human brain (axial slice) acquired with parameters: TR = 150 ms, TE = 4.6 ms and flip angle = 60°. A distinguishing feature is that CSF appears dark. White matter and grey matter are also distinguishable in these images as white matter appears brighter. (Image adopted from Mcrobbie et al., 2006)

The T_1 weighting is commonly adopted in clinical CE-MRI for the detection of brain tumour and stroke. The T_1 weighting is capable of imaging contrast agent uptake in brain tissue that accompanies these pathologies (due to the leakiness of the blood brain barrier), in addition to offering a good range of contrast. In this project, T_1 weighting will also be adopted to image the possible transfer of contrast agent from the CSF spaces into the brain tissue (chapter 3). More specifically, a 3D T_1-weighted gradient-echo sequence will be employed, otherwise known as the 3D fast low angle shot (FLASH) sequence.

2.4.2 T_2-weighted image

In T_2-weighted MRI, contrast depends on the T_2 relaxation time of different tissues. A T_2-weighted image can be acquired from a SE sequence (for the removal of T_2* specific effects). A long TR is chosen to minimise T_1-driven contrast, and a long TE is chosen to allow sufficient time for T_2 contrast to develop. In a T_2-weighted image, tissues with long T_2 appear bright (e.g. CSF) whereas tissues with short T_2 appear dark (e.g. white matter) (figure 2.13).

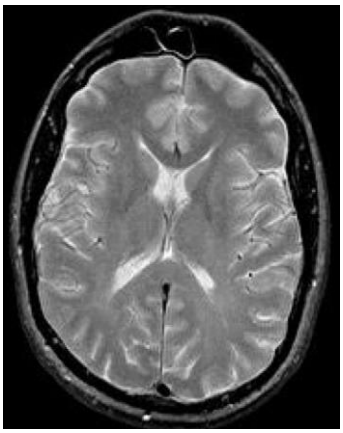

Figure 2.13: A SE T_2-weighted image of the human brain (axial slice) acquired with parameters: TR = 2000 ms, TE = 80 ms. A distinguishing feature is that CSF appears bright whereas white matter appears relatively dark. (Image adopted from Brown and Semelka, 2003)

In this PhD project, I primarily utilise two specialised sequences for the imaging of systemic gadolinium contrast agent transfer into the CSF spaces (chapter 3); a) heavily T_2-weighted Magnetic Resonance Cisternography (MRC) sequence b) the Fluid-Attenuated Inversion Recovery (FLAIR) sequence (parameters carefully chosen to exhibit a high degree of T_2 appearance – section 3.2.5).

A magnetic resonance cisternography (MRC) sequence is utilised for the imaging of CSF spaces in the brain. An MRC sequence should therefore be heavily T_2-weighted

to image components with very high T_2 relaxation values (such as the CSF), whilst attenuating signal from other brain compartments (e.g. brain parenchymal tissue). In other words, an MRC sequence provides an anatomical reference scan of the brain's fluid-filled spaces. An MRC image can be generated from a spin-echo (or fast spin-echo) sequence by selecting very high TR and TE values in order to obtain a heavily T_2-weighted image (for the cost of lower SNR however).

A FLuid Attenuating Inversion Recovery (FLAIR) sequence on the other hand is usually employed for the nulling of CSF signal. A common use of the FLAIR sequence in clinic is for the imaging of lesions (i.e. areas of tissue T_2 prolongation) that are difficult to see on conventional images, including meningeal diseases and lesions in proximity to CSF such as cerebral cortical lesions (Bakshi *et al*., 2001). An extended utility of the FLAIR sequence corresponds to the imaging of brain CSF movement/flow (Jost *et al*., 2017) in a contrast enhanced setting (section 2.6). In this scenario, the FLAIR sequence is adopted to null the signal from the CSF (in the pre-contrast scan) in order to detect the presence of small amounts of contrast agent entering the CSF spaces following systemic delivery (in the post-contrast scans) through the changes it induces in CSF T_1 and T_2 relaxation times. For this specific application, the FLAIR sequence can be heavily T_2-weighted in order to null the signal from parenchymal brain tissue, hence it can be regarded as an MRC sequence but with an additional inversion recovery pulse for the specific nulling of CSF signal. For the generation of this specific type of FLAIR image, a spin-echo sequence with very long TE and TR values should be adopted (with an inversion recovery pulse as suggested by the name). Figure 2.14 demonstrates example MRC and FLAIR images.

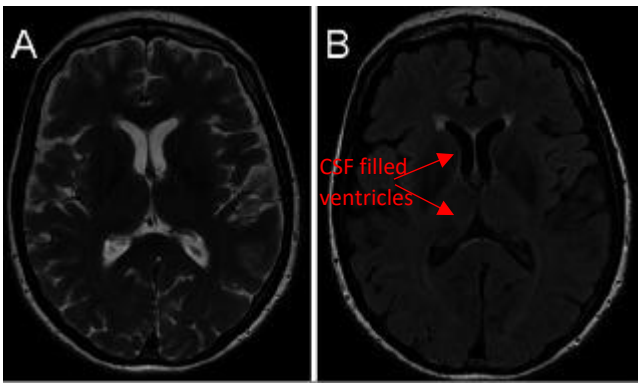

Figure 2.14: Axial brain slices from the human brain. A- In the heavily T_2-weighted image (i.e. MRC), the CSF spaces are readily identified. B- Application of an inversion recovery pulse (i.e. a FLAIR sequence) has nulled the signal from the CSF (e.g. ventricular CSF signal has been nulled as indicated by red arrows). Note that this

sequence specifically nulls CSF signal and does not null the signal from other tissue compartments such as the fat layer underlying the skull, hence the bright signal around the edges of the brain. (Images adopted from Rosenberg et al., 2013)

2.5 Diffusion-weighted MRI

Another specialised sequence that will be utilised in this PhD project is based on the diffusion of water molecules. Briefly, in chapter 5, I will make an attempt to null/crush the signal in the blood vessels by sensitising the diffusion-weighted sequence to the perfusion of blood (i.e. by the application of 'diffusion crushers'). Hence below, I will briefly describe the fundamental principles behind diffusion-weighted MRI.

Diffusion-weighted (DW) MRI is increasingly being used in diagnosis and investigation of specific structural properties (it is particularly useful in tumour and stroke imaging (Chilla *et al*., 2015, Allen *et al*., 2012)). Diffusion is a transport mechanism and involves the movement of molecules in a system. In biological tissues, diffusion of water molecules is not free and it depends on the surrounding environment (e.g. tissue structure, size, temperature). In pathology, the diffusion pattern is sometimes markedly altered therefore abnormalities can be detected by imaging changes in diffusion behaviour of the water molecules. Contrast in DW imaging depends on the difference in rate of apparent water diffusion between tissues (Chilla *et al*., 2015). For the generation of a DW image, additional magnetic field gradients are applied to the conventional MR sequences.

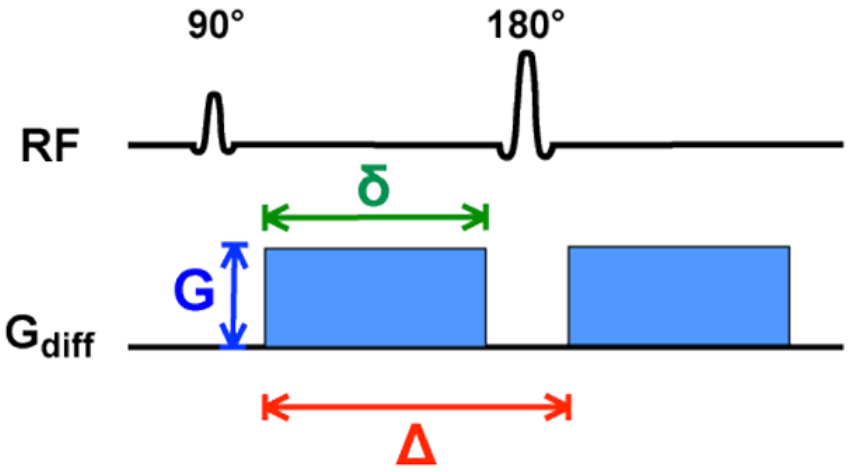

Figure 2.15: Diffusion-weighted spin-echo sequence. Additional (diffusion) gradients are added to the spin echo sequence. The first gradient is called the dephasing gradient and the second (which is usually opposite in direction) is called the rephasing gradient (note second gradient in this case has same direction due to the presence of 180°*pulse). Both gradients have equal magnitude (G) and duration (δ) and are*

separated by a specific time interval (Δ). (Image adopted from www.mriquestions.com)

As shown on figure 2.15, these additional diffusion gradients have equal magnitude (G) and duration (δ) and are separated by a specific time interval (Δ). Spins diffusing after application of the first gradient acquire a phase shift depending on their positions (i.e. de-phase). Upon application of the second (opposite) gradient, spins rephase (to reverse the changes made by the first gradient). In the case of static spins (i.e. with no net proton movement), opposite phase shifts cancel each other out and there is no signal attenuation. However, if protons diffuse, there won't be a complete rephasing of the spins after application of the second gradient and this leads to signal reduction. The apparent diffusion of spins in tissue is estimated based on this signal reduction. For example, spins within CSF can diffuse more freely compared to spins within the brain parenchyma, this leads to relatively greater signal loss and therefore ventricles appear dark in a diffusion-weighted image. The signal loss is explained by Stejskal-Tanner equation:

$$S = S_0 e^{-bD} \tag{1.7}$$

where S refers to the signal received, *b* or '*b-value*' is the diffusion weighting (units $s.m^{-2}$), S_0 is the signal strength without applying diffusion gradients and *D* is diffusion or 'Apparent Diffusion Coefficient' (*ADC*). The *b-value* itself is given by the equation:

$$b = \gamma^2 . G^2 . \Delta^2 . (\Delta - \delta/3) \tag{1.8}$$

where γ is the gyromagnetic ratio of hydrogen proton (42.58 MHz/T), G is the magnitude of applied gradient, δ is the duration of gradient and Δ is the time between the application of the two gradients.

2.5.1 Intravoxel Incoherent Motion

Intravoxel Incoherent Motion (IVIM) MRI has roots in diffusion-weighted MRI (it is an extension of the conventional diffusion-weighted MRI). IVIM refers to translational movements which within a given voxel and during the measurement time present a distribution of speeds in orientation and/or amplitude (Le Bihan, 2019). Although molecular diffusion is the main driver of signal attenuation in IVIM (similar to the conventional diffusion-weighted MRI), an additional factor contributing to the MRI signal attenuation is the blood microcirculation in the capillary network (i.e. perfusion). The collective motion of blood water molecules in a network of randomly oriented capillaries (i.e. the perfusion component) causes randomness and mimics a pseudo-diffusion process. This pseudo-diffusion model assumes that blood changes direction

several times during the encoding time, a condition that is met when blood flow is fast, capillary segments are short and the encoding time is long enough to accommodate those direction changes (Le Bihan, 2019). The blood microcirculation component signal decays 10 times faster than the tissue diffusion component and therefore the overall MRI signal attenuation in IVIM follows a biexponential pattern of decay. Since the pseudo-diffusion coefficient (*D**) is an order of magnitude larger than the diffusion coefficient (*D*), the perfusion and the diffusion terms can be separated in IVIM depending on the choice of the *b*-value (Le Bihan, 2019). For example, the higher the *b-value*, the stronger the diffusion effects but also more noise and therefore lower SNR (this is because signal from both white matter and grey matter structures diminishes as gradient strength increases (Burdette *et al*., 2001)). On the other hand, at smaller *b*-values both diffusion and perfusion terms are present and DW imaging with smaller ('perfusion-sensitive') *b*-values can suppress the vascular signal (Le Bihan, 2019, Silva, Williams and Koretsky, 1997). In addition to effective suppression of perfusion effects, at relatively lower *b*-values a higher SNR can be obtained (Takahara and Kwee, 2012).

As mentioned, a diffusion sensitive sequence will be implemented in chapter 5 in an attempt to null the time-varying intravascular signal intensity in the CE-MRI examinations (i.e. following administration of contrast agent). Since CE-MRI is the central platform in this PhD project, below, CE-MRI imaging will be explained in detail.

2.6 Contrast enhanced (CE) MRI & gadolinium contrast agents

Despite the inherent contrast generated by MRI (section 2.4), many clinical examinations could benefit from enhanced contrast in the MR images. Contrast agents significantly increase the sensitivity of MRI and improve diagnostic accuracy in many clinical scenarios (e.g. imaging stroke, cardiac perfusion, breast tumour and musculoskeletal injury). In routine CE-MR imaging, usually a baseline/pre-contrast image is acquired followed by the post-contrast acquisition(s). If the intent of CE-MRI examination is visualisation of veins or arteries (i.e. magnetic resonance angiography), scans are acquired immediately after contrast agent delivery, and if the intent for imaging is detection of stoke or tumour (i.e. conditions that imply blood brain barrier breakdown), post contrast scans are delayed (usually up to 10 minutes) to allow for the distribution of contrast agent into the lesion/tissue (Dieke-Hofmann *et al*., 2019). It should be noted that in MR images contrast agents are not directly detected, it is their presence that causes changes in the relaxation times of the

surrounding water that modulates the measured signal. Metal ions such as gadolinium, manganese, dysprosium and iron are all paramagnetic agents capable of inducing changes in tissue relaxation times (with gadolinium being the most widely explored). Gadolinium based contrast agents (GBCAs) affect the MRI signal in 2 ways; positive contrast effect and negative contrast effect.

2.6.1 Gadolinium positive contrast effects

When gadolinium is placed inside a magnetic field, magnetic field inhomogeneities are induced and this accelerates both T_1 (longitudinal) and T_2 (transverse) relaxation rates, thereby shortening T_1 (due to more rapid transition between spin states) and T_2 (due to rapid dephasing of protons) relaxation times. The term describing the relationship between these relaxation times (ΔT) and the concentration [C] of the GBCA is called relaxivity (r, L/mmol.s) of the contrast agent, by definition:

$$1/\Delta T_1 = r1.[C] \quad \& \quad 1/\Delta T_2 = r2.[C] \qquad (1.9)(1.10)$$

Common clinical doses of gadolinium are between 0.1 - 0.2 mmol/kg (although concentrations as high as 0.4 mmol/kg are administered for purposes such as magnetic resonance angiography). At these concentrations, the T_1 shortening effects dominate and overwhelm the milder T_2 effects (figure 2.16). Tissues which take up contrast agent therefore achieve positive contrast by demonstrating an enhanced signal intensity on T_1-weighted images (i.e. an increased signal from baseline).

2.6.2 Gadolinium negative contrast effects

At very high gadolinium concentrations however, T_2 (or T_2*) effects will dominate leading to negative contrast (i.e. reduced signal relative to baseline). The T_2 relaxation time is also dependant on the magnetic field strength and at higher magnetic fields it can shorten the T_2 relaxation times even further. Figure 2.16 illustrates the dependence of tissue signal intensity (i.e. induced tissue contrast in the MR image) on gadolinium concentration and depicts the competing T_1 and T_2 effects that can be noticeable on both T_1 and T_2-weighted images.

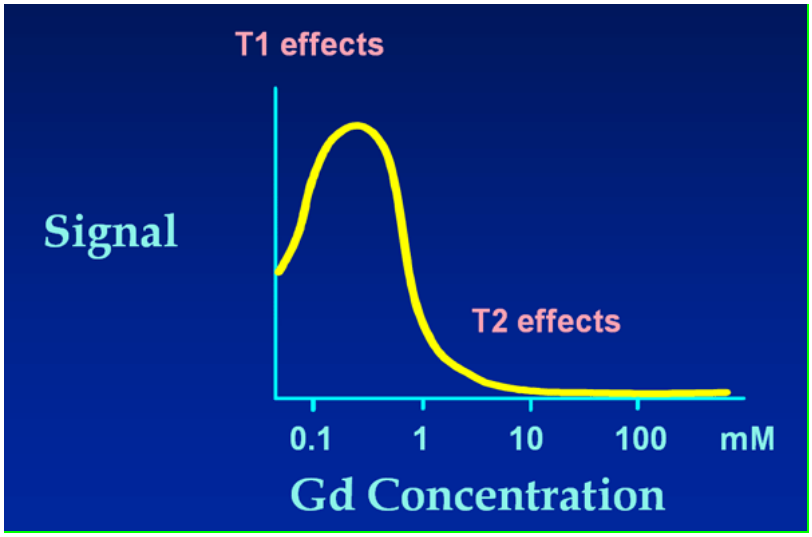

Figure 2.16: Dependence of tissue signal intensity (i.e. induced tissue contrast in the MR image) on gadolinium concentration. The schematic depicts the competing T_1 and T_2 effects that can be noticeable on both T_1 and T_2-weighted images. At very high concentrations (~ >1 mM) the T_2 shortening effects dominate the T_1 shortening effects, leading to a negative contrast. Note the relationship between the observed MR signal and gadolinium concentration shown above is non-generic and in practice, is dependant on MR-related factors (such as sequence parameters and field strength (1.5T in this figure)). (Image adopted from http://mriquestions.com/what-is-relaxivity.html)

The negative contrast effects of gadolinium at very high concentrations (~ >1 mM) were discussed above (where T_2 (or T_2*) shortening effects dominate). In practice however, it is possible to observe the negative contrast effects of gadolinium at much lower concentrations than this (through its T_2* shortening effects). In addition to accelerating T_1 and T_2 relaxation rates, magnetic field inhomogeneities induced by paramagnetic contrast agents also accelerate the T_2* relaxation rate and result in susceptibility-induced signal loss. Susceptibility induced signal losses are more readily observed at lower gadolinium concentrations on T_2* images as T_2*-weighted sequences are most sensitive to changes in T_2* (e.g. GE-EPI sequence). The described susceptibility induced signal loss is in fact the basis of dynamic susceptibility contrast (DSC) MRI.

2.6.3 Gadolinium safety profile and recent concern of gadolinium retention in the brain

Millions receive MRI gadolinium based contrast agents worldwide annually. Since free gadolinium ion is toxic the ions are bound in stable complexes known as chelates

that can be safely excreted via the kidneys. Based on their chemical structure, GBCAs can be divided into two groups; linear and macrocyclic agents (although they can be further subdivided based on their charge (ionic or non-ionic)). Linear and macrocyclic agents exhibit different thermodynamic/kinetic complex stabilities in vivo (Caravan *et al*., 1999). As shown on figure 2.17, the linear structure consists of an elongated ligand (with relatively weak bonds) that wraps around the gadolinium ion (similar to a constrictor snake wrapping around its egg), whereas in the macrocyclic agent the gadolinium ion is "caged" in the cavity of the ligand (clamp-shell like structure), hence lower rates of dissociation and are thus considered to be the most "stable" between the two. In 2008, Frenzel *et al.* (Frenzel *et al*., 2008) categorised all GBCAs into 3 classes based on their stability: macrocyclic, ionic linear and non-ionic linear in the order of decreasing stability.

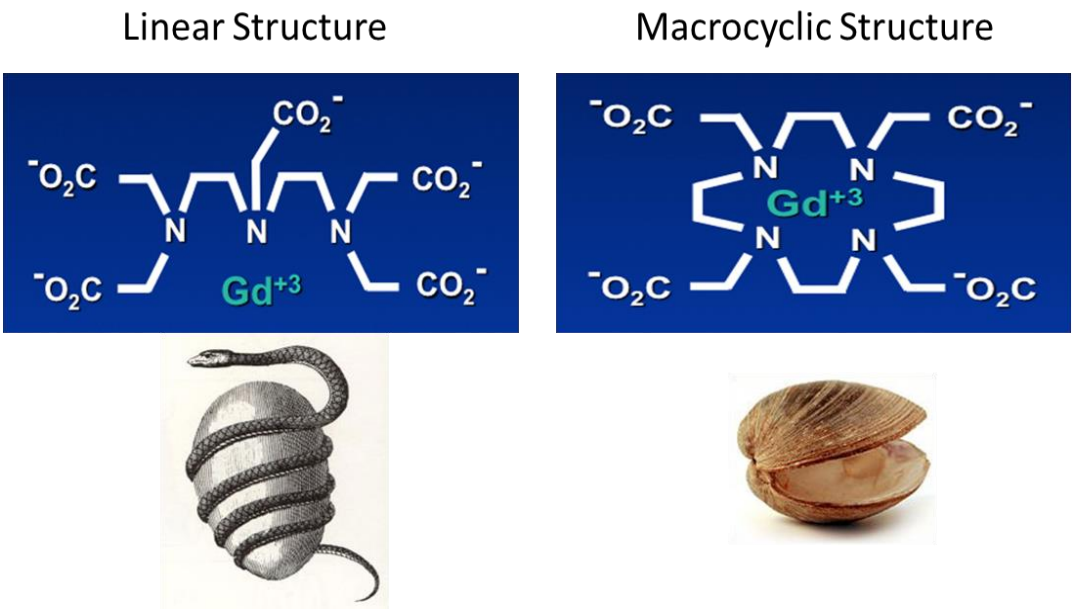

Figure 2.17: Structure of a linear gadolinium based contrast agent where an elongated ligand wraps around the gadolinium ion, similar to a constrictor snake wrapping around its egg (left) and the structure of a macrocyclic gadolinium based contrast agent where the gadolinium ion is trapped inside the cavity of the ligand, in a clamp-shell like structure (right). (Image adopted from http://mriquestions.com/so-many-gd-agents.html)

GBCAs were generally considered to have an excellent safety profile (Matsumura *et al*., 2013), until recently. Initially described by Kanda *et al*. in a retrospective study (Kanda *et al*., 2014), signal hyperintensity (in unenhanced images) was observed in the deep brain regions of patients who had previously received 6 or more GBCA doses, all with normal renal function. This finding raised significant safety concerns

within the MRI community. As a result of this concern, many more recent publications have since replicated these findings (retention of gadolinium in the brain) and moreover, it has now been demonstrated that the previously described safety concern regarding gadolinium retention in the brain is specific to the linear class of GBCAs (Kanda *et al.*, 2015, Radburch *et al*., 2015, Errante *et al*., 2014), possibly due to the higher dissociation propensity of linear GBCAs. As a result, linear GBCAs were suspended and only macrocyclic contrast agents are currently FDA approved. Recently, in order to investigate the clinical findings of gadolinium retention in the brain, Jost *et al*. (Jost *et al*., 2016) took a pre-clinical approach. They demonstrated signal hyper-intensities in the dentate nucleus region of the rat brain, following repeated injections of linear GBCAs (2.5 mmol/kg daily for 10 days). The rats who had received macrocyclic GBCAs demonstrated no signal hyper-intensity. Interestingly however, all GBCAs, independent of their chemical structure penetrated the ventricular system (possibly via the choroid plexus) (Jost *et al*., 2017). Further penetration from the CSF spaces into the brain parenchyma could not be concluded however in their study, but it was suggested to be facilitated by the glymphatic pathway (Jost *et al*., 2017).

Confirmation (or otherwise) of this hypothesis (i.e. glymphatic transport of GBCA from the CSF into the brain tissue) will have a significant implication for the CSF-ISF exchange research field; it provides first-hand evidence regarding physiological exchange of CSF with ISF (essentially GBCA/CSF in ventricles will be transferred into the brain parenchyma/interstitial space). Hence, in the next chapter I will describe my efforts to develop a methodology for the non-invasive assessment of CSF-ISF exchange using MRI by tracking the hypothesised delivery of GBCAs in the CSF to the brain tissue.

Chapter 3: Methods development - optimising the non-invasive platform for in-vivo imaging of fluid movement in the brain

This chapter describes the methods development/optimisation experiments for the construction of the first non-invasive MRI CSF-ISF exchange measurement platform. Before starting this PhD, all CSF-ISF exchange (e.g. glymphatic system) assessment techniques at my host laboratory were derived from invasive techniques for the injection of exogenous material (such as contrast agents or aberrant proteins) directly into the CNS. Additionally, to the best of my knowledge, there were no techniques/publications regarding the non-invasive assessment of glymphatic function (or more broadly, CSF-ISF exchange). Towards my goal of developing a non-invasive MRI technique to assess CSF-ISF exchange, I noted a relevant study that captured the infiltration of GBCAs into the cerebral ventricular system of the rat brain following IV GBCA injection (Jost et al., 2017). This led me to the idea of developing a new MRI method that, building on this observation (Jost et al., 2017), could then track the hypothesised delivery of GBCAs in the CSF to the brain tissue as a novel, and non-invasive, measure of CSF-ISF exchange (figure 3.1). In this chapter I will describe a series of methodical development studies that I performed towards this aim.

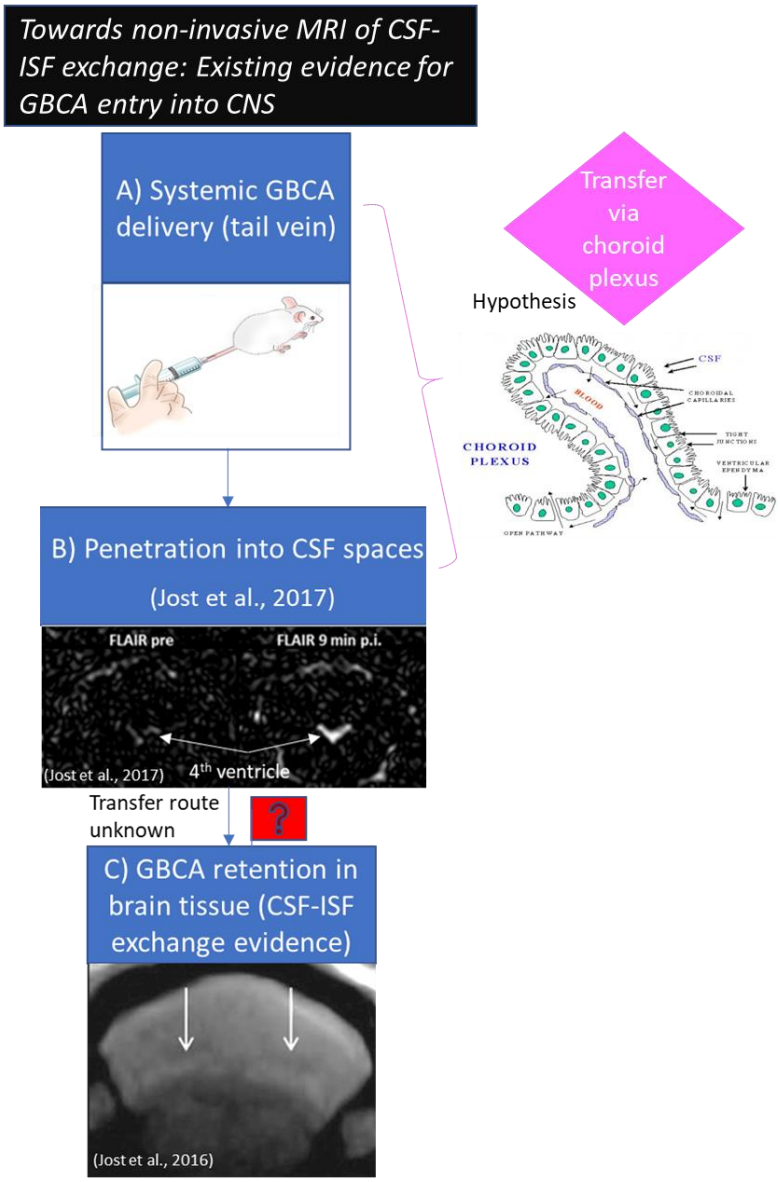

Figure 3.1: Flow diagram of GBCA entry into the CNS. GBCA retention in the brain tissue has been reported in unenhanced T_1-weighted images (in patients with a history of repeated contrast enhanced MRI examinations), which provides indirect evidence for CSF-ISF exchange. The complete route of GBCA transfer into brain tissue is not known. Towards this question, it has been shown that systemic GBCA penetrates the CSF spaces following IV injection (Jost et al., 2017). Although direct evidence does not exist, it is believed that this transfer occurs at the level of the choroid plexus. Route of further GBCA transfer (from the CSF spaces into the brain tissue) is not known however. (Images adopted from Jost et al., 2017, Jost et al., 2016, www.brainimmune.com & www.encapsula.com)

3.1 Introduction

The utilisation of GBCAs is a central component of my novel approach, introduced in this thesis, to capture CSF-ISF exchange with minimally invasive MRI methods. Since gadolinium ion (Gd^{3+}) is toxic to imperative physiological processes associated with (but not limited to) muscle tissue and neurons (e.g. competitive inhibition of voltage gated calcium channels) (Rogosnitzky and Branch, 2016), there are constrains preventing administration of large doses of GBCAs (due to possible de-chelation of gadolinium from the GBCA complex leading to the release of free Gd^{3+} ions). Additionally, GBCA exposure/administration has been associated with nephrotoxic effects and it could cause nephrogenic systemic fibrosis (NSF) in patients with renal insufficiency (Rogosnitzky and Branch, 2016). In this section I sought to maximise the amount of contrast in the MR images by identifying the highest GBCA dose that can be administered in mice (IV) without generating any adverse reactions in the measured physiology of the animals. As a result, in this section I will introduce the majority of the commercially available MRI contrast agents, as well as the criteria that need to be considered for the selection of the appropriate GBCA dose.

The choice of MRI sequence parameters is critical to the realisation of the aims of this work. Utilising MRC and FLAIR sequences in the rat brain, the primary route/location of GBCA infiltration/entry into the CNS, was suggested to be the ventricular system (Jost *et al*., 2017). Although no direct evidence was provided, the choroid plexus (i.e. the blood CSF barrier – BCSFB) was suggested to be responsible for the transfer of GBCA from the circulation into the CSF spaces (Jost *et al*., 2017). Interestingly, the blood-CSF barrier has been known to be more permeable than the blood-brain barrier, primarily due to the fenestrated nature of the choroid plexus capillaries which lack tight junctions (Laterra *et al*., 1999). Since the rate of GBCA transfer from blood to CSF following IV delivery is believed to occur rather quick (few minutes) in the rodent brain and since the FLAIR sequence adopted by Jost *et al*. had a relatively low temporal resolution (16 minutes), in this section, an aim of mine is to confirm the findings of Jost *et al*. but with a higher temporal resolution (i.e. less than one minute). This is in order to more precisely capture the dynamic temporal profile of the blood-to-CSF transfer of the contrast agent. In this section, I will describe the process of optimising a high temporal resolution MRC-FLAIR sequence for the detection of CSF spaces and the capturing of rapid transfer of GBCA from the blood to the ventricles (in turn to provide supporting evidence for the role of choroid plexus in GBCA transfer from the blood and into CSF spaces).

The MRC-FLAIR sequence that I employed is specifically designed for the visualisation of the CSF spaces and the infiltration of GBCA into the ventricles. As it is a heavily T_2-weighted sequence, it suppresses all the signal from parenchymal brain regions, hence it is not possible to follow/image the transfer of GBCA into the brain tissue that I hypothesise to occur and aim to measure for the first time, therefore, an alternative sequence needs to be devised (e.g. a T_1-weighted sequence). A T_1-weighted MRI approach is commonly adopted in clinical CE-MRI for imaging of GBCA uptake in brain tissue (e.g. in tumour/lesion due to the leakiness of the blood brain barrier) (Villanueva-Meyer, Mabray and Cha, 2017). A challenge in CE-MRI is the normalisation of tissue signal intensity to correct/account for the undesired signal contributions from the blood vessels (i.e. intravascular compartment), when visualising extravascular GBCA accumulation. MRI inherently suffers from limited spatial resolution and as a result, partial volume effects (PVEs) from the intravascular compartment when analysing parenchymal GBCA uptake are inevitable. Since intravascular signal is increased after standard clinical doses of contrast agent (T_1 dominating effects – figure 2.16), it is difficult to differentiate the signal increase due to actual extra-vascular tissue contrast penetration/uptake (i.e. uptake due to the hypothesised CSF-mediated GBCA transfer into the brain tissue) from signal increases due to intravascular signal increase. Thus, time-varying intravascular effects represent a key consideration when interpreting experimental data of this nature. In an ideal scenario, the contrast agent would rapidly infiltrate into the brain tissue and rapidly clear from the circulation at the same time, so that the signal contribution from the intravascular compartment (i.e. blood vessels) would be constant over time (i.e. no time-varying effects), hence any spatial-temporal signal intensity changes in the brain tissue, would indicate inflow/penetration of contrast agent into the brain tissue. However, in routine CE-MRI, GBCA is not rapidly cleared from the circulation, therefore, any subtle GBCA inflow into the brain tissue from the CSF (what I aim to measure in this work), which may only create subtle signal intensity increase, is likely to be masked by the stronger intravascular signal increase (this is because the acquired tissue signal is not perfect and is contaminated by contributions from the intravascular compartment due to the limited resolution of MRI and the associated PVEs as described earlier). This is potentially the reason why contrast penetration into brain tissue had been left unnoticed until recently (Kanda *et al*., 2014). My main aim in this section is therefore, to develop a novel, non-invasive MRI platform that aims to differentiate MRI signal changes that originate from GBCA in the tissue (extravascular compartment) versus the signal changes that originate from GBCAs in the blood vessels (intravascular compartment), towards CSF-ISF

exchange monitoring (i.e. movement of solutes (gadolinium in this case) in the brain parenchyma) and a meaningful characterisation of CSF-mediated parenchymal GBCA uptake.

Image analysis and data post processing are also crucial factors to optimise extraction of information from the imaging datasets. Valuable information could be hidden in the raw images that are not readily visualised by the naked eye. High level image processing techniques such as image registration, subtraction, thresholding, averaging and time-course extraction are all examples of post processing steps I have implemented that have been highly influential in uncovering CSF-ISF exchange pathway correlate measures from the acquired data. Hence, below I will provide all the details of the computational work I completed for the development of the image analysis pipeline.

3.2 Methods

3.2.1 Animal preparation procedures

In the interest of consistency, all experiments in this section were performed on male C57Bl6 wild-type mice (Charles River UK Ltd) at approximately 3 months of age. All experiments were performed in mice in accordance with the European Commission Directive 86/609/EEC (European Convention for the Protection of Vertebrate Animals used for Experimental and Other Scientific Purposes) and the United Kingdom Home Office (Scientific Procedures) Act (1986) with project approval from the Institutional Animal Care and Use Committee. Presentation of data complies with the ARRIVE guidelines (Kilkenny *et al*., 2010, McGrath *et al*., 2010). Anaesthesia was induced and maintained with 2.5% and 1.5% isoflurane respectively [in a mixture of 0.4L/min medical air and 0.1L/min O2]. Core body temperature and respiration were monitored using a rectal probe and pressure pad (SA instruments). Body temperature was maintained at 37 ± 0.5 °C using a warm water circulatory system or a heat pad. For contrast agent delivery, either IV or IP cannulation was performed using a 25G butterfly needle and a heparinised saline infusion line (to prevent a blood clot building up at the tip of the needle and blocking the flow of contrast). For IP cannulation, a needle was inserted in the lower right/left quadrant of the abdomen to avoid damage to the urinary bladder, cecum and other abdominal organs (the needle was secured in place using surgical tape). For IV injections, tail vein cannulation was performed. After making sure that the IV/IP cannulation had been successfully performed, saline infusion line was replaced with the contrast agent infusion line. The bolus of the contrast agent was then delivered via a programmable infusion pump (Harvard

Instruments). Bench experiments for dose selection were continued for up to 4 hours post administration of the proposed dosage to monitor the physiology of the animals (n=2) and to detect any possible adverse side effects (e.g. depression of respiration and thermoregulation, and also myoclonus and tremors which are indicators of animal distress). For MRI experiments, following induction of anaesthesia, cannulation (IV (n=4), IP (n=1)) was performed outside the scanner whilst laying on the cradle (animal bed), and then transferred into the scanner and baseline scanned before contrast agent infusion. Head motion was minimised by using MR compatible head holder and animals were imaged for up to 3 hours post contrast injection.

3.2.2 Selection of contrast agent, it's corresponding dose and route of delivery

Experiments were performed to identify the GBCA that would allow the maximum GBCA dose, without any detrimental effects to mice. In addition to clinically available contrast agents (GBCAs), pilot experiments were also carried out using more experimental (non-clinical) contrast agents, such as the free gadolinium ion administered as the $GdCl_3$ chelate ($GdCl_3$ displays higher MR relaxivity values and theoretically results in greater sensitivity/contrast enhancement). The greatest amount of contrast agent dose in animals is constrained by the LD50 (toxicity) values but also rigorous home-office regulations. LD50 or 50% medical lethal dose, is defined as the dose of a substance that kills half of the subjects in a tested population. As different GBCAs exhibit different LD50s, I searched for the GBCA with the highest LD50. The project licence also defines stringent regulations on the volume of substances that can be delivered to mice. Table 3.1 below defines the maximum volume of injection that is permitted for each route of delivery.

	Routes and Volumes (ml/kg)						
	s/c	i/p	i/m	Oral gavage	i/v Bolus infusion <1 min	<5 mi	I/t
max. no. of doses	24	24	6	20	14		24
max. daily volume	20	20	0.05ml	(see below)	5	20	20µl
no. of doses daily for ≤7 days	3x	2x	2x	2x	2x	2x	2x
no. of doses daily for >7 days	2x	1x	1x	1x	1x	1x	1x

Table 3.1: Dosing table defined in the home-office project licence. Maximum IV/IP dose allowed is 20 ml/kg (although for IV delivery of this amount a 5 min delivery time should be allowed).

3.2.3 MRI methods

A 9.4T VNMRS horizontal bore MRI scanner with a 205/120HD gradient set was used (Agilent Inc., USA). A 72 mm inner diameter volume coil and a 2 channel array surface coil (Rapid Biomedical) was used for radiofrequency transmission and reception. 1st and 2nd order shimming was performed to reduce magnetic field inhomogeneities around the brain prior to image acquisition (typical linewidth (Full Width Half Maximum) was approximately 50 Hz).

3.2.4 Magnetic Resonance Cisternography (MRC) sequence development process

An MRC sequence was implemented & optimised in order to clearly visualise the main CSF structures in the mouse brain:

For T_2-weighted imaging, a fast spin-echo multi-slice (FSEMS) sequence with long TR and TE values was nominated (section 2.4.2). Hence pilot scans were acquired and optimised by a trial and error basis with a range of relatively long TRs [4.5s, 6.25s, 8.4s, 9s, 10.4s, 14.65s] and effective TEs ($\mathrm{TE}_{\mathrm{eff}}$ [96ms, 144ms, 196ms]. In the early stages of the optimisation process, I observed that wrap-around artefacts were prevalent for small fields of view (FOV<15x15mm) (figure 3.2 – left). Wrapping artefacts may be resolved by swapping the read and phase encoding directions or by increasing the FOV. In order to address this artefact, the FOV was increased to 20x20mm. This modification also improved SNR for the cost of lower spatial resolution (and increased PVEs). An MRC sequence is designed to preferentially detect signal from the CSF. Therefore, PVEs from the brain tissue should be minimised when trying to cleanly extract the signal from the CSF spaces. Any partial volume from the surrounding parenchymal blood vessels, would cause an unwanted signal contribution from GBCA in the circulation. The contribution of these PVEs can

be reduced by either having a high in-plane spatial resolution (& small slice thickness) and/or having an even higher T_2 weighting (i.e. higher TR/$\mathrm{TE}_{\mathrm{eff}}$ so that the signal from other tissues are highly attenuated). At relatively lower TR/$\mathrm{TE}_{\mathrm{eff}}$ values (e.g. TR = 4.5s and $\mathrm{TE}_{\mathrm{eff}}$ = 96ms), some PVEs from surrounding parenchymal tissue could be observed as the T_2 weighting was not strong enough. By using longer TR/$\mathrm{TE}_{\mathrm{eff}}$ values (TR = 9s, $\mathrm{TE}_{\mathrm{eff}}$ = 144ms) within the MRC sequence, I ensured that the signal from the brain tissue is effectively nulled, whilst maintaining a reasonable temporal resolution (i.e. less than one minute). After visually inspecting the initial pilot images, I concluded that the SNR was prohibitively low for very high image resolutions (<0.08mm; FOV = 20x20mm, matrix size = 256x256), hence the matrix size was reduced to 128x128 in order to improve SNR (for the cost of lower spatial resolution). However, a suspected Gibbs ringing artefact could be visualised following this modification (figure 3.2 – right).

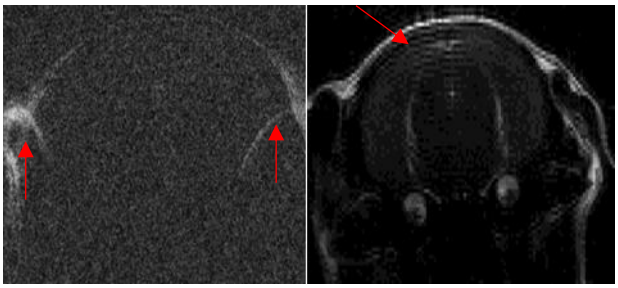

Figure 3.2: Left- illustration of the wrap-around artefact on the MRC images (red arrows), due to small FOV definition. The SNR is also low due to high image resolution. Right- illustration of the suspected Gibbs ringing artefact (red arrow) as a result of low spatial resolution.

Gibbs ringing artefact may be resolved by increasing the image resolution. Hence the matrix size was modified to 192x128 in order to improve resolution in the read direction and to avoid any increase in acquisition length (i.e. temporal resolution). The final parameters of the optimised MRC sequence (heavily T_2-weighted fast spin-echo multi-slice) are as follows:

TR = 9s, $\mathrm{TE}_{\mathrm{eff}}$ = 144ms, FOV = 20x20mm, ETL = 32, matrix size = 192x128, number of slices = 16, slice thickness = 1mm, number of averages (NA) = 4, scanning time = 2.5 mins.

3.2.5 FLuid Attenuating Inversion Recovery (FLAIR) sequence development process

Next, I sought to capture the rapid infiltration of systemic GBCA into these CSF spaces. Hence the MRC sequence was followed by a FLAIR sequence approach to make a combined MRC-FLAIR technique. A FLAIR sequence is essentially an inversion recovery sequence employed to null the signal from CSF/fluids in the pre-contrast (baseline) condition. Hence this approach will be very sensitive to small amounts of contrast agent entering the CSF spaces following IV delivery (in the post-contrast scans) through the changes it induces in CSF T_1 and T_2 relaxation times. In order to find the null point of the CSF signal in the pre-contrast condition (to attenuate the CSF signal and increase sensitivity to inflow of GBCA into the CSF spaces post injection), the sequence was optimised by manually inspecting (i.e. trial and error basis) images at 8 different inversion times (TI). FLAIR imaging with TIs of 1, 1.5, 2, 2.5, 3, 3.5, 4 and 4.5s were carried out. An inversion time of 1.5s shown to provide the highest CSF attenuation. Also, as described earlier, a high temporal resolution acquisition is required in order to more precisely capture the dynamic temporal profile of the blood-to-CSF transfer of the contrast agent, hence TR value should not be significantly long. Considering these criteria, the FLAIR sequence was implemented and optimised with the following parameters:

TR = 9s, $\mathrm{TE_{eff}}$ = 144ms, ETL = 32, TI = 1.5s, FOV = 20x20mm, matrix size = 192x128, number of slices = 16, slice thickness = 1mm, NA = 1, temporal resolution = 37s.

3.2.6 3D T_1-weighted GE sequence optimisation process

A high spatial resolution is required for a detailed visualisation of possible CSF-mediated GBCA infiltration into the brain parenchyma, hence a 3D sequence was used. A gradient echo sequence is ideal for generation of high resolution T_1-weighted images (relatively short TR and TE). Hence in this study, a 3D T_1-weighted Gradient Echo (GE) sequence was employed, otherwise known as a 3D fast low angle shot (FLASH) GE sequence. A GE T_1-weighted image was sought as it is sensitive to the presence of gadolinium in the parenchymal brain tissue (unlike MRC-FLAIR sequences) and it can also provide both negative and positive contrast in the intravascular compartment depending on the concentration of the contrast agent (section 2.6). This characteristic was exploited to differentiate GBCA-induced signal changes that originate from GBCA in the tissue versus the signal changes that originate from GBCAs in the intravascular compartment (section 3.3.4.2). The parameters of the implemented 3D FLASH sequence are as follows:

TR = 15ms, TE = 3.4ms, flip angle = 15°, NA = 3, FOV = 1.28 × 1.28 × 1.92cm, scanning time = 12.5 min, matrix size = 128 × 128 × 128, yielding an image resolution of 0.1 × 0.1 × 0.15mm.

3.2.7 Data analysis pipeline

MATLAB 2013a & 2018b (MathWorks, USA), NifTK (Ourselin *et al*., 2000), ITK-SNAP (Yushkevich *et al*., 2006), Statistical Parametric Mapping 12 (SPM12) (Penny *et al*., 2011), MarsBar toolbox (Brett *et al*., 2002), GraphPad Prism 6 (GraphPad Software Inc) and ImageJ (Abràmoff, Magalhães and Ram, 2004) software were used for data analysis.

This work predominantly uses in-house MATLAB scripts and routines from the SPM12 toolbox. The image analysis pipeline underwent large improvements throughout the course of this PhD, for example from manual to an automated region of interest (ROI) definition and time-course extraction.

3.2.7.1 Niftii file conversion

Niftii file format is the compatible file format for the use of majority of image analysis platforms (e.g. SPM, niftyReg, MarsBar and ITK-SNAP software). All the acquired data underwent initial pre-processing steps in order to be compatible with the mentioned image processing platforms. Data files were converted into niftii format using in-house written MATLAB scripts together with the niftii toolbox (MathWorks, USA). Originally in a text file format (.fdf), images were initially converted into MATLAB format (.mat) and then into niftii (.nii) format. Voxel sizes used for preclinical imaging (mice) are usually an order of magnitude smaller than the ones typically used for human brain imaging. Since SPM was originally designed for the analysis of the human brain, all voxel dimensions were increased by a factor of 10 in order to facilitate use of SPM software.

3.2.7.2 ROI analysis (manual) - signal intensity time-courses

In order to evaluate contrast agent uptake by different regions of the brain, attempt was made for the manual definition of ROIs and the subsequent extraction of signal intensity time-courses. For each subject, ROI signal intensity time-courses were extracted by the manual definition of ROIs, using the ‘polygon tool’ of the ITK-SNAP software. For the FLAIR images, signal intensity time-courses were derived from the aqueduct, lateral, third and fourth ventricles. Time-courses were then transferred to an excel spreadsheet where data were normalised to percentage signal change by subtracting the baseline (pre-contrast) value from all post-contrast values and then

dividing by the baseline. For the 3D T_1-weighted scans, ROIs were additionally drawn on cerebellum, hypothalamus, periventricular region, longitudinal hippocampal vein and the anterior cerebral artery. Time-courses were normalised as previously described. Figure 3.3 demonstrates examples of these manually drawn ROIs (on T_1-weighted images). Regions have been colour coded for illustration purposes only.

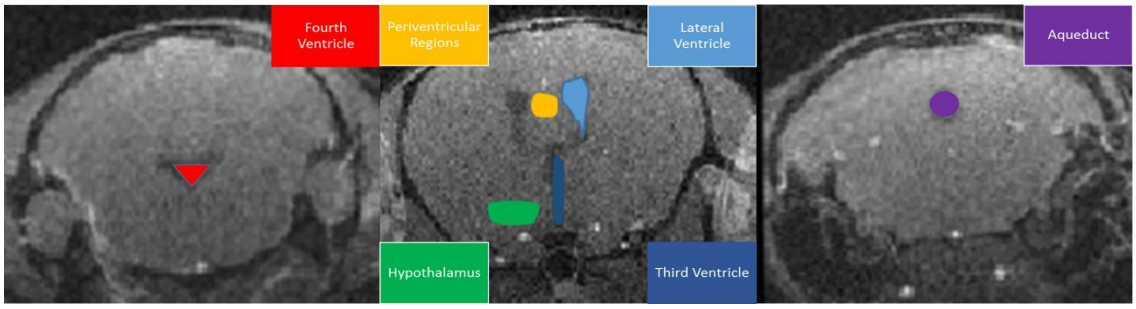

Figure 3.3: ROIs manually drawn on the 3D T_1-weighted images corresponding to the CSF and parenchymal brain regions.

Accurate segmentation/labelling of blood vessels in the mouse brain however is not straightforward and there are no comprehensive digital vascular atlases that can be used. The anterior cerebral artery (ACA) was identified by comparing coronal slices of the 3D T_1-weighted GE images to the MR angiography images of a mouse brain previously acquired in our lab (figure 3.4 - Holmes *et al*., under review). The longitudinal hippocampal vein was identified (figure 3.5) by comparing the MR images to a mouse cerebral vasculature atlas (Dorr, Sled and Kabani, 2007).

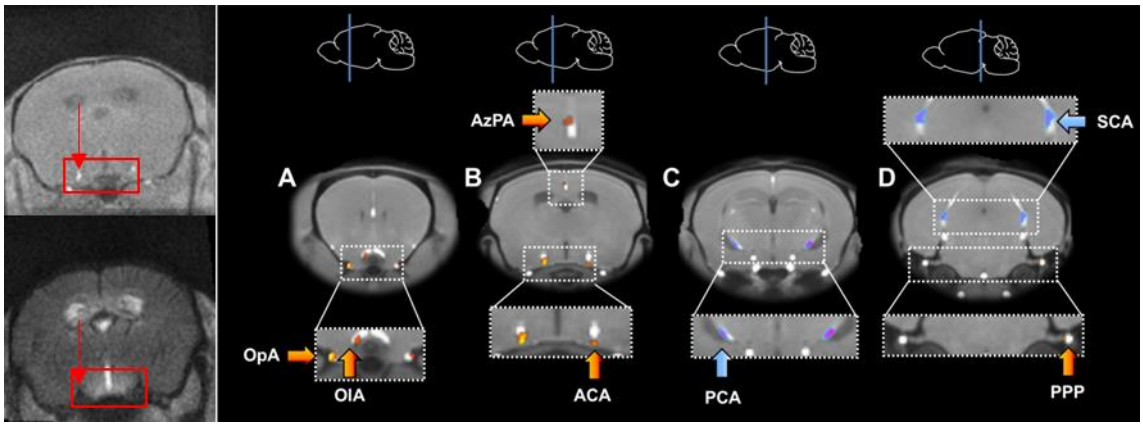

Figure 3.4: Anterior cerebral artery on the acquired 3D T_1-weighted GE images (left – red arrows on the pre (top) and post (bottom) contrast images) identified using an MR angiography of a mouse brain (right). (Image adapted from Holmes et al., under review)

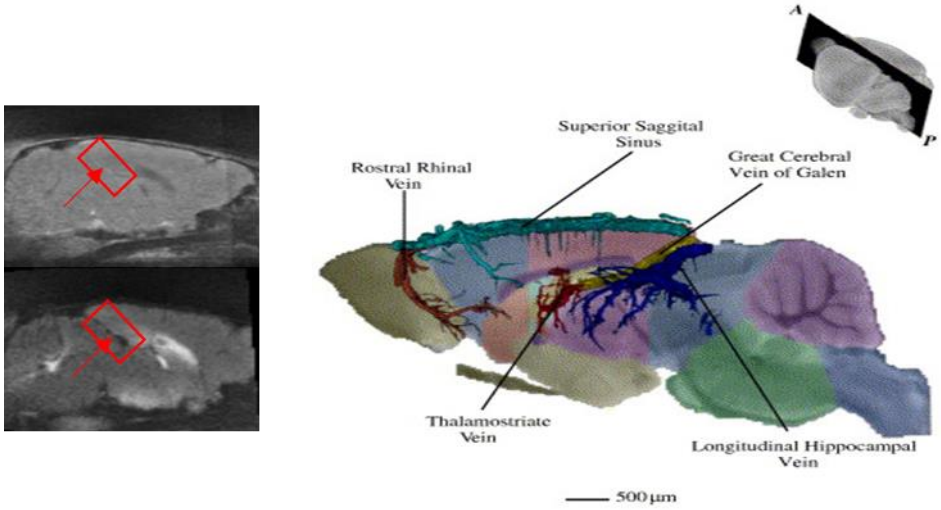

Figure 3.5: Longitudinal hippocampal vein (left- red arrows on pre (top) and post (bottom) contrast images) identified using a mouse cerebral vasculature atlas (right). (Image adapted from Dorr, Sled and Kabani, 2007)

3.2.7.3 Surface coil inhomogeneity correction

For radiofrequency signal reception a surface coil was used (section 3.2.3). The surface coil suffers from a non-uniformity in profile reception, that is a progressively decreased signal further from the coil. The 'nifTK4BiasFieldCorrection' routine of the NifTK toolbox (Clarckson *et al*., 2015) corrects low frequency intensity non-uniformity present in MRI datasets. Hence the non-uniformity in all the imaging datasets in this study were corrected using this routine.

3.2.7.4 Normalisation of ROIs by a control region

Throughout the course of the project and the optimisation process, attempts were made to minimise the contribution of intravascular PVEs in the T_1-weighted images. Data analysis was performed using an exploratory normalisation technique and time-intensity curves were normalised by the time-intensity curve of a control/reference region (a technique similar to those seen in clinical CE-MRI studies). Cerebellum is commonly adopted as a control region for normalisation purposes in clinical CE-MRI studies (Radbruch *et al*., 2015, Robert *et al*., 2015). Additionally, cerebellum region seemed to have relatively much lower GBCA uptake compared to most brain regions upon inspection of the images, hence it may be a sensible candidate as a control/reference region for implementation of such a normalisation technique and this approach was explored in this work.

3.2.7.5 Thresholded subtraction images for improved sensitivity to GBCA uptake

For post-contrast image visualisation purposes, all T_1-weighted scans were subtracted from the baseline scan and subsequently thresholded subtraction images were obtained by setting a threshold value of zero (see section 3.3.4.3.2 for a detailed explanation). In other words, all voxels with a negative value (below zero) within a specific ROI, were assigned a value of zero (i.e. diminishing/devaluing their negative weighting to essentially a neutral weighting), hence minimising their negative contribution to the average signal within that ROI (extracted time-courses) and therefore increasing sensitivity to GBCA uptake (for visualisation purposes).

3.3 Results

3.3.1 Selection of contrast agent, it's corresponding dose and route of delivery

In this section I sought to optimise the GBCA dose in order to achieve the maximum possible contrast in the MR images and to differentiate GBCA-induced signal changes that originate from GBCA in the tissue versus the signal changes that originate from GBCAs in the intravascular compartment (section 3.3.4.2 and figure 2.16). According to figure 2.16, at doses above ~2 mmol/kg the T_2* shortening effects dominate the T_1 enhancing effects that leads to negative contrast (relative to baseline) in the intravascular compartment (due to high GBCA concentration in the blood vessels) and therefore differentiation of intravascular and extravascular derived signal contributions becomes feasible. However, the dose cannot be infinitely increased as these contrast agents become toxic at relatively high doses (dose is constrained by Home Office project licence regulations and LD50 value). The commercially available GBCAs are shown in figure 3.6 below.

Brand Name	T1 Relaxivity (L/mmol-s)	T2 Relaxivity (L/mmol-s)
Magnevist®	4.1	4.6
MultiHance®	6.3	8.7
Omniscan™	4.3	5.2
Dotarem®	3.6	4.3
ProHance®	4.1	5.0
Gadavist®	5.2	6.1
Eovist®	6.9	8.7

Figure 3.6: Commercially available GBCAs and their corresponding T_1 and T_2 relaxivities at 1.5T. (Image adopted from http://mriquestions.com/what-is-relaxivity.html)

Among the agents listed in figure 3.6, Magnevist, Omniscan and ProHance could be sourced by my host laboratory, hence the choice of contrast agent was narrowed down to 3 (out of 7 clinically available agents). Also, pilot experiments with experimental $GdCl_3$ (n=2) revealed the high toxicity of this agent (IV LD50 value of 0.64 mmol/kg in mice) as both animals died relatively soon after injection. Hence this agent was excluded from further consideration. In theory, an agent with the highest relaxivity provides the highest image contrast for the same amount of dose, hence high relaxivity agents allow lower concentration targets to be detected by MRI (Dumas *et al*., 2010). The two commercially available GBCAs with the highest relaxivites and LD50s (IV in mice), were Omniscan (Gadodiamide) and Prohance (Gadoteridol) with T_1 relaxivities of 4.3 and 4.1 L/mmol-s and LD50s of 30 and 12 mmol/kg respectively. Since Omniscan had markedly greater LD50 value and slightly increased relaxivity (figure 3.6), the optimal contrast agent for the subsequent experiments moving forward was chosen to be Omniscan.

Omniscan can be obtained commercially in a 0.5 mmol/ml solution. A maximum volume of 20 ml/kg of this solution (as permitted by the project licence), is equivalent to a dose of 10 mmol/kg (20 ml/kg x 0.5 mmol/ml), well below the LD50 value (3x less). This dose is two times higher than the dose (2.5 mmol/kg) reported in other pre-clinical studies (Jost *et al*., 2016) and approximately 8 times higher than the standard

human clinical dose (0.1 mmol/kg) based upon body surface area normalisation between mice, rats and humans (Nair and Jacob, 2016).

Next, in order to ensure the safety of this relatively higher dose and to detect any possible adverse reactions, two bench experiments were conducted where animals' physiological parameters (such as body temperature and respiration) were carefully monitored for up to 4 hours post administration of the proposed Omniscan dosage. Both animals demonstrated stable physiological conditions with no signs of adverse reactions for the entire duration of the experiment. Hence, for the subsequent experiments moving forward, a final dose of 10 mmol/kg Omniscan was selected. Figure 3.7 illustrates the experimental setup of these bench experiments.

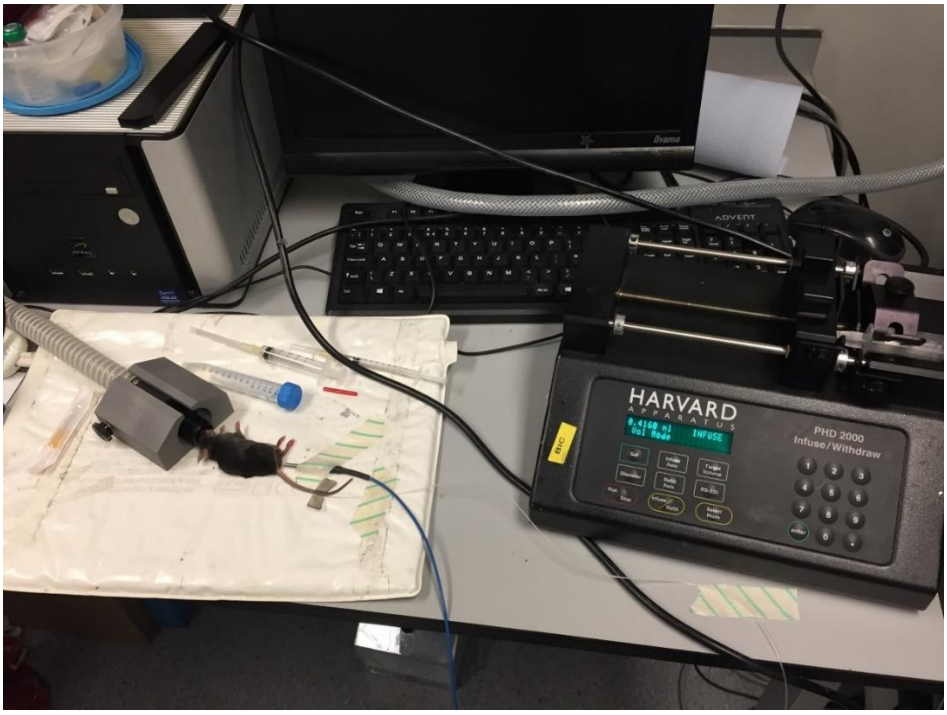

Figure 3.7: Experimental setup of dose selection bench experiments. A bolus of 10 mmol/kg was delivered intravenously in 5 minutes using an infusion pump. Animals were under anaesthesia for the entire length of the experiments (4 hours). Subjects were physiologically stable & no adverse reactions were seen during the entire course of the experiment.

Popular routes of drug/agent delivery in rodent studies include intravenous (IV), intraperitoneal (IP), intramuscular (IM) and subcutaneous (SC). In terms of GBCA administration, the IV and the IP routes are the most commonly explored routes (with IV route considered the gold standard). The IP route is advantageous due to the relatively simpler administration technique (although it is a relatively indirect method of contrast agent delivery to the circulation). On the other hand, performing tail IV

cannulation (specifically in mice) is highly technically challenging. Mastering this skill requires a keen eye and a steady hand and is gained through extensive practice and experience. Following many months of IV cannulation practice and extensive training sessions, I was able to reproducibly administer contrast agents via mouse tail vein cannulation.

Pilot experiments demonstrated the higher efficacy of GBCA delivery following the IV route compared to the IP route with the amount of generated contrast in the brain following IP delivery markedly reduced (data not shown). Therefore, for the subsequent experiments moving forward, the IV route of contrast agent delivery was chosen.

3.3.2 Magnetic Resonance Cisternography (MRC) sequence

For the visualisation of the CSF spaces, a specialised sequence (MRC) was optimised and implemented. Figure 3.8 illustrates example coronal slices derived from the optimised MRC sequence.

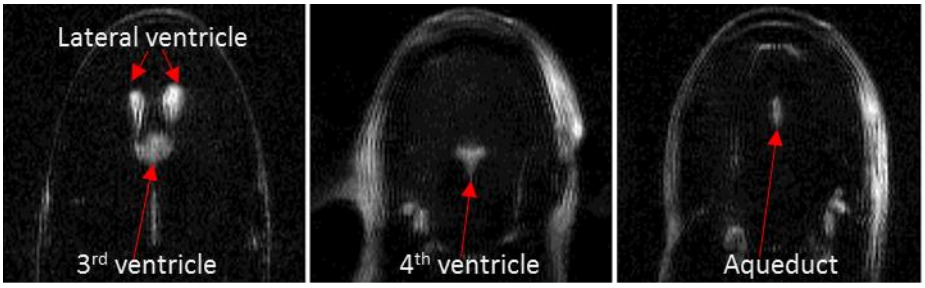

Figure 3.8: Coronal slices from the optimised MRC sequence centred on the aqueduct, lateral, 3rd and 4th ventricles. Signal from these CSF spaces readily standout whereas signal form the brain tissue is highly attenuated.

The optimised sequence has attenuated the signal from the brain tissue, whereas signal from CSF spaces readily standout (figure 3.8). These slices are centred on the aqueduct, lateral, 3rd and 4th ventricles.

3.3.3 FLuid Attenuating Inversion Recovery (FLAIR) sequence

Having identified the CSF spaces by the MRC sequence, next a combined MRC-FLAIR sequence was designed and optimised to monitor the primary route of GBCA infiltration into the brain (with the aim of reproducing the observations of ventricular GBCA infiltration reported by Jost *et al*. (Jost *et al*., 2017). The high temporal resolution (37.5s) of the MRC-FLAIR sequence, enabled monitoring of GBCA inflow into the CSF spaces, likely infiltrating the CNS from the primary source of CSF production, the choroid plexus. The long TE enabled non-CSF derived signals from

the surrounding tissue to be nulled in order to minimise PVEs. The FLAIR sequence was acquired for 20 minutes post contrast injection to allow enough time to completely capture GBCA inflow into the CSF spaces. The optimised FLAIR sequence was applied to 2 individual animals (figure 3.9B).

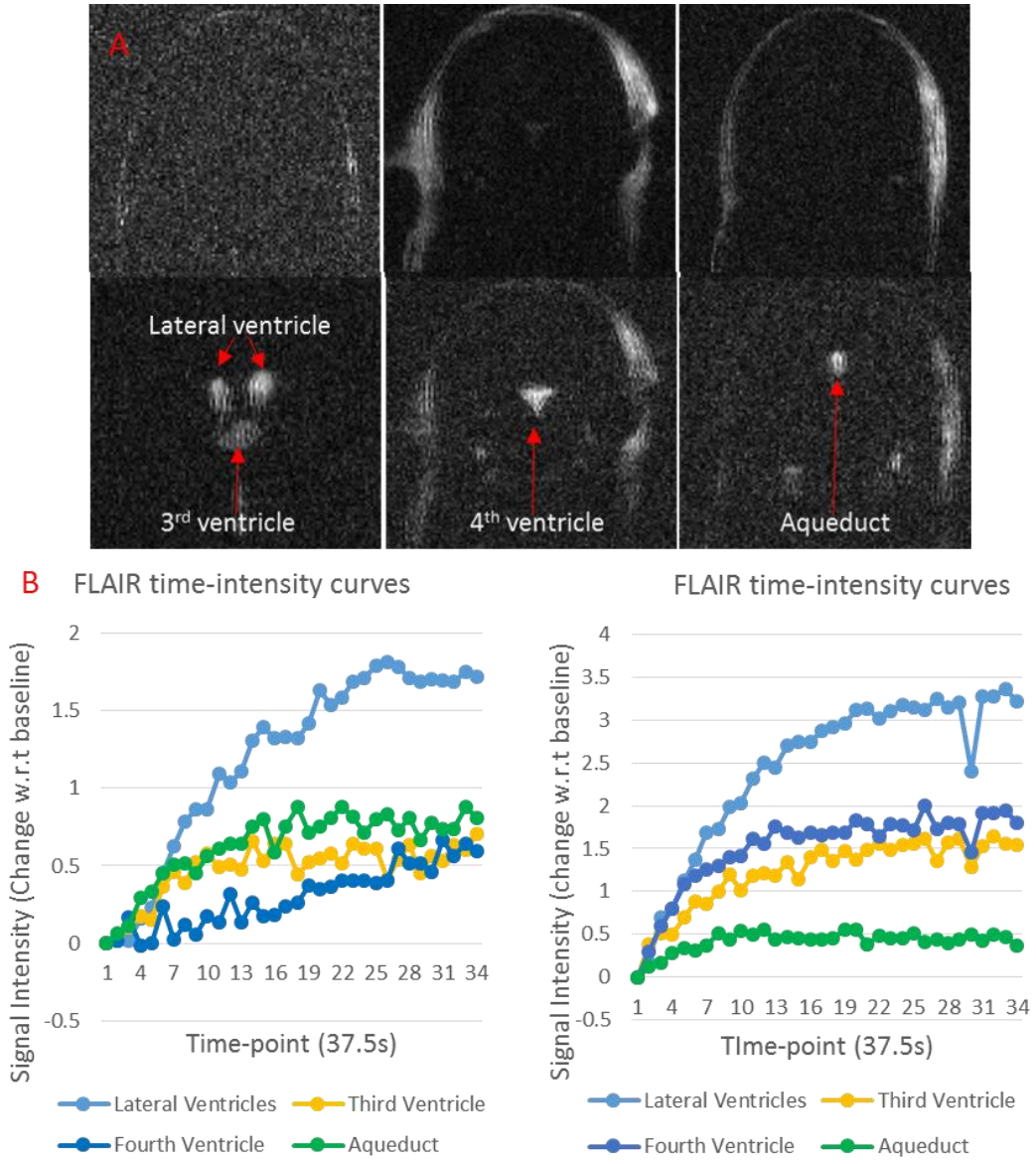

Figure 3.9: A- Example FLAIR images from a single animal. Pre-contrast (top row) and 187.5s post contrast injection (bottom row) FLAIR images (images centred on the aqueduct, lateral, 3rd and 4th ventricles. B- Normalised w.r.t baseline FLAIR time-intensity curves of subject 1 (left) and subject 2 (right) demonstrating inflow pattern in 4 major CSF spaces for 20 minutes post contrast injection.

The implemented FLAIR sequence was able to successfully null the signal from the CSF spaces (figure 3.9A – top row). The FLAIR sequence was therefore capable of capturing the rapid infiltration of the systemically injected GBCA into the ventricular

system with high temporal resolution (37.5s – figure 3.9B). This is a rather intriguing finding as the transfer of GBCA into the CSF spaces occurs rapidly after few minutes following the IV delivery of the agent. This is evident by the sharp increase in the signal intensities seen in all four major CSF spaces at 187.5s post contrast injection (figure 3.9A – bottom row).

3.3.4 3D T_1-weighted GE sequence for monitoring contrast inflow into the brain parenchyma

3.3.4.1 Unnormalised (raw) images and signal intensity time-courses

A 3D T_1-weighted GE sequence was implemented, primarily to monitor possible GBCA infiltration from the CSF spaces into the brain tissue (images were acquired for 3 hours post contrast injection). Figure 3.10 corresponds to unnormalised raw (A) and surface coil inhomogeneity corrected (B) baseline and 25 min post contrast images from a single subject. In order to evaluate contrast agent uptake by different regions of the brain (i.e. ROI analysis), time-courses from different brain regions were then extracted from the images (figure 3.11).

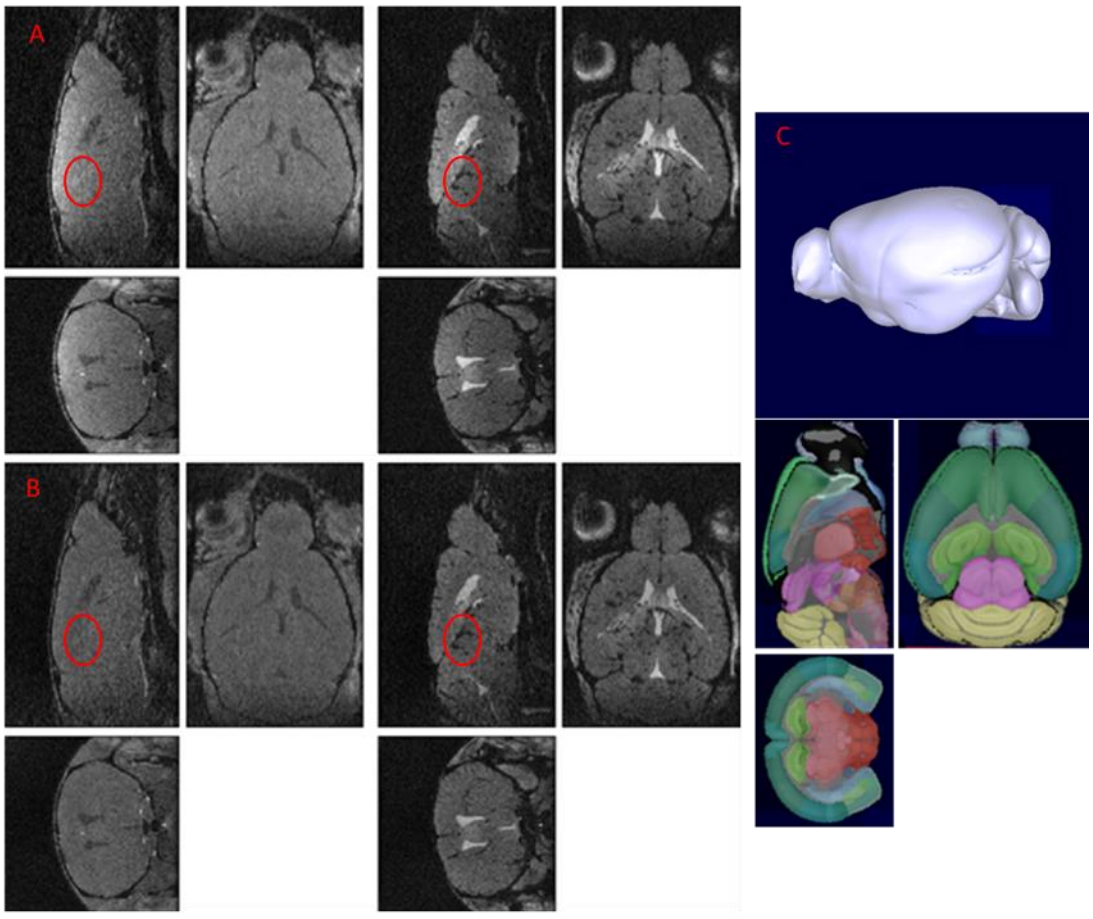

Figure 3.10: A- Pre-contrast (left) and 25 minutes post-contrast (right) images (sagittal, axial and coronal views) from a single mouse obtained using the described 3D T_1-weighted gradient echo sequence. Accumulation of GBCA in the CSF spaces is prominent on these images. Also, signal intensity decrease/drop-out (i.e. negative contrast relative to baseline) in the intravascular compartment (due to very high concentration of GBCA) is evident (an example intravascular ROI has been circled in red). B- The 3D T_1-weighted images are corrected for surface coil inhomogeneity. C- A 3D mouse brain schematic (sagittal view - top) and cross sectional sagittal, axial and coronal slices (from the Allen mouse brain atlas) to aid visualisation of MR images (i.e. orientation map). This orientation key is applicable to the subsequent MR images displayed in this format (i.e. sagittal, axial and coronal slices).

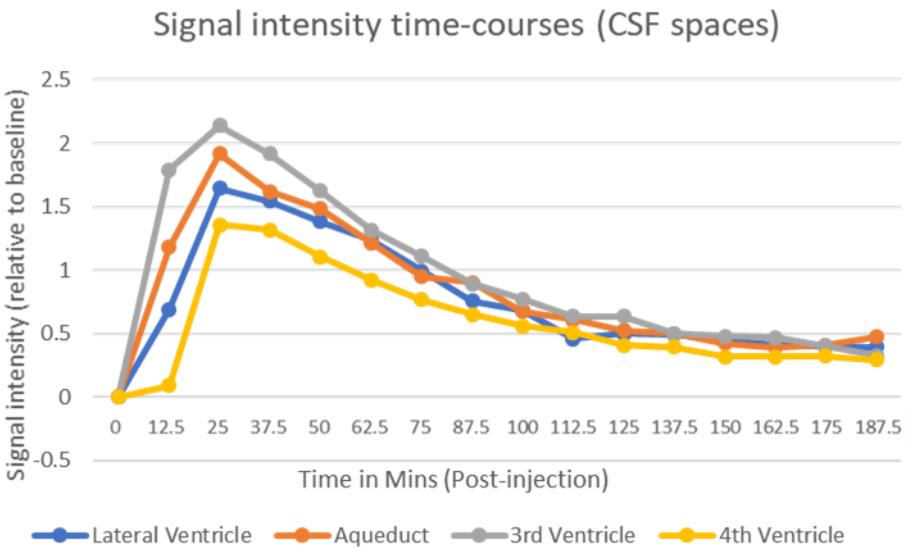

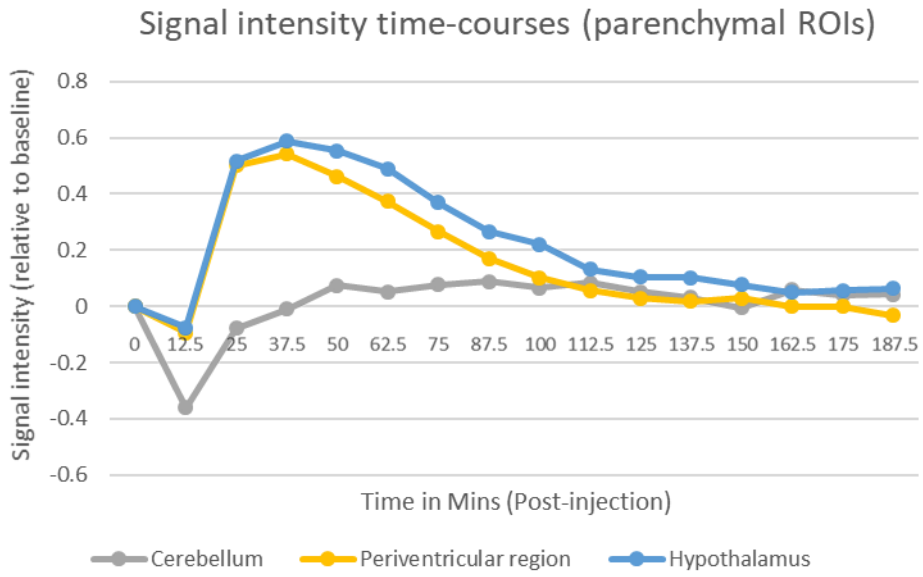

Figure 3.11: Time-intensity curves (relative to baseline) from a single mouse extracted from the CSF spaces (aqueduct, lateral, third and fourth ventricles, top) and also parenchymal brain regions (cerebellum, periventricular region and hypothalamus, bottom).

It can be seen in the raw T_1-weighted images (figure 3.10A) that regions closer to the surface coil (i.e. top) display relatively higher intensity compared to the lower brain regions. This is because the acquisition suffers from progressively decreased signal further from the receiver coil. This non-uniformity of profile reception, could lead to under/over-estimated results if one were to compare one region of the brain to another (section 3.3.4.3.1). Hence the non-uniformity in all the imaging datasets in this study were corrected as described earlier (section 3.2.7.3).

Evident by the marked signal increase in CSF spaces, the infiltration of the GBCA into the CSF spaces is detected by this sequence (although with lower temporal resolution compared to the FLAIR sequence) (figure 3.10A). Importantly, what is evident is the signal intensity decrease/drop-out (i.e. negative contrast relative to baseline) in the intravascular compartment (due to very high concentration of GBCA) (figure 3.10 – red circles). This effect is also observed within the parenchymal tissue (figure 3.11 - bottom), where the signal intensity has been reduced by the presence of highly concentrated GBCA in the microvasculature (e.g. the capillary network) that is present in all brain tissue voxels (e.g. at time-point 2 (12.5 mins post contrast injection)). The induction of signal reduction in brain tissue voxels due to the presence of high concentration GBCA in the blood was a desired feature of the method in order to make accurate inferences into the transport of GBCAs from the CSF into parenchymal brain regions (see below). Although CSF-mediated transport within the raw images is difficult to visualise by the naked eye, further image analysis/post-processing techniques yield images of putative GBCA infiltration from the CSF and into brain tissue (described below).

3.3.4.2 Differentiating GBCA-induced signal changes that originate from GBCA in the tissue (extravascular compartment) versus the signal changes that originate from GBCAs in the blood vessels (intravascular compartment) – a novel measure of contrast agent uptake in brain tissue

As described earlier, a meaningful measure of brain tissue contrast agent uptake from the CSF following IV delivery is challenging due to the difficulties in differentiating the GBCA-induced signal changes that originate from GBCA in the tissue versus the

signal changes that originate from GBCAs in the intravascular compartment. This could potentially be the reason why brain tissue contrast uptake (except in pathological break down of BBB) had been left unnoticed in routine clinical imaging until recent safety concerns of gadolinium retention in the brain (Kanda *et al*., 2014). In this study, by exploiting the usually undesired T_2* lowering susceptibility effects (section 2.6), the intravascular (blood vessel) and extravascular (brain tissue) compartments can be partially separated (i.e. differentiated). In order to discern the time-varying behaviour of the intravascular compartment signal in the acquired images (i.e. at 9.4T and 10 mmol/kg of GBCA), signal intensity time-courses from intravascular ROIs were extracted (figure 3.12). An ROI was manually drawn on a major vein (longitudinal hippocampal vein) and care was taken to ensure that the ROI is not affected by PVEs from the surrounding tissue (figure 3.5, section 3.2.7.2). In order to ensure that the curve obtained from the vein fairly represents the global intravascular signal (i.e. signal from all the blood vessels in the brain), a time-intensity curve was also obtained from an artery (anterior cerebral artery) (figure 3.4, section 3.2.7.2). There may be differences in the levels of blood oxygenation and haematocrit between arteries and veins and comparison of these two time-courses, will reflect these differences.

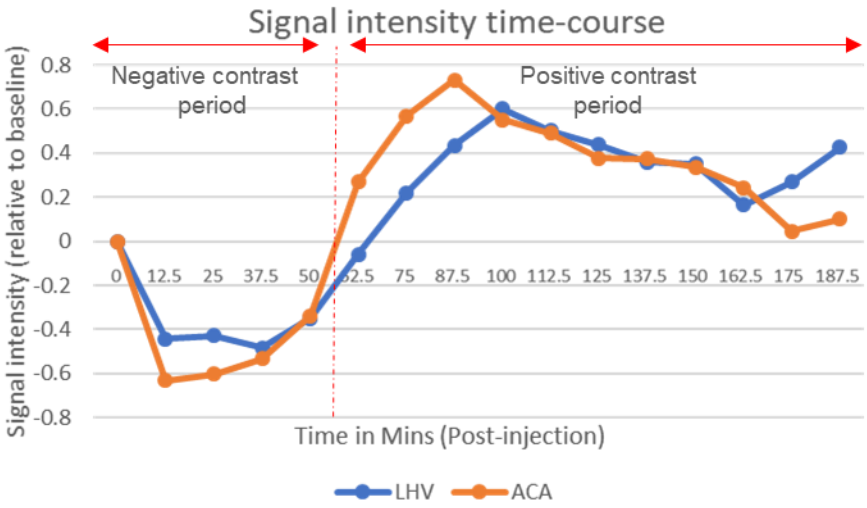

Figure 3.12: Example time-intensity curves (relative to baseline) from a single mouse derived from the longitudinal hippocampal vein (LHV) and the anterior cerebral artery (ACA). Both curves demonstrate a similar time-varying behaviour despite possible differences in blood oxygenation and haematocrit. In the first four/five time-points (~ 50 mins post injection), the intravascular signal intensity is markedly lower than the baseline (i.e. negative contrast relative to baseline). After about time-point five/six (~ 60 mins post injection), the concentration of GBCA in the blood vessels is lowered

(due to clearance from the circulation) and the intravascular signal intensity rises above the baseline value (i.e. positive contrast relative to baseline).

Despite possible differences in blood oxygenation and haematocrit, both LHV & ACA demonstrate a similar time-varying behaviour. In the first four/five time-points (~ 50 mins post injection), the intravascular signal intensity is markedly lower than the baseline (i.e. negative contrast relative to baseline), due to very high concentration of GBCA in the blood. If we assume that there is no inflow of GBCA into any parenchymal region, all parenchymal time-courses must display a similar pattern to that of LHV/ACA (due to PVEs from the intravascular compartment), i.e. they too must demonstrate a signal intensity lower than the baseline in the first four time-points. Therefore, it is safe to conclude that, if there are any brain regions with a higher signal intensity relative to baseline in the first four time-points, then this reflects a parenchymal inflow of GBCA into that region. The rationale being that, the 'signal increasing' (relative to pre-contrast baseline) contribution from this parenchymal inflow is greater than the 'signal decreasing' partial volume from the intravascular compartment on the overall measured signal intensity (the assumption being that the concentration of GBCA (i.e. uptake) in parenchymal tissue is significantly lower than the systemic GBCA concentration. Essentially these two factors are the only factors modulating the measured signal intensities and they are competing (in the first four time-points). After about time-point five/six (~ 60 mins post injection), the concentration of GBCA in the blood vessel is lowered (due to clearance from the circulation) and the intravascular signal intensity rises above the baseline value as the T_2/T_2* values recover (i.e. positive contrast relative to baseline – figure 3.12) and the two modulating factors are no longer competing. Hence it becomes more difficult to differentiate the contribution of each factor after this time (similar to the scenario seen in routine CE-MRI imaging with standard clinical dose as discussed previously).

By extension of the above discussion, it can be reasonably concluded that there is GBCA uptake in the periventricular and the hypothalamus regions of the brain (figure 3.11 - by looking at the first four time-points only as explained). No conclusions can be made regarding GBCA uptake in the cerebellum as there is no increase in signal intensity (relative to baseline) in these early first four time-points.

3.3.4.3 Alleviating sensitivity-lowering PVEs from intravascular compartment

3.3.4.3.1 Normalisation by a control region

Despite providing a meaningful measure of GBCA uptake (in the first four time-points), the technique described above suffers from a limitation, lowered sensitivity to GBCA uptake in the extravascular parenchymal tissue. The parenchymal time-courses are clearly affected by the negative (signal/sensitivity lowering) PVEs from the (global) intravascular compartment which reduces sensitivity to GBCA uptake (e.g. time-point 2 on figure 3.11 – bottom). Throughout the course of the project and the optimisation process, attempts were made to minimise these intravascular PVEs.

Data analysis was performed using an exploratory normalisation technique and all time-intensity curves were normalised by the time-intensity curve of a control/reference region (a technique similar to those adopted in other CE-MRI studies (Jost *et al*., 2016)). The cerebellum seemed to be commonly adopted as a reference region for the normalisation process in clinical CE-MRI studies (Radbruch *et al*., 2015, Robert *et al*., 2015). Additionally, cerebellum region seemed to have relatively much lower GBCA uptake compared to most brain regions upon visual inspection of the images, hence in theory it would be an ideal candidate as a control/reference region for implementation of a normalisation technique (a region with low tissue contrast uptake (i.e. with only GBCA present in the intravascular compartment) is able to correct for intravascular contributions). However, a limitation of this technique is that it's not able to completely correct for all intravascular signal contributions. In practice, there are considerable differences in cerebral blood volume (CBV) in different brain regions and normalisation by a control region may lead to over/under-estimated results depending on the corresponding CBV (supplementary material - table S3.1). Despite eliciting some insight regarding GBCA uptake (figure 3.13), and despite the common adoption of such regional normalisation techniques in clinical studies (Radbruch *et al*., 2015, Robert *et al*., 2015), I came to the conclusion that this exploratory technique is rather qualitative and that the full picture of the inflow pattern could not be concluded with sufficient rigour, primarily due to the differences in CBV in different brain regions (Table S3.1).

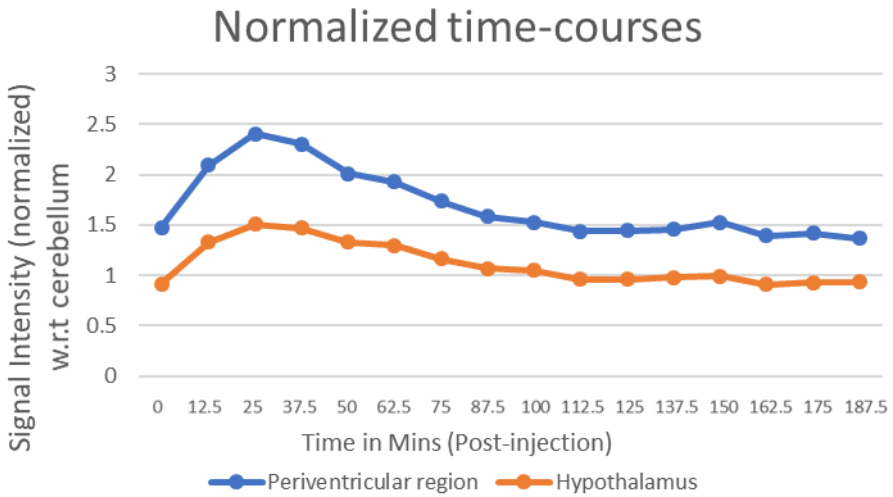

Figure 3.13: Parenchymal time-courses were normalised by a control/reference region (cerebellum) to correct for the intravascular PVEs. Normalisation of hypothalamus and periventricular region time-courses by that of cerebellum, resulted in over-estimated results due to differences in CBV (evident by the positive offset from zero at time-point 1 (i.e. baseline scan) for example).

3.3.4.3.2 Thresholded subtraction images

In a second attempt to minimise the signal/sensitivity lowering intravascular PVEs, a more conservative technique was devised. Time-courses extracted from different ROIs/brain regions, represent the mean signal value from all the voxels in that ROI (hence PVEs from signal lowering intravascular compartment/voxels, could falsely imply no GBCA uptake in that ROI). Therefore, in order to identify the voxels with higher signal intensity with respect to the baseline (i.e. voxels corresponding to extra-vascular areas with definite GBCA uptake) a subtraction method was devised. All post-contrast scans were subtracted from the baseline scan, so that all voxels with definite GBCA uptake would have a positive value (above zero). No conclusion regarding GBCA uptake could be made regarding the voxels with negative value (below zero), except that they could potentially be confounded by PVEs from the intravascular compartment (e.g. capillary bed). In order to minimise the effect of these negative PVEs, all voxels with negative value (below zero), were assigned a value of zero (i.e. the subtraction images were thresholded to a value of zero). This would in turn increase the sensitivity of the extracted time-courses (i.e. a post processing technique for an artificially improved image sensitivity). Essentially ROI time-courses are average of all voxels in that ROI as mentioned, hence averaging the positive voxels with less negative (i.e. zero in this case) voxels, would help unmask a greater GBCA uptake within any specific region. In other words, the voxels with a negative

value were devalued by assigning them a value of zero (i.e. diminishing their negative weighting to essentially a neutral weighting), hence minimising their negative contribution to the average signal within that ROI (extracted time-courses) and therefore increasing sensitivity to GBCA uptake. In this way, the images presented in figure 3.14 will not report false-positives with regard to the presence of GBCAs in the intravascular tissue but are likely to have false negatives. The subtracted, thresholded images provide qualitative maps of the spatial-temporal patterns of parenchymal GBCA extravascular tissue infiltration.

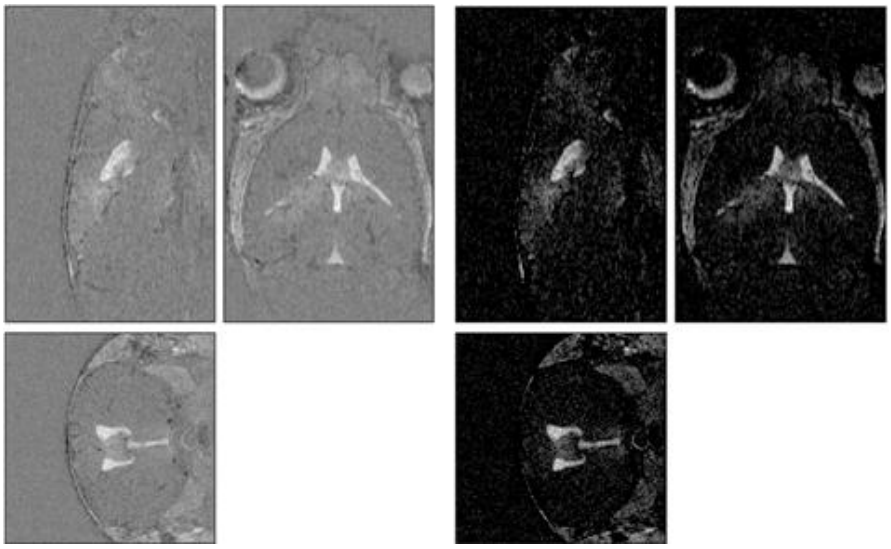

Figure 3.14: Subtraction (left) and thresholded (>0) subtraction image (right) of the fourth time-point scan (37 mins post injection) from the baseline.

Figure 3.14 demonstrates an example subtraction image and the corresponding thresholded subtraction image 37 mins post injection (4th time-point), where GBCA uptake in parenchymal brain regions is more readily visualised. Although the thresholded subtraction technique does not completely correct the signal/sensitivity lowering intravascular PVEs, it minimises their contribution to the extracted time-courses (essentially intravascular voxels have been set to zero weighting rather than a larger negative weighing).

3.4 Discussion

In this chapter, which moves towards my aim of tracking systemic GBCA entry into the CNS, I sought to optimise the GBCA dose to achieve maximum amount of contrast in the MR images. The contrast agent dose however is limited by their toxicity (constrained by home office regulations and its LD50 value). In this section, different commercially available contrast agent solutions (as well as routes of delivery and dosage) were considered in order to discover the protocol that provides the maximum

amount of GBCAs delivered to CSF spaces to allow us to be sensitive to its subsequent, hypothesised, delivery into the brain tissue. The optimised protocol consisted of a 10 mmol/kg bolus of contrast agent Omniscan (delivered intravenously in 5 minutes) and provided stable physiological parameters during the entire course of the bench experiments (4 hours). The nominated dose, is 8 times higher than the standard clinical dose (0.1 mmol/kg) and 2 times higher than the dose adopted in the study by Jost *et al*. (2.5 mmol/kg, Jost *et al*., 2016), based upon body surface area normalisation between mice, rats and humans (Nair and Jacob, 2016). Of note, depending on the nature of the examination, the clinical GBCA dose can be as high as 0.4 mmol/kg (e.g. MRA examination), which is equivalent to half of the dose that was administrated here (after body surface area normalisation).

Having identified a suitable contrast agent regime, in order to capture the complete route of GBCA transfer from the circulation into the CNS, I sought to replicate the findings of Jost *et al*. (Jost *et al*., 2017). Jost *et al*. provided compelling evidence regarding the transfer of GBCA from the circulation into the CNS (using a FLAIR sequence with a temporal resolution of 16 mins). The choroid plexus is believed to be the primary site of GBCA infiltration into the CSF spaces. In fact, the choroid plexus is the primary source of CSF secretion in the brain and is known to be more permeable than the blood-brain barrier to many molecules, primarily due to the fenestrated nature of the choroid plexus capillaries which lack tight junctions (Laterra *et al*., 1999). In this section I implemented and optimised a combined MRC-FLAIR sequence centred on all major CSF spaces for the high temporal resolution imaging of systemic GBCA transfer into the ventricular system. The findings of Jost *et al*. were replicated but with markedly higher temporal resolution (37s), further suggesting that the primary route of GBCA infiltration into the brain is likely to be via the choroid plexus and into the ventricular system.

For the achievement of the main goal of this chapter, that is non-invasive imaging of GBCA transfer into brain tissue from the CSF (i.e. as a non-invasive measure of CSF-ISF exchange), a T_1-weighted CE-MRI was devised.

Difficulty in differentiating GBCA-induced signal changes that originate from GBCA in the brain tissue (extravascular compartment) versus the signal changes that originate from GBCAs in the blood vessels (intravascular compartment) for a meaningful measure of brain tissue GBCA uptake (evidence of CSF-ISF exchange) is a major challenge in CE-MRI examinations. As both intravascular and extravascular compartments usually generate positive contrast following contrast agent delivery at

clinical doses and at clinical field strength (1.5-3T), it is most challenging to differentiate the contributions from each compartment, mainly attributed to the limited spatial resolution of MRI (i.e. PVEs). In this study, a unique characteristic of CE-MRI was exploited to overcome the aforementioned challenges and to provide the first non-invasive, dynamic, imaging of CSF driven GBCA inflow into the brain parenchyma. Differentiation of intravascular and extravascular signal compartments in the MR image was achieved by implementing a relatively high dose of GBCA (IV) at 9.4T. Briefly, in a GE T_1-weighted image, at relatively high concentrations of GBCA, T_2* shortening effects dominate the T_1 shortening effects (i.e. susceptibility effects dominate - section 2.6) resulting in a signal loss from the regions with very high GBCA concentration (i.e. intravascular compartment), and regions with relatively lower tracer concentration (i.e. brain tissue compartment) will generate positive contrast. This technique enabled the differentiation of intravascular and extravascular compartments in the first 4 time-points (i.e. up to 37 mins post contrast injection) and provided a meaningful visualisation, albeit qualitative, of contrast uptake in parenchymal brain regions (i.e. a non-invasive approach for the assessment of brain clearance function – chapter 4). This is a unique advantageous exploitation of the susceptibility effect that was deemed undesirable in previous routine clinical CE-MRI examinations (see section 3.3.4.2 for a detailed explanation).

3.5 Conclusion

In this chapter, the ideal contrast agent regime (solution, dose, route of delivery) for the purpose of imaging CSF-ISF exchange was identified. I was able to identify the highest GBCA dose (10 mmol/kg) that can be administered in mice without generating any adverse reactions in the measured physiology of the animals. This was in order to achieve the maximum amount of GBCAs delivered to CSF spaces to allow us to be sensitive to its subsequent, hypothesised, delivery into the brain tissue. Additionally, a combined MRC-FLAIR sequence was implemented and optimised for the high temporal resolution imaging of IV GBCA infiltration into the CSF spaces. The implemented sequence successfully identified CSF spaces (ventricular system) and captured the rapid transfer of IV GBCA into the ventricular system with high temporal resolution. Subsequently, a 3D T_1-weighted MRI sequence was implemented for the non-invasive real-time imaging of CSF-ISF exchange. This sequence allowed accurate inferences to be made about the major routes of GBCA penetration into the brain tissue from the CSF by exploiting the initial reduction in MRI signal from high concentrations of GBCA tracer in the blood vessels. Finally, high level data processing techniques for the analysis of the acquired images were introduced and

implemented. These steps were vital for visualisation of CSF-ISF exchange and identification of the new CSF-ISF exchange pathway that will be described in the next chapter.

3.6 Limitations

Choice of contrast agent was a limitation when identifying the contrast agent that would provide the maximum amount of contrast in the MR images. Among the agents listed in figure 3.6, Magnevist, Omniscan and ProHance could be sourced by my host laboratory (with Omniscan being chosen as the optimal contrast agent). As a result, 3 commercially available contrast agents (MultiHance, Gadovist and Eovist) that offer higher T_1 and T_2 relaxivities compared to Omnicsan had to be excluded from consideration. A contrast agent with higher T_1 and T_2 relaxivity is theoretically capable of providing higher image contrast for a given dose (i.e. it allows a reduction in dose for the generation of the same amount of contrast). Hence, it could be beneficial to re-consider the choice of contrast agent when planning future studies.

The FLAIR sequence implemented in this chapter suffers from a relatively low spatial resolution (0.1 x 0.15 x 1mm). As a result, the CSF spaces on the FLAIR images (and the corresponding signal intensity time-courses) may have been potentially affected by PVEs from the surrounding periventricular tissues. However, the contribution of these unwanted PVEs is believed to be insignificant due to the very high degree of T_2-weighting that was adopted in the FLAIR sequence which significantly nulled the tissue signal.

Perhaps the main limitation of the introduced platform is the relatively high GBCA dose that was administered (8 times higher than the standard human clinical dose based upon body surface area normalisation between mice and humans). This limitation will be discussed in more detail in chapter 5 where attempts will be made to lower the high GBCA dose of the platform.

Due to the induction of negative contrast (relative to baseline) in the intravascular compartment (as a result of high GBCA concentration), the platform suffers from globally lowered sensitivity (due to PVEs) which also complicates a quantitative readout from the method. Techniques were introduced to alleviate the signal/sensitivity lowering PVEs from the global intravascular compartment (normalisation and thresholded subtraction techniques), with the latter technique being more successful in achieving this goal.

In addition to the global lowered sensitivity, the platform suffers from the susceptibility

effect extending to regions outside the blood vessels (i.e. creates an apparent blood vessel thickening effect around the edges of the blood vessels which 'masks' the signal from the immediate surrounding tissue (figure 3.15)). This is due to the influence of paramagnetic gadolinium ions in the blood vessels on surrounding/proximal spins, even outside the blood vessels (near the edges). Hence, there may be regions in the brain with GBCA inflow, but their detection could also be masked by this extension of susceptibility effect (e.g. the subarachnoid and paravascular spaces which are in close proximity to large vessels).

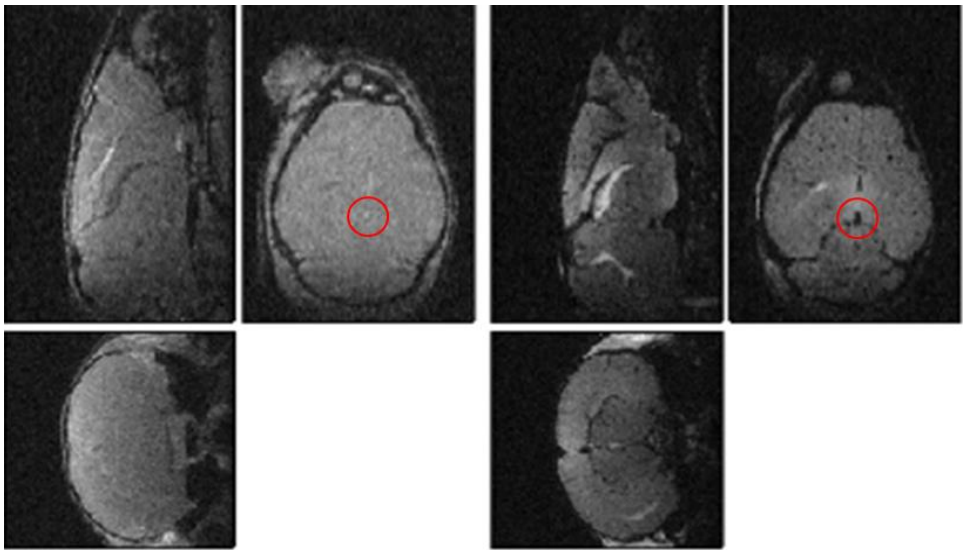

Figure 3.15: Blood vessel thickening effect which is a limiting extension of the susceptibility effect. Susceptibility effect extending to the outside edges of the blood vessels (red circles) causes a signal drop out from the immediate surrounding tissue, lowering the overall image sensitivity (left- baseline image, right- 25 min post contrast injection image).

The sensitivity constraint discussed above is a limitation of this platform, and it was imposed by the deliberately induced negative contrast (relative to baseline) in the intravascular compartment (in order to differentiate between intravascular and extravascular compartment signals - section 3.3.4.2). Future work will focus on attempts to completely correct for these undesired side-effects or even eliminate the need for the induction of negative contrast in the intravascular compartment. Potential directions include susceptibility mapping MRI, equilibrium-contrast MRI (Flett *et al*., 2010) or even diffusion sensitive sequences (diffusion crushers) to eliminate blood vessel signal. The latter will be explored in more detail in Chapter 5.

Finally, the created thresholded subtraction images may be susceptible to false positives due to noise. In this approach, in addition to de-valuing the voxels that

demonstrate lower signal intensity in the post contrast images relative to baseline (due to intravascular susceptibility effects - section 3.3.4.3.2), the voxels that are negatively affected by noise (i.e. voxels demonstrating lower signal intensity in the post contrast images relative to baseline) are also artificially de-valued by setting them to zero (assuming the specific voxel in question is not greatly influenced by either intravascular or extravascular GBCA). On the other hand, the voxels that are positively affected by noise (i.e. voxels demonstrating increased signal intensity in the post contrast images relative to baseline) are not artificially altered in any way (i.e. the approach is biased towards positive voxels). In practice however, the influence of intravascular/extravascular GBCA is global and is believed to dominate noise effects/contributions, hence the determining factor in regards to the signal intensity obtained from any voxel in an image. The false positive rate due to noise in the thresholded subtraction images is therefore believed to be insignificant (in chapter 5 experiments will be conducted to validate this assumption).

3.7 Supplementary material

Region	**Total CBV (%)**
Amygdala	4.3 ± 0.4
Arbor vitae	4.0 ± 0.4
Cerebral cortex	7.9 ± 0.7
Cerebellar cortex	6.6 ± 0.5
Corpus callosum	3.1 ± 0.5
Hippocampus	3.7 ± 0.4
Hypothalamus	4.3 ± 0.5
Medulla	7.9 ± 0.5
Midbrain	5.6 ± 0.6
Olfactory bulbs	6.9 ± 0.4
Pons	4.4 ± 0.5
Striatum	2.8 ± 0.3
Thalamus	3.7 ± 0.5
Total brain	5.8 ± 0.4

Table S3.1: CBV values for thirteen different brain regions (reported as mean ± SEM). (Adopted from Chugh et al., 2009)

3.8 Acknowledgements

I would like to thank my colleagues John Connell and May Thin for their assistance and extensive training sessions to perform tail IV cannulation in mice.

Chapter 4: VECTOR - VEntricular Cerebral TranspORt

Towards my goal of non-invasive imaging of CSF-ISF exchange (glymphatic system), in the previous chapter, I developed the first non-invasive CE-MRI platform that was capable of tracking systemic CSF-mediated GBCA inflow into the CNS in real-time. Originally with the hope of non-invasive imaging of the glymphatic pathway, employment of my non-invasive platform on a cohort of wild-type mice revealed a new CSF-ISF exchange pathway, a pathway that appeared to be different to that described in the glymphatic hypothesis. I coined this novel CSF-ISF exchange pathway, the 'VEntricular Cerebral TranspORt (VECTOR)' pathway. In this chapter I will describe this new non-invasively derived pathway in detail and discussions will focus on its characteristics and dynamics.

4.1 Introduction

Brain clearance is essential for the integrity of brain homeostasis as impaired clearance and subsequent accumulation of waste proteins, such as amyloid beta and tau, in the CNS are the hallmarks of Alzheimer's diseases. The compartmental exchange of CSF with ISF is believed to facilitate brain clearance. For example, tracer studies injecting contrast media into the CSF spaces (or directly into the brain parenchyma) have revealed exciting results regarding the role of CSF-ISF exchange in the clearance of metabolites and waste products from the brain (e.g. two photon microscopy of glymphatic system (Iliff *et al*., 2012)). A common limitation of these measurement techniques is their invasive nature which may also confound the assessment of CSF-ISF exchange dynamics (e.g. cranial window, injection of bulk fluid into brains microenvironment). The absence of a non-invasive, clinically relevant CSF-ISF exchange measurement technique has hampered the widespread and routine clinical assessment of brain fluid dynamics in the healthy and the diseased state. Since the incidence of neurodegenerative conditions is climbing to epidemic proportions (likely due to the global ageing population growth), it is vital to provide an unperturbed and physiologically intact assessment of brain clearance function (i.e. CSF-ISF exchange pathway). In the previous chapter I implemented and optimised a non-invasive and physiologically relevant CE-MRI platform for the assessment of CSF-ISF exchange (using a single IV injection of gadolinium contrast agent (GBCA) and clinically relevant MRI measures). The introduced CE-MRI platform is an ideal candidate for the imaging of CSF-ISF exchange due to its non-invasiveness and deep tissue imaging capability (3D imaging). Essentially, the CE-MRI platform provides evidence for brain clearance by imaging GBCA transfer into brain tissue – i.e.

entry/movement of GBCA within the brain tissue is representative of CSF flow into the brain and exchange with ISF. In this section, I will employ this non-invasive CE-MRI platform for the characterisation of CSF-ISF exchange in a cohort of healthy mice.

4.2 Methods

4.2.1 Experimental methods

All experiments in this section were performed on male C57Bl6 mice (Charles River UK Ltd) at 3 months of age (n=6, average weight of 25.6 ± 3.3 g). Briefly, anaesthesia was induced and maintained with 2.5% & 1.5% isoflurane respectively [in a mixture of 0.4L/min medical air and 0.1L/min O2]. Physiological parameters were monitored at all times. Head motion was minimised by using MR compatible head holder. Following anaesthesia, whilst the animal was lying on the cradle (animal bed), tail IV cannulation was performed outside the scanner, using a heparinised saline infusion line. After making sure that the IV cannulation had been successfully performed, saline infusion line was replaced with the contrast agent infusion line (as the animal had to be transferred into the scanner and baseline scanned before contrast agent infusion). Following baseline scanning, a 5 min infusion, delivering 10 mmol/kg of Omniscan solution (Gd-DTPA-BMA) was started. Inflow of contrast agent was monitored for approximately 3 hours (16 time-points) post-injection using a 3D T_1-weighted GE sequence (temporal resolution: 12.5 min) (all MRI methods were performed as previously described (Chapter 3)).

4.2.2 Data analysis

For data analysis, an automated ROI analysis approach was taken (see below-section 4.2.2.1), where scans from all subjects were registered into the same space and time-courses were extracted (using the 'Extract ROI' routine of the Marsbar toolbox) from automatically defined ROIs (a detailed description of the methods is given below – section 4.2.2.1). Time-courses were then normalised to relative signal change by subtracting the baseline (pre-contrast) value from all signal intensity values and then dividing by the baseline. For statistical evaluation, a separate paired t-test was performed for each brain region to evaluate GBCA uptake 37 minutes post contrast injection. In order to correct for multiple comparisons, Bonferroni correction was conducted.

Moreover, the 'ImCalc' routine of the SPM12 software was used for creating group averaged images. Group-average thresholded subtraction images were subsequently created. Group average time-courses were then automatically extracted from 8

desired ROIs. Finally, 3D reconstructions (volume rendering) of the thresholded subtraction images (overlaid on the baseline image) were created using the 'digital reconstructed radiograph (DRR)' routine of the Amira 5.4 software (Thermo Fisher Scientific). Reconstructions were then pseudo coloured (using the 'volrenGreen' colormap) for ease of contrast visualisation.

4.2.2.1 Automated ROI analysis

In studies involving a large number of animals/subjects, manual ROI definition for the extraction of time-courses can be rather time-consuming for the operator but more importantly, it could potentially introduce bias and between-subject variability (e.g. for the comparison of contrast agent uptake between subjects). Automatic definition of ROIs helps to reduce the bias introduced as a result of manual drawing of ROIs. In addition, once an ROI is defined on the reference image, it can be extended to the same region in all other subjects (provided all subject scans are registered into the same space – section 4.2.2.1.3), reducing the manual ROI definition burden on the operator. In addition to the aforementioned advantages of an automated image analysis pipeline, registration of multiple subjects into the same space, provides the opportunity for more advanced group analyses, such as group experiments studying the effect of a particular drug on a specific physiological parameter, as it will be described in chapter 6.

4.2.2.1.1 Allen Mouse Brain Atlas – parenchymal ROI definition

The Allen mouse brain histology atlas (Lein *et al*., 2007), is the histology atlas of a C57Bl6J strain (wild type) mouse. In this study, the Allen atlas (25 μm resolution) was utilised for the automatic definition of ROIs. This atlas is advantageous as it provides high labelling resolution. Each region of the Allen brain atlas has a specific id/intensity, and each region is organised in a hierarchy with a root/parent and its corresponding sub regions/children. Each one of these sub regions may have their own sub regions and so on. For example, the hippocampal formation (id:4249) is subdivided into many other sub-regions such as the dentate gyrus (id:12891). Dentate gyrus itself is also subdivided into smaller regions. Figure 4.1 below is a code snippet corresponding to the Allen mouse brain atlas ontology (left column), demonstrating the hierarchical nature of this annotation volume. The coronal slices correspond to the hippocampal formation (right column - top) and its sub-division dentate gyrus (right column - bottom).

```
{
 "id": 4249,
 "atlas_id": 4243,
 "ontology_id": 7,
 "acronym": "HiF",
 "name": "hippocampal formation",
 "color_hex_triplet": "FFC466",
 "graph_order": 124,
 "st_level": null,
 "hemisphere_id": 3,
 "parent_structure_id": 4219,
 "children": [
  {
   "id": 12891,
   "atlas_id": null,
   "ontology_id": 7,
   "acronym": "DG",
   "name": "dentate gyrus",
   "color_hex_triplet": "FFB566",
   "graph_order": 125,
   "st_level": null,
   "hemisphere_id": 3,
   "parent_structure_id": 4249,
   "children": [
    {
     "id": 4258,
     "atlas_id": 4252,
     "ontology_id": 7,
     "acronym": "DG",
     "name": "dentate gyrus, left",
     "color_hex_triplet": "FFB566",
     "graph_order": 126,
     "st_level": null,
     "hemisphere_id": 1,
     "parent_structure_id": 12891,
     "children": []
    },
    {
     "id": 4267,
     "atlas_id": 4261,
     "ontology_id": 7,
     "acronym": "DG",
     "name": "dentate gyrus, right",
     "color_hex_triplet": "FFB566",
     "graph_order": 127,
     "st_level": null,
     "hemisphere_id": 2,
```


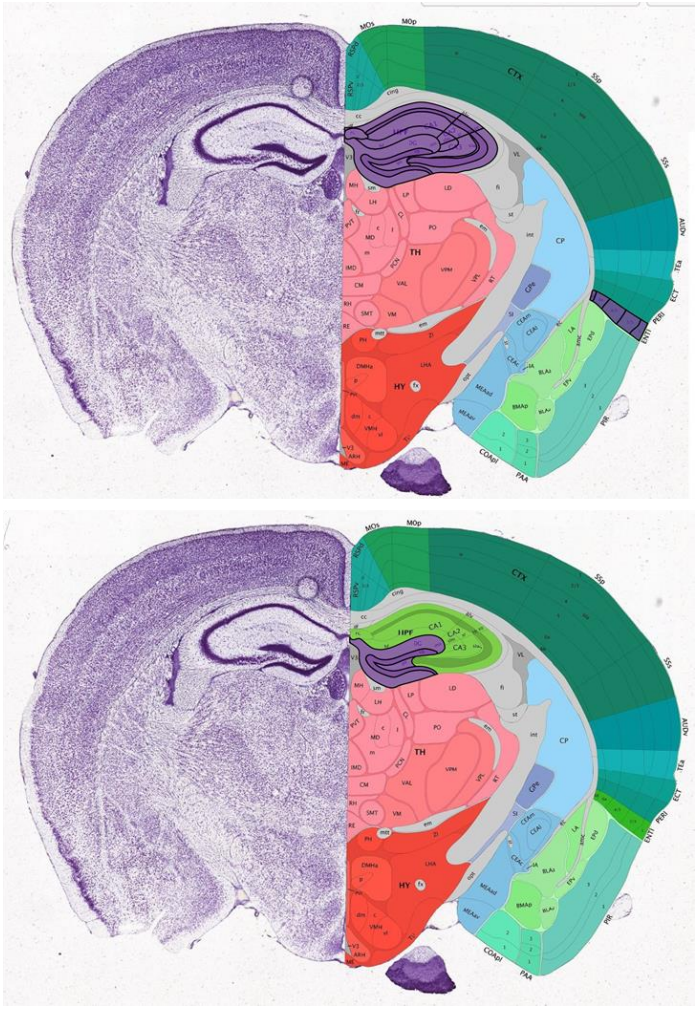

Figure 4.1: Allen mouse brain atlas. Left column: An example code snippet of the annotation volume demonstrating hippocampal formation and dentate gyrus id numbers. Right column – top: Coronal histology slice of the atlas corresponding to the hippocampal formation volume (highlighted in purple colour). Right column – bottom: Dentate gyrus (highlighted in purple) is a child of the hippocampal formation. It can be seen that all other brain regions each have a specific colour/code.

The Allen histology atlas and the corresponding annotation volume were also converted into niftii file format to be compatible with image analysis software. As before, voxel sizes were also increased by a factor of 10 for the use of SPM12 software. After an initial reconstruction of this atlas however, it was realised significant preparatory work were required, mainly concerned with visualisation and registration (figures 4.2 and 4.5).

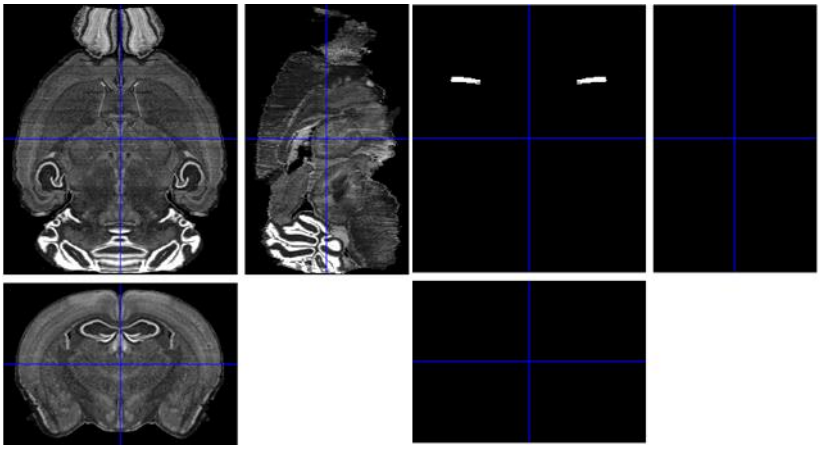

Figure 4.2: Representative images of the initial reconstruction of the Allen mouse brain atlas template (left) and its corresponding annotation volume (right). It seems that only two regions of the brain had been labelled in this volume. This is due to the windowing effect as a result of the rather counter-intuitive distribution of labels given to each ROI (some ROIs have intensity values in the range of 100 million whereas most others are in the range of 1000s).

Figure 4.2 (right) is dissimilar to the annotation volume observed in figure 4.1. The underlying reason for this discrepancy, is the rather counter-intuitive distribution of labels given to each ROI. The bright regions in Figure 4.2 (right) have intensity values in the range of 100 million whereas most of the other regions are in the range of 1000s. As a result, low intensity regions appear dark due to a windowing effect. This distribution of intensity values seems unusual given only ~1000-2000 brain regions have been labelled in this atlas. The visualisation of atlas labels allows verification of registration quality which is in turn necessary for an unbiased and clean ROI signal extraction. Hence, in order to create and visualise the required ROIs, in-house MATLAB codes were written, that automatically searched for the corresponding labels and their sub regions. The code automatically assigns a value of 1 to all the corresponding label ids and assigns zeros to any other brain region. This process will result in a binary/ROI image of the desired ROI, with no unusual labelling intensities and windowing effects. For example, the Midbrain ROI (label id: 313), is composed of sub regions Midbrain- sensory related, Midbrain- motor related and Midbrain-behavioural state related (label ids: 339, 323 and 348 respectively). Example ROIs (Midbrain, cerebellum and thalamus) are shown on figure 4.3. All ROIs were defined using the ‘ROI definition’ routine of Marsbar toolbox.

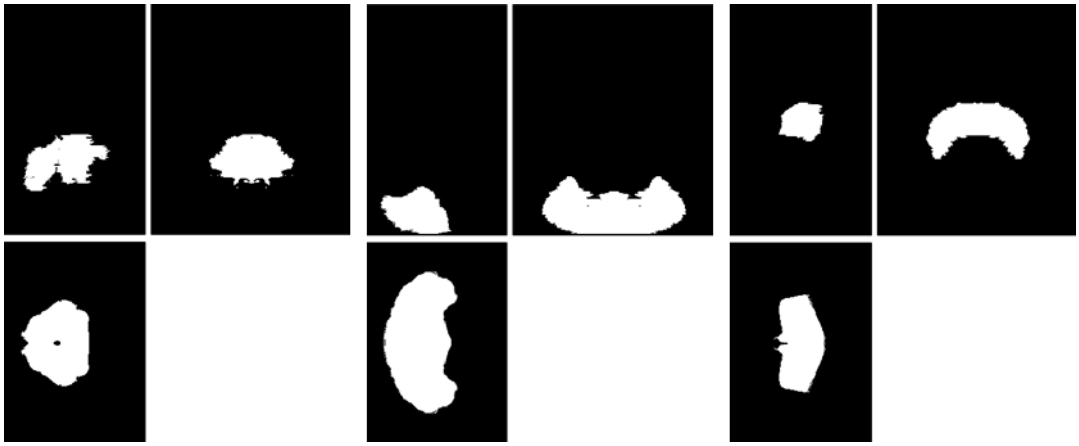

Figure 4.3: Binary images of the midbrain (left), cerebellum (middle) and thalamus (right) automatically defined from the Allen mouse brain atlas. All the relevant ids for each brain region were assigned a value of 1 and any other brain region was assigned a value of 0. All example images are displayed as sagittal, axial and coronal slices as described earlier (display format similar to figure 3.10).

4.2.2.1.2 CSF ROI definition

The above methodology can only be utilised for the definition of parenchymal brain regions as the Allen atlas does not include labelling of the CSF spaces (aqueduct and all ventricles are assigned a value of zero). Hence for CSF ROI definition, typically spheres of radius 2-5 mm were manually centred on the desired ROI on the reference image (using Marsbar's built-in *'ROI definition'* routine), and the same ROI was extended for all other subjects (all registered into the same space – see below) to reduce the bias (between subject variability) in the group analyses.

4.2.2.1.3 Image registration

All image registration in this project was performed using NiftyReg. Registration is necessary for group studies in which manual definition of ROIs could potentially bias the results. Here, I registered the MR images of all subjects as well as the Allen mouse brain atlas (and its labels) to the MR image of the first subject, i.e. all scans were registered to the same space. Image registration is the process of deforming image data sets and transforming them into one coordinate system. The image to be transformed is called the 'floating image' and the reference image is called the 'target image'. One of the simplest forms of image registration is called a rigid registration. This type of registration has only 6 degrees of freedom (translation along the x, y, and z dimensions and rotation around the x, y, z axes). Therefore it preserves the original shape and size of the image (hence mainly utilised for motion correction purposes). However different subjects have different brain shapes and a rigid transformation

cannot account for these differences. An affine registration allows for up to 12 degrees of freedom therefore it could alter the shape and size of the object by introducing sheer and scaling whilst preserving the broader integrity of the object. In order to ease the registration of the MR images, all scans were initially registered to the desired space using only a rigid transformation and the result of that transformation was registered again using affine transformation. An important principle in any registration process is to use more bridges between the target and the source image in order to ease the registration process. This process worked well for all the 3D T_1-weighted scans. An example is demonstrated below (figure 4.4).

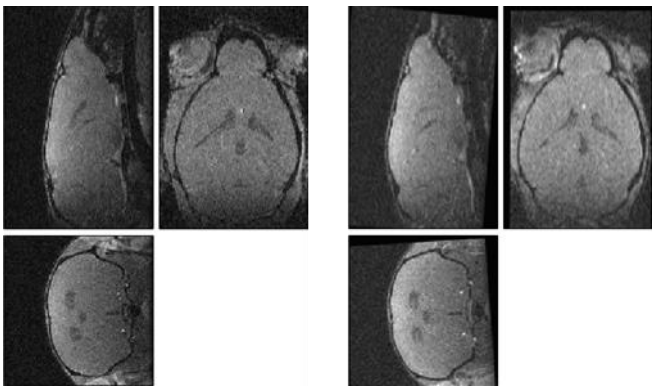

Figure 4.4: Successful registration (rigid + affine) of the baseline 3D T_1-weighted scan of subject 5 (right) to that of the first subject (left).

For both rigid and affine transformations, the 'reg_aladin' routine of the NiftyReg software was utilised. Briefly, 'reg_aladin' uses the Aladin block-matching algorithm which can be regarded as an optimisation algorithm (minimising the cost-function – least trimmed squares) learning the optimal deformation to be applied to the floating image.

Another useful feature of the 'reg_aladin' routine is that it will also generate the final transformation matrix of the registration. Hence once the baseline/pre-contrast image of each subject has been transformed into the reference space, the corresponding transformation matrix can be propagated to the subsequent images of the same subject (i.e. for the transformation of post-contrast acquisitions to the reference space). This can be done by the 'reg_transform' routine of the NiftyReg software and it is advantageous as it reduces the number of transformation executions. However, this routine is utilised under the assumption that all scans (i.e. pre-contrast scan and all subsequent post contrast scans) are in the same space and there is no head motion between the acquisitions. Under experimental conditions (isoflurane anaesthesia) and secure head positioning (e.g. using ear and bite bars) this seems

to be a fair assumption. Despite this rather safe assumption, throughout the course and the optimisation process of the registration platform, all post-contrast scans of each subject were initially rigidly transformed to their corresponding pre-contrast scan (to correct for possible motion artefacts) and then transformed into the reference space (using the propagated transformation matrix as described before).

Registration of the high resolution histology Allen mouse brain atlas however, was not as straightforward, illustrated in figure 4.5 below.

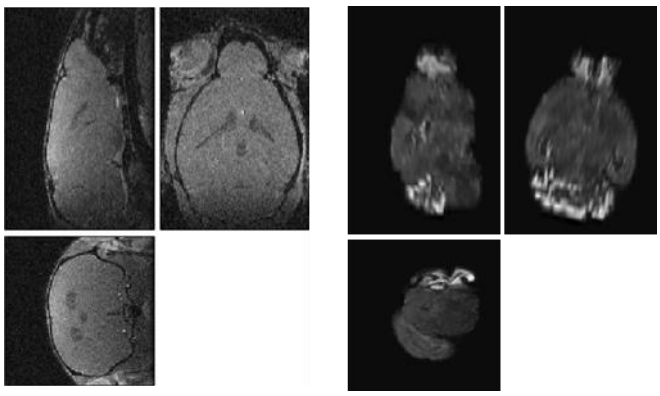

Figure 4.5: Failed registration of Allen mouse brain atlas (right) to the baseline T_1-weighted scan of the first subject (left).

There are several potential factors which make the registration of the Allen mouse brain atlas to the MR images, that I acquired, quite challenging. Firstly, the mouse brain atlas has a very high resolution (0.025 x 0.025 x 0.025 mm), whereas the 3D T_1-weighted MRI scans have comparably much lower resolution (0.1 x 0.1 x 0.15 mm). Also, the strong signal obtained from the fat layer underlying the skull in the MR image, creates confusion for the registration algorithm. In most cases, the boundaries are incorrectly aligned with respect to this fat layer (and not the true outer brain boundary). In these cases, manual masking of the brain is required.
In order to overcome this registration failure, extra steps/bridges were added to the registration pipeline. Instead of directly registering the brain atlas to the first subject space, the atlas was registered (rigid followed by affine) to an MRI anatomical reference scan with higher contrast (T_2-weighted structural scan), which had been previously successfully registered into the first subject space (figure 4.6). This extra step helps the registration algorithm to identify the main anatomical landmarks used for registration (such as the ventricles) more readily and reduces the chances of getting trapped in local minima. Figure 4.7 demonstrates a successful registration of the brain atlas to the anatomical reference scan. A manually created mask of the

anatomical reference scan, ensured that the atlas brain boundary is correctly aligned to the reference scan brain boundary (and not to the fat layer underlying the skull).

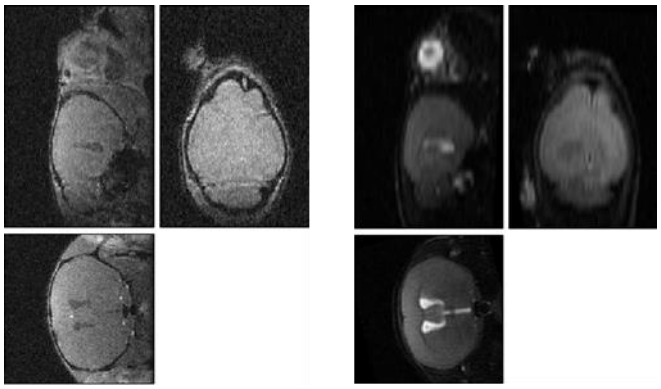

Figure 4.6: Higher contrast T_2-weighted anatomical reference scan (right) registered to the T_1-weighted scan of the first subject (left) as a middle/extra step to ease the registration of the atlas.

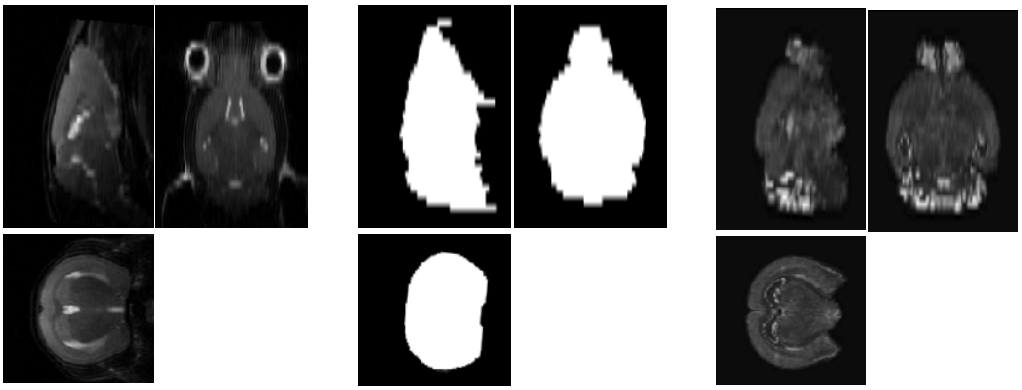

Figure 4.7: Successful registration of the Allen mouse brain atlas (right) to the T_2-weighted anatomical reference scan (left). A manually created mask of the T_2-weighted structural scan (middle), ensured correct brain boundaries are identified and registered.

Figure 4.8 below, demonstrates the final result of all the registration steps described above, i.e. a successful registration of atlas to the 3D T_1-weighted image of the first subject.

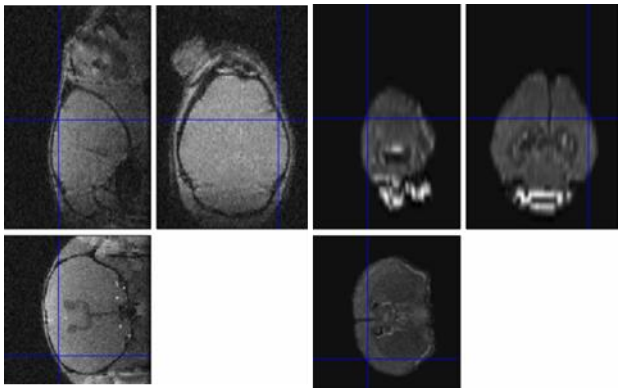

Figure 4.8: Successful registration of the Allen mouse brain atlas (right) to the T_1-weighted scan of the first subject (left).

4.3 Results

4.3.1 ROI analysis - raw MRI signal intensity time-courses

Figure 4.9 illustrates the baseline T_1-weighted images of all 6 animals, successfully registered into the same space.

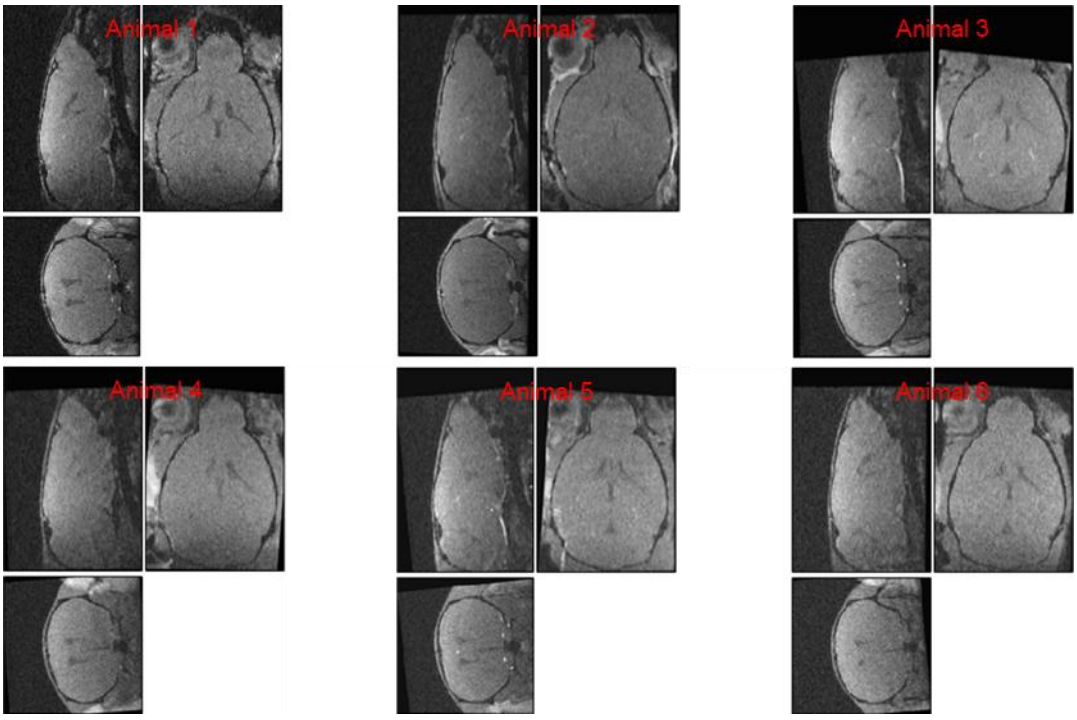

Figure 4.9: Baseline T_1-weighted scans of all 6 animals successfully registered into the same space.

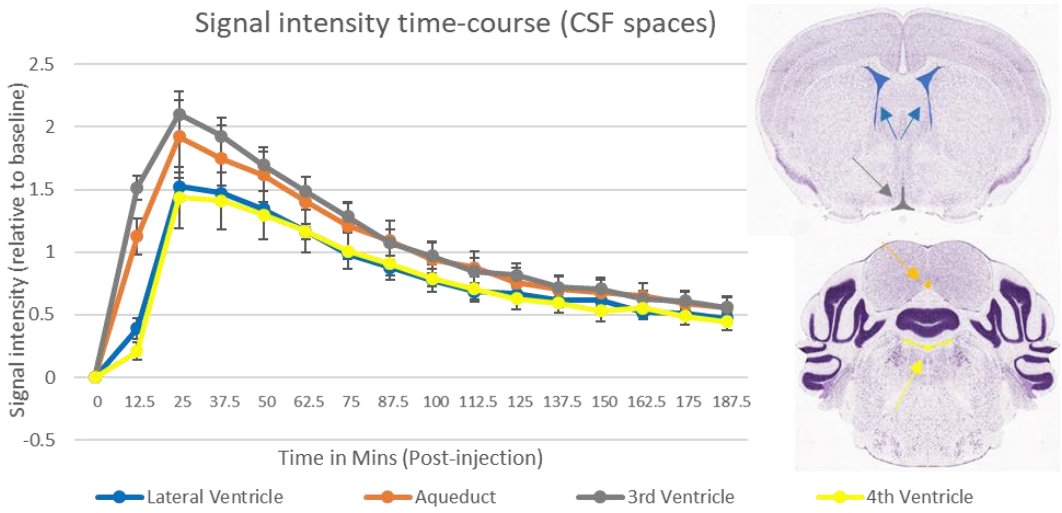

Figure 4.10: Average signal intensity time-courses extracted from 4 different CSF spaces. Time-courses are normalised by baseline. Error bars represent SEM values (n=6).

Figure 4.10 demonstrates rapid infiltration of GBCA into the CSF spaces (aqueduct, lateral, third and fourth ventricles) as they all demonstrate an increase in signal intensity. The time-courses above are consistent with those seen from the FLAIR sequences (section 3.3.3) and further suggest the role of choroid plexus (i.e. the blood-CSF barrier) in the transfer of GBCA from the circulation into the ventricular system.

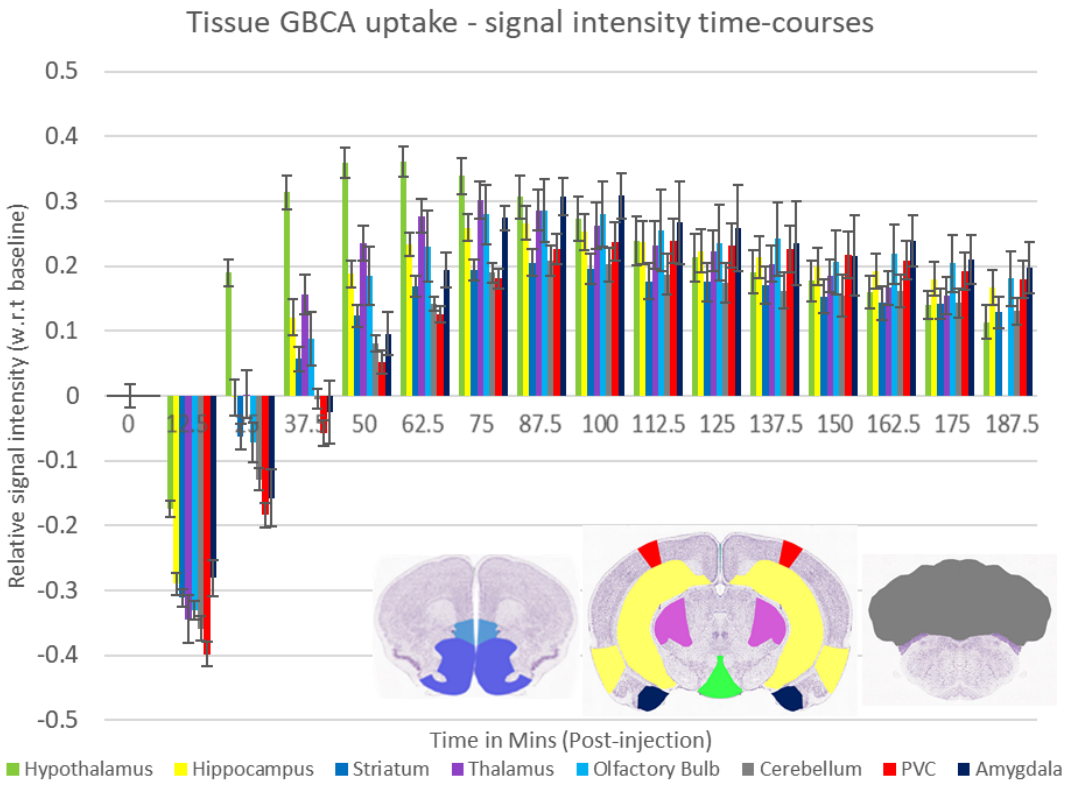

Figure 4.11: Average signal intensity time-courses extracted from 8 different parenchymal brain regions. Time-courses are normalised by baseline. Error bars represent SEM values (n=6).

By only looking at the first four time-points (up to 37.5 mins post injection) as before (section 3.3.4.2), I observed marked extra-vascular GBCA uptake in at least 5 different brain regions: hypothalamus, thalamus, hippocampus, striatum and the olfactory bulb. No conclusions regarding GBCA uptake can be made on the primary visual cortical regions (PVC), amygdalar and cerebellar regions of the brain as they demonstrate no increase in signal intensity (relative to baseline) in the first 4 time-points. It should be mentioned that there are other brain regions (e.g. midbrain) that also exhibit GBCA uptake but data have not been shown on figure 4.11 (primarily for the clarity of the chart presentation - data from only 8 regions were included).

As mentioned in section 3.3.4.2, after about time-point 4/5, the concentration of GBCA in blood vessels is reduced and the T_2* values recover leading to a positive contrast in the intravascular compartment, hence GBCA-induced signal changes that originate from GBCA in the tissue versus the signal changes that originate from GBCAs in the intravascular compartment cannot be differentiated and no sound conclusion can be made regarding brain tissue GBCA uptake (for a meaningful characterisation of contrast uptake in parenchymal brain regions) in these later time-points. Hence, for

the remainder of the chapter, only the early time-points (1-4 (up to 37 mins post injection)) will be the subject of analysis/discussion and data from the later time-points (5-16) will be excluded from further analysis.

4.3.2 Group average raw and thresholded subtraction images – improved sensitivity

One of the advantages of having all the subjects in the same space, is that an average image across a cohort of mice can be obtained by adding all the corresponding voxels together and dividing by the number of subjects. Averaging of subject data will reduce the noise by improving the SNR and hence enhances sensitivity to visualise the spatial-temporal patterns of GBCA uptake. Figure 4.12 demonstrates the relatively higher SNR (x2) of the averaged images compared to single subject images (figure 4.9).

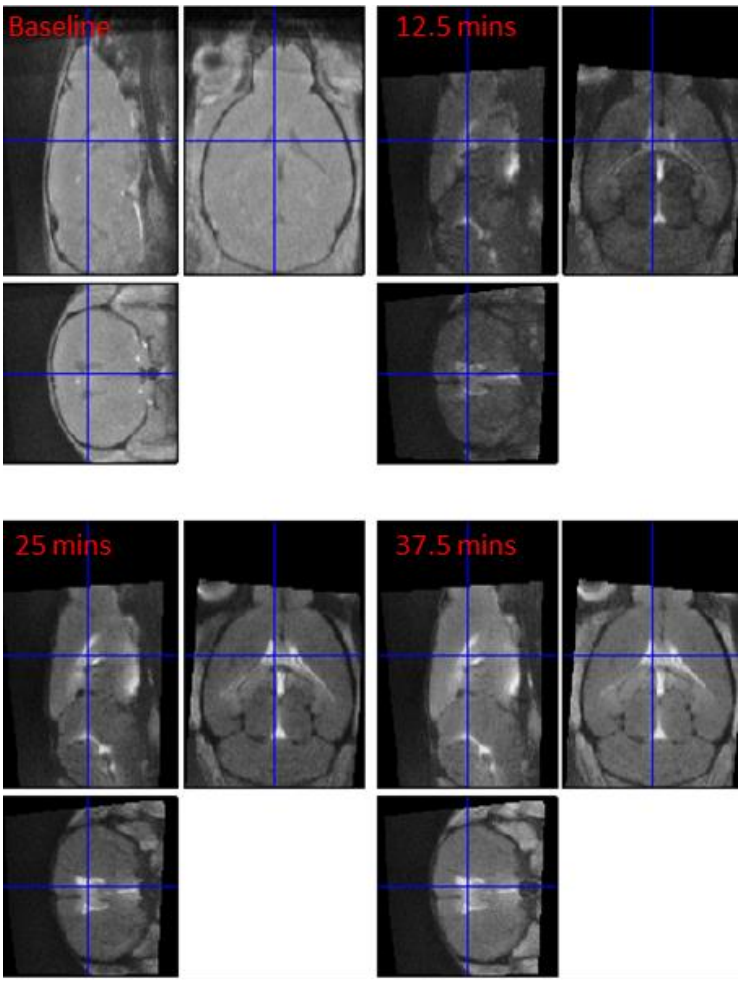

Figure 4.12: Group averaged (n=6) baseline, 12.5, 25, and 37.5 mins post contrast 3D T_1-weighted GE images (i.e. first 4 time-points only). Images are also corrected for surface coil inhomogeneities.

As described in section 3.3.4.3.2, in order to improve sensitivity of the T_1-weighted GE images, thresholded subtraction images were created.

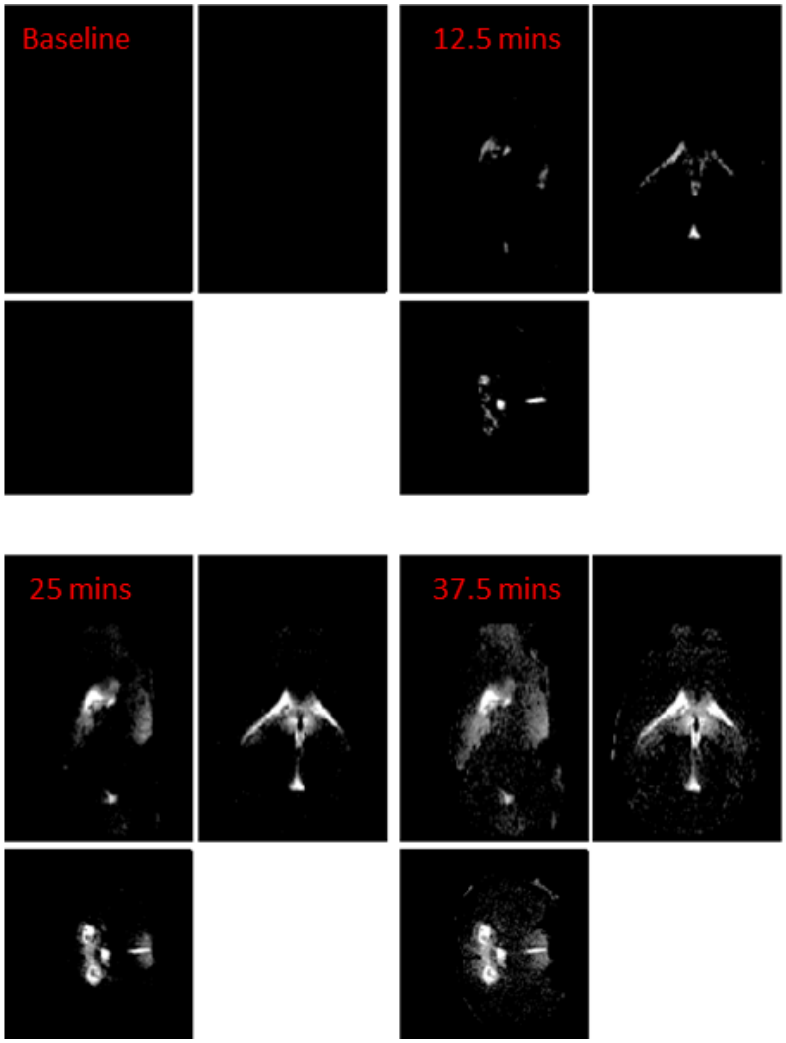

Figure 4.13: Representative group-averaged thresholded subtraction images. This technique increased sensitivity to parenchymal GBCA uptake.

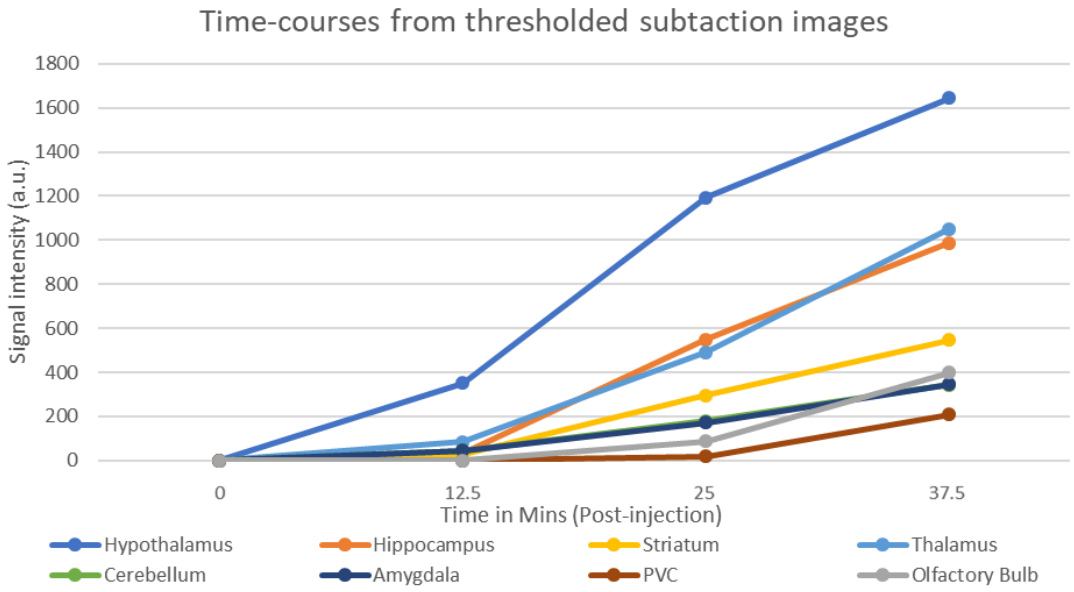

Figure 4.14: Time-courses extracted from the group-averaged thresholded subtraction images. Increased sensitivity is evident as all 8 brain regions now demonstrate GBCA uptake.

Group averaged threhsolded subtraction images indeed increased the sensitivity to parenchymal GBCA uptake. A more brain wide GBCA uptake could be observed on the images (figure 4.13). Additionally, all 8 analysed brain regions demonstrated GBCA uptake (figure 4.14) whereas previously no uptake could be concluded in the PVC, amygdala and cerebellum regions of the brain (figure 4.11).

4.3.3 Rapid ingress of circulatory GBCA into parenchymal brain regions – the VECTOR pathway

The main objective in this study was to investigate the physiologically intact, dynamic pattern of CSF-ISF exchange across the whole brain. Towards that objective, I utilised CE-MRI to determine whether the natural influx of CSF into the brain could be observed by clinically relevant non-invasive MRI measures. I observed a continuous, (3-stage) dynamic transfer of systemic GBCA to the CNS within the imaging timeframe (37 minutes). The first instance of transfer occurred at the level of the blood-CSF barrier (namely stage 1), where intravascular GBCA were delivered to the major CSF compartments in the brain. Subsequent transfer appeared to occur at the level of the ventricular-brain ependymal barrier (namely stage 2) followed by further brain-wide distribution along preferential pathways (namely stage 3).

Blood-CSF transfer (stage 1): The contrast enhanced 3D T_1-weighted MR images (figure 4.15A, pre-contrast) demonstrated clear GBCA uptake within the CSF spaces

by 12 minutes following IV administration of systemic GBCA as noted by the marked hyper-intensity (figure 4.15B). Statistical analysis demonstrated a significant GBCA uptake in the CSF spaces (175% & 193% signal increase from baseline/pre-contrast condition at the level of third ventricle (p-value: <0.0001) and aqueduct (p-value: 0.0012) respectively – figure 4.16D). This exchange is likely to have occurred via the choroid plexus.

CSF-tissue transfer (stage 2): By 25 minutes following GBCA delivery, I had observed clear accumulation of ventricular GBCA in certain regions of the brain parenchyma evident by the hyper-intense periventricular regions (figure 4.15C). The transfer of ventricular GBCA across the ventricular ependymal lining (i.e. ventricular-brain ependymal barrier), was the likely ingress route as the accumulation occurred immediately proximal to the ventricles. Statistical analysis revealed a significant GBCA accumulation in the periventricular regions (e.g. 31% signal increase from baseline/pre-contrast condition at the level of hypothalamus (p-value: <0.0001) – figure 4.16D).

Brain-wide distribution of GBCA: Parenchymal infiltration of GBCA was then followed by further brain-wide distribution (figure 4.15D). That is at 37 minutes post GBCA delivery, the GBCA had extensively travelled away from the ventricular/periventricular regions to reach distant locations of the brain (e.g. olfactory bulb – figure 4.15D, top left panel). Statistical analysis revealed that a significant amount of GBCA had reached distant locations of the brain (e.g. 16% signal increase from baseline/pre-contrast condition at the level of thalamus (p-value: 0.0082) – figure 4.16D).

I have named this continuous, (3-stage) dynamic transfer of systemic GBCA to the cerebral brain tissue, which has been captured non-invasively, for the first time, the VECTOR (VEntricular-Cerebral TranspORt) pathway.

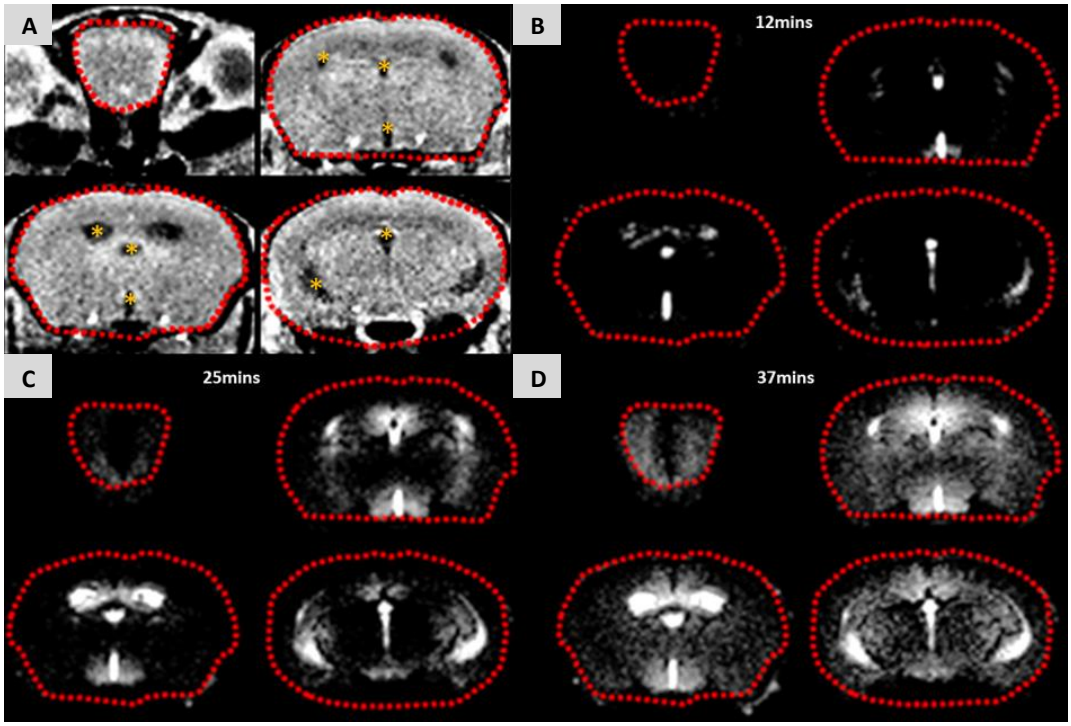

Figure 4.15: Group averaged MR images demonstrating the infiltration of contrast agent into the brain via the VECTOR pathway. The locations of the ventricles are marked by asterisks (left hemisphere only) on the baseline/pre-contrast images (A). This rapid, time-dependant inflow of contrast agent into the brain is initiated by the continuous ventricular filling (B), followed by infiltration into the parenchyma (C) and further brain-wide distribution (D).

4.3.4 3D rendering of the VECTOR pathway

Fluid movement in the brain occurs in all directions, hence 3D rendering (figure 4.16) of the MR images could provide a more comprehensive view of the VECTOR pathway, as opposed to a 2D slice representation of data that are inherently 3D in nature (figure 4.15). Volume rendering of the average MR images further highlighted the time-dependant, dynamic progression of GBCA into the brain in three dimensions. Figure 4.16 displays the coronal (A), sagittal (B) and axial (C) views of this 3D volume, where a distinct regional uptake of GBCA can be observed. ROI analysis in seven different regions of the brain demonstrated significant brain-wide GBCA uptake at 37 mins post contrast injection (p-values of aqueduct: 0.0012, lateral ventricle: <0.0001, third ventricle: <0.0001, fourth ventricle: 0.0015, hippocampus: 0.0022, hypothalamus <0.0001, thalamus: 0.0082). Only thalamus region did not survive the Bonferroni correction (p-values of aqueduct: 0.0084, lateral ventricle: <0.0001, third ventricle: <0.0001, fourth ventricle: 0.0105, hippocampus: 0.0154, hypothalamus <0.0001, thalamus: 0.0574) (Figure 4.16D).

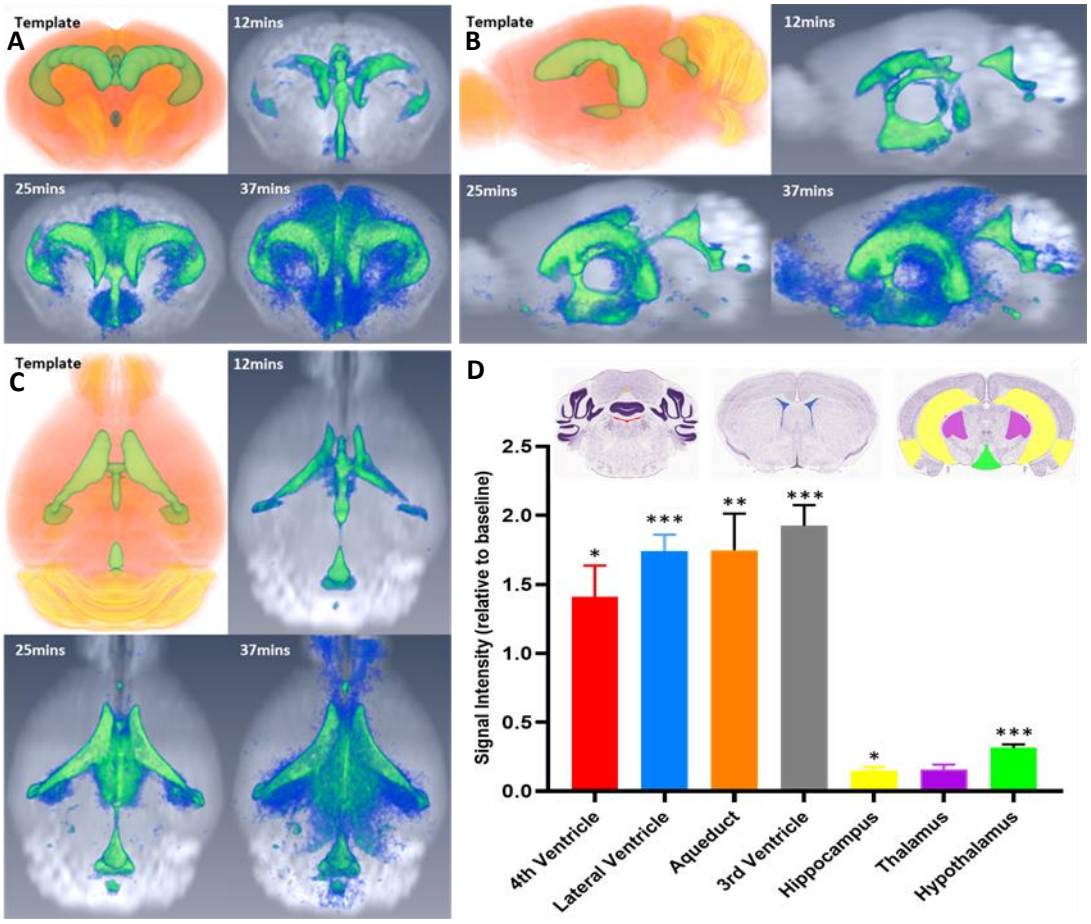

Figure 4.16: 3D rendering of the averaged MR images (Digitally Reconstructed Radiograph - DRR). A-coronal, B-sagittal, C-axial views of the 3D volume. The reconstruction depicts the 3-stage VECTOR infiltration process, where a significant contrast uptake within the highlighted regions was observed 37 minutes post injection (D). p-values of aqueduct: 0.0012, lateral ventricle: <0.0001, third ventricle: <0.0001, fourth ventricle: 0.0015, hippocampus: 0.0022, hypothalamus <0.0001, thalamus: 0.0082. Only thalamus region did not survive the Bonferroni correction (p-values of aqueduct: 0.0084, lateral ventricle: <0.0001, third ventricle: <0.0001, fourth ventricle: 0.0105, hippocampus: 0.0154, hypothalamus <0.0001, thalamus: 0.0574).

4.4 Discussion

To date, probing CSF-ISF exchange (or the glymphatic system), has required either intra-cerebral or intra-ventricular contrast agent injections. These approaches, whether direct injection of fluid into brain tissue or CSF space, may be a confounding factor when studying interstitial fluid transport, as volume, pressure and mode of injection may affect the dynamics of the observed contrast agent distribution. In this chapter, the first non-invasive imaging of CSF-ISF exchange using a single intravenous injection of GBCA and MRI was performed, hence maintaining the fragile

CSF/ISF milieu. I observed the infiltration of systemic GBCA into the CSF spaces which is believed to occur at the level of the blood-CSF barrier (i.e. the choroid plexus). Subsequently, the GBCA passes from the CSF into the brain parenchyma, immediately proximal to the ventricles, with clear accumulation in the periventricular regions and the hypothalamus. Following entry into the brain parenchyma, a brain-wide distribution was observed within 40 minutes, with the contrast agent reaching brain extremities such as the olfactory bulb region of the brain.

I observed the ingress of GBCA along preferential pathways of the brain. For example, I observed ingress towards the midline from the lateral ventricles. This particular directionally has been noted by Bedussi *et al*. (Bedussi *et al*., 2015) where tracers injected into the striatum migrated medially towards the lateral ventricle (i.e. the midline) (supplementary material 4.7.1). A similar observation was made by Panizzo *et al*. (Panizzo *et al*., 2009) for iron-oxide nanoparticles injected into the lateral ventricles (supplementary material 4.7.1). On the other hand, tracers penetrating the third ventricle, migrated in the opposite direction and away from the midline. This is in alignment with the findings of Rodriguez and colleagues (Rodríguez, Blázquez and Guerra, 2010), where intra-ventricularly delivered HRP penetrated the walls of the third ventricle and diffused into the adjacent brain tissue and migrated in a medial-lateral manner (supplementary material 4.7.2). Additionally, no uptake of GBCA could be observed in the rostrally cortical areas, whereas migration of GBCA towards caudally cortical areas was evident. Perhaps most interestingly, GBCA penetrating the brain from the third and the lateral ventricles, seemed to follow a distinct pathway towards the frontal areas of the brain. GBCA appeared to follow the rostral migratory stream (RMS) towards the olfactory bulb region of the brain (supplementary material 4.7.3). The rostral migratory stream is a specialised route for the migration of neuroblasts from the subventricular zone (a major source of new cells in the adult brain located near the lateral ventricle) to the olfactory bulb. It is mainly developed in the brain of rodents and its importance lies in the transfer of neuronal precursor cells to degenerated/damaged areas in the olfactory bulb to refine and even change an animal's sensitivity to smell (Sun, Kim and Moon, 2010). Additionally, these observations seem to support the findings of Scranton *et al*. (Scranton *et al*., 2011), where it was shown that the RMS provides a major access path for intra-nasally delivered radioligands into the CNS (brain wide distribution of tracers was visualised (olfactory bulb, hippocampus, cortex and cerebellum)). Interestingly, when the authors surgically transected the RMS, no

statistically significant quantities of radioligands were observed in the brain, alluding the importance of RMS in the intranasal delivery of drugs to the rodent CNS.

A complete picture of the CSF exit routes is not clear. However, several sites of CSF drainage are documented and include the arachnoid villi (Pollay, 2010), the nasal lymphatics (Kida, Pantazis and Weller, 1993), cranial and peripheral nerves, peri-vascular routes (Carare *et al*., 2008; Cserr, 1988; Iliff *et al*., 2012) and meningeal lymphatic vessels (Louveau *et al*., 2015). Here, the movement of GBCA towards the olfactory areas may support the role of nasal lymphatics in VECTOR pathway. In support of this observation, one CNS elimination route for immune cells and antigens have been shown to be via the RMS towards the distal olfactory bulb and into the cervical lymph nodes (Mohammad *et al*., 2014). Additionally, it was shown that the tracer F-500 reaches the nasal turbinates through the cribriform plate when injected intra-striatally (Bedussi *et al*., 2015). In this chapter, meaningful imaging of VECTOR pathway (for characterisation of brain tissue GBCA uptake) was limited to 37 mins (due to systemic GBCA clearance and the following enhancement in intravascular signal intensity – section 3.3.4.2) which precludes a full assessment of the exit routes.

In the pioneering work of Iliff *et al*. (Iliff *et al*., 2012) introducing the glymphatic system, subarachnoid CSF rapidly entered the brain via the paravascular spaces. Minimal entry of tracer from the ventricles into the brain tissue was reported. In this thesis, contrary to the findings of Iliff *et al*., a significant amount of GBCA penetrated the ependymal wall of the ventricles and entered brain interstitium. In the data acquired here, the subarachnoid CSF and its influx along the paravascular spaces could not be clearly observed (see the following paragraph for a detailed discussion). The observed differences between the VECTOR and the glymphatic pathway (in terms of tracer entry routes into the brain) is possibly explained by the discrepancies in the adopted experimental protocols (such as route of tracer delivery, size and chemical structure of the tracer). Iliff *et al*., injected fluorescent tracers directly into the brain (intracisternal and intraventricular), whereas in this study, commercially available MRI tracers (GBCA) were delivered using a less invasive, and importantly, clinically relevant route (IV). Amid these discrepancies, I believe the VECTOR and the glymphatic pathway ultimately identify distinct solute transport mechanisms (and emphasise the existence of regional differences), acting in parallel towards a more efficient brain-wide solute clearance.

As mentioned, the main glymphatic clearance driver, that is the subarachnoid CSF and its influx along the fine paravascular channels, could not be imaged in this study.

These data, however does not dismiss the existence of this transport route, but rather suggests that transport via ventricles may be more dominant. In fact, non-appearance of this transport route on the MR images could be as a result of a limitation of the MRI platform as it captures a rather conservative pattern of CSF-ISF exchange (which may include false negative findings). The imaging of the subarachnoid and the paravascular spaces (microscopic scale) is limited by the inherently low spatial resolution of MRI (0.1 mm in this study). Additionally, the susceptibility artefact that was induced around the edges of the blood vessels (due to the high concentration of GBCA in vasculature) likely contributes to the masking of the subarachnoid and the paravascular spaces. The induction of this dominating susceptibility effect (i.e. negative contrast relative to baseline) in the intravascular compartment was necessary for the partial separation of extravascular (interstitial) signal compartment from the intravascular signal compartment (section 3.3.4.2). Briefly, the acquired MRI signal is influenced by both intravascular (blood vessel) and extravascular (non-vessel/brain tissue) compartments due to PVEs (as a result of relatively low MRI spatial resolution). At lower standard doses where gadolinium creates a positive contrast in the blood vessels, it is challenging to differentiate the contributions from each compartment (since both will induce a positive contrast and increase the MRI signal). At higher GBCA doses however, the intravascular compartment negatively impacts the total MRI signal (i.e. acts to reduce the signal) and this enables the differentiation of positive extravascular (interstitial) signal compartment from the total signal. This is a rather unusual technique as T_2*effects are usually deemed an undesirable artefact in routine CE-MRI imaging. Here, I have taken advantage of this unexploited characteristic, to null/drop-out the blood vessel signal and only image, albeit qualitatively, tracer uptake in brain parenchyma.

Previously it was believed that gadolinium based contrast agents are not able to penetrate the healthy brain and ought to remain in the intravascular compartment due to the integrity of the blood brain barrier. They were considered to have an excellent safety profile (Matsumura *et al*., 2013) until recent safety reports of gadolinium retention in the brain (Kanda *et al*., 2014) which resulted in FDA reports advising suspension of some of these contrast agents. Initially reported in a retrospective MRI study by Kanda *et al*. (Kanda *et al*., 2014), hyperintense regions were seen in the dentate nucleus (DN) and globus pallidus (GP) regions of the brain. The retention of GBCA in the brain of healthy patients raised safety concerns in the MRI research and radiology communities and several questions were raised. Perhaps most crucially, how does gadolinium enter the brain and distribute itself in these two regions which

are anatomically distinct and far from any potential blood brain barrier disruption. Towards that important question, Jost *et al*. (Jost *et al*., 2017) provided compelling evidence regarding the transfer of systemic GBCA into the ventricular system, however limited evidence regarding tissue infiltration was provided. In this study it was demonstrated that systemically injected GBCA can infiltrate the healthy brain via the VECTOR pathway and widely distribute. Having identified a penetration route, the underlying cause for gadolinium retention however could not be concluded in this study and requires further investigation. It is suspected that this retention (which is only specific to the linear class of these agents) is due to the permanent de-chelation of the gadolinium ion from the contrast agent structure and the subsequent binding of the free ion to other sites such as ligands, proteins and macromolecules (Boyken *et al.*, 2019). Generally, linear GBCAs have higher propensity to release of gadolinium and have higher rates of dissociation. This is because the gadolinium ion, is “caged” in the cavity of the ligand (clamp-shell like structure) for macrocyclic GBCAs, however this cage is not fully closed in linear GBCAs. Macrocyclic agents are thus considered to be the most stable between the two.

The size and the molecular weight (MW) of a tracer or a drug, is a deciding factor in regards to entry to the CNS from the circulation with smaller sized molecules more freely entering the CNS. The blood-CNS barriers; the blood brain barrier (BBB) and the blood CSF barrier (BCSFB) are the two barriers that protect the brain from blood-borne molecules that could be detrimental to neuronal microenvironment. In this study, the paramagnetic MRI contrast agent gadodiamide (Omniscan, MW 0.59 kDa) was utilised. Omniscan has a linear non-ionic structure and it exhibits lower thermodynamic and kinetic stabilities in vivo compared to macrocyclic agents resulting in higher rates of gadolinium dissociation/de-chelation (due to relatively weaker chemical bonds – section 2.6.3). At physiological conditions (pH 7.4), the half-life of gadolinium dissociation was calculated to be 9.3 hours (Baranyai *et al*., 2015). It is plausible that during the acquisition time (37 minutes), a small amount of gadolinium in the circulation becomes permanently de-chelated and presents as free ions. Since the de-chelated gadolinium has a smaller MW (0.16 kDa), one may reasonably argue that this could lead to an overestimated measure of tracer uptake/penetration into the brain (as smaller gadolinium ion can more freely penetrate the blood-CNS barriers compared to the chelated state). This may be of primary concern to the radiology and the MR safety community but from the CSF-ISF exchange point of view, this potentially exaggerated penetration may be of less concern as gadolinium ion transfer into the brain may still be a useful tracer of CSF-

ISF exchange pathway function (as other feasible theoretical gadolinium ion entry routes such as metal transporters and transferrins seem unlikely (Garcia, Liu and Louie, 2017)). Nevertheless, the dissociation of gadolinium and the associated overestimation of tracer uptake in the brain is believed to be negligible for the duration of imaging in this study. Firstly, there is a lack of evidence for BBB permeability to free gadolinium ion (Garcia, Liu and Louie, 2017), and this is further supported by the regional nature of tracer uptake observed in this study. If free gadolinium ions were to penetrate the BBB, then a more uniform tracer uptake would have been observed in the brain. Second is the relatively long dissociation rate of Omniscan (9.3h). Finally, free gadolinium ion is very toxic and detrimental for many biological processes (Rogosnitzky and Branch, 2016). The fact that no adverse reactions were seen in mice receiving this relatively higher dose of Omniscan implies that free gadolinium does not penetrate the brain to any pathologically relevant extent. However further confirmatory investigation using macrocyclic GBCAs (with higher stability) is required to validate this claim.

Interestingly, there are structures in the brain which possess a BBB markedly more permeable to many substances, known as the circumventricular organs (CVOs). These structures mostly surround the ventricular system of the brain, hence one might assume that penetration of GBCA into the parenchyma is facilitated by these CVOs rather than transfer across the ventricular-brain tissue ependymal barrier. Hence in order to certify that GBCA parenchymal penetration in VECTOR pathway does indeed occur at the level of the ventricular ependymal barrier (and not promoted by the leaky CVOs), the CVO literature was extensively reviewed. These structures are mainly responsible for the release of hormones into the blood stream and they include (but not limited to) the median eminence, sub-fornical organ (SFO), sub-commissural organ and the pineal gland. It has been shown that despite moving within the parenchyma of the CVO, blood borne molecules are not able to move into the parenchyma of the neighbouring tissue (Morita and Miyata, 2012, Fry, Hoyda and Ferguson, 2007). Maness and colleagues (Maness, Kastin and Banks, 1998) also provided evidence that blood-borne IL-1a protein entering the CNS at the SFO is greatly restricted to the SFO and does not freely penetrate into the surrounding regions. Similarly, blood-derived low molecular weight tracer Dex3k and fluorescein isothiocyanate (FITC) did not diffuse to the outside of the sensory CVOs providing further evidence that neuronal circuits are protected from blood-derived neurotoxic and bioactive substances (Miyata, 2015). In a separate study, horseradish peroxidase (HRP) injected into the subarachnoidal CSF reached the intercellular space of the

median eminence, however the arcuate nucleus-median eminence barrier prevented HRP to reach the neighbouring arcuate nucleus (Rodríguez, Blázquez and Guerra, 2010). According to this literature, it is apparent that the contribution of CVOs to the brain-wide infiltration of GBCA to be minimal/negligible, however unambiguous confirmation of this statement requires further investigation.

CE-MRI and paramagnetic contrast agents (GBCAs) are prevalent in the clinical setting and have been widely available for the past 3 or 4 decades. Since contrast agents are intravenously administered for the vast majority of CE-MRI examinations, it's intriguing that the physiological pattern of GBCA infiltration into the brain tissue (the natural ingress and excretion process) had never been visualised before. The most plausible explanation for this void in the literature is that CE-MRI examinations are routinely prescribed/performed for the detection of an underlying disease/abnormality (such as lesions, tumours, stoke). Therefore, the attention of the radiologist will be focused on the detection of that pathology, and as a result noticing unfamiliar/weak signal enhancement off-site (e.g. signal enhancement due to natural GBCA presence in other brain tissue or CSF cavity) may be of low chance/interest or even ignored. In fact, in these settings, imaging slices are usually centred on or around the site of the lesion/pathology, this further reduces the chances of detecting unexpected signal changes in other brain regions. Another contributing factor could be the imaging timeframe. If the intent for examination is visualisation of veins or arteries (i.e. magnetic resonance angiography), scans are acquired immediately after GBCA delivery, and if the intent for imaging is detection of tumours/lesions, the scans are delayed (usually up to 10 minutes) to allow distribution of GBCA into the tissue/lesion (Dieke-Hofmann *et al*., 2019). Assessment of CE-MR images outside this timeframe has been rarely performed, and this may be the reason why enhancement of intact brain tissue (which may take longer than this time frame based on my observations in the mouse brain), had been left unnoticed in the MRI literature. Additionally, intact brain tissue tracer uptake manifests at relatively lower concentrations, therefore the inherently low sensitivity of MRI could be a limiting factor (Dieke-Hofmann *et al*., 2019). This implies that imaging intact brain tissue tracer uptake (i.e. natural ingress of GBCA into the brain), requires relatively higher GBCA dosages compared to the routine clinical dose (to increase MRI sensitivity to small amounts of tracer in the brain tissue). Fairly recently (relative to the advent of clinical CE-MRI 3 or 4 decades ago) more appropriate and specialised sequences for imaging very low concentrations of GBCA in the CNS, such as hT_2w-FLAIR were defined in CE-MRI scientific literature (Naganawa *et al*., 2011). In short, the

combination of inappropriate imaging sequences, time frames, locations and dosage as well as a lack of interest in imaging GBCA infiltration into the brain (as it was previously assumed GBCAs do not cross the healthy brain), has contributed to the void in literature regarding the natural ingress of GBCA into the brain.

4.5 Conclusion

In this chapter, a completely new pattern of CSF-ISF exchange in the brain of healthy mice was revealed. The results are striking and reveal a pattern of cerebral fluid movement and exchange that has never before been visualised. Due to the distinct nature of this exchange (from ventricles to cerebral tissue), I coined this pathway, the '*VEntricular Cerebral TranspORt (VECTOR)'* pathway. This platform is the first to capture unperturbed and physiologically intact whole-brain CSF-ISF exchange, using a single IV injection of gadolinium based contrast agent and MRI. Therefore, VECTOR shows great promise for clinical translation and could potentially be an ideal candidate for the clinical assessment of CSF-ISF exchange in the healthy and the diseased state.

4.6 Limitations

Considering previous reports of gadolinium retention in the brain (Kanda *et al*., 2014), the main limitation of VECTOR pathway imaging is perhaps the need for a relatively high GBCA dose (8 times higher than the standard human clinical dose based upon body surface area normalisation between mice and humans). This limitation will be discussed in more detail in chapter 5 where attempts will be made to lower the high GBCA dose of the platform.

In this chapter, despite identifying/imaging a penetration route into the CNS for systemically delivered GBCA, no evidence was provided that could explain the underlying cause of gadolinium retention in the brain. This was not surprising as the experimental methodology in this study was not designed for investigating gadolinium retention in the brain and therefore, both, the aims and findings of this chapter had limited clinical resemblance in this regard (e.g. gadolinium retention in the brain had been observed in subjects with a history of repeated contrast enhanced MRI examinations whereas in this study only a single high dose GBCA bolus was administered). Investigating gadolinium retention in the brain following this single high dose bolus of GBCA was also not possible in the current experimental setting as the imaging window was limited to 37 mins post contrast injection (which also precluded a full assessment of GBCA exit routes and clearance dynamics). In chapter 5, attempts will be made in order to extend the imaging window.

Two other limitations associated with the administration of a high GBCA dose that should be noted are a) possible hyperosmolality effects which may disrupt BBB integrity (this limitation will be discussed in more detail in chapter 5 where attempts will be made to lower the high GBCA dose of the platform) and b) sensitivity lowering intravascular PVEs (due to the induced susceptibility effects – section 3.3.4.2) which implies that the acquired images capture a conservative pattern of CSF-ISF exchange (this limitation was discussed in more detail in section 3.6) in addition to complicating a quantitative readout from the method (although in chapter 5 attempts will be made for the quantitative estimation of brain tissue GBCA uptake).

4.7 Supplementary material

4.7.1 Lateral-medial directionally of tracers in communication with lateral ventricles

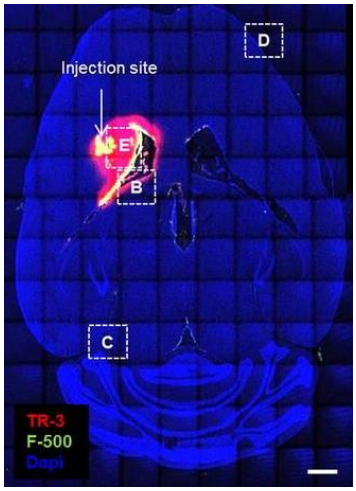

Figure S4.1: Bedussi et al. (Bedussi et al., 2015) reported migration of tracers injected into the striatum towards the lateral ventricles. This lateral-medial directionally of tracers that are in communication with the lateral ventricles is consistent with the findings of this study.

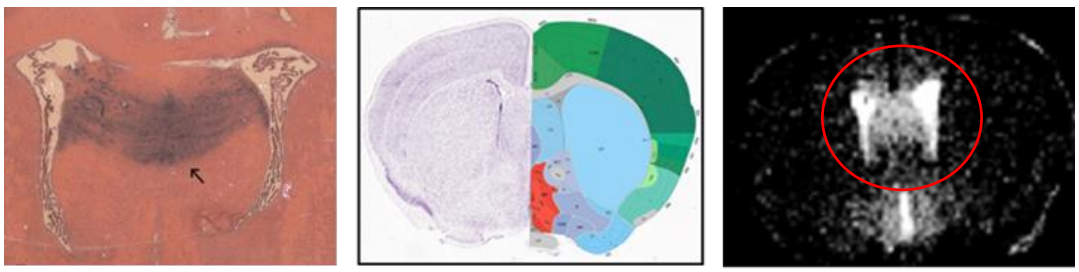

Figure S4.2: Iron-oxide nanoparticles (Endorem) when injected into the lateral ventricles, penetrate the parenchyma in a lateral-medial manner (left) (Panizzo et al., 2009), consistent with the MRI findings of this study (right).

4.7.2 Medial-lateral directionally of tracers in communication with third ventricle

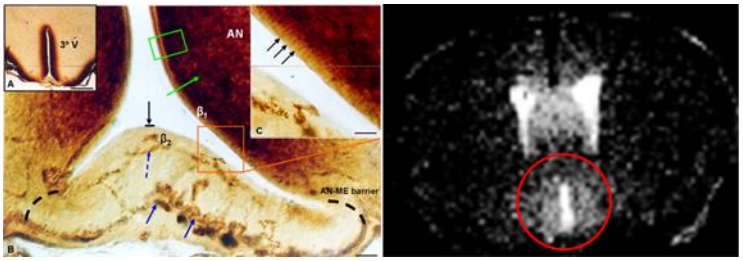

Figure S4.3: Intra-ventricularly delivered HRP penetrated the walls of the third ventricle and diffused into the adjacent brain tissue and migrated in a medial-lateral manner (left) (Rodríguez, Blázquez and Guerra, 2010) consistent with the MRI findings of this study (right).

4.7.3 VECTOR pathway seems to be facilitated by transport along Rostral Migratory Stream (RMS)

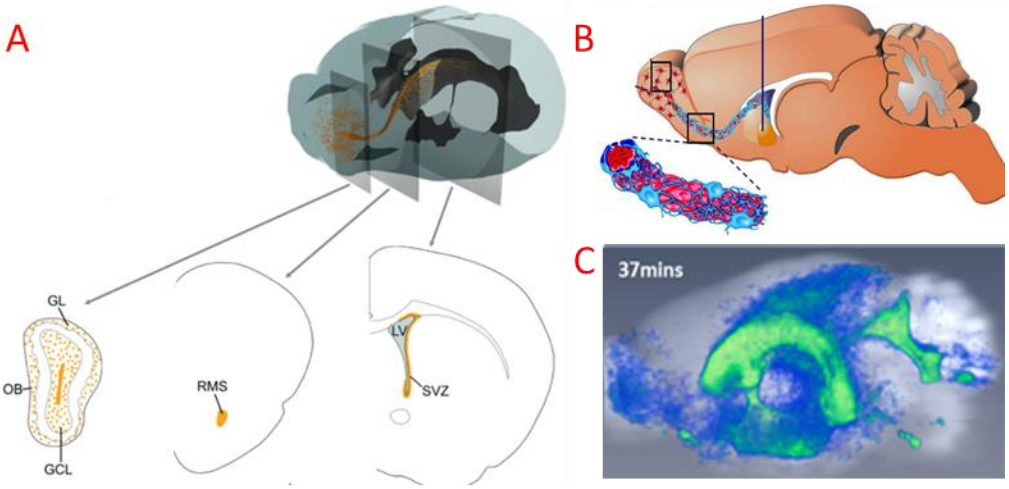

Figure S4.4: A- Neural stem cells (NSCs) located near the walls of the lateral ventricle (i.e. the subventricular zone (SVZ)) migrate towards the olfactory bulb (OB) via the rostral migratory stream (Fiorelli et al., 2015). B- Sagittal view of the migration of NSCs towards the OB via the RMS (adopted from http://neuro-science.blogspot.com/2011/10/subventricular-zone.html). C- VECTOR transport of GBCAs towards the OB also seems to be facilitated by the RMS.

Chapter 5: Validation of VECTOR pathway dynamics

In chapter 3, a non-invasive MRI platform for the purpose of CSF-ISF exchange imaging was developed. In the previous chapter, application of that novel platform lead to the identification of a new CSF-ISF exchange pathway (the VECTOR pathway). In this chapter, I sought to perform additional confirmatory experiments using independent imaging techniques to provide supporting evidence for my previous findings and to address some of the limitations of the MRI platform, such as the relatively high dose of GBCAs, as well as sensitivity and spatial resolution constraints. In this chapter, a mass spectrometry technique will be deployed for the high-resolution assessment of the VECTOR pathway. An autoradiography technique with high sensitivity will also be deployed to support the previous MRI findings but with a more clinically relevant tracer dosage (attempts will also be made for the quantitative estimation of brain tissue GBCA uptake). Additionally, attempts will be made to reduce the MRI platform contrast agent dose and to ensure reduction of dose does not alter VECTOR dynamics. Finally, a new MRI sequence will be implemented for the extended imaging of the VECTOR pathway (i.e. beyond 37 minutes post contrast injection).

5.1 Introduction

A key challenge associated with CE-MR image interpretation, is the differentiation of GBCA-induced signal changes that originate from GBCA in the tissue versus the signal changes that originate from GBCAs in the intravascular compartment, due to the limited spatial resolution of MRI. In the ideal experimental condition, the contrast agent would rapidly clear from the circulation, hence signal from the intravascular compartment would stay constant over time (i.e. no time-varying signal intensity changes). However, such an ideal contrast agent simply does not exist (although macromolecular MRI contrast agents (mCAs) have been developed (Tang *et al*., 2013) that display extended retention in the blood circulation and therefore exhibit milder time-varying behaviour, however these agents are not widely available in the clinical setting). Here, in order to ensure that the previous MRI findings are not confounded by the time-varying signal contributions from the intravascular compartment (due to PVEs), I sought to employ a laser ablation inductively coupled plasma mass spectrometry (LA-ICP-MS) technique. Animals whose brains are to be analysed by the LA-ICP-MS technique, need to be perfused with saline before brain dissection/slicing. Hence, LA-ICP-MS analysis of brain tissue samples is completely free from undesired intravascular contributions (as perfusion of animal with saline

eliminates the intravascular compartment – methods section). LA-ICP-MS is a powerful analytical technique that enables highly sensitive elemental and isotopic analysis to be performed. LA-ICP-MS is a means of mapping where an element is located within a tissue, with a fine spatial resolution (laser spot size as low as 4µm). Here, this high-resolution imaging technique will be implemented for the robust mapping of GBCA uptake in brain tissue and also to validate the spatial pattern of GBCA distribution previously observed on the MR images.

For a more complete characterisation of the VECTOR pathway however, information is needed regarding actual GBCA concentration/uptake in brain tissue. CE-MRI provides an indirect measure of brain tissue tracer uptake as MRI is not sensitive to the contrast agent itself but rather to the changes it induces in tissue T_1/T_2 values. Hence the measured MRI signal itself cannot provide a robust quantification of brain tissue tracer uptake. LA-ICP-MS is also a qualitative technique for mapping element distribution within tissue, hence it does not provide a quantitative estimation of brain tissue tracer uptake.

Autoradiography on the other hand is a highly sensitive bio-analytical method that captures the distribution of radioactively labelled substances within a tissue sample. Although there are limitations associated with autoradiography (such as low spatial resolution and image blurring), it can be utilised for the quantitative estimation of tracer uptake within a sample (using calibration standards). Hence, in this section autoradiographic validation of VECTOR dynamics will be conducted with more clinically relevant (lower) tracer dosage to ensure a) previous results are not confounded by the relatively high GBCA dose administered in the MRI platform, b) results are not confounded by the time-varying intravascular effects (i.e. PVEs from the intravascular compartment) and c) for the quantitative estimation of whole-brain tissue tracer uptake.

LA-ICP-MS and autoradiography are both highly sensitive analytical techniques and could therefore, in principle, successfully image the VECTOR pathway with considerably lower contrast agent dose. However, they are both terminal procedures and hence, not clinically relevant. The VECTOR pathway was originally identified from a non-invasive, relatively high dose CE-MRI platform. The initial dose (10 mmol/kg) was 2 times higher than the dose reported in previous pre-clinical rat studies (Jost *et al*., 2016) and approximately 8 times higher than the standard clinical human dose (0.1 mmol/kg) based upon body surface area normalisation between mice, rats and humans (Nair and Jacob, 2016) (the dose of 0.1 mmol/kg is the typical dose for non-

vascular CE-MRI studies (e.g. tumour and stroke imaging) whereas for MR angiography a higher dose (up to 0.4 mmol/kg) is usually required (Ledneva *et al*., 2009)). Clinical translation of this relatively high GBCA dose may be considered unethical considering the recent safety concerns of gadolinium retention in the brain. Additionally, the integrity of the blood brain barrier following the initial high GBCA dose was questioned previously due to possible hyperosmolality effects (Zamani *et al*., 1982). Hence in this section, attempts will be made to lower the MRI platform GBCA dose (towards a more clinically relevant dose) and to validate the VECTOR dynamics with more clinically relevant doses (to build extra confidence in the platform and to address the possible BBB disruption concerns).

As described earlier, the non-invasive CE-MRI identification of VECTOR pathway was based on the partial separation (differentiation) of intravascular and extravascular signal compartments, by the induction of negative contrast (relative to baseline) in the intravascular compartment due to the relatively high GBCA dose at 9.4T (section 3.3.4.2). However, this limited the VECTOR imaging window to 37 minutes post contrast injection. In this chapter I sought to implement an MRI sequence that would eliminate the need for the induction of negative contrast in the intravascular compartment. In other words, a non-invasive sequence that is independent of the intravascular signal contributions and capable of providing a more linear correlate of GBCA uptake in the brain tissue. Implementation of such sequence, if successful, would provide invaluable advantages including a) possibility to image VECTOR dynamics beyond 37 minutes post contrast injection, b) imaging with a lower dose (more clinically relevant) and c) avoiding the signal loss/susceptibility around the edges of the blood vessels (section 3.6 – figure 3.15). Diffusion-weighted (DW) MRI is an ideal candidate as it could be sensitised to the perfusion of blood, therefore in theory, one could suppress the vascular signal by the appropriate selection of imaging parameters (e.g. small *b*-values – Takahara and Kwee, 2012). In other words, this technique is equivalent to the application of ‘diffusion crushers’ for the nulling of the intravascular signal compartment. Contrast in DW imaging depends on the differences in rates of diffusion between tissues (Chilla *et al*., 2015), where additional magnetic field gradients are added to conventional MR sequences to generate a DW image (section 2.5 - figure 2.15). In this section a diffusion-weighted spin-echo MRI sequence will be implemented and an attempt will be made for the extended imaging of VECTOR pathway using this sequence.

5.2 Methods

5.2.1 Laser ablation inductively coupled plasma mass spectrometry (LA-ICP-MS) methods

5.2.1.1 Animal preparation

3 healthy male (C57Bl6) mice were used in total. Anaesthesia was induced and maintained with 3% & 2% isoflurane respectively [in 1 L/min O2]. Core body temperature and respiration were monitored using a rectal probe and pressure pad. Core body temperature was maintained at 37 ± 0.5 °C using a heat pad. Following anaesthesia, a 5 min IV infusion, delivering 10 mmol/kg (20 ml/kg) of Omniscan (mice 1 and 2) or saline (mouse 3) was started. The first and the third mouse were euthanised 37.5 min post IV delivery of GBCA with an IP injection of pentobarbital (0.1 mL). The second mouse was euthanised 120 min post IV injection. The thoracic cavities were opened and the mice perfused through the left ventricle with 15–20 mL of saline (0.9%) followed by 30 mL of buffered formal saline at a flow rate of 2 mL/min. After perfusion, the animal was decapitated, the brain removed from the skull, and tissue snap frozen in isopentane pre-chilled on dry ice. Frozen brain tissue was embedded in optimal cutting temperature compound and 150 µm sections cut using a Leica CM3050 S cryostat (specimen temperature, -18°C, chamber temperature, -22°C) onto SuperFrost® Plus microscopy slides.

5.2.1.2 LA-ICP-MS interrogation of brain samples

LA-ICP-MS analysis of brain sections were undertaken using a New Wave Research NWR213 laser ablation system (Electro Scientific Industries, Portland, Oregon, USA) coupled to an iCAP Q ICP-MS (Thermo Fisher Scientific, Hemel Hempstead, UK). For laser ablation the following conditions were used; 50 or 100 µm diameter laser spot size, fluence 2 J/cm2, scan speed 166 µm s-1 and repetition rate of 20 Hz. Helium was used as the cell gas which was run as a flow of 0.8 mL min-1. The ICP-MS was used in KED mode with helium as the collision gas. The isotope monitored was 158Gd. The dwell time used for each isotope was 0.05 s. Image generation was achieved using Iolite v3 (Paton *et al*., 2011) within Igor Pro 6.36 (Wavemetrics Inc. Oregon, USA). Images were then pseudo coloured to provide ease of contrast visualisation for comparison to adjacent histological slices (bright = high signal intensity, dark = low signal intensity).

5.2.2 Autoradiography methods

5.2.2.1 Preparation of radioactivity

^{111}In-DTPA (indium-diethylenetriaminepentaacetic acid) was prepared by adding ~440 MBq stock $^{111}InCl_3$ (Malinckrodt) to a 50 µL solution (pH 7.4, 50 mM) of DTPA (Sigma Aldrich) which was diluted with 0.9% saline to give a final concentration of 100 MBq per 100 µL. Radiochemical purity was then analysed with thin layer chromatography (TLC), using aluminium foil-backed silica gel matrix strips (1cmx10cmx200 mm; Sigma Aldrich) as the stationary phase. A drop of the sample (0.2 µL) was loaded at a designated origin and left to air dry, before eluting with water as the mobile phase, taking care that the sample origin was not immersed. A control sample of stock $^{111}InCl_3$ was prepared in the same way. Unchelated ^{111}In remains at the origin, whereas ^{111}In-DTPA migrates with the solvent front. TLC strips were cut into thirds and activity from each section quantified using a gamma counter (Wizard2, Perkin Elmer). Radiochemical purity of the ^{111}In-DTPA was calculated as the percentage of the total activity from the strip that was in the top third, and was assessed as >99 %, compared to <0.1% for the unbound $^{111}InCl_3$. This was checked in duplicate. Neutral pH of the ^{111}In-DTPA solution was confirmed before injection.

5.2.2.2 Animal preparation

3 healthy male (C57Bl6) mice were used in total. Anaesthesia was induced and maintained with 3% & 2% isoflurane respectively [in 1L/min O2]. Core body temperature and respiration were monitored using a rectal probe and pressure pad. Core body temperature was maintained at 37 ± 0.5 °C using a heat pad. Following anaesthesia, a 5 min IV infusion, delivering ~100 Mbq (~100 µL) of ^{111}In-DTPA was started (the net amount of radioactivity delivered was later determined to be 90, 100 and 80 Mbq for the three mice respectively – determined using the CURIEMENTOR 4 isotope calibrator (PTW Freiburg) by measuring the amount of activity in the syringe before and after injection (i.e. by measuring the remaining radioactivity in the dead space of the syringes)). For the second mouse, ^{111}In-DTPA was mixed with an extra solution of saline to control for any possible volume effects (total volume injected to be 20 ml/kg (~500 µL)). Third mouse, received an extra solution of Omniscan instead of saline to control for any possible osmolality effects. 37.5 min post injection, mice were terminally euthanised with an IP injection of pentobarbital (0.1 mL). The thoracic cavities were opened and the mice perfused fixed through the left ventricle with 15–20 mL of saline (0.9%) followed by 30 mL PFA at a flow rate of 2 mL/min. After perfusion, the animal was decapitated, the brain removed from the skull, and tissue

snap frozen in isopentane pre-chilled on dry ice. Frozen brain tissue was embedded in optimal cutting temperature compound and 150 µm sections cut using a Leica CM3050 S cryostat (specimen temperature, -18°C, chamber temperature, -22°C) onto SuperFrost® Plus microscopy slides.

5.2.2.3 Phosphor imaging plate-based digital autoradiography

Internal standards used for activity calibration were prepared by serial dilution of the ^{111}In-DTPA solution (7.8 – 1000 Bq). Brain sections and internal standards were exposed to a phosphor screen (BAS-IP MS; GE Healthcare) overnight before phosphor imaging (Typhoon 9210 instrument, GE Healthcare) for ^{111}In activity quantification. For the quantitative estimation of whole-brain tissue tracer uptake/activity, integrated density measurements were obtained (ImageJ software). For whole-brain integrated density (raw signal intensity) measurement, ROIs were manually drawing on all microscopy slides mounted with brain samples/slices. For the measurement of the integrated density (raw signal intensity) of the calibration standards (with known amounts of radioactivity), ROIs were manually drawn around each calibration dot (8 dots - serially diluted from 1000 to 7.8 Bq as mentioned). Whole-brain integrated density was then normalised by the calibration standards integrated density (by fitting a linear model to the calibration curve). Images were then pseudo coloured to provide ease of contrast visualisation (bright = high signal intensity, dark = low signal intensity).

5.2.3 Methods for CE-MRI experiments with reduced GBCA dose

All MRI and experimental methods were performed as previously described (section 4.2), except that CE-MR imaging was performed with half, third and fifth of the initial GBCA dose, that is with 5, 3 and 2 mmol/kg Omniscan (n=1 each). All data analysis was performed as previously described.

5.2.4 Methods for diffusion-weighted CE-MRI experiments

All experimental methods were performed as previously described (section 4.2). Briefly, 6 healthy male C57Bl6 mice at an age of 3 months were utilised. All subjects received a 10 mmol/kg 5 min IV bolus of Omniscan and imaging was performed for 125 minutes (12 time-points) (except one animal which was imaged for 84 minutes (8 time-points)). All data analysis was performed as previously described.

5.2.4.1 MRI methods

A 2D diffusion-weighted spin echo multi-slice sequence (DW-SEMS) with the following parameters was implemented: TR: 1300 ms, TE: 22.35 ms, Diffusion

crusher/*b*-value: 199.04 s/mm^2, Diffusion gradient separation: 10.80 ms, Diffusion gradient duration: 2.4 ms, Diffusion gradient amplitude: 18 G/cm, Matrix size: 96 x 96, FOV: 12.8 x 12.8 mm, Resolution: 0.13 x 0.13 mm, Slices: 35, Thickness: 0.3 mm, Averages: 5, Acquisition time: 10 minute 24s.

5.3 Results

5.3.1 High-resolution LA-ICP-MS imaging of VECTOR pathway

LA-ICP-MS interrogation was conducted in brain samples of 3 healthy mice for the high spatial resolution characterisation of the GBCA uptake pattern in the brain tissue following IV delivery, unconfounded by systemic effects (i.e. no intravascular signal contributions). Here, there were no signal contributions from intravascular GBCA as perfusion of the animal with saline, washes out all the intravascular GBCA (Gage, Kipke and Shain, 2012). Hence, in theory, any signal hyperintensity seen on the images, can be solely attributed to the extravascular presence of GBCA (i.e. brain tissue uptake). LA-ICP-MS analysis of the brain samples 37 mins post IV delivery, revealed GBCA uptake in the brain evident by signal hyperintensity in the ventricular and also the periventricular regions of the brain (figure 5.1). Signal hyperintensity could also be observed in brain regions distant from the ventricular spaces. Interestingly, signal hyperintensity could be observed around the edges (surface) of the brain which possibly represents subarachnoid/perivascular CSF/GBCA influx into the brain (figure 5.1).

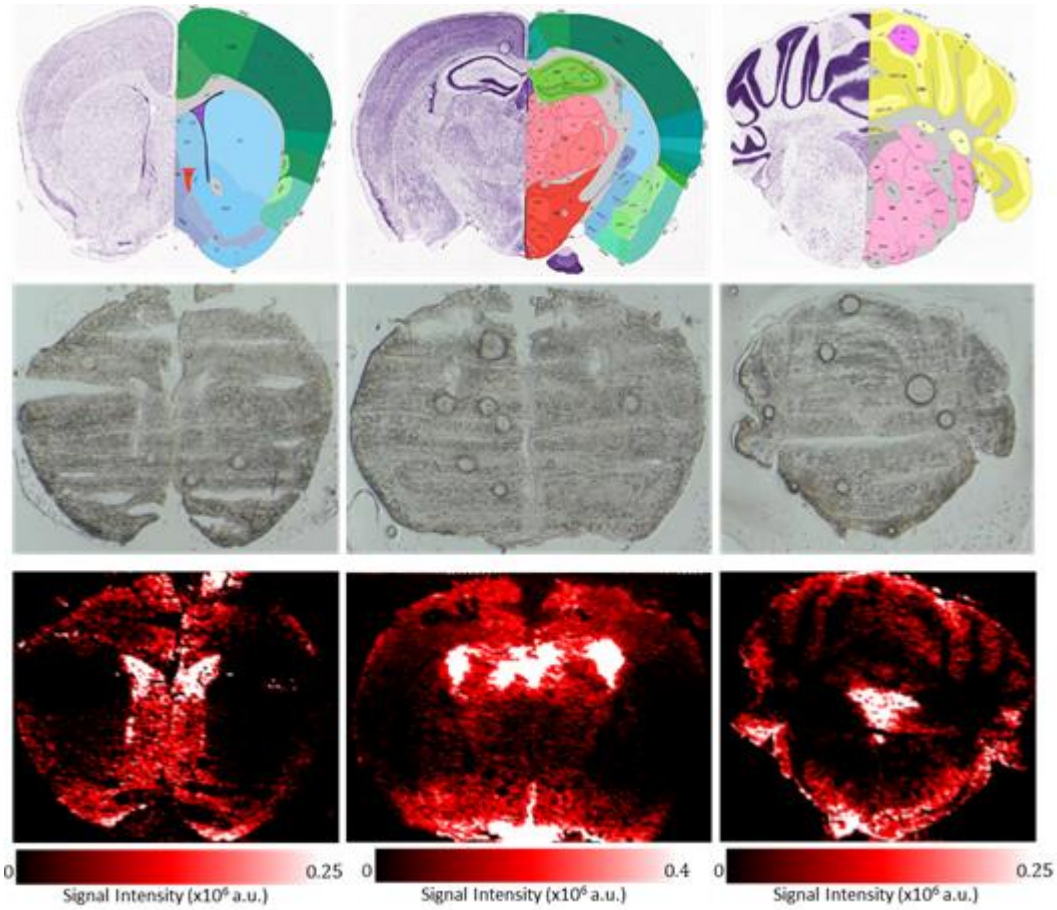

Figure 5.1: LA-ICP-MS analysis (50 µm resolution) of brain samples 37 mins post IV delivery (bottom row) revealed GBCA uptake primarily in the ventricular and the periventricular brain regions. GBCA uptake was also evident around the edges of the brain and in locations distant from the ventricular spaces. The corresponding anatomical locations (from Allen mouse brain atlas) and the raw brain tissue samples are also displayed to aid visualisation (top and middle rows respectively).

When the brain samples underwent LA-ICP-MS interrogation 120 mins post IV delivery (figure 5.2), a more brain wide GBCA presence could be observed (compared to the images at 37 mins post injection – figure 5.1) with the greatest signal hyperintensity also in the ventricular/periventricular regions (figure 5.2). The more brain-wide spreading of signal hyperintensity from 37 mins to 120 mins is suggestive of a dynamic progression of GBCA in the brain and provides further evidence regarding the physiological exchange of CSF with ISF (i.e. solute transport). LA-ICP-MS analysis of the brain of the mouse receiving saline (control - figure 5.3, 5.4), demonstrated negligible GBCA presence in the brain tissue (approximately x1000 less – figure 5.3, 5.4).

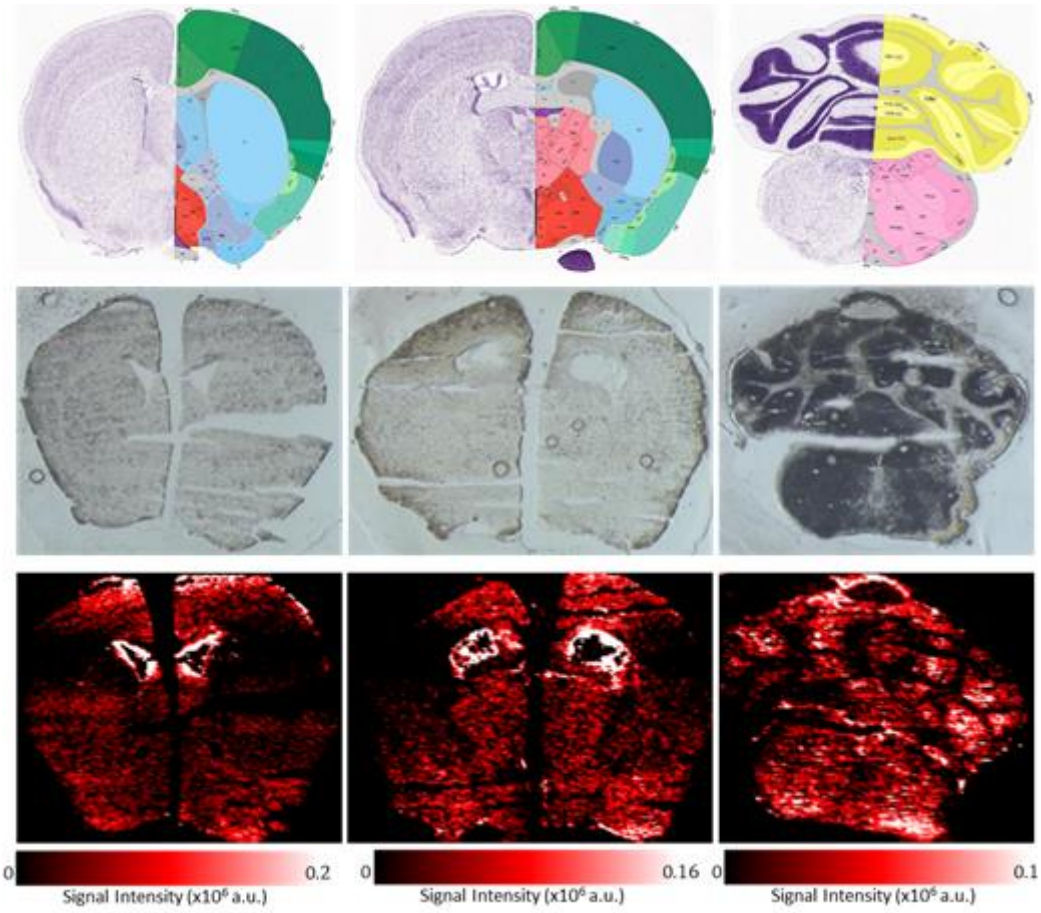

Figure 5.2: LA-ICP-MS analysis (50 µm resolution) of brain samples 120 mins post IV delivery (bottom row) revealed a more brain-wide GBCA uptake (compared to images at 37 mins post injection – figure 5.1), suggestive of a dynamic progression of GBCA in the brain (i.e. evidence for solute transport). The greatest signal hyperintensity was attributed to the ventricular/periventricular regions as before. The corresponding anatomical locations (from Allen mouse brain atlas) and the raw brain tissue samples are also displayed to aid visualisation (top and middle rows respectively).

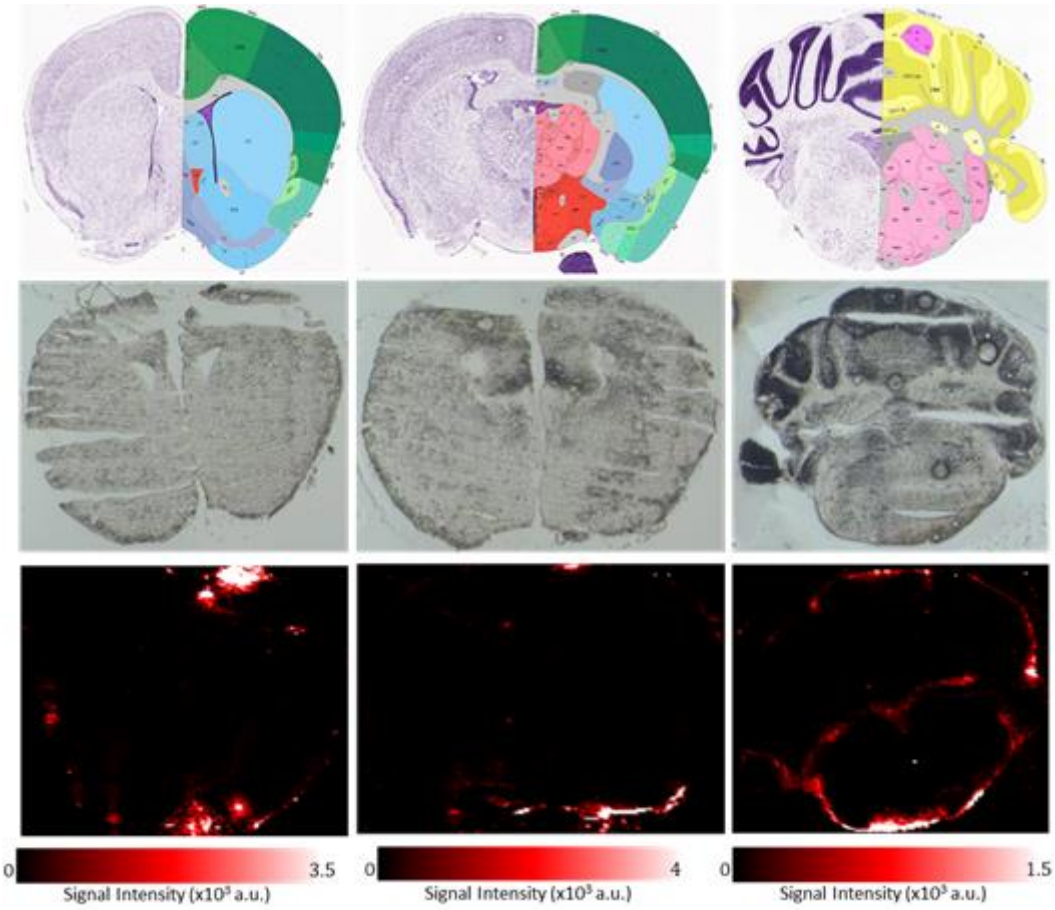

Figure 5.3: LA-ICP-MS analysis (50 µm resolution) of brain samples of the mouse receiving IV saline (i.e. control) 37 mins post injection revealed only traces of gadolinium in the brain (bottom row). Note that the colour bars are 3 orders of magnitude smaller than the colour bars associated with the animals who received IV GBCA. The corresponding anatomical locations (from Allen mouse brain atlas) and the raw brain tissue samples are also displayed to aid visualisation (top and middle rows respectively).

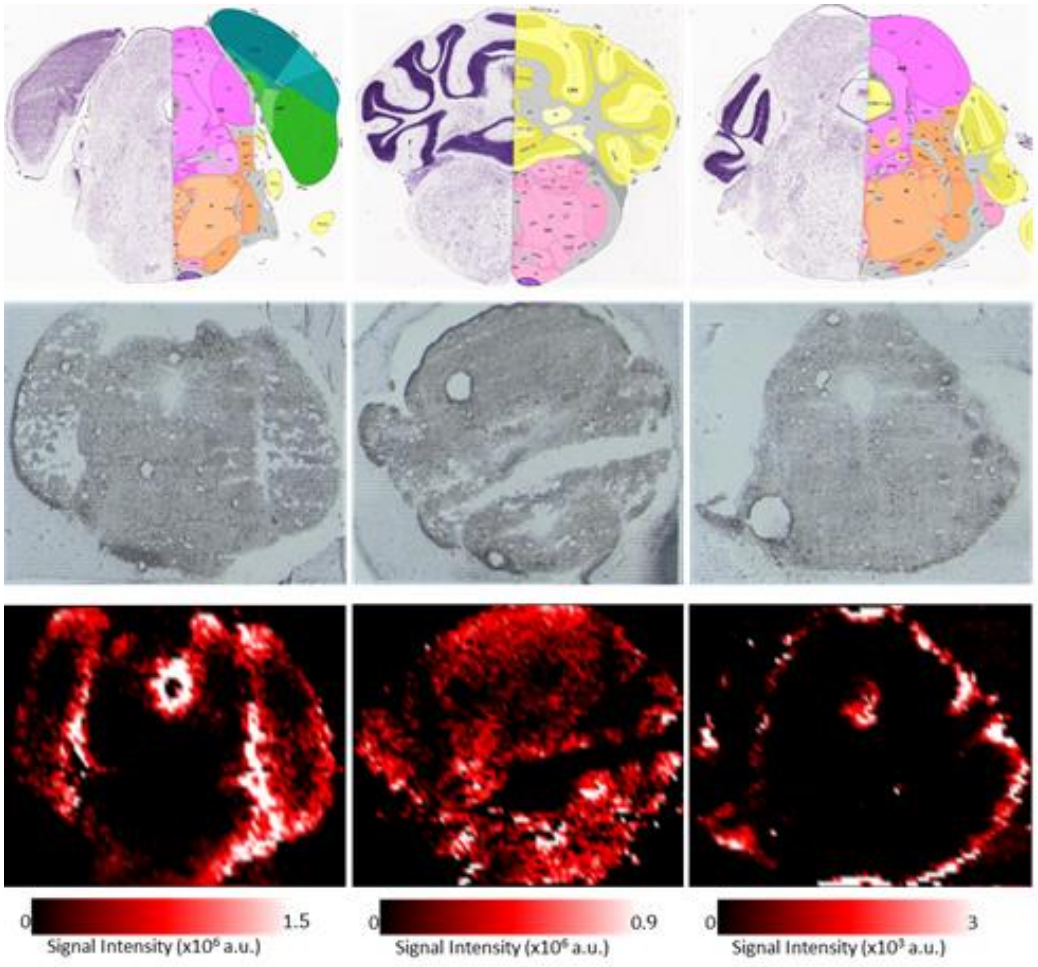

Figure 5.4: LA-ICP-MS interrogation of brain slices corresponding to mice 1, 2 and 3 (left, middle and right columns respectively) at 100 µm resolution (instead of 50 µm). Gadolinium detected in the control mouse brain (i.e. saline treatment) was approximately 1000 times less (3 orders of magnitude) than the brains of mice who received IV GBCA. The corresponding anatomical locations (from Allen mouse brain atlas) and the raw brain tissue samples are also displayed to aid visualisation (top and middle rows respectively).

The LA-ICP-MS analyses was concordant with the previous MRI findings as a similar pattern of GBCA uptake could be observed. Both imaging modalities revealed the greatest signal hyper-intensity in the ventricular system and the parenchymal periventricular regions (figure 5.5). As mentioned in chapter 3 (section 3.6), the MRI platform suffers from a lowered sensitivity due to the negative contrast that is induced in the intravascular compartment. As a result, it was suggested that MRI signal increase due to GBCA presence/uptake may have been attenuated (or even masked), specifically in regions close to dense vascular networks such as subarachnoid spaces and perivascular spaces (Hirano, Cervós-Navarro and Ohsugi,

1976, Zhang, Inman and Weller, 1990). Figure 5.5 supports this summation as the signal hyperintensity around the edges (surface) of the brain (which possibly represents subarachnoid CSF/GBCA influx) on the LA-ICP-MS images was not observed on the MR images. Hence, as previously described, the MR images display a rather conservative pattern of CSF-ISF exchange (i.e. some false negatives are anticipated - that is the MR images fail to reveal brain tissue GBCA uptake in some regions where GBCA is indeed present), but nonetheless the spatial patterns are highly consistent with an independent imaging technique (LA-ICP-MS – figure 5.5).

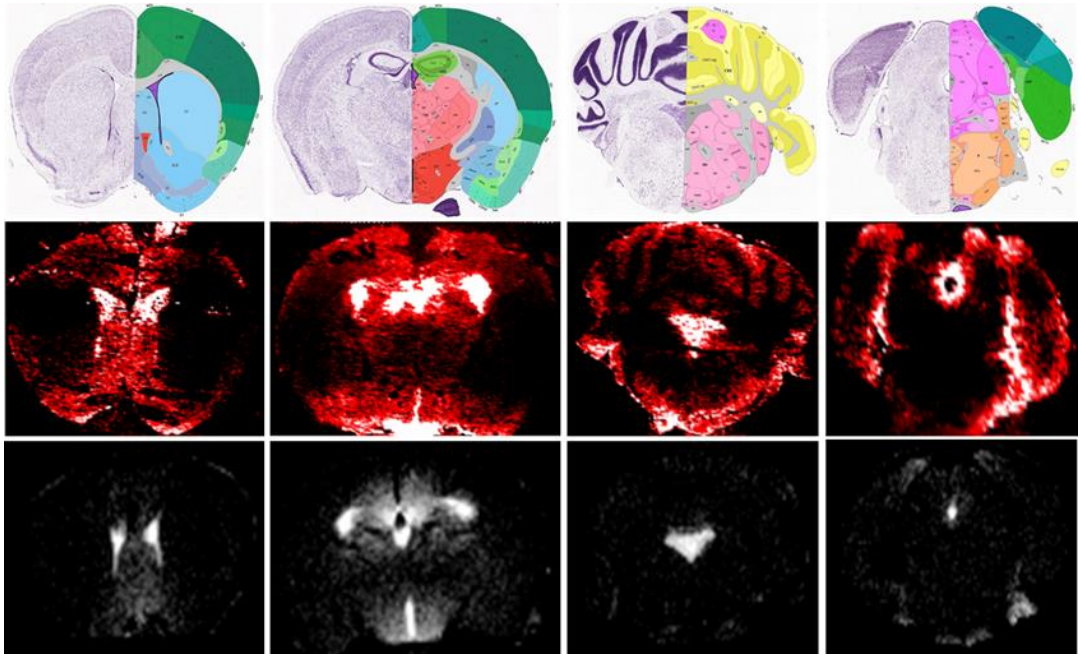

Figure 5.5: LA-ICP-MS (middle row) and thresholded subtraction T_1-weighted MR (bottom row) images of the mouse brain 37 mins post IV delivery of GBCA. Both imaging modalities demonstrated GBCA uptake in the ventricular and periventricular regions of the brain. Further brain-wide GBCA transport is also observed on the MR images however this is more readily observed on the LA-ICP-MS images due to the higher sensitivity of the technique. LA-ICP-MS images also demonstrate signal hyperintensity around the edges of the brain which possibly represents subarachnoid/perivascular CSF/GBCA influx into the brain (an element that cannot be observed on the MR images). Overall, both imaging modalities provided similar spatial patterns as evidence for the physiological exchange of CSF with ISF. The corresponding anatomical locations (from Allen mouse brain atlas) are also displayed (top row).

5.3.2 Phosphor imaging plate-based digital autoradiography assessment of VECTOR pathway

The LA-ICP-MS analyses of mouse brains provided high-resolution characterisation of brain tissue GBCA uptake following IV delivery. However, for a more complete characterisation of the VECTOR pathway, quantitative information is needed regarding actual brain tissue GBCA concentration/uptake as LA-ICP-MS is only a qualitative measure. Hence, for the quantitative estimation of whole-brain tissue GBCA uptake, autoradiography was performed. Also, in order to ensure the previous MRI (and LA-ICP-MS) results are not confounded by the relatively high GBCA dose (e.g. BBB disruption due to osmolality effects), a more clinically relevant tracer dosage was adopted. In autoradiography, similar to LA-ICP-MS, there are no blood vessel signal contributions as perfusion with saline clears all the radioactive tracers in the blood vessels. Hence any signal hyperintensity seen on the raw images can be attributed to extra-vascular, brain tissue tracer uptake. All three animals demonstrated brain-wide tracer uptake following digital autoradiography with ^{111}In-DTPA, evident by the signal hyperintensity observed on the raw images (figure 5.6 – dark regions). VECTOR pathway was further validated using this independent imaging technique as the pattern of brain tissue contrast uptake was comparable to the MRI (and LA-ICP-MS) findings 37 mins post contrast injection in all animals, despite the lower ^{111}In-DTPA dose (i.e. greatest hyperintensity demonstrated in the periventricular regions (figure 5.7)). The relatively weaker signal observed in the ventricles (compared to the periventricular regions), is due to the escape/loss of CSF from the ventricles as perfusion fixation with PFA causes shrinkage/collapse of the ventricles. Autoradiography images also demonstrated hyperintensities around the edges (surface) of the brain (similar to the LA-ICP-MS images (figure 5.5)), which could be representative of the subarachnoid CSF/tracer influx into the brain parenchyma (an element that could not be observed on the MR images as discussed above).

Despite the inherently limited spatial resolution of the autoradiography images (and the associated blurring effect), an attempt was made for quantitative estimation of whole-brain tissue tracer uptake. Whole-brain tracer uptake/activity was calculated by normalising the integrated density obtained from all the brain slices by the integrated density obtained from the calibration standards (by fitting a linear model to the calibration curve). Images were then pseudo coloured to provide ease of contrast visualisation for comparison to adjacent histological slices (figure 5.7). Whole-brain

tracer uptake 37 mins post injection was calculated to be 109, 86 and 77 Kbq in the three mice respectively (approximately 0.1 % of the total volume injected).

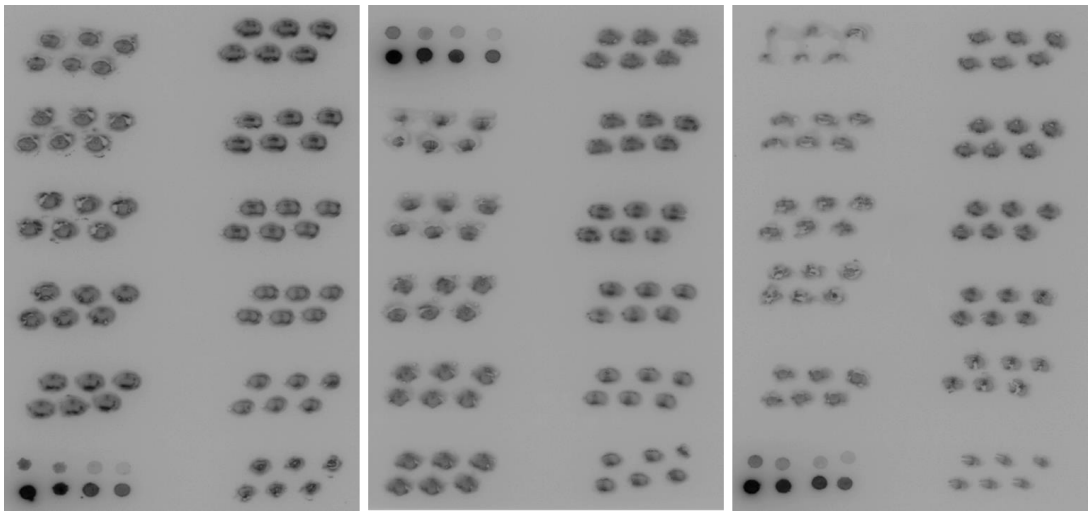

Figure 5.6: Phosphor imaging plate-based digital autoradiography of VECTOR pathway 37 mins post IV GBCA (raw data - left: mouse1, middle: mouse2, right: mouse3). All 3 animals displayed brain-wide tracer uptake evident by the marked signal hyperintensity (dark regions). In each image, the sub-panel with 8 hyperintense drops represents the calibration standards.

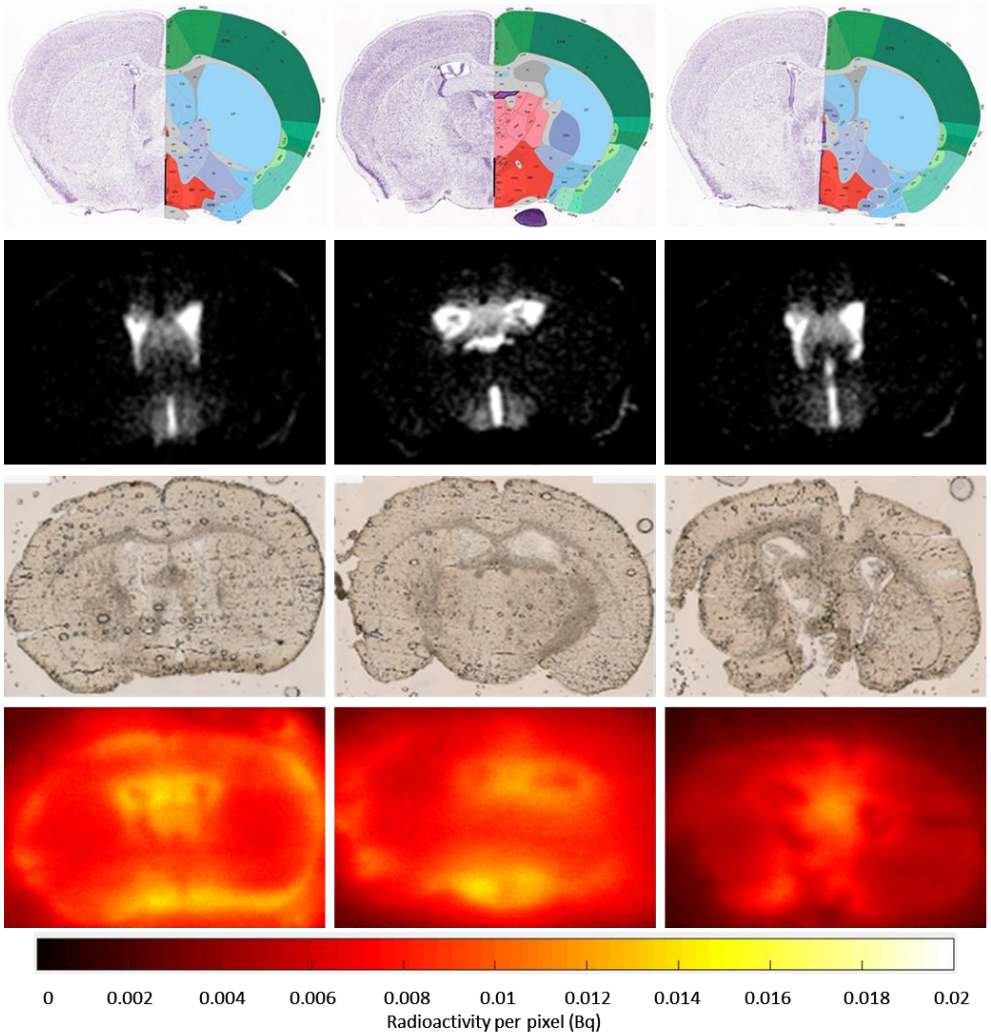

Figure 5.7: Digital autoradiography with ^{111}In-DTPA (bottom row) demonstrated a similar pattern of contrast uptake and was comparable to the MRI findings (2nd row) at 37 minutes post injection. Autoradiography images are normalised (to injected activity), pseudo coloured and magnified (mouse 1 (left), mouse 2 (middle) and mouse 3 (right)). Images are centred on the ventricular/periventricular regions and acquired 37 minutes post contrast injection. The corresponding anatomical locations (from Allen mouse brain atlas) and the raw brain tissue samples are also displayed to aid visualisation (1st and 3rd rows respectively).

5.3.3 Imaging VECTOR with more clinically relevant MRI contrast agent dose

The VECTOR pathway was originally identified from a CE-MRI platform with relatively high GBCA dose (10 mmol/kg). Clinical translation of such high dose would likely be considered unethical due to the recent safety concerns of gadolinium retention in the brain. Hence, here attempts were made to reduce the GBCA dose. Additionally, the

integrity of BBB had been questioned following delivery of such high GBCA dose (due to osmolality effects) (Zamani *et al*., 1982). An additional aim of these experiments was therefore to address this concern and to ensure the same pattern of GBCA uptake/inflow would be seen following imaging with a lower GBCA dose (i.e. uptake pattern is not exaggerated by the high dose due to possible BBB disruption). CE-MRI experiments with 5 and 3 mmol/kg Omniscan, demonstrated a similar pattern of contrast uptake and was comparable to the original description of the VECTOR pathway (10 mmol/kg dose). That is, GBCA transfer from the circulation into the ventricles and subsequent ingress into the periventricular regions (evident by the signal hyperintensity seen in the ventricles and the periventricular regions – figure 5.8).

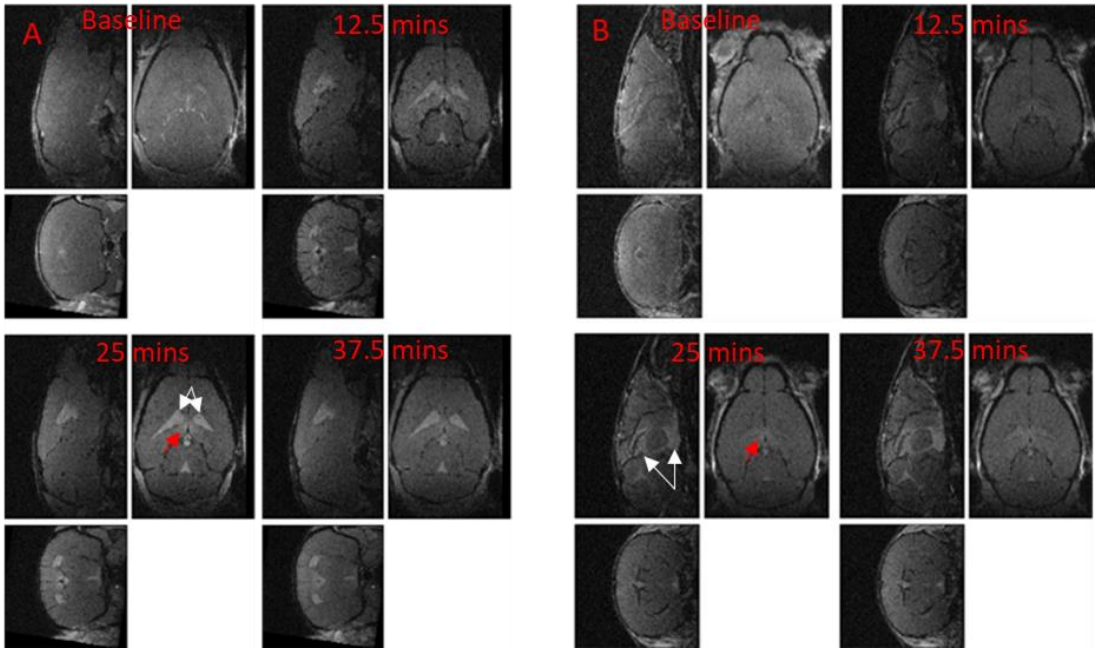

Figure 5.8: VECTOR pathway was imaged with half and a third of the initial GBCA dose (i.e. CE-MRI with 5 (A) and 3 (B) mmol/kg Omniscan) and revealed a pattern of contrast ingress into the brain, that was similar to the original description of VECTOR pathway (i.e. transfer of systemic GBCA to the ventricles and subsequent ingress into the periventricular regions). White arrows point to an example ventricular ROI (lateral ventricles) and red arrows point to an example periventricular region (on the 25 mins post injection images of each subject).

Inspection of the raw images however (figure 5.8), demonstrated lower GBCA uptake compared to the initial high dose imaging of VECTOR pathway (i.e. weaker signal hyperintensity). Hence, in order to enhance the visibility of brain tissue GBCA uptake on T_1-weighted images, thresholded subtraction images were created as previously

described (figure 5.9). In addition, the images were smoothed (SPMs smooth routine) using a Gaussian kernel (Full Width Half Maximum (FWHM) of 2 voxels) in order to improve SNR and suppress noise.

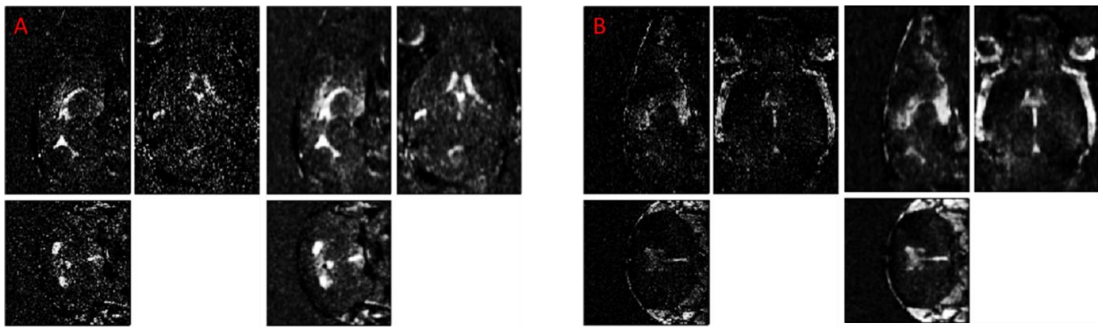

Figure 5.9: VECTOR pathway imaging with 5 (A) and 3 (B) mmol/kg Omniscan (37 minutes post contrast injection). Smoothing the thresholded subtraction images (left) with a gaussian kernel (FWHM of 2 voxels) enhanced the quality of the images (right).

Smoothing the thresholded subtraction images with a gaussian kernel (FWHM of 2 voxels) greatly enhanced the quality of the images. Signal intensity time-courses derived from these images (i.e. ROI analysis), also demonstrated GBCA uptake in different brain regions as expected (figure 5.10).

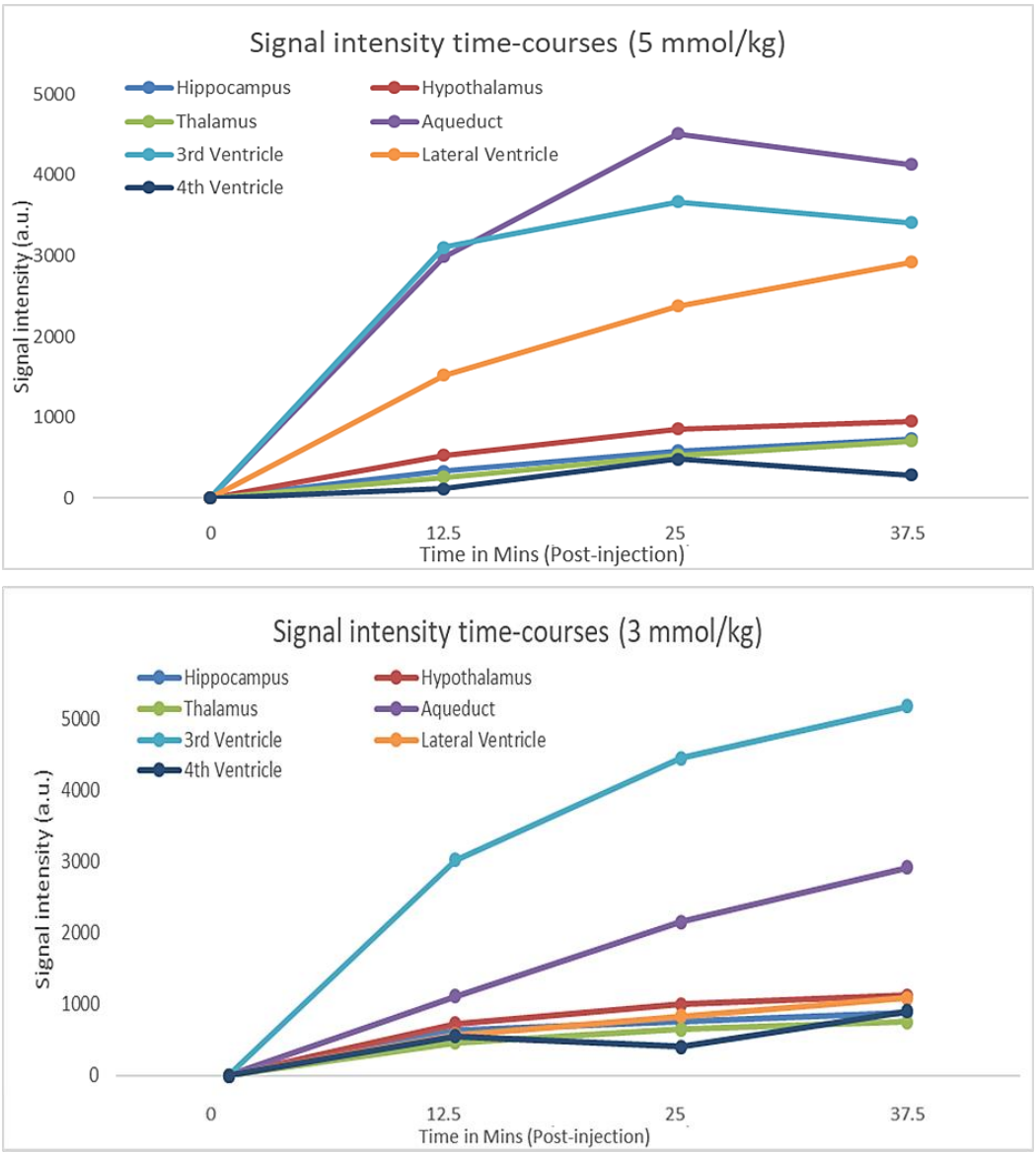

Figure 5.10: Signal intensity time-courses derived from the thresholded subtraction images (5 (top) and 3 (below) mmol/kg Omniscan experiments). Despite lower GBCA dose (compared to initial experiments with higher GBCA dose – 10 mmol/kg), ROI analysis from 7 different brain regions revealed a brain-wide GBCA uptake.

The 3 mmol/kg dose of Omniscan, was the lowest amount of dose that could induce negative contrast (relative to baseline) in the intravascular compartment (i.e. the lowest dose that allowed differentiation of GBCA-induced signal changes that originate from GBCA in the tissue versus the signal changes that originate from GBCAs in the intravascular compartment – section 3.3.4.2). Upon inspection of the veins and arteries it was realised that a dose of 2 mmol/kg was not able to induce sufficient susceptibility effects in the intravascular compartment as the concentration of GBCA was not high enough (i.e. no negative contrast relative to baseline as signal

reducing T_2* effects did not dominate the signal enhancing T_1 effects). Since the intravascular compartment signal demonstrated a signal enhancement (i.e. positive contrast) post GBCA injection (similar to the extravascular compartment signal), partially differentiating GBCA-induced signal changes that originate from GBCA in the tissue versus the signal changes that originate from GBCAs in the intravascular compartment, and therefore characterisation of brain tissue GBCA uptake was not possible (red circles - figure 5.11). Hence the data from this experiment were excluded from further analysis.

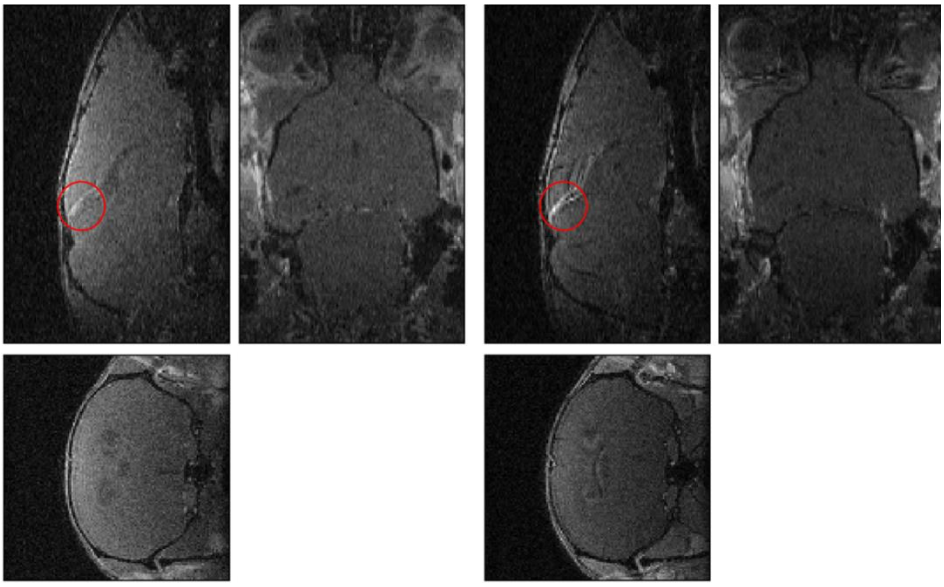

Figure 5.11: VECTOR pathway imaging attempted with 2 mmol/kg Omniscan. Due to the low GBCA dose administrated, signal in the intravascular compartment (red circles) increases post contrast injection (baseline (left) and 12 min post injection (right) images). Since both intravascular and extravascular compartment signals demonstrate signal enhancement post injection, a meaningful characterisation of brain tissue GBCA uptake was not possible.

5.3.4 Extended imaging of the VECTOR pathway – a diffusion-weighted MRI sequence

VECTOR pathway imaging window has been limited to 37 mins post contrast injection because differentiating GBCA-induced signal changes that originate from GBCA in the tissue versus the signal changes that originate from GBCAs in the intravascular compartment, and therefore meaningful characterisation of brain tissue GBCA uptake is not possible after this time (due to GBCA clearance and the following enhancement in intravascular signal intensity – section 3.3.4.2). Here, a diffusion-weighted MRI sequence was implemented that aimed to minimise the intravascular signal

contributions that would enable VECTOR imaging beyond 37 mins post contrast injection.

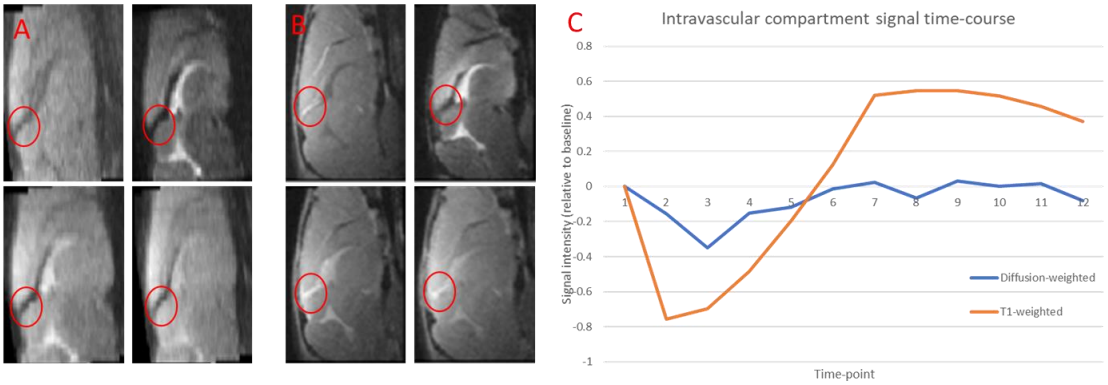

Figure 5.12: The DW-SEMS sequence markedly diminished the intravascular compartment signal (A) compared to the T_1-weighted sequence used thus far (B). The highlighted region (red circle) demonstrates a blood vessel from which the signal has been nulled. Group averaged images correspond to the baseline, 4th, 8th and the 12th time-points (note the duration of time-points is ~ 2 mins lower in the DW-SEMS sequence compared to the T_1-weighted sequence). Representative average DW-SEMS intravascular time-course (normalised to baseline) is shown in blue (for the entire imaging time (125 min)). The orange line represents that of the T_1-weighted sequence (C).

The implemented DW-SEMS sequence suppressed the signal from blood vessels by the application of diffusion crushers (figure 5.12A). Figure 5.12A demonstrates that the intravascular compartment signal (red circles) was suppressed throughout the entire duration of the experiments (125 minutes) whereas the intravascular signal from the T_1-weighted sequence used thus far, demonstrates a time-varying signal behaviour (figure 5.12B). The representative intravascular signal time-courses (figure 5.12C) further demonstrates that the signal from the blood vessels had been nulled significantly in the DW-SEMS sequence compared to the T_1-weighted sequence used thus far. The slight offset/deviation from zero in the DW-SEMS intravascular time-course could be attributed to PVEs from the neighbouring parenchymal tissues due to relatively low spatial resolution of the sequence (0.1 x 0.1 x 0.3 mm). For example, the negative offset in the earlier time-points (2-4), could be due to susceptibility effect that is extended to (neighbouring) regions outside the blood vessels (due to high concentration of GBCA in the blood vessels - section 3.6, figure 3.15).

Imaging VECTOR pathway with the developed DW-SEMS sequence revealed a similar pattern of contrast agent uptake and was comparable to the conventional 3D

T_1-weighted MR images of VECTOR pathway up to approximately 37 mins post injection (i.e. in the first 4 time-points - note the duration of time-points is ~ 2 mins lower in the DW-SEMS sequence compared to the T_1-weighted sequence), providing further confidence of the VECTOR pathway dynamics (figure 5.15). I observed accumulation of systemic GBCA in the ventricular system and subsequent ingress into the periventricular regions, evident by marked signal hyperintensity in these regions (figure 5.15). The penetration of GBCA into the brain tissue (immediately proximal to the ventricles) was followed by further brain-wide distribution of GBCA as seen before. DW-SEMS sequence allowed VECTOR pathway imaging beyond time-point 4 (37 mins post injection) by nulling of the intravascular compartment and revealed a much more profound global distribution of GBCA at these later time-points (figure 5.14).

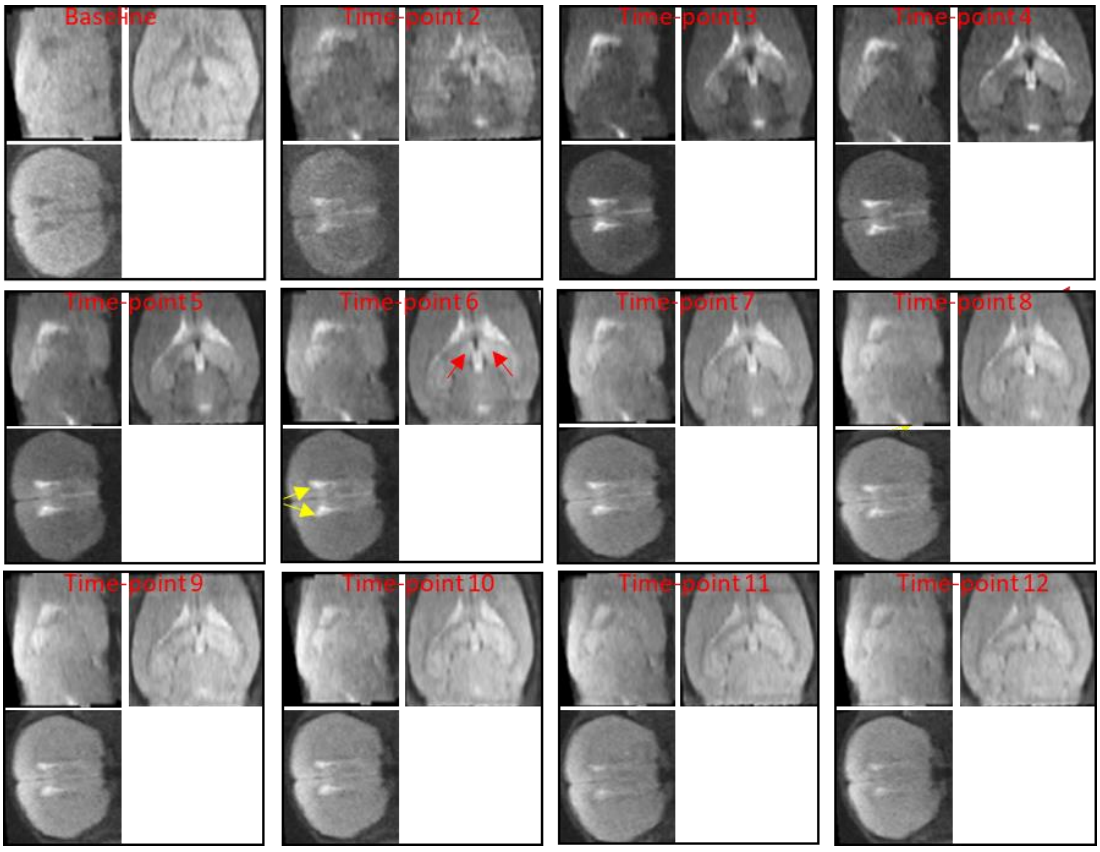

Figure 5.13: Group averaged raw DW-SEMS images (n=5) corresponding to the entire duration of imaging (125 mins, time-points 1-12). Similar to the conventional T_1-weighted MR images of VECTOR pathway, the raw DW-SEMS images also demonstrate signal intensity enhancement in the ventricular/periventricular regions of the brain following systemic GBCA delivery. Yellow arrows point to an example ventricular ROI (lateral ventricles) and red arrows point to an example periventricular region (on the 6th time-point images).

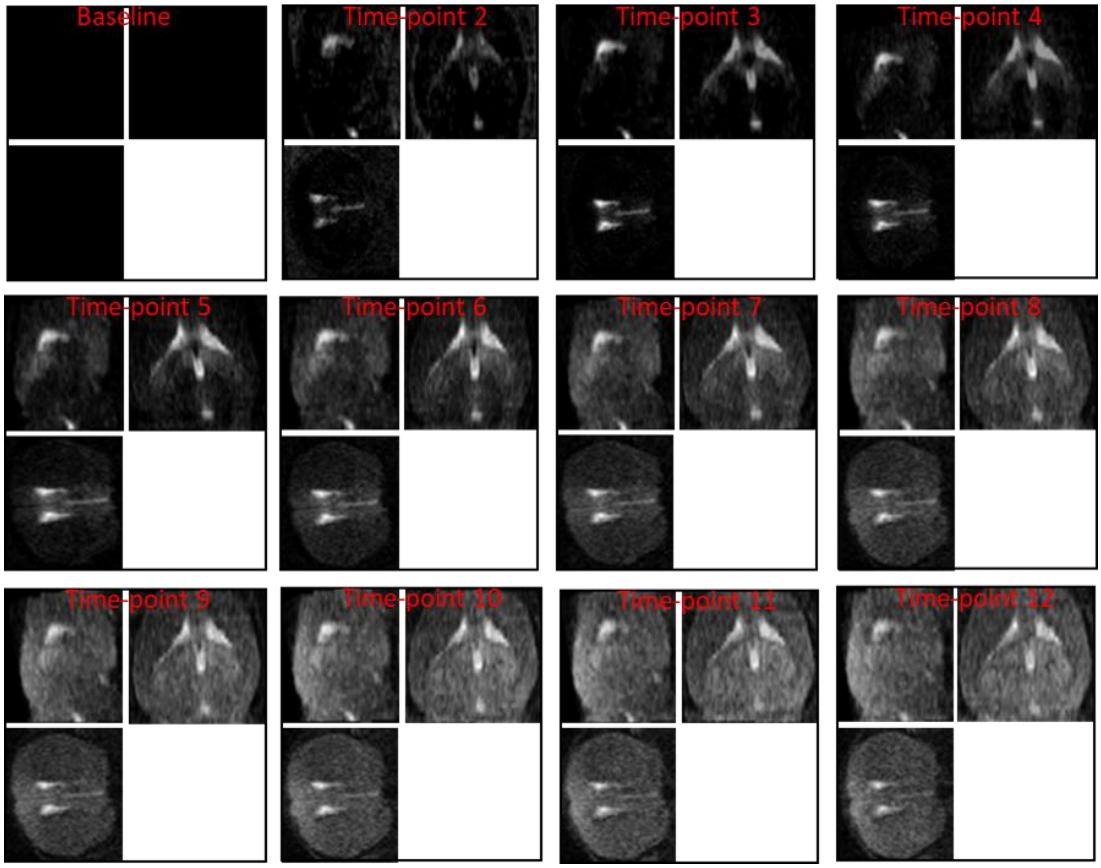

Figure 5.14: Group averaged DW-SEMS thresholded subtraction images for the entire duration of the imaging (12 time-points – 125 mins). Extended imaging of VECTOR pathway beyond 37 mins post injection (i.e. beyond time-point 4), revealed a more profound global GBCA uptake compared to the uptake seen in the earlier time-points.

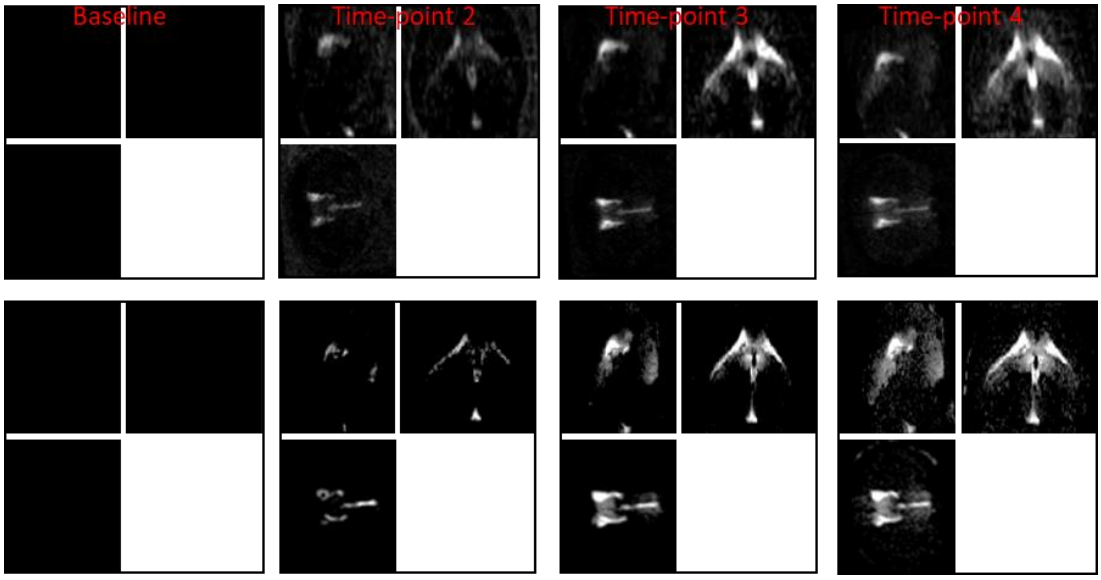

Figure 5.15: Group averaged DW-SEMS (top row) and T_1-weighted (bottom row) thresholded subtraction images. The two independent MRI sequences captured a

similar pattern of GBCA uptake in the brain (first 4 time-points - up to 37 mins post contrast injection).

Prior to this stage, only the infiltration/entry of GBCA into the brain was characterised and no insight was provided regarding the clearance/egress of GBCA from the brain. Extended imaging of the VECTOR pathway using the DW-SEMS sequence facilitated this opportunity and provided insight regarding the clearance of GBCA from the brain (assuming negligible intravascular signal contribution due to the presence of the diffusion crusher gradients (figure 5.16)). From the CSF time-courses it can be seen that the peak signal intensity in CSF spaces is reached at time-point 4/5 (~ 40 minutes post injection - figure 5.16B). After time-point 4/5 a gradual decrease in signal intensity is evident which corresponds to the clearance of GBCA from the ventricles. The clearance phase of parenchymal brain regions on the other hand lags behind the CSF regions and occurs about 80 minutes post injection (~ time-point 9 - figure 5.16C). Although the clearance phase was not completed during the imaging time (125 minutes), an exponential model fitting provided estimated clearance times for both CSF and parenchymal regions. Following fitting a one-term exponential model, the elimination half-life (50% clearance time) was estimated to be approximately 100 minutes and 7 hours for CSF and tissue regions respectively (supplementary material 5.7.1).

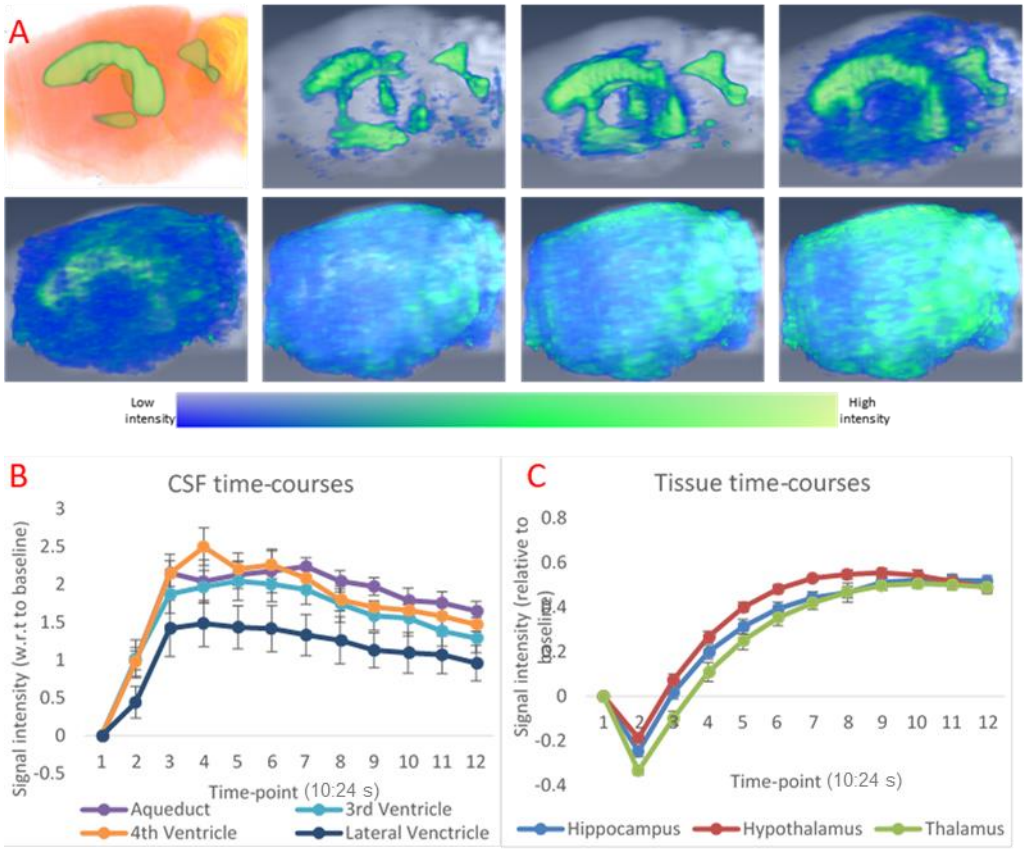

Figure 5.16: 3D rendering (Digitally Reconstructed Radiograph - DRR) of the averaged DW-SEMS images (A - time-points 1-8). The pattern of contrast uptake is consistent with the previous T_1-weighted MR image renderings in the first four time-points (up to 37 mins post injection - figure 4.16). At later time-points a more brain-wide tracer uptake is revealed by the new sequence that could not be visualised by the T_1-weighted images. Average DW-SEMS signal intensity time-courses derived from CSF and parenchymal brain regions (B & C respectively). GBCA uptake/infiltration is evident in all 7 brain regions analysed. Additionally, the time-courses provide insight regarding the clearance of GBCA from the brain. Complete clearance of GBCA however is not achieved during the imaging time.

Despite nulling the intravascular compartment signal, the sequence suffers from the susceptibility effect that extends beyond the blood vessels (i.e. around the edges of the blood vessels). In theory, this sequence only nulls the signal from the intravascular compartment but is still vulnerable to the susceptibility that extends beyond the intravascular compartment (i.e. around the edges of the blood vessels). This susceptibility effect is more clearly observed in the early time-points of the parenchymal time-courses (e.g. time-point 2 – figure 5.16C) where the concentration of GBCA is relatively high in the blood vessels. The sequence therefore suffers from reduced sensitivity to brain tissue GBCA uptake due to PVEs from these extended

susceptibility effects. However, these susceptibility effects are believed to be markedly reduced compared to the traditional T_1-weighted sequence used thus far as the DW sequence relies on T_2 relaxation (as opposed to T_2* in the T_1-weighted sequence).

5.4 Discussion

In chapter 4, the VECTOR pathway was identified from a non-invasive, relatively high-dose GBCA-enhanced MRI platform. Here, in order to validate the VECTOR pathway and to ensure results are not confounded by the time-varying intravascular effects (due to PVEs) and also the relatively high GBCA dose of the MRI platform (due to possible BBB disruption), independent confirmatory imaging techniques were devised. LA-ICP-MS is a powerful analytical technique for mapping element distribution in the brain. In this high-resolution imaging technique (laser spot size as low as 4μm), prior to brain dissection and slicing for laser ablation, the animals are perfused with saline (to wash out all the remaining blood), hence unlike the MR images, there are no contributions from the intravascular compartment signal and all the hyperintensities seen on the images can be attributed to actual brain tissue tracer uptake. LA-ICP-MS interrogation of the brain of the mice receiving IV GBCA, demonstrated a similar spatial pattern and was comparable to the original T_1-weighted images of VECTOR pathway. These findings confirmed that the MR images were not confounded by the time-varying intravascular effects in that there were no false positive effects, as hypothesised.

Interestingly, the brain of the mouse which did not receive IV GBCA, also demonstrated traces of gadolinium. This finding was rather surprising as no gadolinium was expected to be seen in this brain. LA-ICP-MS interrogation is a very sensitive technique and gadolinium traces were detected in this brain by LA-ICP-MS, albeit significantly lower amount compared to the animals who received the IV GBCA (approximately x1000 less – figure 5.4). The traces of gadolinium observed in the brain of this animal could be attributed to the cross-contamination of the brain slices, perhaps during the slicing process, although I believe this to be unlikely. A more plausible explanation for the presence of gadolinium traces in the brain, could be the presence of gadolinium in the food chain of the animals. In fact, Kulaksız and Bau (Kulaksız and Bau, 2011) found a considerable amount of anthropogenic gadolinium in municipal tap water from Thames river (London's drinking water) (Ebrahimi and Barbieri, 2019). Although the FDA has not identified adverse health effects from gadolinium retained in the brain, the potential long-term effects of low-dose

gadolinium retention is not known. Hence, it would be interesting to know the gadolinium species in our drinking water (i.e. chelated or bound to other chemical species as free ion), as free gadolinium ion is highly prone to off-site binding and retention. However, a limitation of LA-ICP-MS is that it cannot distinguish between different gadolinium forms and hence development of analytical techniques that would allow gadolinium speciation would aid understanding of gadolinium presence in the brain (Jost *et al*., 2017).

Next, in order to ensure the MR images are not confounded by the relatively high GBCA dose (due to possible BBB disruption), a confirmatory technique was devised that would allow more clinically relevant tracer dosage to be administered. Autoradiography is highly sensitive to small amounts of radioactivity (^{111}In-DTPA in this study) in an image, hence more clinically relevant tracer dosage can be delivered to image CSF-ISF exchange. Indeed, a similar pattern of contrast agent uptake (to the MRI and LA-ICP-MS images) was seen on the autoradiography images despite the relatively lower dose/volume (5x less) of tracer that was delivered (20 versus 4 ml/kg). In autoradiography, similar to LA-ICP-MS, the animal is perfused with saline prior to brain sample analysis, hence there are no contributions from the time-varying intravascular effects, further confirming VECTOR pathway dynamics.

Autoradiography, despite being an invasive, ionizing, low-resolution and single time-point technique, was an appropriate imaging technique to validate the MR images for several reasons; a) sensitivity (and independent of intravascular signal contributions) which allowed VECTOR imaging with more clinically relevant tracer dose, b) both MRI and autoradiography used similar molecular weighted tracers (^{111}In-DTPA is essentially the autoradiography equivalent of Gd-DTPA which is used in MR imaging – both ions have a charge of 3+ and essentially the gadolinium ion is principally replaced with indium ion in autoradiography) and c) it is a quantitative technique and allowed quantitative estimation of brain-wide GBCA uptake (0.1% of injected volume).

In the original definition of VECTOR pathway (chapter 4), the main transport route of systemic GBCA into the brain parenchyma appeared to be via the ventricular system, and subarachnoid/perivascular CSF/GBCA influx into the brain parenchyma was not readily identified (a defining element of the glymphatic pathway (Iliff *et al*., 2012)). Evidence for the importance of this transport route was not diminished by these data but instead, it suggested that this transport route could have been ‘masked’ on the MR images due to limited spatial resolution and also lowered sensitivity as a result of intravascular-derived susceptibility effects. Moreover, surface coil sensitivity

limitations (decreasing with increasing distance from the coil) may contribute to the non-appearance of this transport route on the MR images (e.g. lack of tissue GBCA uptake in the caudal MRI slices - figure 5.5, third column). LA-ICP-MS and autoradiography images suggested that this was the case as the observed signal hyperintensities around the edges (surface) of the brain (which possibly reflects glymphatic related subarachnoid/perivascular CSF/GBCA influx), could not be observed on the MR images (figures 5.1, 5.5 and 5.7). The subarachnoid/perivascular CSF/GBCA influx into the brain parenchyma, may therefore represent an alternative pathway, important in CSF-ISF exchange dynamics.

CE-MRI with both 5 and 3 mmol/kg Omniscan validated the initial VECTOR findings as a similar pattern of contrast agent uptake could be observed (that is, the infiltration of systemic GBCA into the ventricular system and subsequent penetration into selected parenchymal regions (i.e. periventricular regions)). A brain-wide GBCA uptake was also observed (e.g. in the thalamus region) but not as readily as that observed in the higher dose platform (which is expected due to lower amount of tissue GBCA uptake). Optimising the MRI sequence and the data analysis pipeline even further to achieve greater SNR/sensitivity for detection of lower amounts of GBCA uptake would be an avenue of future investigation (e.g. increasing the number of MR averages/acquisitions (for the cost of lower temporal resolution however)). Here, image post processing (smoothing with a gaussian kernel) did improve SNR and aided visualisation of brain tissue GBCA uptake. A dose of 2 mmol/kg, however, could not differentiate GBCA-induced signal changes that originate from GBCA in the tissue versus the signal changes that originate from GBCAs in the intravascular compartment (as the concentration of intravascular GBCA was relatively low, negative contrast (relative to baseline) was not induced in the intravascular compartment (section 3.3.4.2)). Hence, the lowest amount of dose that could identify the VECTOR pathway in this study, was 3 mmol/kg (which is only 2.5 times higher than the standard clinical dose based upon body surface area normalisation (Nair and Jacob, 2016)).

As previously described, the integrity of the blood brain barrier following the initial higher GBCA dose had been questioned (due to possible BBB disruption as a result of increase in plasma osmolality). However, confirmatory experiments with more clinically relevant doses (detailed above) suggested that this is unlikely. In order to investigate this possibility in more detail, the blood brain barrier opening literature was extensively reviewed. Indeed, hypertonic agents such as mannitol have been utilised for the artificial opening of the BBB in order to facilitate drug and protein delivery

across the brain. It is the hyperosmolality of these solutions that increase permeability of the BBB (Hayakawa, Morris and Katzberg, 1989, Grainger, 1980), but for these purposes, mannitol is usually delivered directly into intra-arterial or intra-carotid locations. The aim is to exceed the associated osmolality thresholds required for the opening of BBB. On the other hand, mannitol therapy is also the most common technique for the management of cerebral oedema and intracranial pressure (ICP) in the clinic (Chen *et al*., 2013). The current guidance recommends a dose of 0.25-1.0 g/kg body weight (and no more than 2 g/kg) to be given by IV infusion over 20–30 min (Shawkat, Westwood and Mortimer, 2012). Chen *et al*. (Chen *et al*, 2013) demonstrated that at clinical doses (0.5 g/kg), IV delivery of mannitol has no effect on BBB permeability to both large proteins (evans blue dye, molecular weight 0.96 kDa) and small molecules (sodium fluorescein dye, molecular weight 0.38 kDa), whereas intra-arterial delivery of the same dose indeed disturbed the BBB integrity. Similarly, intra-arterial injections of contrast media are known to disrupt the BBB whereas no evidence exist regarding the disruption of BBB following intravenous delivery of contrast media. Towards this claim, Wilcox and colleagues (Wilcox, Sage and Evill, 1984) demonstrated that even at large intravenous dose (8 ml/kg) of sodium iothalamate (Conray-420, molecular weight 0.64 kDa) the BBB remains intact as no extravasation of Evans blue or pertechnetate (molecular weight, 0.16 kDa) was detected. Here, initially a 10 mmol/kg (i.e. 20 ml/kg) dose of Omniscan was administrated intravenously. Assuming a 25g mouse to be the subject of analysis, this equates to the injection of a 0.39 milliosmole (mOsm) solution (supplementary material 5.7.2), whereas the total amount of osmolality that was delivered by Wilcox and colleagues was 0.5 mOsm for a similarly sized animal (supplementary material 5.7.3). Hence even at the high GBCA dose of 10 mmol/kg, the amount of injected osmolality (0.39 mOsm) is below the recorded osmolality that does not induce BBB disruptions. Based on the evidence provided above, it is likely that the BBB integrity is not compromised upon intravenous delivery of the contrast agent in this study, even at the relatively higher concentration/dose that was initially delivered (10 mmol/kg).

Throughout the development phase of the project, I sought to introduce a technique that would provide a straightforward and more robust characterisation of VECTOR pathway. Towards this goal, I implemented a diffusion sensitive MRI sequence that aimed to minimise intravascular signal contributions and, in turn, allowed the extended imaging of VECTOR pathway dynamics (125 minutes). At low *b*-values (< 200 s/mm^2), the diffusion-weighted sequence is mainly influenced by tissue perfusion and water diffusivity (fraction of volume of water flowing in capillaries), whereas at

high *b*-values the sequence is more sensitive to water molecules with slow and restricted motion (diffusion effects) (de Figueiredo, Borgonovi and Doring, 2011, Morani *et al*., 2013). Hence for the effective nulling of the intravascular compartment, a *b*-value of approximately 200 s/mm^2 was chosen (i.e. diffusion crushers were applied that would specifically null the signal from the intravascular compartment). The pattern of GBCA uptake was consistent with the T_1-weighted images in the early time-points (i.e. up to 37 mins post injection). Additionally, extended imaging of VECTOR pathway, revealed a more profound brain-wide GBCA uptake at later time-points.

After time-point five/six (~ 50 mins post injection), the concentration of GBCA is reduced in the intravascular compartment (due to systemic clearance) and the T_2 effects no longer dominate the T_1 enhancing effects. Although the signal from the (inside of) blood vessels are nulled by the application of diffusion crushers, any quick T_1 relaxation of blood water molecule spins and subsequent transfer/exchange to the extravascular/interstitial space will influence the tissue signal. Hence, at later time-points (>5/6), any transfer of relaxed blood water into the tissue, could be misinterpreted as GBCA uptake in brain tissue (i.e. creates false positives). However, this is likely to be quite a small effect, as the TR is relatively short (1300 ms). Effectively, inflow during TR is being imaged and from standard ASL, it is known that the amount of water transferred during that kind of time period is just a few percent (Alsop *et al*., 2015, Ferré *et al*., 2013). In theory, this sequence inherently differentiates GBCA-induced signal changes that originate from GBCA in the tissue versus the signal changes that originate from GBCAs in the intravascular compartment, without the need for high GBCA concentration to induce negative contrast in the intravascular compartment, and thus provides the potential to image VECTOR pathway with lower and more clinically relevant GBCA doses (which will be the avenue of future research).

5.5 Conclusion

In this chapter, using independent brain imaging techniques (LA-ICP-MS and autoradiography), I confirmed the previous MRI findings demonstrating the ability of blood-borne contrast agents to infiltrate the brain via the VECTOR pathway. Both independent imaging modalities revealed a pattern of tracer uptake that was similar and comparable to the original MR images (chapter 4). Overall, these findings provide merit as it was previously believed that systemic contrast agents are not able to

penetrate the healthy brain and ought to remain in the intravascular compartment (due to presence of intact blood-brain barrier).

Additionally, it was demonstrated that VECTOR pathway imaging is possible with a relatively lower dose of 3 mmol/kg Omniscan (approximately two clinical CE-MRI examinations based upon body surface area normalisation between mice and humans). Finally, a diffusion-weighted MRI sequence was developed that minimised intravascular PVEs by crushing the blood vessel signal. This feature provided the opportunity to image VECTOR pathway for an extended period of time (125 minutes) and potentially allows a reduction in GBCA dose. These advantages position the DW-SEMS sequence as a promising approach for imaging VECTOR pathway dynamics.

5.6 Limitations

Autoradiography images of VECTOR pathway suffered from image blurring that lead to the apparent spreading of contrast across the images (due to the limited spatial resolution of the technique). This limitation may introduce inaccuracies when quantifying the amount of tracer uptake in the tissue. Moreover, the tracer uptake quantification process required manual ROI analysis which may introduce bias in the results (relative to the automated atlas registration approach I implemented for MRI data analysis). Additionally, although perfusion fixation of the animal with PFA causes collapse of the brain ventricles and therefore loss/escape of CSF, any residual CSF in the ventricles may lead to overestimated whole-brain tissue tracer uptake value. However, the contribution of residual CSF in the ventricles (if any) to the whole-brain tissue tracer uptake estimate is not believed to be significant. Future work will include manual segmentation of all ventricular regions (on all individual brain slices) to subtract their contribution from this estimate (however as mentioned, manual ROI analysis has its own limitations and moreover, manual ROI analysis of all brain slices can be rather labour intensive).

In this chapter VECTOR pathway was imaged with relatively lower GBCA doses (5 and 3 mmol/kg compared to the initial 10 mmol/kg dose). However, only one animal was imaged with each dose and hence small sample size was a limitation of these specific MRI experiments. Future work includes increasing the sample size in order to further validate the current findings and to improve reproducibility.

Similar to the conventional T_1-weighted sequence, the DW-SEMS sequence also suffered from sensitivity lowering intravascular PVEs in the early time-points (<5 – approximately up to 50 mins post injection) originating from the susceptibility effect that extends beyond the blood vessels (due to the high GBCA concentration in blood

vessels, the paramagnetic gadolinium ions influence the surrounding/proximal spins, even outside the blood vessels (near the edges)), which implies that the acquired images capture a conservative pattern of CSF-ISF exchange. For example, the subarachnoid/perivascular CSF/GBCA influx into the brain parenchyma (identified by LA-ICP-MS and autoradiography) could not be readily identified. In the later time-points (>5) susceptibility effects are alleviated but due to a more global (i.e. brain-wide) GBCA uptake, it is also difficult to detect hyperintensities that could be solely attributed to subarachnoid/perivascular CSF/GBCA influx.

The DW-SEMS sequence facilitated the extended imaging of VECTOR pathway and mice were imaged for 125 mins. The clearance of GBCA from the brain tissue however was not completed during this time and therefore only an estimation of GBCA elimination rate could be provided. Moreover, since GBCA clearance phase was not completed during this time, it was also not possible to investigate the possibility of gadolinium retention in the brain following a single high dose GBCA bolus. Future work includes longitudinal studies where follow up scans will be acquired in the same animals who will be given a single high dose GBCA bolus in order to investigate the possibility of gadolinium retention in the brain.

5.7 Supplementary material

5.7.1 Estimation of CSF and brain tissue GBCA clearance time

For the estimation of CSF and brain tissue GBCA clearance time, the time-courses from the 4 CSF spaces (figure 5.16B) were averaged to obtain a single CSF time-course (figure S5.1-left). Similarly, the 3 parenchymal time-courses previously analysed (figure 5.16C) were averaged to obtain a single representative tissue time-course (figure S5.1-right).

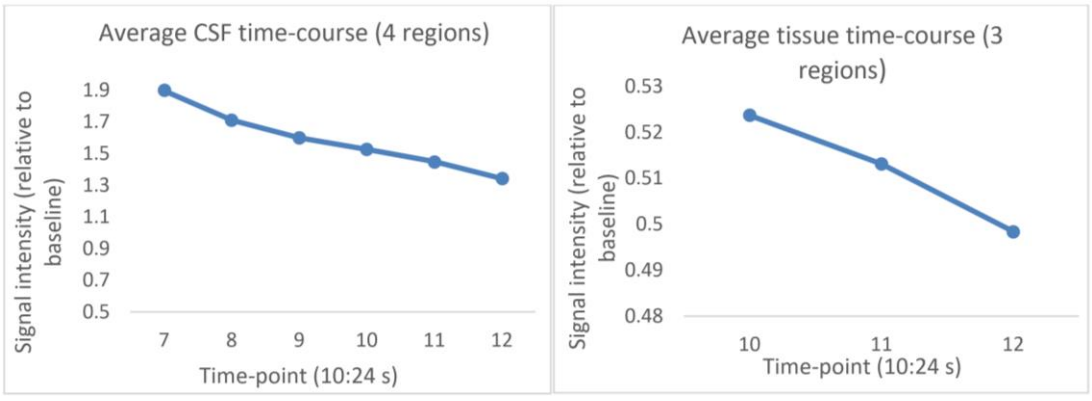

Figure S5.1: Average CSF and parenchymal time-courses. Time-points shown correspond to the clearance phase.

A one-term exponential model was then fit to the data to obtain the estimated clearance time (figure S5.2).

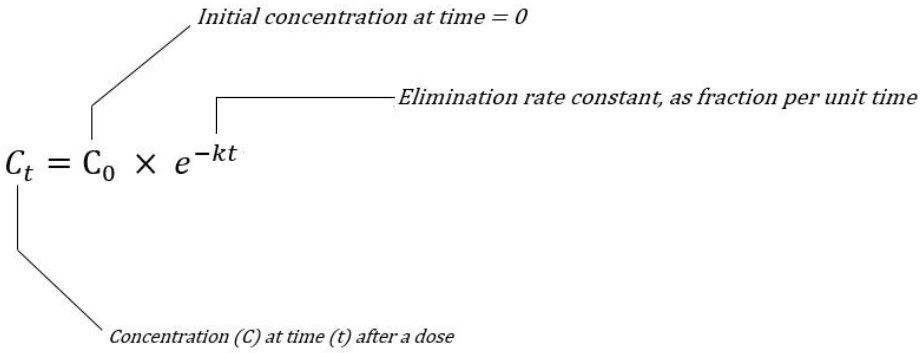

Figure S5.2: One-term exponential model applied to the data for the estimation of GBCA clearance time. (Image adopted from https://derangedphysiology.com)

For the CSF time-course the rate constant (k) was calculated to be 6.935 x 10e-3 and that for the parenchymal time-course was calculated to be 1.65 x 10e-3. Finally, the elimination half-life (50% clearance time) was calculated to be approximately 100 minutes and 7 hours for CSF and parenchymal time-courses respectively.

5.7.2 Osmolality delivered in this study

Total volume of Omniscan solution delivered for a 25 g mouse: 20 ml/kg * 25 g = 0.5 ml.

Osmolality of Omniscan is 780 mOsm/kg.

Hence total osmolality delivered is 780 * 0.5/1000 = 0.39 mOsm.

5.7.3 Osmolality delivered by Wilcox and colleagues (Wilcox, Sage and Evill, 1984)

Total volume of Conray-420 solution delivered for a 25 g mouse: 8 ml/kg * 25 g = 0.2 ml.

Osmolality of Conray-420 solution is: 2500 mOsm/kg (Lyons *et al*., 1984).

Hence total osmolality delivered is 2500 * 0.2/1000 = 0.5 mOsm.

5.8 Acknowledgments

I would like to say special thanks to everyone who assisted me in conducting the mass spectrometry and the autoradiography experiments in this chapter. I would like to thank the CABI nuclear medicine group (Tammy Kalber, Stephen Patrick, John

Connell) for their assistance in the procurement, preparation and quantification of radioactivity and also Ian Harrison and May Thin for their assistance in mouse perfusion and slicing of the brain samples.

Also, many thanks to my collaborators at Public Health England (Tim Marczylo and Adam Laycock) for the mass spectrometry interrogation of my brain tissue samples with great attention to detail and enthusiasm.

Chapter 6: Pharmacological modulation of VECTOR pathway dynamics

In the methods development section (chapter 3), I introduced a novel non-invasive MRI platform for the imaging of CSF-ISF exchange. I then applied this method to dynamically visualise a new CSF-ISF exchange pathway (the VECTOR pathway - chapter 4). Next, I provided corroborative evidence to support my MRI findings, using laser ablation inductively coupled plasma mass spectrometry and autoradiography (chapter 5). In this chapter, in order to investigate the sensitivity of the new MRI method in detecting pathophysiologically relevant modulations to CSF-ISF exchange, I carried out both transgenic mouse model and pharmacological intervention studies. By doing so, the sensitivity of VECTOR pathway to modulations in CSF-ISF exchange (which is hypothesised to occur in selected transgenic and pharmacologically treated mice) will also be assessed. Additionally, using invasive surgical procedures (intracerebral injection of tau protein) I will assess the clearance of aberrant proteins following pharmacological intervention.

6.1 Introduction

Due to the extensive similarity between the human and the mouse genome, preclinical studies on transgenic mice provides a great opportunity for better understanding of disease phenotype and pathology. Interestingly, alterations have been observed in the glymphatic clearance of many animal models of disease such as diabetes, TBI and amyloid accumulation (Jiang *et al*., 2017, Xiong, Mahmood and Chopp, 2018, Peng *et al*., 2016). An interesting avenue of CSF-ISF exchange research is related to the study of aquaporin-4 (AQP-4) channels, as they are believed to be involved in brain water homeostasis (Nielsen *et al*., 1997). The perivascular AQP-4 pool is critically involved in osmosensing and volume control (Benfenati *et al*., 2011, Jo *et al*., 2015, Mola *et al*., 2016) and it has been shown that deletion of AQP-4 in mice reduces brain edema after acute water intoxication (i.e. excessive systemic water intake) and ischemic stroke (Manley *et al*., 2000). Additionally, it has been suggested that perivascular AQP-4 channels are vital for the clearance of waste products from brain (Iliff *et al*., 2012). Therefore, tight regulation and polarisation of AQP-4 channels is important for the maintenance and integrity of brain water homeostasis. Here, in order to assess the effect of altered expression of aquaporin-4 channels (and the hypothesised perturbation to CSF-ISF exchange) on VECTOR pathway dynamics, CE-MRI will be performed in a cohort of alpha-syntrophin knockout (αSyn -/-) mice. αSyn -/- mice display an altered expression of AQP-4

channels where they demonstrate a reduction in the perivascular AQP-4 pool by ~90% (but not the total level of AQP-4 in the brain (Neely *et al*., 2001)). Hence, this animal model provides a unique opportunity for studying the consequences of CNS changes in AQP-4 localisation on VECTOR, unconfounded by systemic factors (AQP-4 in stomach and kidney persists without αSyn in this mouse model whereas usually in other mouse models such as the AQP-4 knockout mice, deletion of (AQP-4) gene is not only specific to the brain, but rather deletes AQP-4 channels globally (e.g. in kidneys), which may complicate interpretation when specifically studying brain disorders).

Dysfunction of brain clearance mechanisms may result in build-up of harmful proteins in the brain that are observed in many neurodegenerative conditions. Therefore, early identification/diagnosis of brain clearance abnormalities is necessary for the success of pharmacological intervention (therapeutic) strategies aiming to improve CSF-mediated brain clearance. For example, although anaesthesia is not specifically a pharmacological intervention per se, an increased solute transport via the glymphatic pathway was observed in the rat brain following anaesthesia with medetomidine compared to an isoflurane anaesthetic regime (Benveniste *et al*., 2017), providing encouragement regarding the possibility of modulating CSF-ISF exchange dynamics following drug delivery. Here, for investigating the sensitivity of the MRI platform in detecting the hypothesised modulations to VECTOR measurements as a result of pharmacological intervention, CE-MRI was performed in a cohort of healthy mice, with the ultimate goal of improving VECTOR dynamics (i.e. towards the identification of effective therapeutic strategies). Moreover, utilising a variety of commercially available drugs, MRI VECTOR signal changes will be monitored following pharmacological intervention. Additionally, I will investigate the impact of pharmacological intervention on the clearance of aberrant brain proteins using a direct clearance measurement approach (by intra-cerebral infusion of tau protein). As such, data from this section provide new evidence towards pharmacological modulation of VECTOR pathway dynamics.

6.2 Methods

6.2.1 Experimental methods for imaging transgenic mice

Generation of transgenic mice has been previously described (Neely *et al*., 2001). Briefly, female mice homozygous for targeted disruption of the gene encoding α-syntrophin at 4-5 months of age were acquired (n=5). Age-matched wild-type C57Bl6 mice were used as controls (n=4). αSyn −/− mice were bred on a C57Bl6 background to avoid effects of differing genetic strains (Neely *et al*., 2001). All experimental, MRI and data analysis methods were performed as previously described (section 4.2). Physiological monitoring was performed as previously described and animals were imaged for 90 minutes post contrast injection.

6.2.2 Experimental methods for pharmacological intervention studies

Male wild-type mice (C57Bl6) at an age of 3 months were anaesthetised with isoflurane and were treated with IP injections of either TGN 020 (250 mg/kg in 20 ml/kg body weight, n=6), captisol (20 ml/kg body weight, n=6), acetazolamide (1 g/kg in 20 ml/kg body weight, n=1), vasopressin (60 I.U/kg in 4 ml/kg body weight, n=7), mannitol (5 g/kg in 23 ml/kg body weight, n=2), sodium nitroprusside (SNP) (5 mg/kg in 4 ml/kg body weight, n=1), furosemide (15 mg/kg in 4 ml/kg body weight, n=2), or saline/water as control (n=7) approximately 30 minutes prior to GBCA infusion. A separate cohort of mice (n=4), received a medetomidine anaesthetic regime (0.4 mg/kg subcutaneous bolus followed by 0.8 mg/kg/hr infusion initiated 10 min after bolus) instead of isoflurane to study the effects of different anaesthetics on VECTOR pathway dynamics (although 0.5% isoflurane was simultaneously administered throughout to ensure efficacy of the medetomidine anaesthesia). All animals were imaged for 90 minutes post contrast injection. All MRI and data analysis methods were also performed as previously described except that automatically defined ROIs (from Allen atlas) were manually adjusted to slightly smaller volumes to ensure negligible PVEs from neighbouring tissues (to ensure high quality of comparison between groups).

6.2.3 Experimental methods for protein clearance studies (methods adapted from Harrison *et al*., under review)

6.2.3.1 Experimental methods

Male wild-type mice (C57Bl6J) were anaesthetised with 2% isoflurane delivered in O2 at a delivery rate of 1 L/min and positioned in a stereotaxic frame in the horizontal skull position. Mice were treated intraperitoneally with either vasopressin (60 I.U/kg

in 4 ml/kg body weight), mannitol (5 g/kg in 23 ml/kg body weight) or vehicle (0.9% saline, 20 ml/kg) 15 mins prior to intracerebral infusion of tau (n=5 per group). In the meantime, a midline incision was made on the top of the head to expose the underlying skull. A small burr hole was made, using a microdrill, above the location of the intracerebral injection. 50 ng tau containing brain homogenate (see below for preparation) was infused into the left striatum (anteroposterior, -0.2mm, mediolateral, +2mm and ventral to dura, -1.75mm, relative to bregma 76) using a 10 µl glass Hamilton syringe (2.5 µl at 0.25 µl/min, total time 10 min). 15 mins after the start of the intracerebral infusion, with the needle left in situ, a midline incision was made at a midpoint between the skull base and the occipital margin to the first vertebrae. The underlying muscles were parted to expose the atlanto-occipital membrane and dura mater overlaying the cisterna magna, which was thoroughly cleaned with saline. A durotomy was performed using a 23-gauge needle, allowing CSF to be collected using a narrow bore pipette tip (5-8µl of CSF was collected from mice). The animal was then euthanised with an IP injection of pentobarbital (10 ml/kg) and striatal tissue was collected.

6.2.3.2 Preparation of Tau-Containing Brain Homogenate

Tau was prepared by euthanising an aged rTg4510 mouse (9 months of age) and dissecting out the cortex and hippocampus. Tissue was frozen in isopentane on dry ice for storage at -80°C. Frozen tissue was weighed, thawed, and gently mixed in a mortar with a few strokes of a pestle in 10% w/v volumes of cold Tris-buffered saline (TBS) containing protease inhibitor cocktail, phenylmethylsulfonyl fluoride, and phosphatase inhibitor cocktails I and II (all Sigma, UK), at a final dilution of 1:100. To estimate total human tau content, an Enzyme Linked Immunosorbent Assay (ELISA) of the brain homogenate was performed (Human Tau (total) ELISA Kit (Invitrogen, UK) as per the manufacturer's instructions, see below) and stock solution tau concentration adjusted to 20 µg/ml with homogenisation buffer, and stored at -20°C until intracerebral infusion.

6.2.3.3 Tau Enzyme Linked Immunosorbent Assays

Concentration of human tau in homogenised striatal tissue and CSF samples was quantified using ELISAs. Total tau was quantified using Human Tau (total) ELISA Kit (#KHB0041, Invitrogen, UK), as per the manufacturer's instructions. Brain homogenates and CSF samples were diluted in diluent buffer prior to being incubated in capture antibody coated wells for 2hrs at room temperature. Wells were washed several times before being incubated in detection antibody for 1hr at room

temperature. Wells were washed again before being incubated with horseradish peroxidase conjugated secondary antibody for 30 mins at room temperature. Wells were then washed again before being incubated with stabilised chromogen for 30mins at room temperature. After this incubation, stop solution was added to each well and the plate was read at 450nm. A set of standards of known Tau concentration (0, 31.25, 62.5, 125, 250, 500, 1000, 2000 pg/ml were run in parallel for each experiment for quantification of sample tau content from the standard curve.

6.2.3.4 Data analysis

Data is expressed as concentration (for CSF samples) and percentage of tau protein injected still in brain tissue (for excised brain tissue). For statistical evaluation of tau in the CSF, a one-way analysis of variance (ANOVA) was performed between the three cohorts (drug treatment was set as the independent factor). For statistical evaluation of tau in the brain tissue, a two-way ANOVA was performed (drug treatment and brain hemisphere set as independent factors). Post-hoc Bonferroni correction was also conducted to correct for multiple comparisons.

6.3 Results

6.3.1 Investigating modulation to the VECTOR pathway in the alpha-syntrophin knockout mouse model

CE-MRI was performed in a cohort of alpha-syntrophin knockout mice (αSyn −/− mice) and their wild-type littermates in order to study the effect of altered AQP-4 localisation on VECTOR pathway. ROI analysis in several different regions of the brain demonstrated no significant difference in GBCA uptake between the transgenic and the wild-type mice (figure 6.1A). Group averaged thresholded subtraction images were also created for an improved sensitivity to GBCA uptake and to reveal any possible subtle difference in GBCA uptake, however no difference in GBCA uptake was seen between the two groups after this image processing technique (figure 6.1B-C).

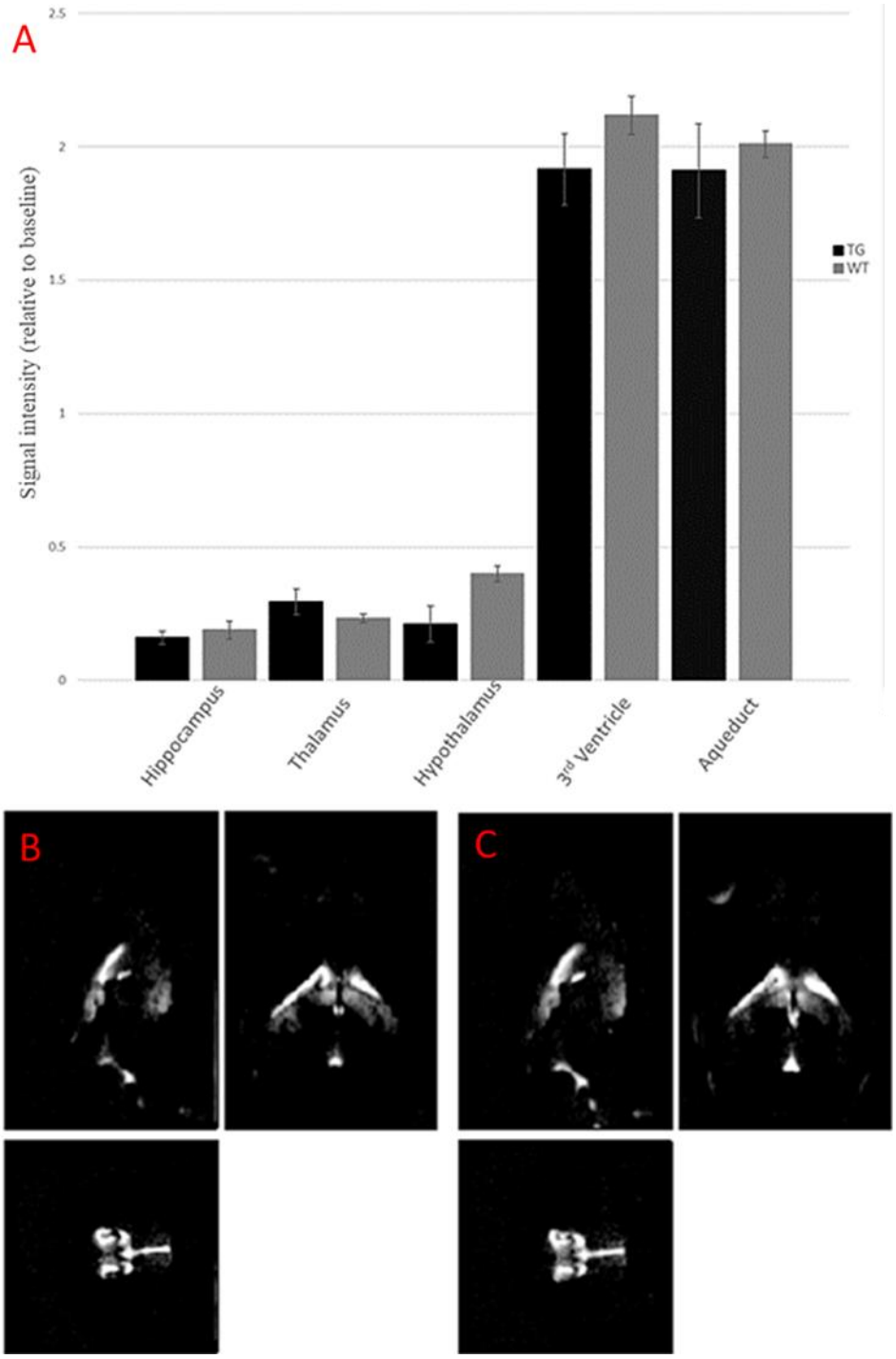

Figure 6.1: ROI analysis (37 minutes post contrast injection - A) demonstrated no significant difference in brain GBCA uptake between the transgenic and the wild-type group in hippocampus, thalamus, hypothalamus, 3rd ventricle and aqueduct regions of the brain. Error bars represent SEM values (n=5 and n=4 for transgenic and wild-type groups respectively). Group averaged thresholded subtraction images of the transgenic (B) and the wild-type (C) cohort 37 mins post contrast injection (displayed as sagittal, axial and coronal slices). GBCA uptake appears to be similar in both cohorts.

6.3.2 Pharmacological modulation of VECTOR pathway dynamics

6.3.2.1 Confounding effects of changes to rates of systemic GBCA clearance introduced by TGN-020, acetazolamide, mannitol, captisol, furosemide and SNP

In order to modulate VECTOR pathway dynamics pharmacologically, a range of commercially available drugs were sourced. All the sourced drugs were carefully chosen based on their potential to alter CSF-ISF exchange dynamics. Upon inspection of the images however, it was realised that several of these drugs (TGN-020, acetazolamide, mannitol, furosemide, captisol and SNP) had also induced undesired systemic effects. These drugs reduced/impaired systemic clearance (renal clearance) which was revealed by the increased retention of GBCA in the blood vessels (evident by the prolonged signal intensity drop-out (i.e. negative contrast relative to baseline) in the intravascular compartment (62 mins post contrast injection - figure 6.2A-F)).

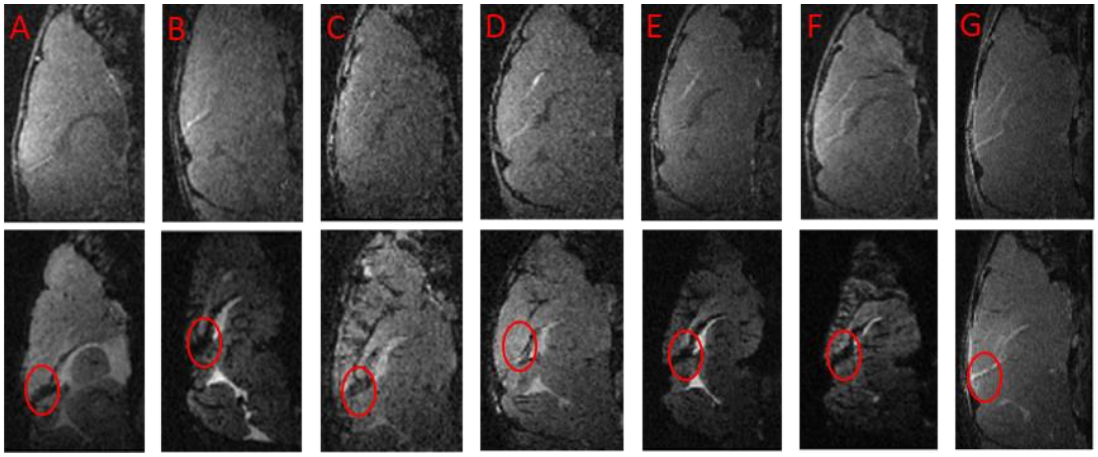

Figure 6.2: Pharmacological intervention with TGN-020 (column A), mannitol (column B), captisol (column C), furosemide (column D), SNP (column E) and acetazolamide (column F) resulted in a reduced systemic GBCA clearance. This is evident by the prolonged signal intensity drop-out (i.e. negative contrast relative to baseline) in the intravascular compartment (red circles) (bottom row corresponds to 62 mins post injection scans and top row corresponds to the baseline scans – all images are displayed as sagittal slices). On the other hand, the intravascular compartment signal from the animal with no drug treatment demonstrated a positive contrast by that time due to normal systemic GBCA clearance (column G).

As mentioned in section 3.3.4.2, due to high GBCA concentration in the blood vessels, negative contrast (relative to baseline) is induced in the intravascular

compartment post contrast injection. If the systemic/renal clearance is not impaired, the negative contrast in the intravascular compartment is expected to be reversed by 60 mins post contrast injection (i.e. after time-point 5/6) due to GBCA clearance from the circulation and the corresponding recovery of T_2/T_2* values (i.e. T_2 shortening effects no longer dominate T_1 shortening effects after this time). However, treatment with TGN-020, acetazolamide, mannitol, furosemide, captisol and SNP appeared to markedly reduce systemic/renal clearance as the negative contrast in the intravascular compartment was extended beyond 60 minutes post contrast injection (i.e. beyond time-point 6) (figure 6.2A-F). On the other hand, the intravascular signal intensity in the animal receiving no drug treatment (figure 6.2G) exhibits positive contrast by this time due to normal systemic GBCA clearance (and corresponding recovery in T_2/T_2*). Therefore, due to altered rates of systemic GBCA clearance and the possible differences in the intravascular compartment signal between the animals who had received these drugs and the animals with no drug treatment, a reliable comparison could not be made regarding brain tissue GBCA uptake (as PVEs from blood vessels could confound brain tissue GBCA uptake comparison). Therefore, data from these animals were excluded from further analysis.

6.3.2.2 Altered VECTOR pathway dynamics following pharmacological intervention with anti-diuretic hormone vasopressin

Unlike the drugs described above, vasopressin treatment did not impede systemic/renal clearance of GBCAs. This was evident by the recovery of the intravascular signal (i.e. T_2/T_2* values) by 60 mins post contrast injection (i.e. the negative contrast (with respect to baseline) in the intravascular compartment was reversed after time-point 5/6, figure 6.3A-B). Inspection of intravascular signal intensity by analysing intravascular ROIs (LHV) demonstrated similar signal intensity changes (w.r.t baseline) in both animals (figure 6.3C).

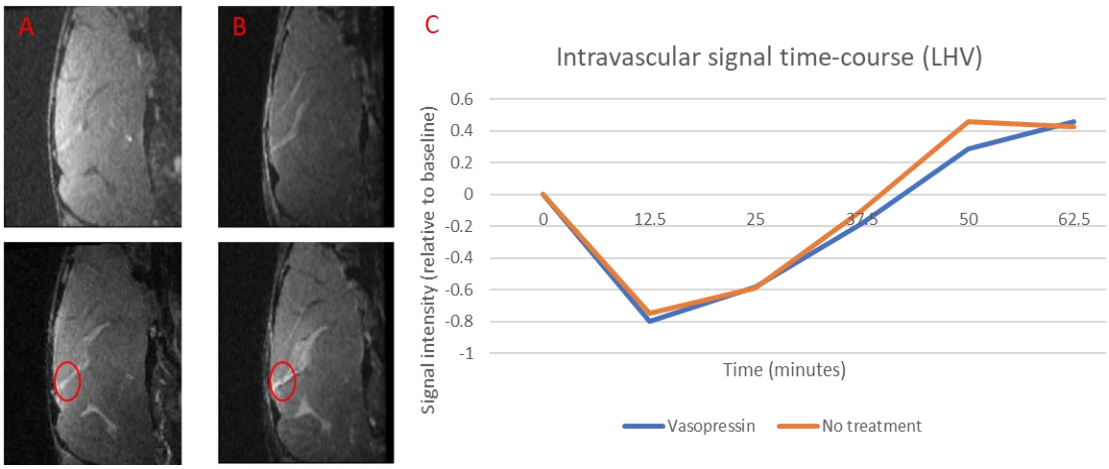

Figure 6.3: Pharmacological intervention with vasopressin (column A) did not hamper systemic GBCA clearance and similar to the animal receiving no drug treatment (column B) the negative contrast (relative to baseline) in the intravascular compartment was reversed by time-point 6 (60 mins post injection, bottom row - red circles) (top row images correspond to the baseline scans). Relatively similar signal intensity time-courses were obtained from the intravascular compartment of both animals (LHV) and therefore rates of systemic GBCA clearance appears similar (C).

Since data from this pilot experiment looked promising, in that the intravascular signal intensity in this animal was not confounded by a reduced rate of systemic GBCA clearance (i.e. no undesired systemic differences), a further 6 animals were treated with vasopressin. A reliable comparison could therefore be made regarding differences in (extravascular) GBCA uptake in the brain as the intravascular compartment signal is consistent in both vasopressin treated and no drug treated cohorts. Vasopressin markedly increased VECTOR signal changes evident by the brain-wide differences observed in the CSF-ISF exchange pattern 37 mins post contrast injection (figure 6.4A-C). In other words, the amount of GBCA 37 mins post contrast injection was significantly higher in the vasopressin group, signifying marked modulation of CSF-ISF exchange dynamics. ROI analysis in 5 regions of the brain (figure 6.4D), revealed significantly higher amount of GBCA in the aqueduct, third ventricle, hippocampus and thalamus relative to control (p-values of 0.0299, 0.0011, 0.0137 and 0.0014 respectively).

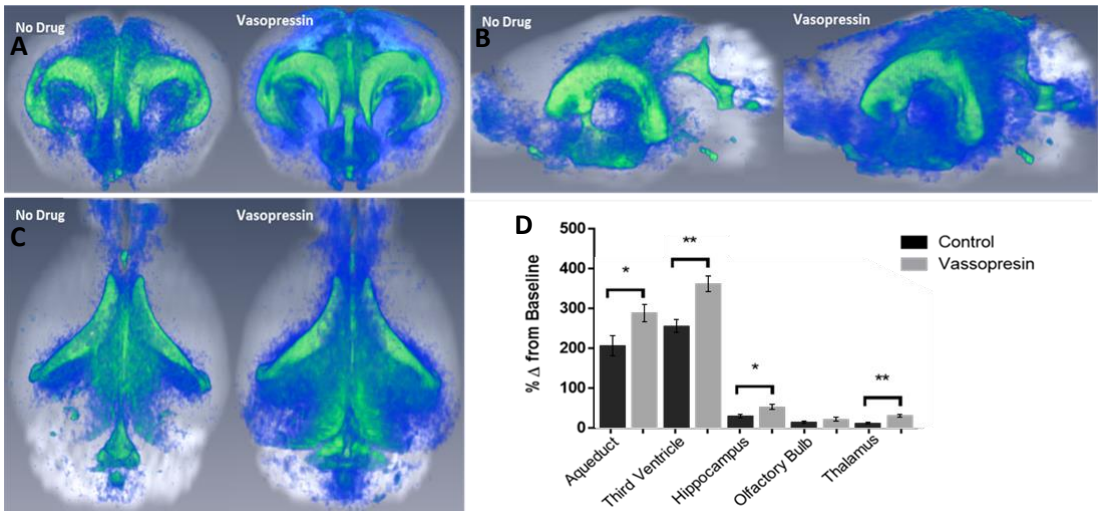

Figure 6.4: 3D rendering of the group averaged thresholded subtraction MR images of the cohorts receiving vasopressin and no drug treatment (37 mins post contrast injection, A- coronal, B- sagittal, C- axial views). Pharmacological intervention with vasopressin markedly increased VECTOR signal changes compared to the cohort

with no drug treatment. ROI analysis revealed a significantly higher amount of GBCA in the brain in comparison to no pharmacological intervention (p-values of aqueduct: 0.0299, third ventricle: 0.0011, hippocampus: 0.0137, thalamus: 0.0014 uncorrected for multiple comparisons). Aqueduct and hippocampus regions did not survive the Bonferroni correction (p-values of aqueduct: 0.1495, third ventricle: 0.0055, hippocampus: 0.0685, thalamus: 0.007) (D). Error bars represent SEM values.

6.3.2.3 Investigating modulation to the VECTOR pathway following anaesthesia with medetomidine

Based on a previous study that reported marked increases in glymphatic transport with medetomidine anaesthesia compared to isoflurane (Benveniste *et al*., 2017), a cohort of mice underwent a medetomidine anaesthetic regime (as opposed to the isoflurane anaesthesia which has been used thus far). Since medetomidine anaesthesia did not induce undesired systemic effects (i.e. similar intravascular signal intensity to isoflurane anaesthesia), ROI analysis in 5 different regions of the brain demonstrated no significant modulation to VECTOR signal changes (figure 6.5A). Created thresholded subtraction images also did not reveal any difference in GBCA uptake between the two groups (figure 6.5B-C).

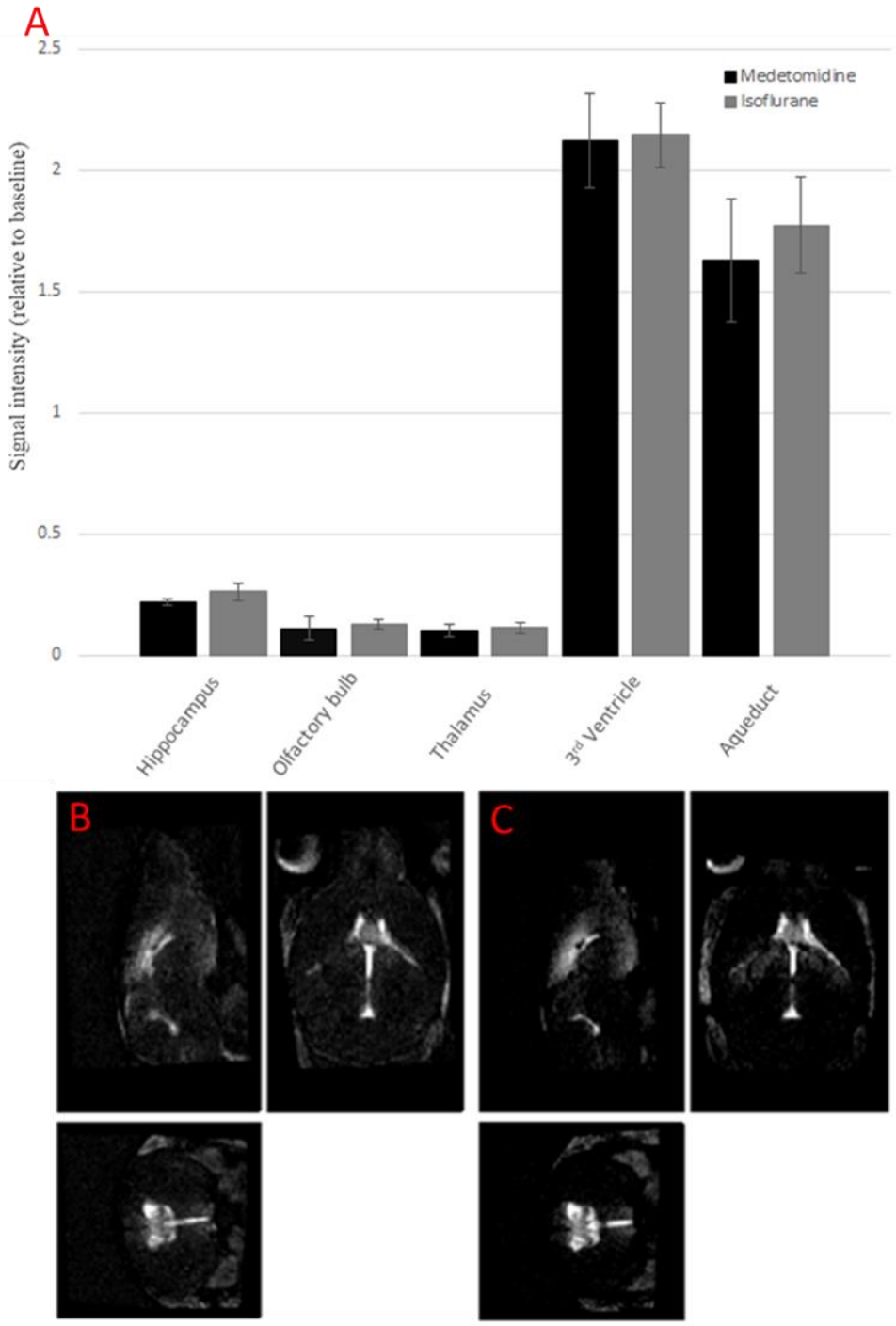

Figure 6.5: ROI analysis (37 minutes post contrast injection - A) demonstrated no significant modulation to VECTOR signal changes in the cohort who underwent a medetomidine anaesthetic regime as opposed to the isoflurane anaesthesia used thus far. Error bars represent SEM values. Group averaged thresholded subtraction images from the cohort who underwent a medetomidine anaesthetic regime (B) and the ones under isoflurane anaesthesia (C) 37 mins post contrast injection. GBCA uptake appears relatively similar in both cohorts (i.e. medetomidine anaesthesia did

not modulate VECTOR signal changes). Images displayed as sagittal, axial and coronal slices.

6.3.3 Clearance/transport of aberrant brain proteins can be altered following pharmacological intervention with vasopressin or mannitol

In order to investigate possible correlations between vasopressin-induced modulations of the VECTOR MRI measurements (section 6.3.2.2) and how vasopressin may change CSF-mediated clearance of tau, a cohort of wildtype mice (n=5) were treated with vasopressin 15 mins prior to intrastriatal infusion of tau containing brain homogenate (figure 6.6A and B). Additionally, a second cohort of mice (n=5) were instead treated with mannitol, a drug with hypothesised opposite mechanism of action to vasopressin (i.e. a diuretic drug with opposite effect on brain fluid movement) (Plog *et al*., 2018). A third cohort of mice received saline as vehicle (n=5). CSF (from cisterna magna) and brain tissue samples were then collected from mice 30 mins post drug/vehicle treatment for measuring tau clearance/transport to CSF. Following treatment with vasopressin, a significant amount of tau remained in the brain tissue compared to controls (93.5% and 52.5% respectively, p-value: <0.001 - figure 6.6C). On the other hand, the vasopressin group had lower levels of tau cleared to the CSF (23.1 and 138.3 ng/ml respectively, p-value: <0.0001 - figure 6.6D). This finding suggests a reduced communication between the brain tissue and CSF compartments (i.e. evidence for marked reduction in CSF-ISF exchange dynamics) and may suggest a retentive/inhibitive effect of vasopressin on CSF-mediated tau clearance. Therefore, this finding may also indirectly suggest that the observed upregulation of the VECTOR pathway with vasopressin may reflect a reduction in CSF-mediated clearance in the brain which results in increased retention of GBCAs in the extra-vascular parenchymal tissue. Interestingly, the cohort which received mannitol, demonstrated opposite results. That is, a lower amount of tau was observed in brain tissue compared to the control group (32.1% and 52.5% respectively, p-value: <0.05 – figure 6.6C) but a greater amount of tau (although not significant) had cleared to the CSF compartment compared to the control group (159.3 and 138.3 ng/ml respectively, figure 6.6D) suggestive of enhanced CSF-mediated clearance. Taken together, these data suggest that marked modulation of CSF-ISF exchange dynamics (i.e. CSF-mediated solute transport) is achievable following pharmacological intervention. These data also support the previous observations of significant VECTOR MRI signal changes following vasopressin administration.

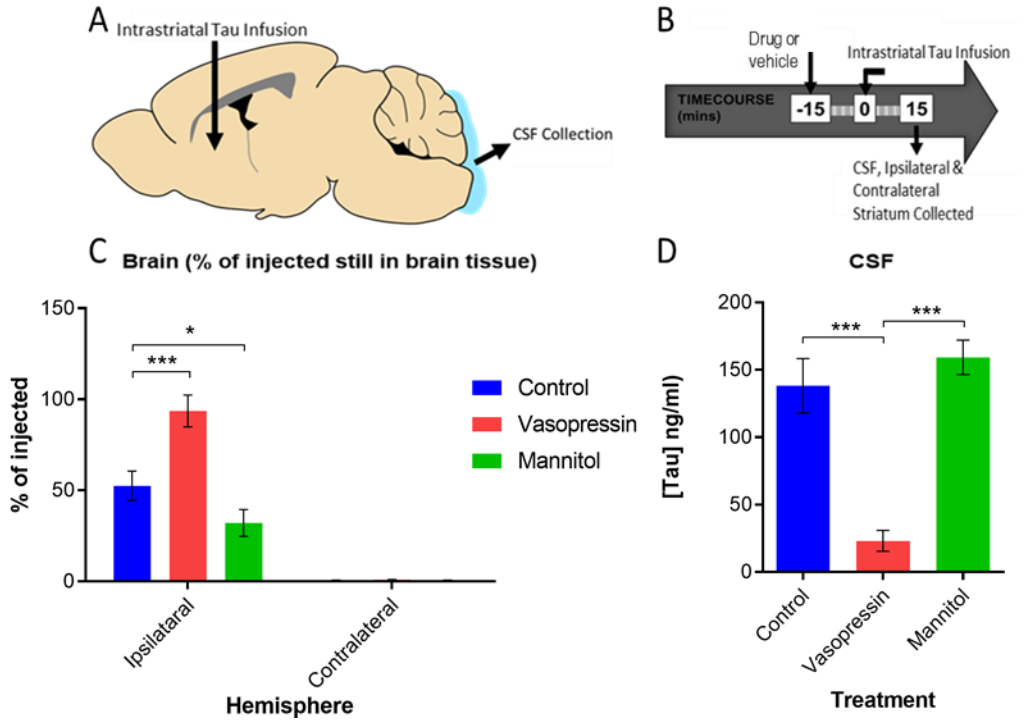

Figure 6.6: Schematic demonstrating locations of tau injection and CSF collection (A). Schematic of the time-course of the experiments (B). Following pharmacological intervention with vasopressin, a significantly greater amount of tau remained in the brain tissue compared to controls (p-value: <0.001) (C) suggestive of a reduction in CSF-ISF exchange dynamics, in fact, a significantly lower amount of tau was detected in the CSF compartment (compared to the controls, p-value: <0.0001) (D). On the other hand, the mannitol cohort demonstrated a lower amount of tau in the brain tissue compared to controls (p-value: <0.05) (C) suggestive of improved tau clearance. Although not significant, a larger amount of tau was detected in the CSF as expected (D). Error bars represent SEM values.

6.4 Discussion

In the preceding chapters, a completely new pattern of CSF-ISF exchange was observed (VECTOR pathway). If VECTOR is reflective of a route of CSF-ISF exchange that plays a physiologically important role in interstitial brain clearance, then its dysfunction may be an important mechanism in many neurodegenerative diseases defined by the presence of aberrant proteins (such as tau). For example, it has been suggested that impairments to the brains' glymphatic clearance, may lead to the abnormal build-up of aberrant brain proteins and therefore it may contribute to disease onset/progression (Iliff *et al*., 2012). Moreover, improvement in glymphatic transport has been observed following mannitol therapy, where impaired glymphatic function was rescued in a murine AD model (Plog *et al*., 2018). Equally, stimulation

of the VECTOR pathway may represent a new therapeutic approach. In this chapter, in order to investigate the sensitivity of VECTOR pathway to modulations in CSF-ISF exchange dynamics and also to investigate whether these hypothesised alterations can be detected by the MRI platform, transgenic mouse and pharmacological intervention studies were performed.

The αSyn knockout mouse model was chosen as it provided a unique opportunity for specifically studying impact of changes in AQP-4 localisation on VECTOR pathway dynamics, unconfounded by systemic factors. This is important as deletion of kidney AQP-4 channels (a condition seen in the AQP-4 knockout mouse model) could impair/alter systemic/renal clearance of GBCAs and potentially confound brain tissue GBCA uptake comparison (due to possible differences in the intravascular compartment signal between the transgenic knockout mice and their wild-type littermates and the corresponding contributions from intravascular PVEs – similar to the systemic confounders that were introduced following pharmacological treatment with the drugs listed in section 6.3.2.1). In fact, CE-MRI imaging of an AQP-4 knockout mouse confirmed this statement as an impaired systemic clearance of GBCA was observed (evident by the extended signal drop-out (negative contrast relative to baseline) in the intravascular compartment - data not shown). Despite providing the opportunity for studying effects of CNS disorders on VECTOR pathway dynamics, no significant CSF-ISF exchange difference could be detected between the alpha-syntrophin knockout mice and their wild-type littermates, suggesting that changes in the polarisation of AQP-4 channels (i.e. reduction in expression of perivascular AQP-4 channels) does not significantly alter VECTOR dynamics. However, this could be attributed to the sensitivity constraints of the developed CE-MRI platform or perhaps due to the mild phenotype seen in these mice, as no overt structural or functional differences have been reported. The αSyn knockout mice demonstrate a reduction in perivascular AQP-4 channels that mainly reside on astrocytic end-feet, however total brain AQP-4 expression is not changed as these mice demonstrate a redistribution of AQP-4 from perivascular to non-endfeet plasma membrane domains of astrocytes (Amiry-Moghaddam *et al*., 2004). The deletion of perivascular AQP-4 channels may impede the influx of perivascular CSF into the brain tissue (a determining route of CSF-ISF exchange in glymphatic transport), hence, if experiments were conducted with the aim of assessing glymphatic transport (e.g. by intra-cisternal tracer delivery and the subsequent imaging of perivascular CSF influx into the brain tissue using two-photon laser scanning microscopy), significant differences in glymphatic transport between αSyn knockout and control mice would

be anticipated. The observed egress of GBCAs into the parenchymal tissue that defines the VECTOR technique on the other hand, is mainly facilitated by direct ependymal transfer of ventricular CSF with ISF, hence it may be less dependant on perivascular CSF transport and therefore less sensitive to altered perivascular AQP-4 expression. Since AQP-4 labelling is retained in the lining of the ventricles in this mouse model (Amiry-Moghaddam *et al*., 2004), it is not surprising that no significant differences were observed in VECTOR between these mice and their wild-type littermates.

Next, in order to induce a more definitive modulation to VECTOR pathway dynamics, a range of commercially available drugs were sourced all based on their ability to alter normal brain water movement. For example, TGN-020 was chosen based on its ability to block aquaporin-4 channels. Vasopressin (an anti-diuretic hormone) and sodium nitroprusside (a vasodilating agent) on the other hand are known to increase ICP whereas acetazolamide (a carbonic anhydrase inhibitor) and furosemide (a diuretic agent) are both known to reduce ICP. Captisol (cyclodextrin) and mannitol are high osmolality agents and theoretically capable of altering plasma osmolarity (mannitol therapy is actually used for lowering elevated ICP in the clinic). Hypertonic agents such as mannitol are known to increase net resorption of ISF (i.e. increase ISF-to-plasma efflux), resulting in decreased ISF volume and therefore reduction in ICP. However, pilot experiments demonstrated that several of the sourced drugs (TGN-020, acetazolamide, mannitol, furosemide, captisol, SNP) induced undesired systemic effects and impaired systemic GBCA clearance from the blood (demonstrated by extended signal drop-out in the intravascular compartment). Thus, data from these experiments had to be excluded from further analysis (as intravascular signal in these mice was markedly different to the no drug treatment (control) group and this could confound assessment of the VECTOR pathway). Systemic administration of the anti-diuretic hormone vasopressin on the other hand, did not induce undesired systemic effects (as revealed by intravascular ROI analysis), hence VECTOR pathway was further assessed by ROI analysis. Vasopressin resulted in marked alteration of CSF-ISF exchange pattern where significant brain-wide MRI signal differences could be observed. This experiment demonstrated the sensitivity of VECTOR pathway to modulations in CSF-ISF exchange caused as a result of vasopressin administration.

The exact mechanisms of action of vasopressin in the CNS are unknown. Vasopressin is usually formed naturally by the hypothalamus and is then released in the blood. Vasopressin regulates the concentration of water in blood. Some clinical

uses of vasopressin include control of frequent urination and water loss due to diabetes and the increase of blood pressure in adults with vasodilatory shock. Systemic injection of vasopressin acts on renal collecting ducts via V2 receptors to increase water reabsorption (hence decreased urine formation) and also on vascular smooth muscle to cause vasoconstriction by binding to V1 receptors. As a result of this increased blood volume and constriction of the blood vessels, the blood pressure will rise. In addition to a significant increase in blood pressure, intracranial pressure (ICP) will also increase (Saladin and Bruni, 1993). It is hypothesised that the observed changes in VECTOR pathway following systemic vasopressin injection, is strongly related to this increase in ICP. The hypothesised mechanism of action is as follows: by increasing water reabsorption into blood (action of V2 receptors), vasopressin will decrease systemic osmolality. Due to the (transient) osmolality imbalance between the systemic circulation (i.e. plasma) and interstitial fluid in the brain (and also the increased hydrostatic pressure), more water will be pulled into the brain from the circulation (i.e. increase in plasma-to-ISF influx). This is consistent with the principle of osmosis which states that water will move from the compartment with lower osmolality (or concentration) to the side with higher osmolality to restore homeostasis/equilibrium. In our context, this means net flow of water into the CNS and an increase in ICP as previously suggested (Saladin and Bruni, 1993). Interestingly, it has been shown that rise or fall in plasma osmolality will be accompanied by a change of osmolality of the tissue fluids of the brain in the same direction (Stern and Coxon, 1964). A plausible explanation for increased VECTOR signal intensity is therefore associated with increased GBCA infiltration into the brain as a result of net movement of water into the brain (the exact mechanism of GBCA inflow has yet to be determined - there has been suggestions regarding the influence of vasopressin on permeability of endothelium and ependyma to water and other solutes). Another plausible factor that may compound the increased MRI signal intensity, is that the clearance of the contrast agent that is delivered into the brain is reduced as it opposes the direction of the osmotic gradient (to balance the osmolality difference between plasma and interstitial fluid as mentioned) and this leads the build-up of GBCA and contributes to the signal hyperintensity.

In order to investigate possible correlations between vasopressin-induced modulations of the VECTOR MRI measurements and how vasopressin may change CSF-mediated clearance of tau, experiments were performed in which tau protein was surgically injected into the striatum. In the mouse cohort that received the systemic injection of vasopressin, there was a significantly higher amount of tau

protein remaining in the striatum compared to the control group (saline) 15 mins post tau injection. Consequently, the amount of tau in the CSF compartment was larger for the control group. In other words, the control group had less tau in brain tissue but more tau in the CSF compartment (reflecting more efficient CSF-mediated brain clearance of tau), and vice versa for the group that received vasopressin. Essentially, this finding indirectly reflects reduced communication between CSF and brain tissue (ISF) in the vasopressin cohort. As described earlier, vasopressin induces a transient osmolality imbalance between plasma and ISF creating an osmolality gradient (i.e. net water movement into the brain), therefore clearance of tau may be hampered as it opposes the direction of the osmolality gradient. This is consistent with the previous MRI findings in that the clearance of GBCA delivered into the brain was also suggested to be reduced as it opposed the direction of the osmolality gradient. These findings may indirectly elucidate the retentive effect of vasopressin on CSF-mediated tau removal and also on VECTOR pathway dynamics.

As mentioned above, following pharmacological intervention with vasopressin, clearance of tau from the brain seemed to be reduced, therefore, next, I sought to study the effect of a drug with opposite hypothesised mechanism of action to vasopressin, that is a diuretic drug that could increase tau clearance and potentially modulate VECTOR pathway dynamics in the opposite direction (i.e. opposite to vasopressin, I would anticipate downregulation of VECTOR MRI signal changes due to lower influx of GBCA into the ventricles/brain parenchyma as it opposes the direction of the osmolality gradient). A feasible candidate was mannitol as mannitol therapy is clinically used for the treatment of raised ICP (i.e. opposite to vasopressin). Mannitol reduces ICP by osmotherapy, a process in which water is drawn out of the brain by the means of an osmotic gradient (Jha, 2003). The exact mechanisms of action of diuretics are also the subject of some debate, however, it is known that mannitol increases plasma osmolality, causing water to move from brain into blood along an osmotic gradient (i.e. increase in ISF-to-plasma efflux), reducing brain water content and ICP (Thenuwara, Todd and Brian, 2002). Consistent with my hypothesis, I saw increased tau clearance from the brain tissue in the group that received mannitol therapy compared to controls. Opposite to what was seen for the vasopressin group, there was a significantly lower amount of tau in the brain tissue but larger amount of tau in the CSF compartment. This finding indirectly elucidates the enhancing effect of mannitol therapy on CSF-mediated tau removal from the brain tissue. However, it was not possible to investigate possible mannitol-induced modulations of the VECTOR

MRI measurements due to the induced undesired systemic effects (impaired systemic GBCA clearance - section 6.3.2.1).

Collectively, data from this chapter suggests that VECTOR pathway can be modulated following pharmacological intervention and is susceptible to perturbations in CSF-ISF exchange dynamics. In addition, data obtained from the (invasive) tau clearance measurement experiments, provide promise for the existence of novel effective therapeutic strategies towards an enhanced brain clearance.

6.5 Conclusion

The CSF-ISF exchange dynamics of VECTOR pathway was pharmacologically perturbed using the anti-diuretic hormone vasopressin, a finding which demonstrates the susceptibility of VECTOR pathway to pharmacological perturbation. These perturbations were detected by the MRI measurements and therefore, provides some encouragement that the novel MRI platform may represent a sensitive, non-invasive technique to study the mechanisms that lead to the parenchymal accumulation of aberrant proteins that define the most common neurodegenerative conditions. Moreover, the pharmacological enhancement of CSF-mediated tau clearance was achieved following mannitol therapy, providing promise towards development of effective therapeutic strategies that may slow down disease progression.

6.6 Limitations

Sensitivity of VECTOR pathway to modulations in CSF-ISF exchange was investigated only in a single transgenic mouse model (the αSyn knockout model that demonstrates a rather mild phenotype - see section 6.1 for more information on this mouse model). It would be interesting to investigate this subject in other transgenic mouse models that demonstrate a more severe pathology (e.g. in amyloid and tau transgenic models of AD).

The MRI platform provides a non-invasive, sensitive technique for detecting perturbations to VECTOR pathway. The platform is therefore believed to be sensitive to VECTOR perturbations that are hypothesised to occur in AD and transgenic mouse models of AD. However, the specific utility of the platform in pharmacological intervention studies (i.e. for studying the effects of a specific drug on VECTOR pathway dynamics) is not as straightforward. For instance, in this chapter, the MR data from the animals who had received specific drug treatments (listed in section 6.3.2.1) had to be discarded due to altered rates of systemic GBCA clearance and the possible differences in the intravascular compartment signal between the animals

who had received these drugs and the animals with no drug treatment. This is because the T_1-weighted sequence suffers from intravascular PVEs which could potentially confound brain tissue GBCA uptake comparison. Therefore, a limitation of the platform is that this comparison is only meaningful as long as the rate of systemic GBCA clearance (and the intravascular signal) is not significantly altered by the injected drug. Future work includes investigating the feasibility of studying the effects of these drugs on VECTOR pathway dynamics using the DW-SEMS sequence (chapter 5) since the intravascular signal is nulled by this sequence and the contribution of intravascular PVEs are minimised (towards a more meaningful comparison of brain tissue GBCA uptake).

Systemic mannitol therapy increased the clearance of intrastriatally injected tau protein from the brain tissue. However, according to the discussion above, it was not possible to monitor the effects of mannitol on brain tissue GBCA clearance (i.e. VECTOR pathway dynamics) with MRI due to the marked impact of mannitol on systemic (renal) GBCA clearance and the associated changes to the MRI intravascular signal intensity that could potentially confound the assessment of VECTOR pathway.

6.7 Acknowledgements

I would like to say special thanks to my colleague Ian Harrison for his extensive assistance in this part of the study. All the surgeries in this section were performed by Ian Harrison under my supervision. Preparation and quantification of tau were also performed by Ian Harrison.

Chapter 7: Summary, limitations and future directions

7.1 Summary

With a global estimate of 135 million people living with dementia by the year 2050, there is an urgent need to identify the causal sequence of pathological events that occurs in disease development, in order to develop early sensitive biomarkers and effective therapeutic strategies.

Many neurodegenerative diseases are characterised by the neuropathological accumulation of aberrant protein aggregates, and in the case of AD these are neurofibrillary tangles (NFTs) and amyloid plaques. Accumulation of these aberrant proteins in the brain can be attributed to increased production and/or reduced clearance of these toxic material (i.e. imbalance between production and clearance). Recent evidence suggests that impairments to brains ability in removing amyloid beta contributes to disease onset/progression in AD (Wildsmith *et al*., 2013, Mawuenyega *et al*., 2010, Iliff *et al*., 2012).

Brain clearance (or solute transport) is partially driven by the compartmental exchange of CSF with ISF. Previous tracer studies have shown that CSF enters the brain interstitium, exchanges with ISF and facilitates solute transport (i.e. glymphatic system). A common limitation of all CSF-ISF exchange assessment techniques to date, is that they all require invasive surgical procedures, and this is the primary reason why brain clearance function is not widely assessed in the clinic. Hence, due to the links between impaired brain clearance and disease onset/progression, there is an urgent need for the development of non-invasive CSF-ISF exchange measurement techniques.

Towards this goal, in chapter 3, a novel, non-invasive platform for the purpose of CSF-ISF exchange imaging was developed. This platform which is comprised of a single intravenous injection of clinically available contrast agent (GBCA) and MRI, is the first to capture the dynamic, whole brain infiltration of contrast agent from the blood to the CSF and into the brain parenchyma, providing evidence regarding the spatiotemporal dynamics that describes the communication of CSF and ISF. CE-MR imaging parameters were carefully chosen in order to increase sensitivity to GBCA uptake in brain, whilst considering temporal resolution constraints (important to capture dynamic progression of GBCA). A relatively high GBCA dose was utilised (x8 higher than the standard clinical human dose) to induce negative contrast (relative to baseline) in the intravascular compartment in order to separate the GBCA-induced

signal changes that originate from GBCA in the tissue versus the signal changes that originate from GBCAs in the intravascular compartment (a common challenge in clinical CE-MR imaging). In doing so, a meaningful depiction of brain tissue GBCA uptake was achieved.

The development of this platform laid the foundations for chapter 4, where application of this platform in a cohort of healthy animals revealed a pattern of cerebral fluid movement and exchange that had never before been visualised. Due to the distinct nature of this exchange (from ventricles to cerebral tissue), I coined this pathway, the '*VEntricular Cerebral TranspORt (VECTOR)'* pathway. In order to improve reliability of results (and to reduce manual ROI analysis burden), an automated data analysis pipeline was developed. In this pipeline, before averaging data from all subjects, data from each subject underwent several post processing steps including: niftii file conversion, transformation to a reference space, automatic ROI/label definition (from the Allen mouse brain atlas) and time course extraction.

In order to address concerns and scepticism regarding the newly identified CSF-ISF exchange pathway, in chapter 5, additional independent confirmatory experiments were devised. The main concerns raised were regarding the relatively high dose of the MRI platform (that could potentially exaggerate and confound the CSF-ISF exchange dynamics due to possible BBB disruption) also in addition to the time-varying intravascular signal contribution to the brain tissue signal (that could potentially introduce false positives and therefore exaggerate and confound the results due to PVEs). Therefore, confirmatory imaging techniques were devised that were independent of intravascular signal contributions (laser ablation inductively coupled plasma mass spectrometry (LA-ICP-MS) and autoradiography of perfused fixed brain slices). Both LA-ICP-MS and autoradiography confirmed the MRI findings as a similar pattern of tracer uptake, comparable to the MR images, was observed (i.e. that reflect blood to CSF to brain tissue transfer). Another advantage of autoradiography was that the VECTOR pathway was imaged with a more clinically relevant tracer dosage, addressing the mentioned concerns regarding the relatively high MRI GBCA dose. Additionally, autoradiography provided a quantitative estimation of brain tissue tracer uptake (37 mins post injection - which was about 0.1% of total volume injected).

Following these confirmatory experiments, confidence was raised in VECTOR pathway, however, the relatively high dose of the MRI platform would be problematic for a possible future clinical translation (considering the recent safety concerns of

gadolinium retention in the brain). Attempts were therefore made to investigate the possibility of imaging VECTOR pathway with half, third and fifth (5, 3 and 2 mmol/kg respectively) of the initial dose. VECTOR pathway was successfully imaged with half and third of the initial dose, although not as readily as the high dose platform due to lower tissue GBCA uptake (i.e. weaker signal enhancement). In terms of gadolinium safety, a 3 mmol/kg dose is equivalent to approximately only two standard clinical CE-MRI examinations (based upon body surface area normalisation between mice and humans). VECTOR pathway could not be imaged with any dose lower than this as differentiation of GBCA-induced signal changes that originate from GBCA in the tissue versus the signal changes that originate from GBCAs in the intravascular compartment (and therefore meaningful characterisation of brain tissue GBCA uptake patterns) was not possible.

VECTOR pathway imaging using the original 3D T_1-weighted gradient-echo sequence (that utilised a relatively high GBCA dose - 10 mmol/kg) was limited to 37 minutes post contrast injection. After this time, positive contrast is generated in the intravascular compartment due to systemic GBCA clearance (and the corresponding recovery of T_2/T_2* values), hence it was not possible to meaningfully separate GBCA-induced signal changes that originate from GBCA in the tissue versus the signal changes that originate from GBCAs in the intravascular compartment. In order to extend VECTOR pathway imaging window beyond 37 mins post contrast injection, an MRI sequence markedly less sensitive to time-varying intravascular contributions was devised. A diffusion-weighted sequence was developed that was designed for the effective nulling of blood vessel signal (by the application of diffusion crushers). Application of the new diffusion-weighted MRI sequence to a cohort of healthy animals, extended imaging of VECTOR pathway (i.e. 125 mins) and revealed a more diffuse, brain-wide transport/uptake of GBCA in the tissue.

In the final chapter, attempts were made to assess VECTOR pathway's sensitivity to modulations in CSF-ISF exchange. In that chapter, pharmacological intervention using the anti-diuretic hormone vasopressin, profoundly altered VECTOR pathway's fluid dynamics evident by significant MRI signal increase in the brain (compared to the controls). In order to further investigate these MRI findings, tau protein was surgically injected in the brains of healthy mice and clearance from the brain was assessed following pharmacological intervention with vasopressin. These experiments confirmed the previous MRI findings as a significantly higher amount of tau was present in the brain tissue compared to controls (suggestive of a retentive effect of vasopressin on VECTOR pathway). Next, with the ultimate goal of improving

brain clearance (i.e. identification of effective therapeutic strategies), clearance of tau protein from the brain was assessed following pharmacological intervention with mannitol, a diuretic hormone with hypothesised opposite mechanism of action to vasopressin. Mannitol therapy significantly enhanced tau clearance from the brain tissue compared to controls, providing promise towards development of effective therapeutic strategies that may slow down disease progression.

7.2 Limitations and future directions

Overall, data presented in this thesis suggest that the imaging and analysis methodology introduced here may represent potential non-invasive biomarker of neurodegenerative conditions. Towards this goal, there are a number of limitations/challenges in the current pre-clinical setting that need to be considered for potential translation to the clinical setting. In this study, the MRI GBCA dose that could readily identify the VECTOR pathway was 10 mmol/kg, which is equivalent to 8 times the standard clinical dose. Clinical VECTOR pathway imaging with such GBCA dose may be considered unethical considering recent safety concerns of gadolinium retention in the brain. A solution could be to utilise macrocyclic instead of linear GBCAs to minimise the amount of gadolinium retention in the brain (a linear chemical structure was utilised throughout this study in the interest of consistency - the majority of the MRI experiments in this PhD projected were conducted prior to the suspension of Omniscan in the UK by the Medicines and Healthcare Products Regulatory Agency (MHRA) in February 2018). In fact, for routine clinical use, only macrocyclic contrast agents are now approved by the FDA. Hence, imaging the VECTOR pathway with macrocyclic GBCAs is an interesting avenue of future research. Despite the relatively high safety profile of macrocyclic contrast agents (high stability and low dissociation rates), it is still desirable to further reduce the GBCA dose of the platform. In this study, the VECTOR pathway was successfully imaged with GBCA dose as low as 3 mmol/kg (about 2.5 times the standard clinical dose) using a T_1-weighted sequence, A diffusion-weighted sequence was next developed that significantly reduced intravascular signal contributions (compared to the T_1-weighted sequence) and thus provides the potential to image VECTOR pathway with lower and more clinically relevant GBCA doses (this is theoretically feasible as the diffusion-weighted sequence nulls the intravascular signal (i.e. no time-varying signal intensity changes) and therefore GBCA-induced signal changes that originate from GBCA in the tissue (extravascular compartment) can be readily identified without the need for the induction of intravascular susceptibility effects (i.e. high GBCA doses) - a condition that was required for the separation of GBCA-induced signal changes that originate

from GBCA in the tissue versus the signal changes that originate from GBCAs in the intravascular compartment when imaging VECTOR with the T_1-weighted sequence). Whether VECTOR pathway, using the new diffusion-weighted sequence, could be imaged with a GBCA dose lower than 3 mmol/kg, will be the avenue of future research.

Imposed as a result of high GBCA dose (and the resulting signal reducing susceptibility effects), a limitation of the study was that the MR images (both T_1-weighted and DW-SEMS sequences) represented a conservative view of CSF-ISF exchange in the brain. For example, signal hyperintensity (tracer uptake) was detected around the edges (surface) of the brain by the autoradiography and LA-ICP-MS techniques (which possibly represents glymphatic related subarachnoid/perivascular CSF/GBCA influx into the brain parenchyma), that could not be observed on the MR images. As described earlier, the diffusion-weighted sequence provides the potential to image VECTOR pathway with lower and more clinically relevant GBCA doses (where susceptibility effects are weaker), whether the diffusion-weighted sequence is able to capture tracer uptake (signal hyperintensity) around the edges of the brain when imaging with lower GBCA doses would be an interesting avenue of research (the relatively lower spatial resolution of this sequence however, may be a limiting factor when imaging GBCA in the fine paravascular channels and subarachnoid spaces).

It is still debated how solutes and macromolecules are removed from the brain's interstitial space and whether transport is facilitated by bulk flow (convection), diffusion or a combination of the two. Classically, solute transport in the brain extracellular space has been thought to be primarily diffusive and nondirectional (Katzman, Schimmel and Wilson, 1968, Fenstermacher and Patlak, 1976, Ichimura, Fraser and Cserr, 1991). Recently however, evidence suggestive of a convective interstitial solute transport, driven by active fluid transport mechanisms has been provided, such as the glymphatic hypothesis (Iliff *et al*., 2012). The methodological complexities associated with these invasive measurements of CSF-ISF exchange dynamics (such as injection of bulk fluid into the brain's microenvironment), is believed to be a central reason for the discrepancies in the experimental data in this field. In this study, assessment of the rate of interstitial fluid transport was not conducted primarily due to induced negative contrast (relative to baseline) in the intravascular compartment (i.e. the signal lowering susceptibility effect). The susceptibility effect reduces sensitivity to brain tissue GBCA uptake by introducing false negatives (as PVEs from blood vessels (e.g. the capillary bed) inevitably affect

brain tissue voxels) and therefore it may lead to an underestimated rate of interstitial solute transport. However, as described earlier, imaging VECTOR pathway with a lower GBCA dose is theoretically feasible with the described diffusion-weighted sequence where signal lowering susceptibility effects are minimised. The diffusion-weighted sequence may therefore provide the opportunity to measure a more robust estimate of the rate of interstitial solute transport (which will be the avenue of future investigation).

Finally, the sensitivity of the potential VECTOR biomarker compared to current clinical biomarkers of dementia should be explored. It would be interesting to investigate whether VECTOR abnormalities precede abnormalities associated with other biomarkers of dementia and how it fits into the dynamic biomarker model of the AD pathological cascade introduced in section 1.2.4.

References

Abramoff, M.D., Magelhaes, P.J., and Ram, S.J. (2004). Image Processing with ImageJ. Biophotonics International 11, 36–42.

Allen, L. M., Hasso, A. N., Handwerker, J., & Farid, H. (2012). Sequence-specific MR Imaging Findings That Are Useful in Dating Ischemic Stroke. RadioGraphics, 32(5), 1285–1297. https://doi.org/10.1148/rg.325115760

Alsop, D. C., Detre, J. A., Golay, X., Günther, M., Hendrikse, J., Hernandez-Garcia, L., … Zaharchuk, G. (2015). Recommended implementation of arterial spin-labeled perfusion MRI for clinical applications: A consensus of the ISMRM perfusion study group and the European consortium for ASL in dementia. Magnetic resonance in medicine, 73(1), 102–116. doi:10.1002/mrm.25197

Amiry-Moghaddam, M., Xue, R., Haug, F.-M., Neely, J. D., Bhardwaj, A., Agre, P., … Ottersen, O. P. (2004). Alpha-syntrophin deletion removes the perivascular but not endothelial pool of aquaporin-4 at the blood–brain barrier and delays the development of brain edema in an experimental model of acute hyponatremia. The FASEB Journal, 18(3), 542–544. https://doi.org/10.1096/fj.03-0869fje

Andreasen, N., & Blennow, K. (2005). CSF biomarkers for mild cognitive impairment and early Alzheimer's disease. Clinical Neurology and Neurosurgery, 107(3), 165–173. https://doi.org/10.1016/j.clineuro.2004.10.011

Asgari, M., de Zélicourt, D., & Kurtcuoglu, V. (2016). Glymphatic solute transport does not require bulk flow. Scientific reports, 6, 38635. doi:10.1038/srep38635

Bakshi, R., Ariyaratana, S., Benedict, R. H. B., & Jacobs, L. (2001). Fluid-Attenuated Inversion Recovery Magnetic Resonance Imaging Detects Cortical and Juxtacortical Multiple Sclerosis Lesions. Archives of Neurology, 58(5), 742. https://doi.org/10.1001/archneur.58.5.742

Baranyai, Z., Brücher, E., Uggeri, F., Maiocchi, A., Tóth, I., Andrási, M., … Aime, S. (2015). The Role of Equilibrium and Kinetic Properties in the Dissociation of Gd[DTPA-bis(methylamide)] (Omniscan) at near to Physiological Conditions. Chemistry - A European Journal, 21(12), 4789–4799. https://doi.org/10.1002/chem.201405967

Bartus, R., Dean, R., Beer, B., & Lippa, A. (1982). The cholinergic hypothesis of geriatric memory dysfunction. Science, 217(4558), 408–414. https://doi.org/10.1126/science.7046051

Bateman, R. J., Xiong, C., Benzinger, T. L., Fagan, A. M., Goate, A., Fox, N. C., … Dominantly Inherited Alzheimer Network (2012). Clinical and biomarker changes in dominantly inherited Alzheimer's disease. The New England journal of medicine, 367(9), 795–804. doi:10.1056/NEJMoa1202753

Bayram, E., Caldwell, J., & Banks, S. J. (2018). Current understanding of magnetic resonance imaging biomarkers and memory in Alzheimer's disease. Alzheimer's & dementia (New York, N. Y.), 4, 395–413. doi:10.1016/j.trci.2018.04.007

Bedussi, B., van Lier, M. G. J. T. B., Bartstra, J. W., de Vos, J., Siebes, M., VanBavel, E., & Bakker, E. N. T. P. (2015). Clearance from the mouse brain by convection of interstitial fluid towards the ventricular system. Fluids and Barriers of the CNS, 12(1). https://doi.org/10.1186/s12987-015-0019-5

Benfenati, V., Caprini, M., Dovizio, M., Mylonakou, M. N., Ferroni, S., Ottersen, O. P., & Amiry-Moghaddam, M. (2011). An aquaporin-4/transient receptor potential vanilloid 4 (AQP4/TRPV4) complex is essential for cell-volume control in astrocytes. Proceedings of the National Academy of Sciences, 108(6), 2563–2568. https://doi.org/10.1073/pnas.1012867108

Benveniste, H., Lee, H., Ding, F., Sun, Q., Al-Bizri, E., Makaryus, R., … Lu, H. (2017). Anesthesia with Dexmedetomidine and Low-dose Isoflurane Increases Solute Transport via the Glymphatic Pathway in Rat Brain When Compared with High-dose Isoflurane. Anesthesiology, 127(6), 976–988. https://doi.org/10.1097/aln.0000000000001888

Bierer, L. M., Hof, P. R., Purohit, D. P., Carlin, L., Schmeidler, J., Davis, K. L., & Perl, D. P. (1995). Neocortical Neurofibrillary Tangles Correlate With Dementia Severity in Alzheimer’s Disease. Archives of Neurology, 52(1), 81–88. https://doi.org/10.1001/archneur.1995.00540250089017

Birks, J. S. (2006). Cholinesterase inhibitors for Alzheimer’s disease. (J. S. Birks, Ed.), Cochrane Database of Systematic Reviews. John Wiley & Sons, Ltd. https://doi.org/10.1002/14651858.cd005593

Blennow, K., & Hampel, H. (2003). CSF markers for incipient Alzheimer’s disease. The Lancet Neurology, 2(10), 605–613. https://doi.org/10.1016/s1474-4422(03)00530-1

Blennow, K., & Zetterberg, H. (2009). Cerebrospinal Fluid Biomarkers for Alzheimer's Disease. Journal of Alzheimer's Disease, 18(2), 413–417. https://doi.org/10.3233/JAD-2009-1177

Boyken, J., Frenzel, T., Lohrke, J., Jost, G., Schütz, G., & Pietsch, H. (2019). Impact of Treatment With Chelating Agents Depends on the Stability of Administered GBCAs: A Comparative Study in Rats. Investigative radiology, 54(2), 76–82. doi:10.1097/RLI.0000000000000522

Bozzao, A., Floris, R., Baviera, M.E., Apruzzese, A., & Simonetti, G. (2001). Diffusion and perfusion MR imaging in cases of Alzheimer's disease: correlations with cortical atrophy and lesion load. AJNR. American journal of neuroradiology, 22 6, 1030-6.

Braak, H., & Braak, E. (1997). Frequency of Stages of Alzheimer-Related Lesions in Different Age Categories. Neurobiology of Aging, 18(4), 351–357. https://doi.org/10.1016/s0197-4580(97)00056-0

Bradbury, M. W., Cserr, H. F., & Westrop, R. J. (1981). Drainage of cerebral interstitial fluid into deep cervical lymph of the rabbit. American Journal of Physiology-Renal Physiology, 240(4), F329–F336. https://doi.org/10.1152/ajprenal.1981.240.4.f329

Brett M., Anton J.-L., Valabregue R., Poline J.-B. (2002). Region of Interest Analysis Using the MarsBar Toolbox for SPM 99.

Brightman, M. W. (1965). The distribution within the brain of ferritin injected into cerebrospinal fluid compartments. II. Parenchymal distribution. American Journal of Anatomy, 117(2), 193–219. https://doi.org/10.1002/aja.1001170204

Brown, M., Semelka, R., John Wiley & Sons, & Wiley-Blackwell. (2003). MRI : Basic principles and applications / Mark A. Brown [and] Richard C. Semelka. (3rd ed.). Hoboken, N.J.: Wiley-Liss.

Brunden, K. R., Zhang, B., Carroll, J., Yao, Y., Potuzak, J. S., Hogan, A. M., … Trojanowski, J. Q. (2010). Epothilone D improves microtubule density, axonal integrity, and cognition in a transgenic mouse model of tauopathy. The Journal of neuroscience : the official journal of the Society for Neuroscience, 30(41), 13861–13866. doi:10.1523/JNEUROSCI.3059-10.2010

Buchhave, P., Blennow, K., Zetterberg, H., Stomrud, E., Londos, E., Andreasen, N., … Hansson, O. (2009). Longitudinal study of CSF biomarkers in patients with Alzheimer's disease. PloS one, 4(7), e6294. doi:10.1371/journal.pone.0006294

Burdette, J. H., Durden, D. D., Elster, A. D., & Yen, Y.-F. (2001). High b-Value Diffusion-Weighted MRI of Normal Brain. Journal of Computer Assisted Tomography, 25(4), 515–519. https://doi.org/10.1097/00004728-200107000-00002

Burns, B.L. (2014). Sparse Image Reconstruction and Artifact Correction of Multi-Dimensional Spectroscopic Imaging Data.

Butterfield, D. A., & Pocernich, C. B. (2003). The Glutamatergic System and Alzheimer's Disease. CNS Drugs, 17(9), 641–652. https://doi.org/10.2165/00023210-200317090-00004

Carare, R. O., Bernardes-Silva, M., Newman, T. A., Page, A. M., Nicoll, J. A. R., Perry, V. H., & Weller, R. O. (2008). Solutes, but not cells, drain from the brain parenchyma along basement membranes of capillaries and arteries: significance for cerebral amyloid angiopathy and neuroimmunology. Neuropathology and Applied Neurobiology, 34(2), 131–144. https://doi.org/10.1111/j.1365-2990.2007.00926.x

Caravan, P., Ellison, J. J., McMurry, T. J., & Lauffer, R. B. (1999). Gadolinium(III) Chelates as MRI Contrast Agents: Structure, Dynamics, and Applications. Chemical Reviews, 99(9), 2293–2352. https://doi.org/10.1021/cr980440x

Chen, K.-B., Wei, V. C., Yen, L. F., Poon, K.-S., Liu, Y.-C., Cheng, K.-S., … Lai, T. W. (2013). Intravenous mannitol does not increase blood–brain barrier permeability to inert dyes in the adult rat forebrain. NeuroReport, 24(6), 303–307. https://doi.org/10.1097/wnr.0b013e32835f8acb

Chilla, G. S., Tan, C. H., Xu, C., & Poh, C. L. (2015). Diffusion weighted magnetic resonance imaging and its recent trend-a survey. Quantitative imaging in medicine and surgery, 5(3), 407–422. doi:10.3978/j.issn.2223-4292.2015.03.01

Chugh, B. P., Lerch, J. P., Yu, L. X., Pienkowski, M., Harrison, R. V., Henkelman, R. M., & Sled, J. G. (2009). Measurement of cerebral blood volume in mouse brain regions using micro-computed tomography. NeuroImage, 47(4), 1312–1318. https://doi.org/10.1016/j.neuroimage.2009.03.083

Clarkson, M. J., Zombori, G., Thompson, S., Totz, J., Song, Y., Espak, M., … Ourselin, S. (2015). The NifTK software platform for image-guided interventions: platform overview and NiftyLink messaging. International Journal of Computer

Assisted Radiology and Surgery, 10(3), 301–316. https://doi.org/10.1007/s11548-014-1124-7

Cohen, A. D., & Klunk, W. E. (2014). Early detection of Alzheimer's disease using PiB and FDG PET. Neurobiology of disease, 72 Pt A, 117–122. doi:10.1016/j.nbd.2014.05.001

Cserr, H. F. (1965). Potassium exchange between cerebrospinal fluid, plasma, and brain. American Journal of Physiology-Legacy Content, 209(6), 1219–1226. https://doi.org/10.1152/ajplegacy.1965.209.6.1219

Cserr, H. F. (1988). Role of Secretion and Bulk Flow of Brain Interstitial Fluid in Brain Volume Regulation. Annals of the New York Academy of Sciences, 529(1 Fourth Colloq), 9–20. https://doi.org/10.1111/j.1749-6632.1988.tb51415.x

Cserr, H. F., Cooper, D. N., & Milhorat, T. H. (1977). Flow of cerebral interstitial fluid as indicated by the removal of extracellular markers from rat caudate nucleus. Experimental Eye Research, 25, 461–473. https://doi.org/10.1016/s0014-4835(77)80041-9

Cserr, H. F., Harling-Berg, C. J., & Knopf, P. M. (1992). Drainage of Brain Extracellular Fluid into Blood and Deep Cervical Lymph and its Immunological Significance. Brain Pathology, 2(4), 269–276. https://doi.org/10.1111/j.1750-3639.1992.tb00703.x

Davies, P., & Maloney, A. J. F. (1976). Selective Loss of Central Cholinergic Neurons in Alzheimer’s Disease. The Lancet, 308(8000), 1403. https://doi.org/10.1016/s0140-6736(76)91936-x

Davis, K. L., Mohs, R. C., Marin, D., Purohit, D.P., Perl, D. P., Lantz, M., … Haroutunian, V. (1999). Cholinergic Markers in Elderly Patients With Early Signs of Alzheimer Disease. JAMA, 281(15), 1401. https://doi.org/10.1001/jama.281.15.1401

de Figueiredo, E. H. M. S. G., Borgonovi, A. F. N. G., & Doring, T. M. (2011). Basic Concepts of MR Imaging, Diffusion MR Imaging, and Diffusion Tensor Imaging. Magnetic Resonance Imaging Clinics of North America, 19(1), 1–22. https://doi.org/10.1016/j.mric.2010.10.005

de la Torre, J. C. (2002). Alzheimer Disease as a Vascular Disorder. Stroke, 33(4), 1152–1162. https://doi.org/10.1161/01.str.0000014421.15948.67

Deike-Hofmann, K., Reuter, J., Haase, R., Paech, D., Gnirs, R., Bickelhaupt, S., … Radbruch, A. (2019). Glymphatic Pathway of Gadolinium-Based Contrast Agents Through the Brain. Investigative Radiology, 54(4), 229–237. https://doi.org/10.1097/rli.0000000000000533

Dong, S., Duan, Y., Hu, Y., & Zhao, Z. (2012). Advances in the pathogenesis of Alzheimer's disease: a re-evaluation of amyloid cascade hypothesis. Translational neurodegeneration, 1(1), 18. doi:10.1186/2047-9158-1-18

Dorr, A., Sled, J. G., & Kabani, N. (2007). Three-dimensional cerebral vasculature of the CBA mouse brain: A magnetic resonance imaging and micro computed tomography study. NeuroImage, 35(4), 1409–1423. https://doi.org/10.1016/j.neuroimage.2006.12.040

Dumas, S., Jacques, V., Sun, W.-C., Troughton, J. S., Welch, J. T., Chasse, J. M., … Caravan, P. (2010). High Relaxivity Magnetic Resonance Imaging Contrast Agents Part 1. Investigative Radiology, 45(10), 600–612. https://doi.org/10.1097/rli.0b013e3181ee5a9e

Ebrahimi, P., & Barbieri, M. (2019). Gadolinium as an Emerging Microcontaminant in Water Resources: Threats and Opportunities. Geosciences, 9(2), 93. https://doi.org/10.3390/geosciences9020093

Errante, Y., Cirimele, V., Mallio, C. A., Di Lazzaro, V., Zobel, B. B., & Quattrocchi, C. C. (2014). Progressive Increase of T1 Signal Intensity of the Dentate Nucleus on Unenhanced Magnetic Resonance Images Is Associated With Cumulative Doses of Intravenously Administered Gadodiamide in Patients With Normal Renal Function, Suggesting Dechelation. Investigative Radiology, 49(10), 685–690. https://doi.org/10.1097/rli.0000000000000072

Ewers, M., Sperling, R. A., Klunk, W. E., Weiner, M. W., & Hampel, H. (2011). Neuroimaging markers for the prediction and early diagnosis of Alzheimer’s disease dementia. Trends in Neurosciences, 34(8), 430–442. https://doi.org/10.1016/j.tins.2011.05.005

Fenstermacher, J. D., & Patlak, C. S. (1976). The Movements of Water and Solutes in the Brains of Mammals. In Dynamics of Brain Edema (pp. 87–94). Springer Berlin Heidelberg. https://doi.org/10.1007/978-3-642-66524-0_16

Ferré, J.-C., Bannier, E., Raoult, H., Mineur, G., Carsin-Nicol, B., & Gauvrit, J.-Y. (2013). Arterial spin labeling (ASL) perfusion: Techniques and clinical use.

Diagnostic and Interventional Imaging, 94(12), 1211–1223. https://doi.org/10.1016/j.diii.2013.06.010

Fiorelli, R., Azim, K., Fischer, B., & Raineteau, O. (2015). Adding a spatial dimension to postnatal ventricular-subventricular zone neurogenesis. Development, 142(12), 2109–2120. https://doi.org/10.1242/dev.119966

Flett, A. S., Hayward, M. P., Ashworth, M. T., Hansen, M. S., Taylor, A. M., Elliott, P. M., … Moon, J. C. (2010). Equilibrium Contrast Cardiovascular Magnetic Resonance for the Measurement of Diffuse Myocardial Fibrosis. Circulation, 122(2), 138–144. https://doi.org/10.1161/circulationaha.109.930636

Forman, M. S., Farmer, J., Johnson, J. K., Clark, C. M., Arnold, S. E., Coslett, H. B., … Grossman, M. (2006). Frontotemporal dementia: clinicopathological correlations. Annals of neurology, 59(6), 952–962. doi:10.1002/ana.20873

Francis, P. T., Palmer, A. M., Snape, M., & Wilcock, G. K. (1999). The cholinergic hypothesis of Alzheimer's disease: a review of progress. Journal of Neurology, Neurosurgery & Psychiatry, 66(2), 137–147. https://doi.org/10.1136/jnnp.66.2.137

Frenzel, T., Lengsfeld, P., Schirmer, H., Hütter, J., & Weinmann, H.-J. (2008). Stability of Gadolinium-Based Magnetic Resonance Imaging Contrast Agents in Human Serum at 37°C. Investigative Radiology, 43(12), 817–828. https://doi.org/10.1097/rli.0b013e3181852171

Frisoni, G. B., Fox, N. C., Jack, C. R., Scheltens, P., & Thompson, P. M. (2010). The clinical use of structural MRI in Alzheimer disease. Nature Reviews Neurology, 6(2), 67–77. https://doi.org/10.1038/nrneurol.2009.215

Fry, M., Hoyda, T. D., & Ferguson, A. V. (2007). Making Sense of It: Roles of the Sensory Circumventricular Organs in Feeding and Regulation of Energy Homeostasis. Experimental Biology and Medicine, 232(1), 14–26.

Gage, G. J., Kipke, D. R., & Shain, W. (2012). Whole Animal Perfusion Fixation for Rodents. Journal of Visualised Experiments, (65). https://doi.org/10.3791/3564

Garcia, J., Liu, S. Z., & Louie, A. Y. (2017). Biological effects of MRI contrast agents: gadolinium retention, potential mechanisms and a role for phosphorus. Philosophical Transactions of the Royal Society A: Mathematical, Physical and Engineering Sciences, 375(2107), 20170180. https://doi.org/10.1098/rsta.2017.0180

Garcia, M. L., & Cleveland, D. W. (2001). Going new places using an old MAP: tau, microtubules and human neurodegenerative disease. Current Opinion in Cell Biology, 13(1), 41–48. https://doi.org/10.1016/s0955-0674(00)00172-1

Gauthier, S., Reisberg, B., Zaudig, M., Petersen, R. C., Ritchie, K., Broich, K., … Winblad, B. (2006). Mild cognitive impairment. The Lancet, 367(9518), 1262–1270. https://doi.org/10.1016/s0140-6736(06)68542-5

Goate, A., Chartier-Harlin, M.-C., Mullan, M., Brown, J., Crawford, F., Fidani, L., … Hardy, J. (1991). Segregation of a missense mutation in the amyloid precursor protein gene with familial Alzheimer's disease. Nature, 349(6311), 704–706. https://doi.org/10.1038/349704a0

Gomez, D. G., Manzo, R. P., Fenstermacher, J. D., & Potts, D. G. (1988). Cerebrospinal fluid absorption in the rabbit. Graefe's Archive for Clinical and Experimental Ophthalmology, 226(1), 1–7. https://doi.org/10.1007/bf02172707

Graeber, M. B., Kösel, S., Egensperger, R., Banati, R. B., Müller, U., Bise, K., … Mehraein, P. (1997). Rediscovery of the case described by Alois Alzheimer in 1911: historical, histological and molecular genetic analysis. Neurogenetics, 1(1), 73–80. https://doi.org/10.1007/s100480050011

Grainger, R. G. (1980). Osmolality of intravascular radiological contrast media. The British Journal of Radiology, 53(632), 739–746. https://doi.org/10.1259/0007-1285-53-632-739

Hardy, J., & Higgins, G. (1992). Alzheimer's disease: the amyloid cascade hypothesis. Science, 256(5054), 184–185. https://doi.org/10.1126/science.1566067

Hayakawa, K., Morris, T. M., & Katzberg, R. W. (1989). Opening of the Blood-Brain Barrier by Intravenous Contrast Media in Euvolemic and Dehydrated Rabbits. Acta Radiologica, 30(4), 439–444. https://doi.org/10.1177/028418518903000421

Hays, C. C., Zlatar, Z. Z., & Wierenga, C. E. (2016). The Utility of Cerebral Blood Flow as a Biomarker of Preclinical Alzheimer's Disease. Cellular and molecular neurobiology, 36(2), 167–179. doi:10.1007/s10571-015-0261-z

Heisey, S. R., Held, D., & Pappenheimer, J. R. (1962). Bulk flow and diffusion in the cerebrospinal fluid system of the goat. American Journal of Physiology-Legacy Content, 203(5), 775–781. https://doi.org/10.1152/ajplegacy.1962.203.5.775

Hirano, A., Cervós-Navarro, J., & Ohsugi, T. (1976). Capillaries in the subarachnoid space. Acta Neuropathologica, 34(1), 81–85. https://doi.org/10.1007/bf00684947

Hollingworth, P., Harold, D., Sims, R., Gerrish, A., Lambert, J. C., Carrasquillo, M. M., … Williams, J. (2011). Common variants at ABCA7, MS4A6A/MS4A4E, EPHA1, CD33 and CD2AP are associated with Alzheimer's disease. Nature genetics, 43(5), 429–435. doi:10.1038/ng.803

Holter, K. E., Kehlet, B., Devor, A., Sejnowski, T. J., Dale, A. M., Omholt, S. W., … Pettersen, K. H. (2017). Interstitial solute transport in 3D reconstructed neuropil occurs by diffusion rather than bulk flow. Proceedings of the National Academy of Sciences, 114(37), 9894–9899. https://doi.org/10.1073/pnas.1706942114

Hutton, M., Lendon, C. L., Rizzu, P., Baker, M., Froelich, S., Houlden, H., … Heutink, P. (1998). Association of missense and 5′-splice-site mutations in tau with the inherited dementia FTDP-17. Nature, 393(6686), 702–705. https://doi.org/10.1038/31508

Ichimura, T., Fraser, P. A., & Cserr, H. F. (1991). Distribution of extracellular tracers in perivascular spaces of the rat brain. Brain Research, 545(1–2), 103–113. https://doi.org/10.1016/0006-8993(91)91275-6

Iliff, J. J., Wang, M., Liao, Y., Plogg, B. A., Peng, W., Gundersen, G. A., … Nedergaard, M. (2012). A Paravascular Pathway Facilitates CSF Flow Through the Brain Parenchyma and the Clearance of Interstitial Solutes, Including Amyloid. Science Translational Medicine, 4(147), 147ra111-147ra111. https://doi.org/10.1126/scitranslmed.3003748

Imazio, M., Andriani, M., Lobetti Bodoni, L., & Gaita, F. (2019). Learning Cardiac Magnetic Resonance. Springer International Publishing. https://doi.org/10.1007/978-3-030-11608-8

Ishii, K. (2013). PET Approaches for Diagnosis of Dementia. American Journal of Neuroradiology, 35(11), 2030–2038. https://doi.org/10.3174/ajnr.a3695

Jack, C. R., Jr, Knopman, D. S., Jagust, W. J., Petersen, R. C., Weiner, M. W., Aisen, P. S., … Trojanowski, J. Q. (2013). Tracking pathophysiological processes in Alzheimer’s disease: an updated hypothetical model of dynamic biomarkers. The Lancet Neurology, 12(2), 207–216. https://doi.org/10.1016/s1474-4422(12)70291-0

Jack, C. R., Jr, Knopman, D. S., Jagust, W. J., Shaw, L. M., Aisen, P. S., Weiner, M. W., … Trojanowski, J. Q. (2010). Hypothetical model of dynamic biomarkers of the

Alzheimer’s pathological cascade. The Lancet Neurology, 9(1), 119–128. https://doi.org/10.1016/s1474-4422(09)70299-6

Jackson, R. T., Tigges, J., & Arnold, W. (1979). Subarachnoid Space of the CNS, Nasal Mucosa, and Lymphatic System. Archives of Otolaryngology - Head and Neck Surgery, 105(4), 180–184. https://doi.org/10.1001/archotol.1979.00790160014003

Jessen, N. A., Munk, A. S., Lundgaard, I., & Nedergaard, M. (2015). The Glymphatic System: A Beginner's Guide. Neurochemical research, 40(12), 2583–2599. doi:10.1007/s11064-015-1581-6

Jha, S. (2003). Cerebral Edema and its Management. Medical Journal Armed Forces India, 59(4), 326–331. https://doi.org/10.1016/s0377-1237(03)80147-8

Jiang, Q., Zhang, L., Ding, G., Davoodi-Bojd, E., Li, Q., Li, L., … Zhang, Z. (2017). Impairment of the glymphatic system after diabetes. Journal of Cerebral Blood Flow & Metabolism, 37(4), 1326–1337. https://doi.org/10.1177/0271678x16654702

Jo, A. O., Ryskamp, D. A., Phuong, T. T. T., Verkman, A. S., Yarishkin, O., MacAulay, N., & Kri aj, D. (2015). TRPV4 and AQP4 Channels Synergistically Regulate Cell Volume and Calcium Homeostasis in Retinal Muller Glia. Journal of Neuroscience, 35(39), 13525–13537. https://doi.org/10.1523/jneurosci.1987-15.2015

Jost, G., Frenzel, T., Lohrke, J., Lenhard, D. C., Naganawa, S., & Pietsch, H. (2017). Penetration and distribution of gadolinium-based contrast agents into the cerebrospinal fluid in healthy rats: a potential pathway of entry into the brain tissue. European radiology, 27(7), 2877–2885. doi:10.1007/s00330-016-4654-2

Jost, G., Lenhard, D. C., Sieber, M. A., Lohrke, J., Frenzel, T., & Pietsch, H. (2016). Signal Increase on Unenhanced T1-Weighted Images in the Rat Brain After Repeated, Extended Doses of Gadolinium-Based Contrast Agents. Investigative Radiology, 51(2), 83–89. https://doi.org/10.1097/rli.0000000000000242

Kanda, T., Ishii, K., Kawaguchi, H., Kitajima, K., & Takenaka, D. (2014). High Signal Intensity in the Dentate Nucleus and Globus Pallidus on Unenhanced T1-weighted MR Images: Relationship with Increasing Cumulative Dose of a Gadolinium-based Contrast Material. Radiology, 270(3), 834–841. https://doi.org/10.1148/radiol.13131669

Kanda, T., Osawa, M., Oba, H., Toyoda, K., Kotoku, J., Haruyama, T., … Furui, S. (2015). High Signal Intensity in Dentate Nucleus on Unenhanced T1-weighted MR Images: Association with Linear versus Macrocyclic Gadolinium Chelate Administration. Radiology, 275(3), 803–809. https://doi.org/10.1148/radiol.14140364

Katzman R., Schimmel, H., & Wilson, C. E. (1968). Diffusion of inulin as a measure of extracellular fluid space in brain. Proc. Rudolf Virchow Medical Society, City of New York, Suppl. to Vol. 26, pp. 254–280

Key, G., Retzius, A. (1875). Anatomie des Nerveusystems und des Bindegewebes, Stockholm

Kida, S., Pantazis, A., & Weller, R. O. (1993). CSF drains directly from the subarachnoid space into nasal lymphatics in the rat. Anatomy, histology and immunological significance. Neuropathology and Applied Neurobiology, 19(6), 480–488. https://doi.org/10.1111/j.1365-2990.1993.tb00476.x

Kilkenny, C., Browne, W. J., Cuthill, I. C., Emerson, M., & Altman, D. G. (2010). Improving Bioscience Research Reporting: The ARRIVE Guidelines for Reporting Animal Research. PLoS Biology, 8(6), e1000412. https://doi.org/10.1371/journal.pbio.1000412

Koh, L., Zakharov, A., & Johnston, M. (2005). Integration of the subarachnoid space and lymphatics: is it time to embrace a new concept of cerebrospinal fluid absorption?. Cerebrospinal fluid research, 2, 6. doi:10.1186/1743-8454-2-6

Kulaksız, S., & Bau, M. (2011). Anthropogenic gadolinium as a microcontaminant in tap water used as drinking water in urban areas and megacities. Applied Geochemistry, 26(11), 1877–1885. https://doi.org/10.1016/j.apgeochem.2011.06.011

Lambert, J.-C., Heath, S., Even, G., Campion, D., Sleegers, K., … Amouyel, P. (2009). Genome-wide association study identifies variants at CLU and CR1 associated with Alzheimer's disease. Nature Genetics, 41(10), 1094–1099. https://doi.org/10.1038/ng.439

Laterra, J., Keep, R., Betz, L. A., & Goldstein, G. W. (1999). Blood—Cerebrospinal Fluid Barrier. In: Siegel, G. J., Agranoff, B. W., Albers, R. W., Fisher, S. K., & Uhler, M. D. Basic Neurochemistry: Molecular, Cellular and Medical Aspects. 6th edition. Philadelphia: Lippincott-Raven. https://www.ncbi.nlm.nih.gov/books/NBK27998/

Le Bihan, D. (2019). What can we see with IVIM MRI? NeuroImage, 187, 56–67. https://doi.org/10.1016/j.neuroimage.2017.12.062

Ledneva, E., Karie, S., Launay-Vacher, V., Janus, N., & Deray, G. (2009). Renal Safety of Gadolinium-based Contrast Media in Patients with Chronic Renal Insufficiency. Radiology, 250(3), 618–628. https://doi.org/10.1148/radiol.2503080253

Lein, E. S., Hawrylycz, M. J., Ao, N., Ayres, M., Bensinger, A., Bernard, A., … Jones, A. R. (2007). Genome-wide atlas of gene expression in the adult mouse brain. Nature, 445(7124), 168–176. https://doi.org/10.1038/nature05453

Louveau, A., Smirnov, I., Keyes, T. J., Eccles, J. D., Rouhani, S. J., Peske, J. D., … Kipnis, J. (2015). Structural and functional features of central nervous system lymphatic vessels. Nature, 523(7560), 337–341. doi:10.1038/nature14432

Lyons, J., Brooks, N., Cattell, M., Isolani-Smyth, E., & Balcon, R. (1984). Comparison of Hexabrix 320 and Conray 420 for left ventriculography in patients with coronary artery disease. The British Journal of Radiology, 57(675), 209–211. https://doi.org/10.1259/0007-1285-57-675-209

Maccioni, R. B., Farías, G., Morales, I., & Navarrete, L. (2010). The Revitalized Tau Hypothesis on Alzheimer's Disease. Archives of Medical Research, 41(3), 226–231. https://doi.org/10.1016/j.arcmed.2010.03.007

Maness, L. M., Kastin, A. J., & Banks, W. A. (1998). Relative contributions of a CVO and the microvascular bed to delivery of blood-borne IL-1α to the brain. American Journal of Physiology-Endocrinology and Metabolism, 275(2), E207–E212. https://doi.org/10.1152/ajpendo.1998.275.2.e207

Manley, G. T., Fujimura, M., Ma, T., Noshita, N., Filiz, F., Bollen, A. W., … Verkman, A. S. (2000). Aquaporin-4 deletion in mice reduces brain edema after acute water intoxication and ischemic stroke. Nature Medicine, 6(2), 159–163. https://doi.org/10.1038/72256

Maragos, W. F., Greenamyre, J. T., Penney, J. B., Jr, & Young, A. B. (1987). Glutamate dysfunction in Alzheimer's disease: an hypothesis. Trends in Neurosciences, 10(2), 65–68. https://doi.org/10.1016/0166-2236(87)90025-7

Márquez, F., & Yassa, M. A. (2019). Neuroimaging Biomarkers for Alzheimer's Disease. Molecular neurodegeneration, 14(1), 21. doi:10.1186/s13024-019-0325-5

Masters, C. L., Bateman, R., Blennow, K., Rowe, C. C., Sperling, R. A., & Cummings, J. L. (2015). Alzheimers disease. Nature Reviews Disease Primers, 1(1). doi: 10.1038/nrdp.2015.56

Matsumura, T., Hayakawa, M., Shimada, F., Yabuki, M., Dohanish, S., Palkowitsch, P., & Yoshikawa, K. (2013). Safety of Gadopentetate Dimeglumine after 120 Million Administrations over 25 Years of Clinical Use. Magnetic Resonance in Medical Sciences, 12(4), 297–304. https://doi.org/10.2463/mrms.2013-0020

Matsuoka, Y., Gray, A.J., Hirata-Fukae, C. *et al*. J Mol Neurosci (2007) 31: 165. https://doi.org/10.1385/JMN/31:02:165

Mattson, M. P., Pedersen, W. A., Duan, W., Culmsee, C., & Camandola, S. (1999). Cellular and Molecular Mechanisms Underlying Perturbed Energy Metabolism and Neuronal Degeneration in Alzheimer's and Parkinson's Diseases. Annals of the New York Academy of Sciences, 893(1 OXIDATIVE/ENE), 154–175. https://doi.org/10.1111/j.1749-6632.1999.tb07824.x

Mawuenyega, K. G., Sigurdson, W., Ovod, V., Munsell, L., Kasten, T., Morris, J. C., … Bateman, R. J. (2010). Decreased Clearance of CNS -Amyloid in Alzheimer's Disease. Science, 330(6012), 1774–1774. https://doi.org/10.1126/science.1197623

McConathy, J., & Sheline, Y. I. (2015). Imaging biomarkers associated with cognitive decline: a review. Biological psychiatry, 77(8), 685–692. doi:10.1016/j.biopsych.2014.08.024

McGrath, J., Drummond, G., McLachlan, E., Kilkenny, C., & Wainwright, C. (2010). Guidelines for reporting experiments involving animals: the ARRIVE guidelines. British Journal of Pharmacology, 160(7), 1573–1576. https://doi.org/10.1111/j.1476-5381.2010.00873.x

McRobbie, D. W., Moore, E. A., Graves, M. J., & Prince, M. R. (2006). MRI From Picture to Proton. Cambridge University Press. https://doi.org/10.1017/cbo9780511545405

Miyata, S. (2015). New aspects in fenestrated capillary and tissue dynamics in the sensory circumventricular organs of adult brains. Frontiers in Neuroscience, 9. https://doi.org/10.3389/fnins.2015.00390

Mohammad, M. G., Tsai, V. W. W., Ruitenberg, M. J., Hassanpour, M., Li, H., Hart, P. H., … Brown, D. A. (2014). Immune cell trafficking from the brain maintains CNS

immune tolerance. Journal of Clinical Investigation, 124(3), 1228–1241. https://doi.org/10.1172/jci71544

Mola, M. G., Sparaneo, A., Gargano, C. D., Spray, D. C., Svelto, M., Frigeri, A., … Nicchia, G. P. (2016). The speed of swelling kinetics modulates cell volume regulation and calcium signaling in astrocytes: A different point of view on the role of aquaporins. Glia, 64(1), 139–154. https://doi.org/10.1002/glia.22921

Morani, A. C., Elsayes, K. M., Liu, P. S., Weadock, W. J., Szklaruk, J., Dillman, J. R., … Hussain, H. K. (2013). Abdominal applications of diffusion-weighted magnetic resonance imaging: Where do we stand. World journal of radiology, 5(3), 68–80. doi:10.4329/wjr.v5.i3.68

Morita, S., & Miyata, S. (2012). Different vascular permeability between the sensory and secretory circumventricular organs of adult mouse brain. Cell and Tissue Research, 349(2), 589–603. https://doi.org/10.1007/s00441-012-1421-9

Mullane, K., & Williams, M. (2013). Alzheimer's therapeutics: Continued clinical failures question the validity of the amyloid hypothesis—but what lies beyond? Biochemical Pharmacology, 85(3), 289–305. https://doi.org/10.1016/j.bcp.2012.11.014

Murtha, L. A., Yang, Q., Parsons, M. W., Levi, C. R., Beard, D. J., Spratt, N. J., & McLeod, D. D. (2014). Cerebrospinal fluid is drained primarily via the spinal canal and olfactory route in young and aged spontaneously hypertensive rats. Fluids and barriers of the CNS, 11, 12. doi:10.1186/2045-8118-11-12

Naganawa, S., Yamazaki, M., Kawai, H., Sone, M., & Nakashima, T. (2011). Contrast Enhancement of the Anterior Eye Segment and Subarachnoid Space: Detection in the Normal State by Heavily T2-weighted 3D FLAIR. Magnetic Resonance in Medical Sciences, 10(3), 193–199. https://doi.org/10.2463/mrms.10.193

Nair, A., & Jacob, S. (2016). A simple practice guide for dose conversion between animals and human. Journal of Basic and Clinical Pharmacy, 7(2), 27. https://doi.org/10.4103/0976-0105.177703

Nedergaard M. (2013). Neuroscience. Garbage truck of the brain. Science (New York, N.Y.), 340(6140), 1529–1530. doi:10.1126/science.1240514

Neely, J. D., Amiry-Moghaddam, M., Ottersen, O. P., Froehner, S. C., Agre, P., & Adams, M. E. (2001). Syntrophin-dependent expression and localisation of

Aquaporin-4 water channel protein. Proceedings of the National Academy of Sciences, 98(24), 14108–14113. https://doi.org/10.1073/pnas.241508198

Nielsen, S., Nagelhus, E. A., Amiry-Moghaddam, M., Bourque, C., Agre, P. C., & Ottersen, O. R. (1997). Specialised membrane domains for water transport in glial cells: High- resolution immunogold cytochemistry of aquaporin-4 in rat brain. Journal of Neuroscience, 17(1), 171-180.

Okamura, N., Furumoto, S., Fodero-Tavoletti, M. T., Mulligan, R. S., Harada, R., Yates, P., … Villemagne, V. L. (2014). Non-invasive assessment of Alzheimer's disease neurofibrillary pathology using 18F-THK5105 PET. Brain, 137(6), 1762–1771. https://doi.org/10.1093/brain/awu064

Okamura, N., Harada, R., Ishiki, A., Kikuchi, A., Nakamura, T., & Kudo, Y. (2018). The development and validation of tau PET tracers: current status and future directions. Clinical and translational imaging, 6(4), 305–316. doi:10.1007/s40336-018-0290-y

Ourselin, S., Roche, A., Prima, S., & Ayache, N. (2000). Block Matching: A General Framework to Improve Robustness of Rigid Registration of Medical Images. In Medical Image Computing and Computer-Assisted Intervention – MICCAI 2000 (pp. 557–566). Springer Berlin Heidelberg. https://doi.org/10.1007/978-3-540-40899-4_57

Panizzo, R., Kyrtatos, P., Price, A., Gadian, D., Ferretti, P., & Lythgoe, M. (2009). In vivo magnetic resonance imaging of endogenous neuroblasts labelled with a ferumoxide–polycation complex. NeuroImage, 44(4), 1239–1246. https://doi.org/10.1016/j.neuroimage.2008.10.062

Parameshwaran, K., Dhanasekaran, M., & Suppiramaniam, V. (2008). Amyloid beta peptides and glutamatergic synaptic dysregulation. Experimental Neurology, 210(1), 7–13. https://doi.org/10.1016/j.expneurol.2007.10.008

Paton, C., Hellstrom, J., Paul, B., Woodhead, J., & Hergt, J. (2011). Iolite: Freeware for the visualisation and processing of mass spectrometric data. Journal of Analytical Atomic Spectrometry, 26(12), 2508. https://doi.org/10.1039/c1ja10172b

Peng, W., Achariyar, T. M., Li, B., Liao, Y., Mestre, H., Hitomi, E., … Deane, R. (2016). Suppression of glymphatic fluid transport in a mouse model of Alzheimer's disease. Neurobiology of Disease, 93, 215–225. https://doi.org/10.1016/j.nbd.2016.05.015

Penny W.D., Friston K.J., Ashburner J.T., Kiebel S.J., Nichols T.E. (2011). Statistical Parametric Mapping: The Analysis of Functional Brain Images. Academic Press.

Plog, B. A., Mestre, H., Olveda, G. E., Sweeney, A. M., Kenney, H. M., Cove, A., … Nedergaard, M. (2018). Transcranial optical imaging reveals a pathway for optimizing the delivery of immunotherapeutics to the brain. JCI Insight, 3(20). https://doi.org/10.1172/jci.insight.120922

Pollay, M. (2010). The function and structure of the cerebrospinal fluid outflow system. Cerebrospinal Fluid Research, 7(1). https://doi.org/10.1186/1743-8454-7-9

Pollay, M., & Kaplan, R. J. (1970a). Diffusion of non-electrolytes in brain tissue. Brain Research, 17(3), 407–416. https://doi.org/10.1016/0006-8993(70)90249-0

Pollay, M., & Kaplan, R. J. (1970b). Effect of the CSF sink on thiocyanate concentration gradient in brain. American Journal of Physiology-Legacy Content, 219(3), 802–808. https://doi.org/10.1152/ajplegacy.1970.219.3.802

Radbruch, A., Weberling, L. D., Kieslich, P. J., Eidel, O., Burth, S., Kickingereder, P., … Bendszus, M. (2015). Gadolinium Retention in the Dentate Nucleus and Globus Pallidus Is Dependent on the Class of Contrast Agent. Radiology, 275(3), 783–791. https://doi.org/10.1148/radiol.2015150337

Rall, D. P., Oppelt, W. W. & Patlak, C. S. (1962). Extracellular space of brain as determined by diffusion of inulin from the ventricular system. Life Sci. Oxford 2, 43-48.

Ray, L., Iliff, J. J., & Heys, J. J. (2019). Analysis of convective and diffusive transport in the brain interstitium. Fluids and barriers of the CNS, 16(1), 6. doi:10.1186/s12987-019-0126-9

Rennels, M. L., Gregory, T. F., Blaumanis, O. R., Fujimoto, K., & Grady, P. A. (1985). Evidence for a “Paravascular” fluid circulation in the mammalian central nervous system, provided by the rapid distribution of tracer protein throughout the brain from the subarachnoid space. Brain Research, 326(1), 47–63. https://doi.org/10.1016/0006-8993(85)91383-6

Ringstad, G., Valnes, L. M., Dale, A. M., Pripp, A. H., Vatnehol, S. S., Emblem, K. E., … Eide, P. K. (2018). Brain-wide glymphatic enhancement and clearance in humans assessed with MRI. JCI insight, 3(13), e121537. doi:10.1172/jci.insight.121537

Robert, P., Lehericy, S., Grand, S., Violas, X., Fretellier, N., Idée, J.-M., … Corot, C. (2015). T1-Weighted Hypersignal in the Deep Cerebellar Nuclei After Repeated Administrations of Gadolinium-Based Contrast Agents in Healthy Rats. Investigative Radiology, 50(8), 473–480. https://doi.org/10.1097/rli.0000000000000181

Roberts, J. S., Dunn, L. B., & Rabinovici, G. D. (2013). Amyloid imaging, risk disclosure and Alzheimer's disease: ethical and practical issues. Neurodegenerative disease management, 3(3), 219–229. doi:10.2217/nmt.13.25

Rodríguez, E. M., Blázquez, J. L., & Guerra, M. (2010). The design of barriers in the hypothalamus allows the median eminence and the arcuate nucleus to enjoy private milieus: The former opens to the portal blood and the latter to the cerebrospinal fluid. Peptides, 31(4), 757–776. https://doi.org/10.1016/j.peptides.2010.01.003

Rogaev, E. I., Sherrington, R., Rogaeva, E. A., Levesque, G., Ikeda, M., Liang, Y., … George-Hyslop, P. H. S. (1995). Familial Alzheimer’s disease in kindreds with missense mutations in a gene on chromosome 1 related to the Alzheimer’s disease type 3 gene. Nature, 376(6543), 775–778. https://doi.org/10.1038/376775a0

Rogosnitzky, M., & Branch, S. (2016). Gadolinium-based contrast agent toxicity: a review of known and proposed mechanisms. BioMetals, 29(3), 365–376. https://doi.org/10.1007/s10534-016-9931-7

Rosenberg, J., Mahta, A., Koppula, K., Borys, E., & Kesari, S. (2013). Cyclophosphamide responsive primary angiitis of the CNS in a 61-year-old female. Clinical neuropathology, 32(1), 66–68. doi:10.5414/NP300513

Rountree, S. D., Chan, W., Pavlik, V. N., Darby, E. J., Siddiqui, S., & Doody, R. S. (2009). Persistent treatment with cholinesterase inhibitors and/or memantine slows clinical progression of Alzheimer disease. Alzheimer's research & therapy, 1(2), 7. doi:10.1186/alzrt7

Saladin, L. K., & Bruni, J. E. (1993). The effects of intracerebroventricular versus intravenous administration of vasopressin on intracranial pressure in the rat. Neurological Research, 15(3), 198–203. https://doi.org/10.1080/01616412.1993.11740135

Saunders, A. M., Strittmatter, W. J., Schmechel, D., St. George-Hyslop, P. H., Pericak-Vance, M. A., Joo, S. H., … Roses, A. D. (1993). Association of apolipoprotein E allele 4 with late-onset familial and sporadic Alzheimer’s disease. Neurology, 43(8), 1467–1467. https://doi.org/10.1212/wnl.43.8.1467

Scranton, R. A., Fletcher, L., Sprague, S., Jimenez, D. F., & Digicaylioglu, M. (2011). The Rostral Migratory Stream Plays a Key Role in Intranasal Delivery of Drugs into the CNS. PLoS ONE, 6(4), e18711. https://doi.org/10.1371/journal.pone.0018711

Shawkat, H., Westwood, M.-M., & Mortimer, A. (2012). Mannitol: a review of its clinical uses. Continuing Education in Anaesthesia Critical Care & Pain, 12(2), 82–85. https://doi.org/10.1093/bjaceaccp/mkr063

Sheikh-Bahaei, N., Sajjadi, S. A., Manavaki, R., & Gillard, J. H. (2017). Imaging Biomarkers in Alzheimer's Disease: A Practical Guide for Clinicians. Journal of Alzheimer's disease reports, 1(1), 71–88. doi:10.3233/ADR-170013

Sherrington, R., Froelich, S., Sorbi, S., Campion, D., Chi, H., Rogaeva, E.A., … St George-Hyslop, P.H. (1996). Alzheimer's disease associated with mutations in presenilin 2 is rare and variably penetrant. Human Molecular Genetics, 5(7), 985–988. https://doi.org/10.1093/hmg/5.7.985

Silva, A. C., Williams, D. S., & Koretsky, A. P. (1997). Evidence for the exchange of arterial spin-labeled water with tissue water in rat brain from diffusion-sensitised measurements of perfusion. Magnetic Resonance in Medicine, 38(2), 232–237. https://doi.org/10.1002/mrm.1910380211

Smith, A. J., Yao, X., Dix, J. A., Jin, B.-J., & Verkman, A. S. (2017). Test of the "glymphatic" hypothesis demonstrates diffusive and aquaporin-4-independent solute transport in rodent brain parenchyma. eLife, 6. https://doi.org/10.7554/elife.27679

Sperling, R. (2011). The potential of functional MRI as a biomarker in early Alzheimer's disease. Neurobiology of Aging, 32, S37–S43. https://doi.org/10.1016/j.neurobiolaging.2011.09.009

Stern, W. E., & Coxon, R. V. (1964). Osmolality of brain tissue and its relation to brain bulk. American Journal of Physiology-Legacy Content, 206(1), 1–7. https://doi.org/10.1152/ajplegacy.1964.206.1.1

Sun, W., Kim, H., & Moon, Y. (2010). Control of neuronal migration through rostral migration stream in mice. Anatomy & Cell Biology, 43(4), 269. https://doi.org/10.5115/acb.2010.43.4.269

Syková, E., & Nicholson, C. (2008). Diffusion in brain extracellular space. Physiological reviews, 88(4), 1277–1340. doi:10.1152/physrev.00027.2007

Takahara, T., & Kwee, T. C. (2012). Low b-value diffusion-weighted imaging: Emerging applications in the body. Journal of Magnetic Resonance Imaging, 35(6), 1266–1273. https://doi.org/10.1002/jmri.22857

Tang, J., Sheng, Y., Hu, H., & Shen, Y. (2013). Macromolecular MRI contrast agents: Structures, properties and applications. Progress in Polymer Science, 38(3–4), 462–502. https://doi.org/10.1016/j.progpolymsci.2012.07.001

Thenuwara, K., Todd, M. M., & Brian, J. E. J. (2002). Effect of Mannitol and Furosemide on Plasma Osmolality and Brain Water. Anesthesiology, 96(2), 416–421. https://doi.org/10.1097/00000542-200202000-00029

Tombaugh, T. N., & McIntyre, N. J. (1992). The Mini-Mental State Examination: A Comprehensive Review. Journal of the American Geriatrics Society, 40(9), 922–935. https://doi.org/10.1111/j.1532-5415.1992.tb01992.x

Villanueva-Meyer, J. E., Mabray, M. C., & Cha, S. (2017). Current Clinical Brain Tumor Imaging. Neurosurgery, 81(3), 397–415. https://doi.org/10.1093/neuros/nyx103

Wang, L., Benzinger, T. L., Su, Y., Christensen, J., Friedrichsen, K., Aldea, P., … Ances, B. M. (2016). Evaluation of Tau Imaging in Staging Alzheimer Disease and Revealing Interactions Between β-Amyloid and Tauopathy. JAMA neurology, 73(9), 1070–1077. doi:10.1001/jamaneurol.2016.2078

Wang, Z., Ying, Z., Bosy-Westphal, A., Zhang, J., Heller, M., Later, W., … Müller, M. J. (2012). Evaluation of specific metabolic rates of major organs and tissues: comparison between nonobese and obese women. Obesity (Silver Spring, Md.), 20(1), 95–100. doi:10.1038/oby.2011.256

Weller, R. O., Kida, S., & Zhang, E.-T. (1992). Pathways of Fluid Drainage from the Brain - Morphological Aspects and Immunological Significance in Rat and Man. Brain Pathology, 2(4), 277–284. https://doi.org/10.1111/j.1750-3639.1992.tb00704.x

Wilcox, J., Sage, M.R., & Evill, C.A. (1984). Effect of intravenous contrast material on the integrity of the blood-brain barrier. AJNR, 5; pp. 41-43

Wildsmith, K. R., Holley, M., Savage, J. C., Skerrett, R., & Landreth, G. E. (2013). Evidence for impaired amyloid β clearance in Alzheimer's disease. Alzheimer's Research & Therapy, 5(4), 33. https://doi.org/10.1186/alzrt187

Xiong, Y., Mahmood, A., & Chopp, M. (2018). Current understanding of neuroinflammation after traumatic brain injury and cell-based therapeutic opportunities. Chinese Journal of Traumatology, 21(3), 137–151. https://doi.org/10.1016/j.cjtee.2018.02.003

Xu, Z., Xiao, N., Chen, Y., Huang, H., Marshall, C., Gao, J., … Xiao, M. (2015). Deletion of aquaporin-4 in APP/PS1 mice exacerbates brain Aβ accumulation and memory deficits. Molecular neurodegeneration, 10, 58. doi:10.1186/s13024-015-0056-1

Yang, L., Kress, B. T., Weber, H. J., Thiyagarajan, M., Wang, B., Deane, R., … Nedergaard, M. (2013). Evaluating glymphatic pathway function utilizing clinically relevant intrathecal infusion of CSF tracer. Journal of translational medicine, 11, 107. doi:10.1186/1479-5876-11-107

Yushkevich, P. A., Piven, J., Hazlett, H. C., Smith, R. G., Ho, S., Gee, J. C., & Gerig, G. (2006). User-guided 3D active contour segmentation of anatomical structures: Significantly improved efficiency and reliability. NeuroImage, 31(3), 1116–1128. https://doi.org/10.1016/j.neuroimage.2006.01.015

Zamani, A. A., Kido, D. K., Morris, J. H., Lisbon, A, & Wang, A. M. (1982). Permeability of the blood-brain barrier to different doses of diatrizoate meglumine-60. AJN 3:631–634

Zhang, E. T., Inman, C. B., & Weller, R. O. (1990). Interrelationships of the pia mater and the perivascular (Virchow-Robin) spaces in the human cerebrum. Journal of anatomy, 170, 111–123.

Zlokovic, B. V. (2005). Neurovascular mechanisms of Alzheimer's neurodegeneration. Trends in Neurosciences, 28(4), 202–208. https://doi.org/10.1016/j.tins.2005.02.001

Zlokovic, B. V. (2011). Neurovascular pathways to neurodegeneration in Alzheimer's disease and other disorders. Nature reviews. Neuroscience, 12(12), 723–738. doi:10.1038/nrn3114